

Deep Observations of the GOODS-North Field from the *e*-MERGE Survey

A thesis submitted to the University of Manchester
for the degree of Doctor of Philosophy in the
Faculty of Engineering and Physical Sciences

2016

Nicholas H. Wrigley
Jodrell Bank Centre for Astrophysics
School of Physics and Astronomy

Contents

Abstract	13
Declaration	15
Copyright	17
The Author	19
Acknowledgements	21
Lay Abstract	23
1 Introduction	27
1.1 Background	27
1.2 Star Forming Galaxies (SFGs)	29
1.2.1 Synchrotron Radiation	32
1.2.2 Bremsstrahlung Radiation (free-free emission)	35
1.2.3 Thermal Emission from Dust	37
1.2.4 Radiometric Redshift Fitting	46
1.3 Active Galactic Nuclei	49
1.3.1 AGN Emission Mechanisms	53
1.4 Cosmological effects on deep field objects	55
1.4.1 Simplifying the Spectral Energy Distributions	59
1.5 Observing the Deep Field at Radio Wavelengths	62
1.5.1 <i>e</i> -MERLIN Galaxy Evolution (<i>e</i> -MERGE) Survey	63
1.5.2 <i>e</i> -MERLIN and JVL A arrays	64
1.5.3 Document Outline	66

2	Radio Telescopes, Beams and Interferometry	69
2.1	Principles of Radio Astronomy	69
2.2	Beam Functions	70
2.3	Radio Synthesis Imaging	75
2.3.1	Sensitivity of an Interferometer	80
2.3.2	Högbom Cleaning	81
2.4	Calibration	82
2.4.1	Radio Frequency Interference	83
2.5	Wide-Field Wide-Band Imaging	83
2.5.1	Curved Sky (w -term)	84
2.5.2	Bandwidth Smearing	85
2.5.3	Integration Time Smearing	86
2.5.4	The Primary Beam of an Interferometer	87
3	Development of wide-field & wide-band imaging techniques	89
3.1	Primary Beam Correction	90
3.1.1	Holography	90
3.2	Fast Wide-Field Imaging	104
3.2.1	Spectral Cleaning	109
3.3	Summary	115
4	Legacy MERLIN + VLA HDF-N imaging	117
4.1	Restoration of Contiguous Image	117
4.2	Measuring Sources	118
4.2.1	Gaussian fitting	118
4.2.2	Largest Angular Size	125
4.3	Angular Size Distribution of MERLIN+VLA Legacy Data	125
4.4	Summary	128
5	e-MERGE Observations and Imaging	129
5.1	e -MERGE Observation Strategy	129
5.2	e -MERLIN L-band data reduction	131
5.3	Imaging the e -MERLIN GOODS-N Field	135
5.3.1	Astrometric accuracy	135
5.3.2	Imaging the e -MERLIN data using Fast Wide Field Imaging	142

5.4	Imaging the JVLA GOODS-N field	144
5.4.1	JVLA C-band data reduction	144
5.4.2	C-Array Source Detections	148
5.5	A & B-array Data	151
5.6	L-band Data	154
5.7	Summary of <i>e</i> -MERGE observations	154
6	Characterising Angular Sizes of Sources in <i>e</i>-MERGE Data	159
6.1	Measuring the angular extent of sources	159
6.1.1	Petrosian Aperture	161
6.1.2	Fitting LAS major and minor axis sizes	162
6.2	Uncertainties	168
6.3	Size Distributions of <i>e</i> -MERGE galaxies	170
6.3.1	Angular Size Distributions	170
6.3.2	Linear sizes of sources	173
6.4	Summary of Angular Size Distribution	177
7	Source Classification and Flux Density Distributions	179
7.1	Classifying Galaxies	179
7.1.1	Machine Learning	180
7.2	Differential Source Counts	190
7.2.1	Generating Differential Source Counts from <i>e</i> -MERGE data . .	198
7.2.2	Probability of Deflection $P(D)$	202
7.2.3	Deriving Probabilities from SVM Data	207
7.2.4	Comparison with simulations	209
7.2.5	Comparison with other methods of classifying sources	216
7.3	Luminosities and star formation rates	218
7.3.1	Star Formation Rates	219
7.4	Summary	221
8	Conclusions and Future Work	223
8.1	Technical Innovations	224
8.1.1	Wide-Band Primary Beam Correction	224
8.1.2	High-Speed Wide-Field Wide-Band Imaging	224
8.1.3	Source Classification using Support Vector Machines	226

8.2	First <i>e</i> -MERGE Data Products	226
8.2.1	Source Size Distribution	227
8.2.2	Linear Size of Sources	228
8.2.3	Prevalence of increasing numbers of SFGs at Lower Flux Densities	228
Appendix I		229
	Source Attributes	229
Appendix II		235
	<i>e</i> -MERGE Source Plots	235
Bibliography		290
Word Count: 50,821		

List of Tables

3.1	Baseline Pair Weights.	99
3.2	<i>e</i> -MERLIN Primary Beam Polynomial Parameters.	103
5.1	<i>e</i> -MERLIN and JVLA correlator configurations.	132
5.2	Flux densities of calibrator sources derived from 3C286 bootstrapping. .	135
5.3	Legacy MERLIN source positions with <i>e</i> -MERLIN differences.	137
5.4	C-Band VLA Perley fit parameters for θ in arc minutes.	146
5.5	Bright sources detected in GOODS-N by the JVLA C-Array at 5 GHz. .	150
5.6	<i>e</i> -MERGE Data Products Sensitivity Summary.	155
7.1	<i>e</i> -MERGE Source Count Correction Factors.	205

List of Figures

1.1	The multi-band WFPC2 Hubble Deep Field.	28
1.2	A MERLIN+VLA composite of M82 at 5 GHz (Fenech et al., 2008). . .	30
1.3	SED of M82.	31
1.4	Synchrotron Radiation.	33
1.5	SED of Nearby Galaxies.	38
1.6	The FIR-Radio Correlation first observed by de Jong et al. (1985)	39
1.7	Optical/Radio Comparison of M82.	44
1.8	SED of the sky.	45
1.9	Spectral Index vs Frequency for Star-Forming Galaxies.	47
1.10	SED of 3C273.	50
1.11	AGN Unification Model.	52
1.12	VLA Image of AGN 3C405.	54
1.13	Cosmological Light Cone Geometry.	57
1.14	SED as a Function of Redshift.	58
1.15	Global SFR Density Plot.	61
1.16	<i>Spitzer</i> view of GOODS-North.	64
1.17	Photographs of <i>e</i> -MERLIN and the JVL A.	65
2.1	Simple Radio Telescope Parabolic Dish.	71
2.2	Aperture illumination distributions and their corresponding beam pat- terns.	73
2.3	A simulated telescope beam.	74
2.4	Multiplying interferometer arrangement.	76
2.5	12 hour sampling function for the <i>e</i> -MERLIN array.	79
2.6	The effects of Bandwidth and Time Smearing.	87
3.1	Holographic Scans of <i>e</i> -MERLIN Telescopes.	92

3.2	Photographs of <i>e</i> -MERLIN Telescopes.	94
3.3	An <i>e</i> -MERLIN telescope aperture illumination distribution model. . . .	95
3.4	Voltage beam derived from FFT of the gridded aperture distribution in Figure 3.3.	96
3.5	Complex Products of Antenna Beams.	98
3.6	Illustration of the <i>e</i> -MERLIN Primary Beam.	101
3.7	Axially Averaged Primary Beam Correction for <i>e</i> -MERLIN.	102
3.8	Lovell vs Non-Lovell <i>e</i> -MERLIN Array Sensitivity Ratio.	105
3.9	Fast Wide-field Imaging - first and second rotation and averaging. . . .	106
3.10	Fast Wide-field Imaging: Final Rotation & Averaging.	107
3.11	Predicted Smearing for Fast Wide Field Imaging.	108
3.12	Illustration of Induced Spectral Index across the <i>e</i> -MERLIN Primary Beam.	111
3.13	Modified Synthesised Beams.	113
3.14	Reduction of Modified Synthesised Beams.	114
4.1	The restored legacy MERLIN + VLA map of the GOODS-North Region at 1.4GHz.	119
4.2	Detection of Sources in Legacy GOODS-N Map.	120
4.3	Peak Flux Density Comparisons.	121
4.4	Gaussian Fitted Angular Sizes for Legacy Data.	122
4.5	Peak Pixel to Fitted Pixel Ratio.	123
4.6	Measuring Largest Angular Size by Direct Visual Inspection.	126
4.7	Largest Angular Size distribution from legacy MERLIN+VLA Observa- tions.	127
4.8	Largest Angular Size (LAS) Distribution of 178 Sources in the MER- LIN+VLA (A,B,C,D arrays), 1.4 GHz GOODS-N field, < 9 arcsec. with a median of 1.2 arcsec.	127
5.1	<i>e</i> -MERGE Pointing Strategy.	130
5.2	Illustration of Flagging RFI.	133
5.3	Astrometry Displacement Vectors Between the Legacy MERLIN and new <i>e</i> -MERLIN data.	136
5.4	RA and DEC Astrometric Offsets.	138
5.5	Quantifying the Radial Stretch Error.	139

5.6	RA and DEC Astrometric Corrections.	140
5.7	Astrometric Correction of the Radial Stretch Error.	141
5.8	Relative rotation of the field is less than 0.02 milliarcsec.	141
5.9	Combing Data from the three <i>e</i> -MERLIN Epochs.	143
5.10	First results from JVLA C-array C-band imaging.	147
5.11	Cross-matching JVLA results with deep VLA L-band observations. . .	149
5.12	The Wide-Angled Tail Source at Different Angular Resolutions. . . .	151
5.13	Comparison Between Fast Wide Field Imaging and CASA.	153
5.14	High Speed Imaging of the JVLA L-band Data.	156
5.15	Noise Map of the Highest Angular Resolution <i>e</i> -MERGE Data at L-band.	157
5.16	A Selection of <i>e</i> -MERGE Sources.	158
6.1	Determining the Petrosian Aperture.	162
6.2	A Source Profile used to find the Petrosian Aperture.	163
6.3	Ripple Noise.	163
6.4	Schematic Representation of Ripple Noise around a Source.	164
6.5	Angular size measurement methodology.	166
6.6	The Automatically Generated LAS of MERLIN+VLA Legacy Data. . .	167
6.7	Integral Flux Density Measurement and Derived Error.	169
6.8	<i>e</i> -MERGE LAS Distribution.	171
6.9	Optical LAS Distribution.	172
6.10	LAS Distributions as function of P_{SFG}	173
6.11	Comparison of a Bright Source at L-band and C-band.	175
6.12	Largest Angular Sizes of SFGs vs Redshift.	176
6.13	Linear Sizes of SFGs vs Redshift.	176
7.1	A typical AGN Characterised Source.	181
7.2	Characteristics of a SFG.	182
7.3	Conceptual Illustration of SVM Separation Method.	184
7.4	Plotting attributes against each other reveals clumping, used by the SVM to determine a higher dimensional hyperplane.	186
7.5	Histogram Showing the SVM Response to the Training Set.	187
7.6	ROC Curves for SVM Training Set.	188
7.7	Distribution of Classified <i>e</i> -MERGE Sources.	189
7.8	A Source with a Marginal SFG Classification.	191

7.9	A Source Classified as SFG Dominated.	192
7.10	A Source Re-classified as AGN by the SVM.	193
7.11	An Example of Euclidean Normalised Differential Source Counts.	194
7.12	Local Luminosity Function for SFGs.	195
7.13	Local Radio luminosity function for AGN (Mauch and Sadler, 2007)	196
7.14	Transformation of a Luminosity Function.	197
7.15	K-Correction Deviations.	198
7.16	The Uncorrected Differential Source Count for <i>e</i> -MERGE Sources.	199
7.17	Uncorrected <i>e</i> -MERGE Source Counts by Classification.	200
7.18	The Vernstrom $P(D)$ Source Count Result.	203
7.19	Comparison between <i>e</i> -MERGE Source Counts and the $P(D)$ result.	204
7.20	Corrected <i>e</i> -MERGE Source Counts Separated by SVM Bisect.	205
7.21	Source Counts SVM Bisect Separated Compared with Models.	206
7.22	Fitting Gaussian Distributions to the Training Set to Determine Source Probabilities.	207
7.23	Probability of AGNs and SFGs from Calibrated <i>Starburstness Scores</i>	208
7.24	Probability of AGN vs LAS does not alone produce a direct correlation.	209
7.25	Illustration of the 'Shell' model used to Simulate the AGN Source Counts.	211
7.26	Results of the AGN Source Count Simulation.	212
7.27	Probability Weighted Source Counts Compared with AGN Simulations.	213
7.28	The S-Cubed Simulation includes a radio faint population of AGN.	215
7.29	Probability Weighted Source Counts Compared with $P(D)$: AGN Residuals.	215
7.30	Q24 plots demonstrate that attributing classification based on FIR/Radio correlation alone can lead to a number of omissions and is considered a blunt discriminator tool for the radio-faint population. Incorporating morphological characteristics decreases the probability of miscategorising sources.	217
7.31	Luminosity of SFGs Plotted against Redshift.	218
7.32	The Starburst SFR Plotted against Redshift.	219
7.33	A Preliminary Global SFR Density Plot.	220
8.1	Planned Fast Wide Band Cleaning of Steep Spectrum Sources.	225

Abstract

The Great Observatories Origins Deep Survey North (GOODS-N) field, first surveyed by the *HST*, has been observed across numerous wavebands revealing populations of both Star Forming Galaxies (SFG) and Active Galactic Nuclei (AGN) over wide ranges of luminosities. It has been surmised that the evolution in the star forming population appears to diverge from that in the AGN population leading to a domination of SFGs at low flux densities. The number of starbursts can only be disentangled from the entire population if each source can be classified individually, which usually requires high angular resolution imaging. This is the motivation behind the *e*-MERLIN Galaxy Evolution survey, *e*-MERGE, which expands the depth of high resolution radio imaging in the GOODS-N field to increase the number of potentially classifiable sources. By use of wide-field imaging techniques, including a new high-speed mapping tool, together with a new semi-empirical primary beam-shape model for the *e*-MERLIN array, a deep wide-field high-resolution map is derived. This is the widest and deepest contiguous imaging yet obtained from *e*-MERLIN and JVLA observations, and yet contains less than 25% of the *e*-MERLIN data so far observed. The majority of the objects are shown to exhibit extended structure, and the angular size distribution place the median size around 1.2 arcsec, peaking between 0.5 and 0.7 arcsec. Automated algorithms are utilised to facilitate a new probabilistic classification tool based on multi-parameter correlations. 248 sources could be classified using the tool, each deriving a probability of AGN or SFG rather than forcing a binary category. Linear sizes of star-formation dominated sources are determined to lie in a range of 4 - 11 kpc, within the optical extent of galaxies. Differential source counting based on probabilistic classifications reveals that an increase in the luminosity evolution of SFGs is likely, although an apparent upturn in AGN may also exist to some lesser degree at low flux densities. The thesis establishes a clear roadmap for the remainder of the *e*-MERGE survey and a path to determine the star formation rate history of the Universe.

Declaration

No portion of the work referred to in this thesis has been submitted in support of an application for another degree or qualification of this or any other university or other institution of learning.

Nicholas H. Wrigley, January 2016.

Copyright

The author of this thesis (including any appendices and/or schedules to this thesis) owns certain copyright or related rights in it (the “Copyright”) and s/he has given The University of Manchester certain rights to use such Copyright, including for administrative purposes.

Copies of this thesis, either in full or in extracts and whether in hard or electronic copy, may be made *only* in accordance with the Copyright, Designs and Patents Act 1988 (as amended) and regulations issued under it or, where appropriate, in accordance with licensing agreements which the University has from time to time. This page must form part of any such copies made.

The ownership of certain Copyright, patents, designs, trade marks and other intellectual property (the “Intellectual Property”) and any reproductions of copyright works in the thesis, for example graphs and tables (“Reproductions”), which may be described in this thesis, may not be owned by the author and may be owned by third parties. Such Intellectual Property and Reproductions cannot and must not be made available for use without the prior written permission of the owner(s) of the relevant Intellectual Property and/or Reproductions.

Further information on the conditions under which disclosure, publication and commercialisation of this thesis, the Copyright and any Intellectual Property and/or Reproductions described in it may take place is available in the University IP Policy (see <http://www.campus.manchester.ac.uk/medialibrary/policies/intellectual-property.pdf>), in any relevant Thesis restriction declarations deposited in the University Library, The University Library’s regulations and in The University’s policy on presentation of Theses.

(see <http://www.manchester.ac.uk/library/aboutus/regulations>)

The Author

The author studied for this degree at the Jodrell Bank Centre for Astrophysics having previously obtained a MSc. by Research in Astronomy and Astrophysics (Distinction) at the University of Manchester in 2011. The results of his latest work are presented in this document.

Acknowledgements

I would like to express my gratitude to all those who have assisted and supported this ambitious project over the years, in particular my supervisor Rob Beswick, my co-supervisor Neal Jackson, principal investigator of *e*-MERGE project Tom Muxlow, my examiners Simon Garrington and Ian McHardy, and my adviser Tim O'Brien. I would also thank the United Kingdom's Science and Technology Facilities Council for funding this project and recognising its value within the sphere of scientific understanding.

Finally I would like to thank my family, friends and numerous colleagues who have all helped to inspire me throughout the development of this thesis.

Lay Abstract

The spectacular Hubble Deep Field (HDF) image, first captured in the late 1990s by the Hubble Space Telescope, resolves thousands of galaxies, each a collection of hundreds of billions of stars, spread across billions of light years and provides evidence for the evolution of galaxies over cosmic timescales. This thesis documents the creation of a radio equivalent image of the HDF (known as the Great Observatories Origins Deep Survey North field) using the United Kingdom's upgraded high resolution *e*-MERLIN 'interferometer' array of optical fibre linked radio telescopes, of which Jodrell Bank Observatory plays a central role. Observations from another radio telescope array in the United States (the Karl G. Jansky Very Large Array) is utilised to complement *e*-MERLIN observations. The resulting picture emerging is the deepest (i.e. farthest) high resolution radio image of the region to date and provides a unique view of its galaxies, since radio waves can pass unhindered through intermediate gas and dust. In particular the *e*-MERLIN observations allow us to discriminate between the two main emission processes powering them, with cosmological implications. An introduction to the astrophysics involved in measuring the two broad types of galaxies is presented, as well as an overview of radio astronomy using interferometer array techniques. It concludes with a taste of things to come from the *e*-MERGE project.

"It is far better to grasp the Universe as it really is than to persist in delusion, however satisfying and reassuring." - Carl Sagan

Nomenclature

Δ CDM	Lambda Cold Dark Matter theory
AIPS	Astronomical Imaging Processing System.
CASA	Common Astronomy Software Applications.
CLEAN	A Deconvolution Algorithm.
DFT	Direct Fourier Transform
FFT	Fast Fourier Transform.
FIR	Far Infra-Red.
GDL	GNU Data Language. An open source version of IDL.
HPBW	Half Power Beam Width.
IDL	Interactive Data Language. A proprietry scientific programming language developed by ITT Visual Information Solutions.
IMF	Initial Mass Function.
LAS	Largest Angular Size.
LNA	Low Noise Amplifier.
P(D)	Probability of Deflection detects the number count of sources below the theoretical noise limit using knowledge of the instrument's beam.
ParselTongue	A Python-like Script used with AIPS.
PBCOR	Primary Beam Correction task within AIPS.

POPS	People Oriented Parsing System.
RFI	Radio Frequency Interference.
SAD	Seek And Destroy.
SEFD	System Equivalent Flux Density.
SERPENT	An Automatic RFI Flagging.
VLBI	Very Long Baseline Interferometry
WIDAR	The JVLA Correlator.
WTMOD	Assigns relative weight to an antenna within AIPS.

Chapter 1

Introduction

1.1 Background

The Hubble Deep Field North (HDF), originally surveyed by the *Hubble Space Telescope* in the mid-1990s, is regarded as an iconic optical image revealing thousands of galaxies spread over depths measured in Gpc. The original image understandably precipitated an intense interest in the region and it has since been observed extensively at multiple wavelengths in what became known as the Great Observatories Origins Deep Survey - North (GOODS-N). Observatories involved include:

- *Hubble Space Telescope* (optical).
- The Karl G. Jansky Very Large Array (radio).
- The Multi Element Remotely Linked Interferometer Network (radio).
- *Chandra* X-ray observatory (X-ray).
- Giant Metrewave Radio Telescope (radio).
- *Spitzer* (Infrared) Space Telescope (IR).
- James Clark Maxwell Telescope (sub-mm).
- Subaru Telescope (optical/IR).
- Canada-France-Hawaii Telescope (optical).

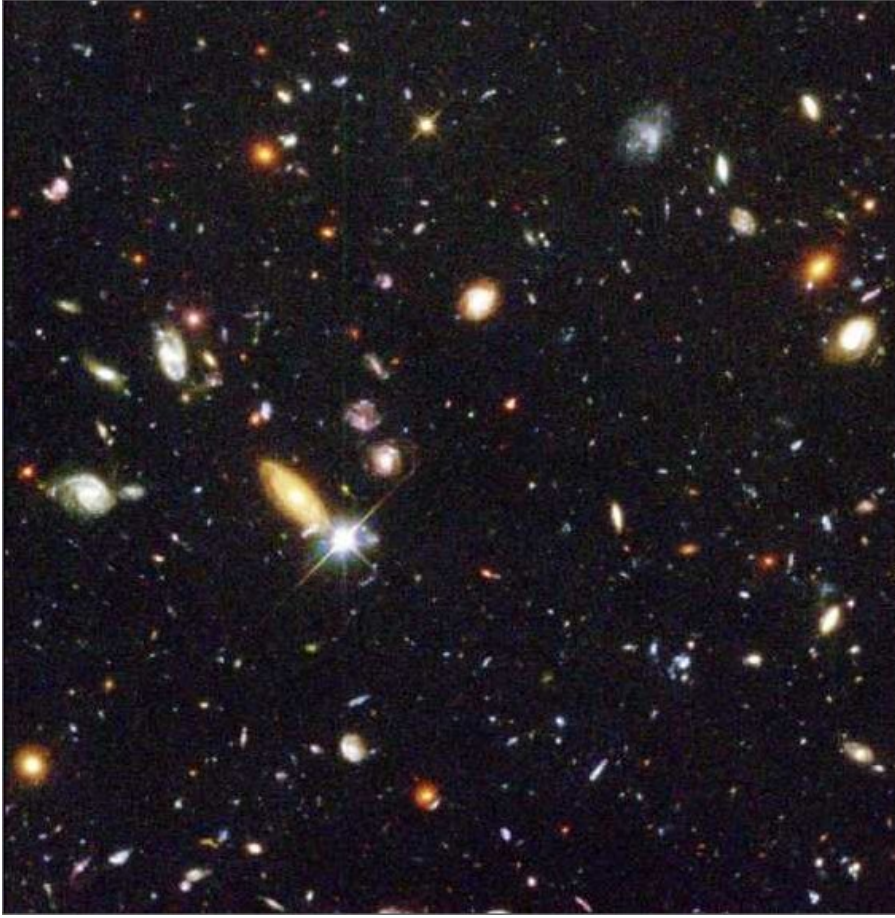


Figure 1.1: The multi-band WFPC2 Hubble Deep Field.

The ensemble of observations catalogues galaxies which can then be classified according to various criteria including morphology, brightness, spectral features or temporal variability. This broad collection of empirical data, along with those collected from other fields, is being used to help assemble models to describe the evolution of galaxies over cosmic time. The current cosmological theory (Λ CDM) places constraints on the age of the Universe of the order of 13.8 Gyr, with all the galaxies obviously evolving since. The picture of galactic evolution is, however, far from complete due to a considerable number of unknowns, for example: the rate of star formation in galaxies appears to increase as a function of redshift, but at which redshift this peaks remains uncertain. The effects that super-massive compact objects have on star-formation within galaxies is another poorly understood subject with views ranging from their encouraging star formation to those of the contrary, quenching it. Theoretical models have been incorporated into semi-empirical simulations ([Wilman et al., 2008](#)) which predict various rates

of the evolution in galaxy populations depending upon fundamental postulates, including the nature of *Dark Matter* and other cosmological parameters. However, these models cannot yet be reliably tested due to an absence of low flux density population data at high redshifts and hence requires instruments with greater sensitivities. Only deeper observations can steer astrophysicists in the right direction in determining the evolutionary history of galaxies in the Universe. The UK’s newly upgraded national radio telescope array, *e*-MERLIN (the *expanded Multi-Element Remotely Linked Interferometer Network*), will help provide such data as part of the *e*-MERGE (*e*-MERlin Galaxy Evolution) survey, capitalising on the ability of radio waves to pass through intervening gas and dust throughout the Universe.

The radio emissions from the galaxies observed within the GOODS-North field can be broadly categorised into two classifications, with some galaxies featuring characteristics of both. They are:

- Star Forming Galaxies (SFG) - whereby radio emissions are thought to be dominated by star-formation processes.
- Active Galactic Nuclei (AGN) - whereby radio emissions appear dominated by the action of super-massive compact objects at the centre of the host galaxies.

It is necessary to describe the likely emission mechanisms from these galaxies as observed in the local Universe, i.e. near redshift $z \approx 0$, before examining more remote galaxies at ancient epochs.

1.2 Star Forming Galaxies (SFGs)

These are galaxies in which the dominant radio emissions are thought to be related to star-formation, generating prominent radio features across the radio bands and also extending into the sub-mm and FIR bands. The most luminous of the SFGs are known as *starbursts*, with one of the most intensely observed being M82 (also known as NGC3034 or the Cigar galaxy) and, due to its relative proximity (~ 3.2 Mpc [Lonsdale et al. 2006](#)), yields a wealth of information about extragalactic star-forming regions. Galaxies with low star-formation rates are often known simply as ‘normal’ galaxies. One of the main objectives of *e*-MERGE is to derive star-formation rates from measured flux densities. The high angular resolution C-band¹ radio image in

¹IEEE C-band covers radio frequencies between 4 GHz and 8 GHz.

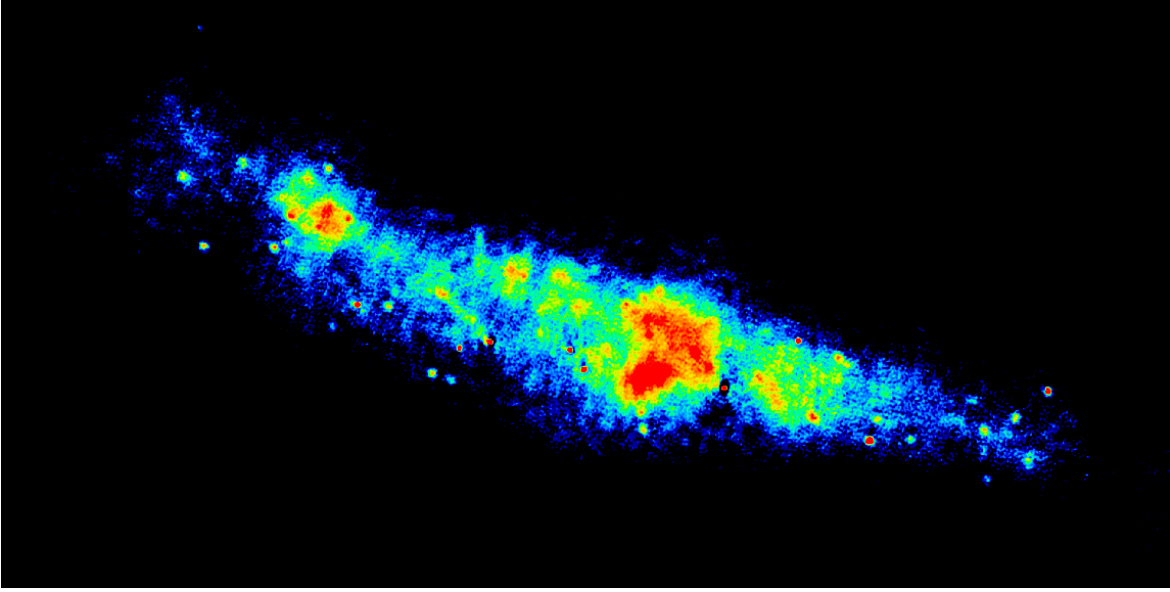


Figure 1.2: A MERLIN+VLA composite of M82 at 5 GHz (Fenech et al., 2008).

Figure 1.2 illustrates strong emissions generated by star-forming regions within M82 (viewed edge on from our vantage point in the Milky Way). Supernova remnants are observed clearly (the smaller bright circular hotspots), and provide powerful evidence of recent star formation activity amongst populations of high mass stars; such supernova events occur only in very massive, but short lived, O and B type stars. Other, more diffuse, emissions are postulated to be more ancient regions of star formation remnants. Of course, none of the more distant galaxies in the GOODS-N field are expected to be resolved to such high spatial resolution (many approximate unresolved point sources) so individual supernovae cannot be observed. Instead, only the integrated emissions of SN remnants from a galaxy are detectable. It is therefore convenient to first examine the spatially integrated *Spectral Energy Distribution* (SED) of nearby star-forming galaxies before moving out to more ancient epochs.

The SED of M82 is presented in Figure 1.3 between 1 GHz and 3000 GHz. Any telescope receiving system is restricted in bandwidth and as such, even a ‘wide-band’ system samples only a relatively narrow part of the electromagnetic spectrum. Hence to assemble an SED of a star-forming galaxy requires numerous observations using a wide range of instruments. Consequently, large populations of galaxies have been observed in relatively narrow wavebands within the SED. This method was used to assemble the SED of M82 in Figure 1.3. It can be well modelled by postulating three

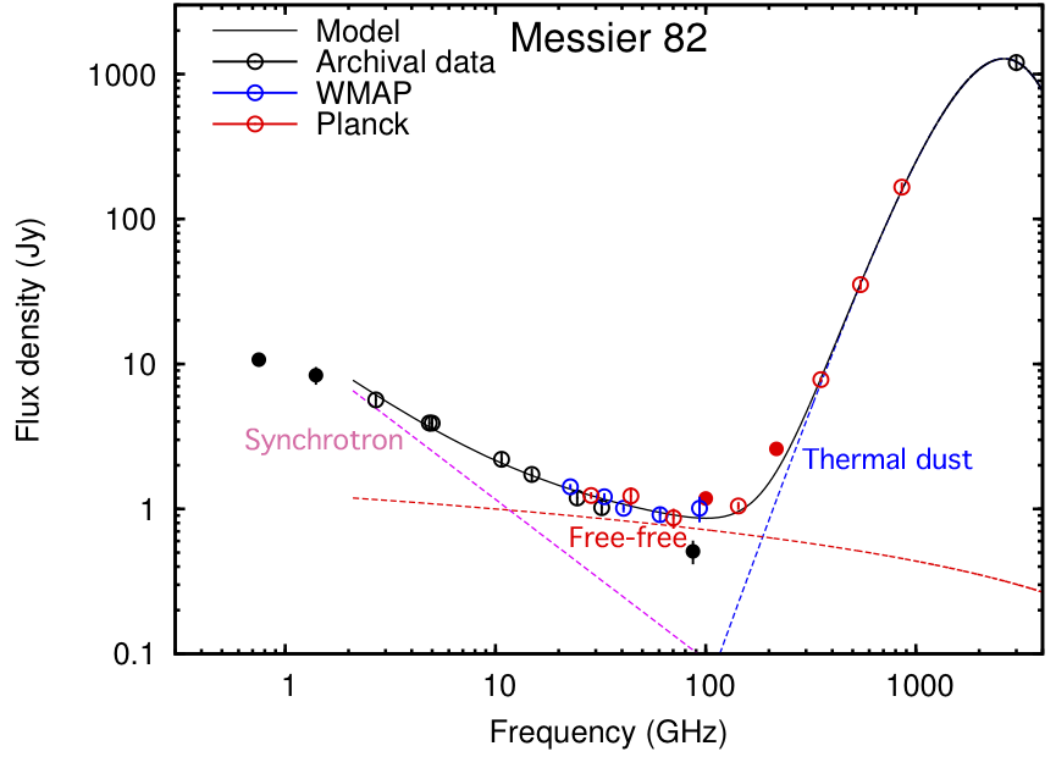


Figure 1.3: Spectral Energy Distribution of M82 derived from WMAP, Planck and other archival data (Peel et al., 2011). The solid line represents the best fit through the measurements. Estimates are derived for the 3 assumed components: Synchrotron, free-free and thermal dust emissions.

distinct emission mechanisms, all of which can, at least in principle, be traced back to star formation processes. The mechanisms are:

- Synchrotron emission,
- Free-free emission (thermal bremsstrahlung),
- FIR emission (thermal dust emission).

The reasoning by which these emissions can be traced back to star formation processes can be summarised as follows:

- Very massive stars end their lives in violent *type II supernova* explosions generating large numbers of relativistic charged particles (i.e. electrons) ([Weiler et al., 2002](#)). Relativistic electrons interact with the magnetic field of the host galaxy to produce synchrotron radiation (peaking within the radio domain).
- Those same massive stars are highly luminous and generate relatively large numbers of high energy ionising photons creating volumes of HII regions (ionised atomic hydrogen) within the surrounding Inter Stellar Medium (ISM) which in turn gives rise to thermal 'free-free' emission (across the spectrum).
- Dust in the host galaxy is opaque to these high energy photons which are therefore absorbed (i.e. the dust is heated). This is then re-radiated in a blackbody-like manner (mainly in the far infrared or FIR i.e. > 100 GHz).

The emission mechanisms are therefore fundamentally coupled to the lives of the massive stars which themselves occupy a small statistical fraction of the entire stellar population. By disentangling the flux related to each of these three mechanisms, an independent method, using each of them, can be derived to determine the number of high-mass stars in a given region. Predictions between the three mechanisms, being rooted in star-formation, are in general agreement and provide a theoretical framework for extending emissions to more remote galaxies. The characterisation of each emission mechanism is outlined in the following sections.

1.2.1 Synchrotron Radiation

It is observed in Figure 1.2 that several small bright circular features are scattered across the disk of M82 which can be reasonably identified as supernova remnants

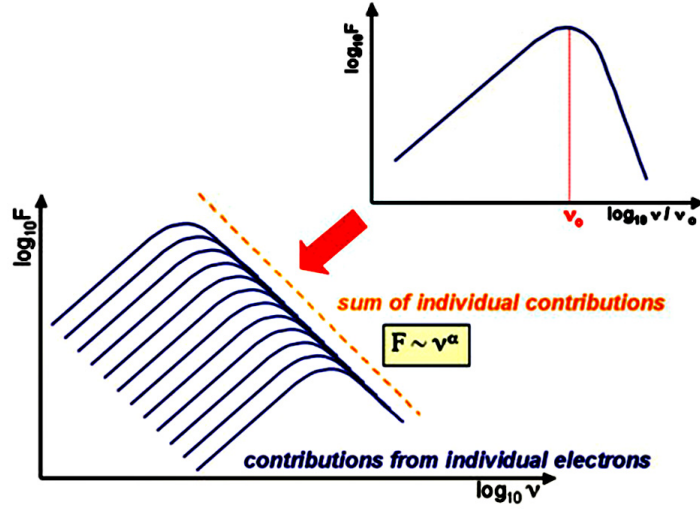


Figure 1.4: The synchrotron power spectrum from a single electron peaks and then, at high frequencies, falls sharply after ν_0 . The sum of numerous spectra from a distribution of synchrotron radiating electrons gives rise to a power law.

(Fenech et al., 2008). These are catastrophic explosions that occur in the final moments in the lives of very massive stars (type O & B). This is confirmed by monitoring the expansion of their shells, several of which have been observed in M82 over the past few decades (Fenech et al., 2010). The radio emissions are thought to be caused by shocked charged particles (electrons) which, caught in the magnetic field B of the host galaxy, tend to spiral as a result of the Lorentz force they experience. Because they are continuously accelerating they emit radiation at frequencies related to their relativistic kinetic energy. A classically accelerated electron emits in a dipole-like manner (cyclotron) but, at relativistic velocities, the beaming effect causes a cone-like radiation pattern to sweep along the helical orbit in the direction of its instantaneous velocity. In the case of a single electron, a static observer would note a brief ‘flash’ of radiation upon each sweep. The duration of each flash is related to the angular width of the beam which is inversely proportional to the Lorentz factor $\gamma = 1/\sqrt{1 - v^2/c^2}$, but the spectra of the radiation from that beam is predicted to be continuous. This continuous power spectrum generated by a single synchrotron emitting electron is emitted in a broad peak around a single frequency:

$$\nu_{crit} \propto B \sin(\theta) \gamma^2. \quad (1.1)$$

The resulting spectrum from a single electron is illustrated in Figure 1.4. In supernova

phenomena there will be numerous shocked electrons with a distribution of relativistic energies and it is the ensemble of all of these that gives rise to continuum synchrotron emission that we observe. The spectra of the sum of all emissions from the electrons likely depends upon;

- the distribution of pitch angles of the electrons relative to the magnetic field because of Equation 1.1 (or conversely the amount uniformity or order in the magnetic vector field),
- the distribution of energies in the population of electrons,
- the opacity of the ISM which is a function of photon frequency (i.e. optically thin or thick).

Distribution of energies of charged particles The derivation of the flux from a region of synchrotron emitting electrons was first given in detail in [Ginzburg and Syrovatskii \(1969\)](#) which is based on the assumption that the distribution of particle energies obeys a power law represented by

$$N(E)dE = N_0 E^{-\delta} dE, \quad (1.2)$$

where δ is known as the *particle exponent*, N is the number of particles of energy E , and N_0 is a normalisation constant. The power law approximation agrees well with cosmic ray observations ([Strong et al., 2011](#)) which are assumed to be the products of ancient high energy shock processes (including supernovae).

A crucial result is that the spectrum derived from the sum of the radiation from the ensemble of all such electrons yields an observed flux that also follows a power law:

$$S_{sync} \propto \nu^\alpha, \quad (1.3)$$

where α is known as the *spectral index* (typically ~ 0.8 for synchrotron) and is related to the particle exponent by $\alpha = \frac{\delta-1}{2}$. The spectral index is an extremely useful observable parameter, e.g. when flux vs frequency is plotted on a log-log scale it appears as the gradient and can be derived from as few as two observations at separate wavelengths.

Synchrotron Self Absorption A deviation from a constant spectral index arises because emitted low frequency photons are absorbed by some of the relativistic elec-

trons themselves (i.e. the electrons appear optically thick to lower energy photons) which introduces a fall-off at the longer wavelengths. The highest frequency at which this synchrotron self-absorption is significant is known as the *low-frequency cut-off* beyond which the spectral index will flatten, at even lower frequencies, before turning over to follow a $S_\nu \propto \nu^{5/2}$ scaling relationship. The frequency of the cut-off depends upon the electron density and temperature of the region i.e. the optical thickness of the ISM. For the electron temperatures (i.e. energy distributions) involved within starburst regions, the low frequency cut-off is of the order of a few MHz (Condon, 1992) and has a negligible effect on the SED in the range of frequencies covered in Figure 1.3. Absorption by other means (i.e. HII clouds) however is a more significant factor in the consideration of a different type of emission present in plasmas: *free-free* emission.

Synchrotron Aging This effect occurs due to the fact that the relativistic electrons are continually losing energy as they radiate. As a consequence they are slowing and have finite lifetimes, i.e. they lose energy until they no longer emit synchrotron radiation. Since higher energy electrons radiate more energy, their relative emission decreases more rapidly, resulting in a steepening of the observed spectral index. This aging process is related to the initial energy of the electron population and the magnetic field strength through which they travel.

1.2.2 Bremsstrahlung Radiation (free-free emission)

Neutral hydrogen (HI) present within the ISM becomes ionised when subjected to UV photons emitted from massive stars; these are the same stars that later become supernovae but are considered contemporary on astronomical timescales. This plasma consists of a mixture of dissociated electrons and protons (an HII region²). Close encounters of these free electrons with the protons give rise to accelerations, altering the trajectories of the electron (and slightly the ion), and each interaction hence emits photons. Because the electron is free both before and after the collision this process is often called ‘free-free’ emission. In a similar manner to synchrotron radiation, continuum emission is generated by the ensemble of numerous radiating electrons undergoing such collisions. The spectrum associated with each electron is generally ‘flat’ up to some maximum frequency where it falls off abruptly, but each spectrum associated

²HII represents ionised atomic hydrogen

with each collision of course depends upon the collision kinetic energy loss. Traditional derivations assume that the power spectrum is continuous up to some maximum value, and for collision properties characterised by a Maxwell-Boltzmann distribution, the plasma can be parametrised by a temperature. These spectra are then integrated over all energies, yielding an average power spectrum, the full derivation of which is available from numerous sources including [Condon and Ransom \(2010\)](#), [Burke \(1998\)](#) and [Longair \(1994\)](#). The acceleration of the ion is usually neglected in most treatments (its inclusion has been modelled in the past, providing a small correction; the 'simple' treatment slightly overestimates the emission) and suffices to approximate the amount of emission expected from high density³ plasma clouds. The flux emerging from the cloud is proportional to the electron temperature T_e and the optical depth τ_{ff} of the HII cloud, since it is both emitting and absorbing the radiation. This *free-free absorption* occurs when the electrons appear optically thick, i.e. at low frequencies, and so a fall-off is observed and it behaves more like a black-body. It can be modelled by the Rayleigh-Jeans Law (the low frequency approximation of Planck's Law):

$$S_{\text{low freq}} \propto kT_e \frac{\nu^2}{c^2}, \quad (1.4)$$

where k is the Boltzmann constant (i.e. S is proportional to ν^2). At the higher frequency part of the spectrum, the emission characteristics of the ensemble of the electron-ion interactions penetrates the cloud, which has an optical depth well modelled by:

$$\tau_{\text{ff}} \propto T_e^{-3/2} \nu^{-2} \overline{g_{\text{ff}}} \int n_e^2 dl, \quad (1.5)$$

([Condon, 1992](#)) where the integral term, evaluated through the line of sight of the cloud depth l with electron density n_e , is known as the *emission measure* (expressed in units $\text{cm}^{-6} \text{ pc}$) and $\overline{g_{\text{ff}}}$ is a correction term known as the *Gaunt factor* which takes into account introduced quantum mechanical deviations from the classical derivation but usually found empirically. The inclusion of the optical depth term yields a reasonable approximation for the bremsstrahlung flux emerging from an HII cloud:

$$S_{\text{free-free}} \propto kT_e \frac{\nu^2}{c^2} [1 - \exp(-\tau_{\text{ff}})] \propto \nu^{-\beta}, \quad (1.6)$$

³A high density in the ISM is regarded as perhaps $\sim 10^2$ atoms per cubic cm - a hard vacuum by laboratory standards!

which has a slope of about $\beta \sim -0.1$, i.e. fairly flat, as can be seen in Figure 1.3.

1.2.3 Thermal Emission from Dust

Dust within the subject galaxy tends to have a high opacity to high frequency radiation (UV) emitted from massive stars and so the energy is absorbed, i.e. the dust is heated. The energy is then re-radiated in a blackbody-like manner and behaves similarly to a cloud of uniform temperature. The distribution of energies of the dust particles is assumed to be Maxwell-Boltzmann-like and can be reasonably modelled by a Planck function, with a modification to account for variation in temperatures across the region caused by different dust sizes and densities. This is achieved by incorporating a spectral index β to the Planck function which parameterises the skew:

$$S_{dust} \propto \frac{h}{k} \frac{\nu^{\beta+3}}{\exp(h\nu/kT_{dust}) - 1} \quad (1.7)$$

The emission from the dust has a theoretical upper limit based on the amount of reprocessed starlight which heats the dust in the first place. The Planck function peaks in the FIR for the temperatures encountered in the ISM.

Reproducing the Spectral Energy Distribution of an entire Galaxy

The application of the physics described above allows a model to be built around each process, which when added together gives rise to a reasonable fit to the observed SED⁴. The method was carried out by [Peel et al. \(2011\)](#) to derive average physical properties of three galaxies given certain assumptions. These assumptions included the electron temperature, T_e , of the plasma regions which, using values derived from the Milky Way, is approximately 8000K. From a regression analysis, fitting to the relationships given above, the relative contributions of synchrotron, free-free and thermal emissions from dust were extracted with dust temperatures derived in the region of 19-25K. These three galaxy SEDs, plotted in Figure 1.5, are similar in appearance and are thought to be typical of numerous starburst galaxies. At low frequencies (radio) the emission is dominated by synchrotron, in the microwave by free-free and in the sub-mm/FIR by heated dust. More sophisticated SED modelling of starburst galaxies ([Groves et al.](#),

⁴Anomalies in the spectrum have been ignored such as the small contribution from spinning dust emissions ([Planck Collaboration et al., 2011](#)).

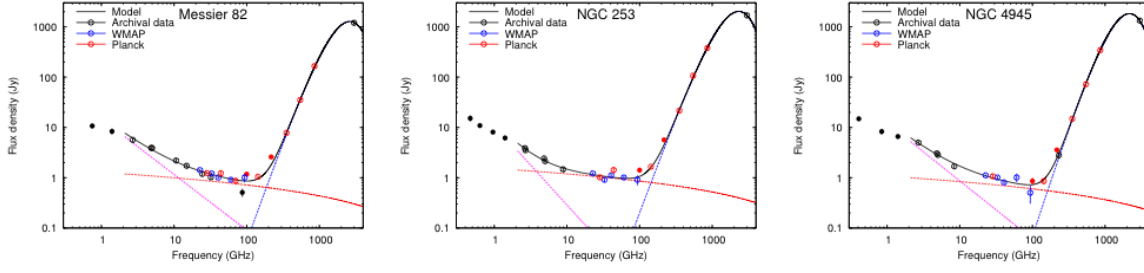


Figure 1.5: Comparison of three Spectral Energy Distributions from nearby 'starburst' galaxies (Peel et al., 2011). The deconvolved components of synchrotron, free-free and thermal dust emissions can be used to determine physical properties.

2008) features line emission over the high frequency SED band including polycyclic aromatic hydrocarbon emission and HII recombination lines, but these lie in regions of the SED not probed by radio or FIR instruments. Of particular note is that the ratio of the flux density received from thermal emissions, to the flux density received in the non-thermal emissions, is approximately the same, a feature which is not insignificant known as the *Radio Far-Infrared correlation*. To summarise, the total Spectral Energy Distribution of a galaxy with emissions dominated by dusty star-forming regions is well modelled using;

$$S_{\text{SFG}} = S_{\text{sync}} + S_{\text{free-free}} + S_{\text{dust}} \quad (1.8)$$

where scaling parameters are used with the relationships given earlier.

The fact that the SEDs in Figure 1.5 appear so similar, in particular the observation that the ratio of the flux in the FIR to the flux in the radio correlates so well, appears to be more than a coincidence. By comparing large populations in the radio bands with those same galaxies observed in the IR bands, a consistent feature emerges: a correlation between the radio flux and the FIR flux. The correlation was first observed by de Jong et al. (1985) (see Figure 1.6) using radio fluxes taken at 4.75 GHz and comparing them to fluxes derived from IRAS⁵ observations at 60 μm . Observations taken over the last 25 years have demonstrated that the correlation holds across populations of galaxies with luminosities that differ by at least five orders of magnitude. The amount of correlation is often quantified by the ratio

$$q = \log_{10} \left(\frac{FIR}{3.75 \times 10^{12} \text{Wm}^{-2}} \right) - \log_{10} \left(\frac{S_{1.4\text{GHz}}}{\text{Wm}^{-2}\text{Hz}^{-1}} \right). \quad (1.9)$$

⁵The InfraRed Astronomy Satellite (IRAS) was launched in 1983 and was the first orbital space-based observatory. It was a US/UK/Netherlands joint venture.

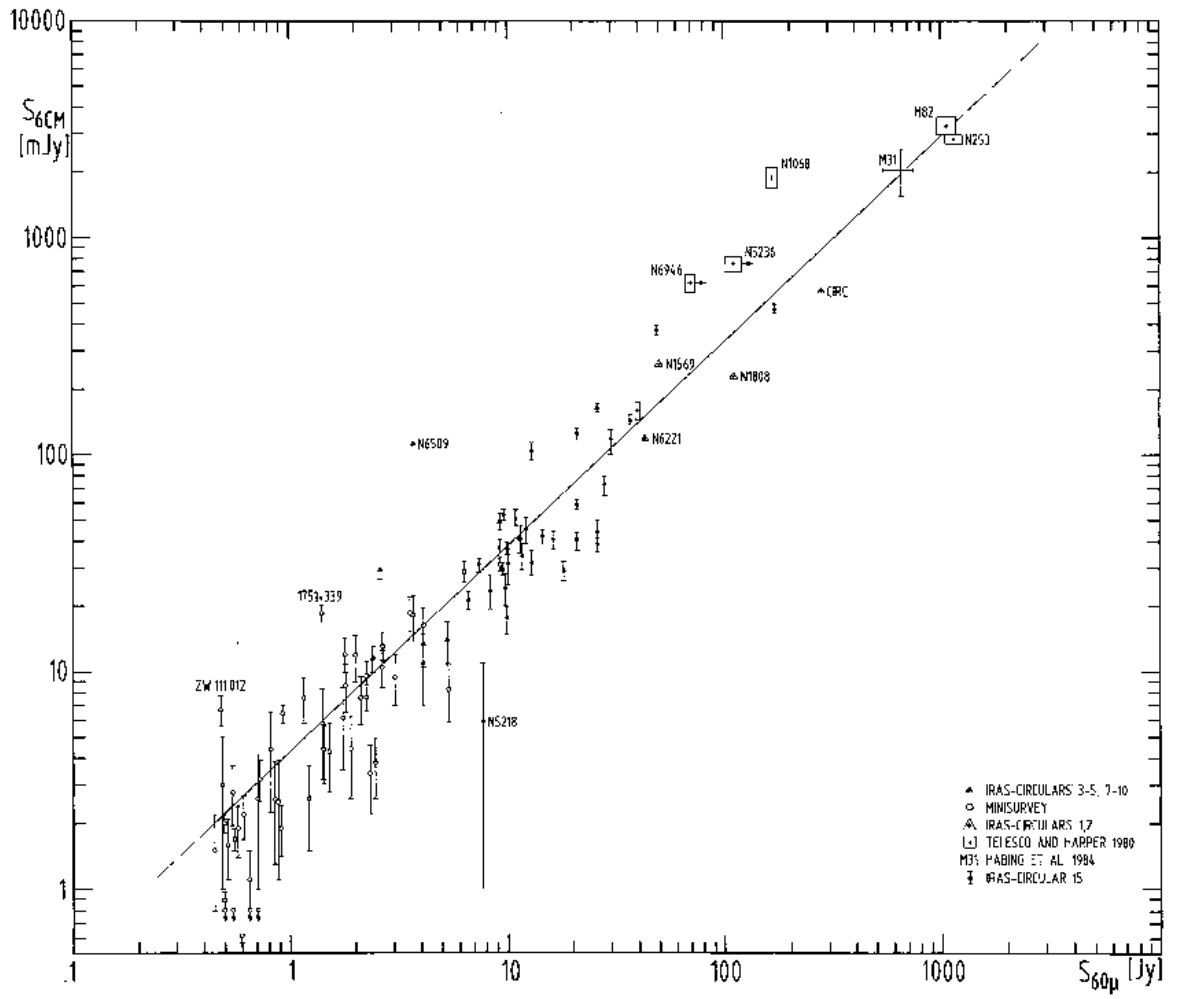


Figure 1.6: The FIR-Radio Correlation first observed by [de Jong et al. \(1985\)](#).

This remarkable linear correlation between non-thermal and thermal emission mechanisms was unexpected because simple models indicate that if the FIR emission traces the UV starlight absorbed by dust, a non-linear relationship is predicted in the radio-FIR correlation (Yun et al., 2001). The motivation for understanding the nature of the correlation is high as it could be used to derive star formation rates with more certainty *if* it can be correctly calibrated.

The physics involved is still not completely understood although several theories have been proposed, attempting to explain the Radio-FIR correlation, which can be divided into two main groups:

- Calorimeter particle confinement models (Völk, 1989),
- Non-calorimeter models (Niklas and Beck, 1997).

Work by Bell (2003) aimed to understand the correlation mechanism by introducing a dust opacity term, altering the amount of starlight re-emitted from lower luminosity galaxies. Although the exact mechanism for the correlation remains unclear, there appears to be sufficient evidence to relate the emissions in the radio band to emissions in the FIR. Rowan-Robinson et al. 1993 derived a single transformation from radio at 1.4 GHz to FIR at $60\mu\text{m}$ by multiplication of a factor of 90. The usefulness of the integrated FIR tracing the *star formation rate* (SFR) is that it can be used to derive the SFR directly. The correlation of the radio with the FIR, combined with the observation that the star formation rate is proportional to the FIR yields, in principle, the derivation of the SFR. The methods outlined below describe how the SFR can be derived from a *single radio observation*.

Star formation rate

O & B class stars are relatively short lived ($\sim 10^{7.5}$ years) objects and as such their presence is an indicator of recent star formation activity. Such massive stars make up only a small proportion of the entire population of stellar bodies forming in any one region. Numerous studies of star forming regions (molecular gas regions called nebulae) allow the derivation of a description of the abundance of masses of stars in a new cluster. The assumption that all such newly forming stars in a cluster did so within a short timescale allows *isochrones* to be established and an *Initial Mass Function* (IMF) to be empirically derived. This was first approximated by Salpeter (1955) who proposed

the form

$$\psi(m) \propto M^{-2.35}, \quad (1.10)$$

where the initial number N of stars formed per mass interval $\frac{dN}{dM} = \psi(M)$ appears as a simple power law in stellar mass M . Subsequent refinements have been made by [Miller and Scalo \(1979\)](#) who flattened the curve below $1M_{\odot}$;

$$\psi(m) \propto M^{-1.4} \quad (0.1 < M < 1M_{\odot}), \quad (1.11)$$

$$\psi(m) \propto M^{-2.5} \quad (1 < M < 10M_{\odot}), \quad (1.12)$$

$$\psi(m) \propto M^{-3.3} \quad (10 < M < 100M_{\odot}), \quad (1.13)$$

and more recently by [Kroupa \(2001\)](#), who broke the law into several log-normal domains. A more detailed review by [Chabrier \(2003\)](#) concludes that a logarithmic description should be tailored to different environments with a galaxy. A complete description of star-formation mechanisms within galaxies is beyond the scope of this project but it appears clear that parameters such as galactic rotation rate or radius from the centre of the galaxy are not significantly variable factors ([Krumholz et al., 2012](#)) when considering a galaxy as a whole. All of the IMF relationships reflect the observations that the number of high mass stars generated in a star-forming region is a small fraction of the total population. If the number of high mass stars forming per unit time can be accurately measured then these functions allow the entire population to be approximated by extrapolation. The dependance of the FIR emission from dust on highly luminous (high mass) stars has, as mentioned earlier, an assumed linear relationship, i.e. $SFR \propto L_{FIR}$. This dependence is predicted by simple scaling models ([Scoville and Soifer, 1991](#)) taking some lower limit for sufficiently luminous stars, m_l , and an upper limit, m_u , to formulate the relationship

$$L_{FIR} = 1.2 \times 10^{10} L_{\odot} \left(\frac{m_l}{1M_{\odot}} \right)^{0.23} \left(\frac{m_u}{45M_{\odot}} \right)^{0.37} \left(\frac{\Delta t_B}{10^8 \text{ yrs}} \right) SFR, \quad (1.14)$$

([Smith et al., 1998](#)) where Δt_B is the lifetime of a starburst event.

Calibration of the star formation rate

To establish solid footing of the Radio-FIR correlation several independent calibration methods are required. Such methods for estimating the SFR include:

- Supernova creation rate,
- Tracing emissions from neutral gases or ionised gases,
- Tracing emissions from dust.

Supernova Creation Rate The first method involves the straightforward counting of supernovae in nearby galaxies (usually scaled per year) which directly yields the number of high mass stars forming in the time interval of the observation. The IMF can then be applied to estimate the total equivalent SFR assuming that there is essentially no upper limit to the mass of supernova progenitors (i.e. up to the most massive stars $\sim 100M_{\odot}$)⁶ and the lower limit being the lowest mass supernova progenitor $\sim 8M_{\odot}$. The number of supernovae per unit interval, ν_{SN} , is therefore defined to be

$$\nu_{SN} = \int_{8M_{\odot}}^{100M_{\odot}} \psi(M) dM \quad (1.15)$$

and the equivalent amount of star formation above $8M_{\odot}$ in the same period is

$$\text{SFR}(> 8M_{\odot}) = \int_{8M_{\odot}}^{100M_{\odot}} M\psi(M) dM . \quad (1.16)$$

The SFR extrapolation depends upon the lower limit mass assumed for the least massive star, a brown dwarf, of perhaps $0.1M_{\odot}$. The Salpeter approximation yields a conversion from ν_{SN} to SFR to be $\text{SFR}(> 0.1M_{\odot}) \approx 135 \nu_{SN} \text{yr}^{-1}$. The more active starburst galaxy ARP220 was recently observed to have at least 49 point sources which were identified as supernovae appearing at a rate of about four per year (Lonsdale et al., 2006). This would predict $\text{SFR}(> 0.1M_{\odot})$ of the order of $540M_{\odot} \text{yr}^{-1}$ in the case of ARP220. Such objects emit greatly in the FIR and are known as Ultra Luminous InfraRed Galaxies (ULIRGs).

Tracing gases Because stars form within dense molecular gaseous *nebulae*, then emissions that trace these regions should, at least in theory, identify star forming processes. This somewhat obvious technique was pioneered by Schmidt (1959) who

⁶Stars more massive than $100M_{\odot}$ have been discovered but these are rare objects and inclusion in the IMF is poorly determined.

proposed the following simple relationship:

$$\Sigma_{SFR} \propto \Sigma_{gas}^n, \quad (1.17)$$

where Σ_{SFR} is a disk averaged *surface* SFR of a galaxy, Σ_{gas} is the disk averaged gas *surface* density and the power index n is a parameter which was found to equal approximately 1.4. The proportionality required in the scaling relationship is known as the star formation rate *efficiency*. The gas surface density could be crudely estimated by tracing columns of neutral hydrogen (HI) emissions over face-on galaxies. A SFR could then be calibrated if the efficiency can be derived. It is therefore expected that the optical extent of galaxies correlate with their radio emissions, at least for star forming galaxies (see Figure 1.7). [Bothwell et al. \(2010\)](#) observed that 1.4 GHz radio emitting regions were more compact than the emissions from CO which is expected to trace optical regions.

Tracing Ionised Gases The Schmidt power law was also reproduced by [Kennicutt \(1998\)](#) by tracing emissions from *ionised* gases in the ISM so excited by radiation from high mass stars which provided independent calibration. The reasoning is as follows - the luminosity of a star is proportional to its mass ($L \propto M^{3.5}$ for main sequence) and, because the temperature of a star is proportional to its luminosity, its potential to ionise the surrounding ISM is also proportion to its mass; a threshold temperature is related to $kT \sim 13.6\text{eV}$, i.e. the ionisation energy of hydrogen. The energised hydrogen clouds (HII regions) produce a cascade of line emissions (upon recombination) including $H\alpha$. The measurement of emission from these regions is mathematically predictable and allows the derivation of the amount of incident radiation depending on the gas density and integrated stellar luminosity. As well as being a more direct star formation tracer, in conjunction with the Kennicutt-Schmidt law above, this method can be used to determine the star formation rate efficiency. From this information [Kennicutt \(1998\)](#) derives total $SFR(> 0.1M_{\odot})$, taking into account extinction caused by dust and adopting a Miller-Scalo IMF to yield

$$SFR(> 0.1M_{\odot}) = \frac{L(H\alpha)}{1.12 \times 10^{41} \text{ergs s}^{-1}} M_{\odot} \text{yr}^{-1}, \quad (1.18)$$

where $L(H\alpha)$ is the total luminosity of hydrogen alpha. This can be used to estimate the SFR independently from the radio-FIR correlation ([Dopita et al., 2005, 2006](#)).

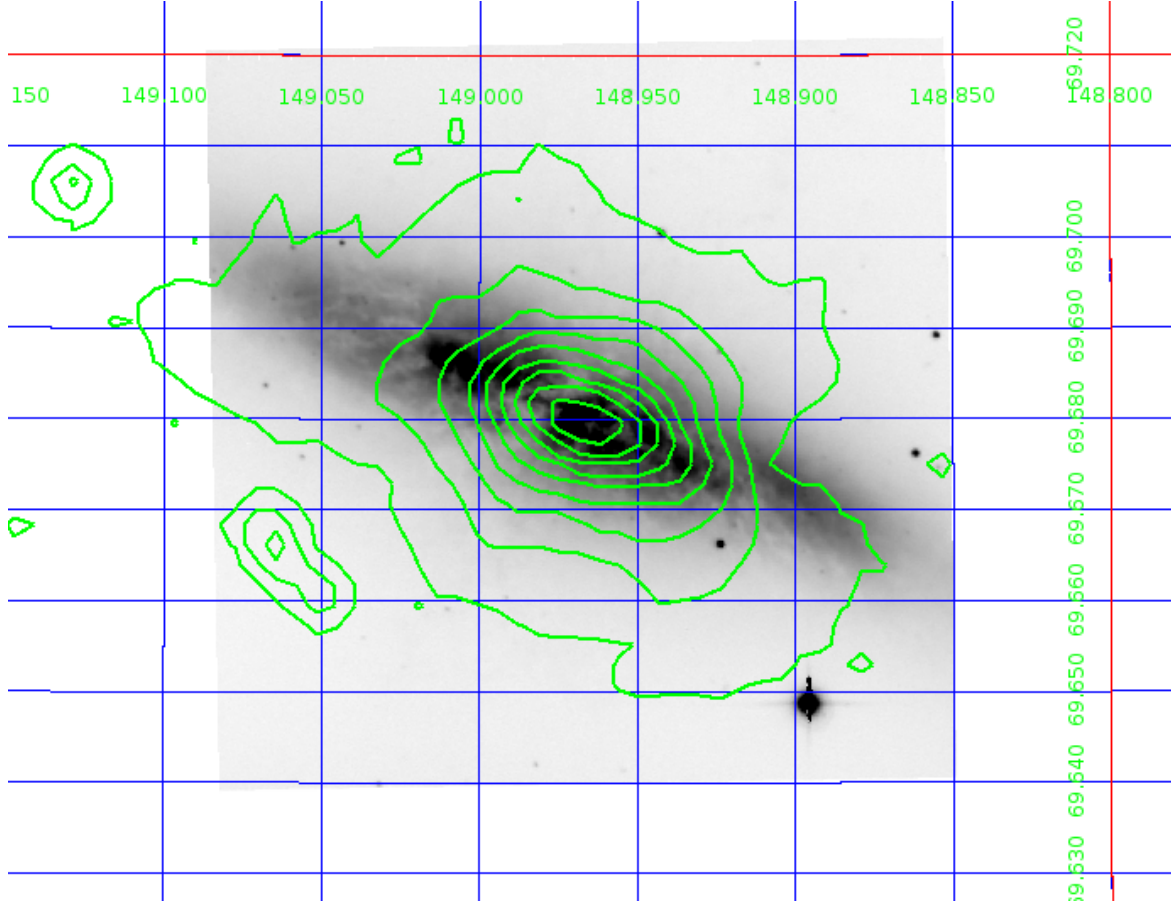


Figure 1.7: M82: Optical observation from SDSS survey (greyscale) with overlaid radio contours taken using the Westerbork array (1.5GHz). The angular extent of radio emissions from galaxies is generally smaller (1kpc from [Fenech et al. 2008](#)) than the optical extent (>10 kpc), and traces the star forming regions.

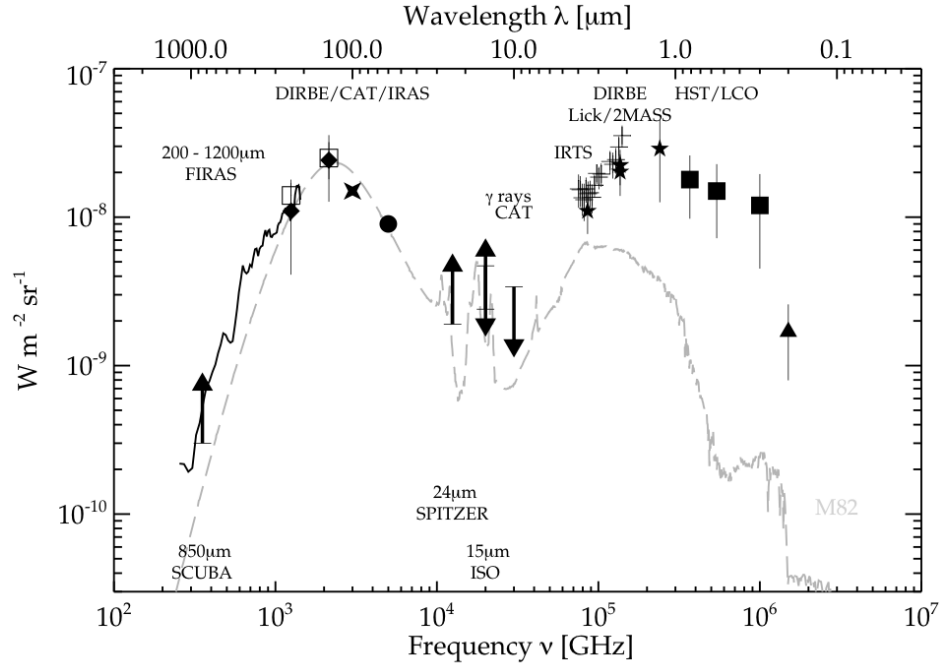


Figure 1.8: SED of spatially integrated extragalactic emissions from the sub-mm and FIR through to the optical and UV (Dole et al., 2006) demonstrating the generality of the 'double-peak'. The light-grey SED is solely that of M82 for comparison.

Other emission lines can similarly be used to provide estimates of ionised regions, which correlate well with the free-free emissions.

Dust The emissions in the FIR, caused by massive stars heating dusty material in the ISM through their absorption of optical & UV photons, re-radiates in a blackbody manner, with a luminosity dependent on the amount of dust, the opacity of the dust and, ultimately, the incident number of UV photons. Figure 1.8 illustrates a double peaked SED, in which the left-hand peak within the FIR region, is due to the re-radiated emission from stars, which forms the right-hand peak in the UV region. Since the luminosity of the dust is proportional to the UV light, and the shortest lived stars generate the largest proportion of UV, then it is reasonable to assume that the FIR luminosity traces the instantaneous SFR.

Summary

The radio emission from galaxies is observed to trace the star forming regions which lie in the plane of the disk of normal galaxies. The correlations between different emissions

in different bands and the star formation rate provide a toolkit and, especially due to the radio-FIR correlation, allow radio (and sub-mm) astronomers to estimate the SFR of an entire galaxy even if star formation regions cannot be individually resolved. Thus the broad angular sizes of such galaxies is also expected to correlate across the bands to some extent. However, it must be borne in mind that there could be, to some extent, a degree of cross-calibration. Caution must be taken when deriving star formation rates from single radio band observations due to the frequency dependance on the synchrotron to free-free ratio. The correlation in the FIR does, however, generate a method of estimating the SFR from a single band radio observations and has been described by [Cram et al. \(1998\)](#) and calibrated to take into account the relative amount of free-free in the SED by [Haarsma et al. \(2000\)](#) yielding

$$SFR_{\nu_{GHz}}(> 5M_{\odot}) = \frac{L_{\nu}}{L_{sync\star}\nu^{-0.8} + L_{ff\star}\nu^{-0.1}} M_{\odot} \text{yr}^{-1}, \quad (1.19)$$

where $L_{sync\star} = 5.3 \times 10^{21}$ and $L_{ff\star} = 5.5 \times 10^{20}$, which can be transformed to $SFR(> 0.1M_{\odot})$ by extrapolation of the IMF. The above relationship assumes that there is no contamination (i.e. additional emission) by an Active Galactic Nuclei (AGN) embedded within the galaxy. The radio emission from many galaxies is instead dominated by such emission, briefly introduced in Section 1.3.

1.2.4 Radiometric Redshift Fitting

Deriving star formation rates requires source redshifts, either from photometric or preferably spectroscopic measurements. Another potential source of obtaining redshifts is by SED fitting radio data. This radiometric technique relies on the assumption that the spectral index of an SFG changes in a continuous, predictable and well-behaved manner within the frequency range of the instrument, *multiplied* by the highest expected redshifts, such that for each redshift there exists a *unique* ratio between two flux density measurements⁷. This unique ratio exists because the emission frequency is transformed by a factor of $1 + z$ so that at reception we receive signals from a different (higher frequency) part of the SED. In the case of the highest (expected) redshift of starburst sources ($z \sim 4$) observed with the 500 MHz reception bandwidth available in

⁷There is a possibility that the SED deviates due to anomalous emission e.g. spinning dust, however this appears to be localised within galaxies and is not detectable in galaxies as a whole ([Peel et al., 2011](#)).

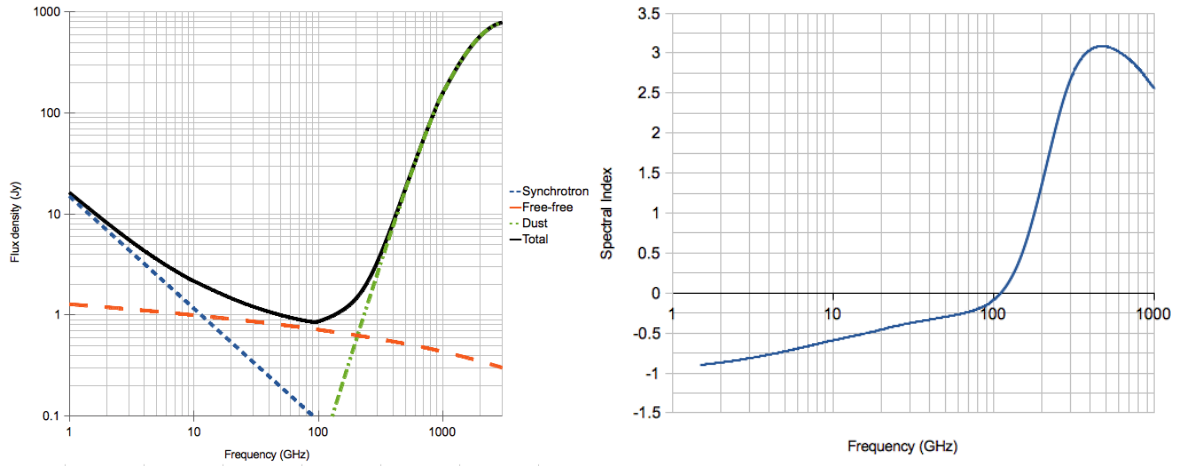


Figure 1.9: Taking the gradient of the SED of a model star forming galaxy (left) yields its spectral index as a function of frequency (right). This demonstrates that a unique flux ratio exists between fixed observing bands, L and C, depending only on the redshift of the source, for $z < 5$ and for emissions less than 90 GHz.

L-band, the integrated bandwidth on emission would be in the 7.5 GHz to 10.5 GHz region. Similarly in C-band, observing a $z = 5$ source between 5GHz and 7GHz, one actually probes an emission band between 36GHz and 42GHz. The spectral index of star-forming galaxies at high redshift therefore appears to flatten as the free-free emission component begins to dominate (assuming that the SED is the same as in nearby galaxies). Recalling the flux density SED model introduced Section 1.2, the spectral index for the emission can be investigated as a function of emission frequency by fitting a model based on physical measurements such as those derived in [Peel et al. \(2011\)](#). The absolute luminosity of the galaxy is not relevant here as the individual components have been observed to scale together, i.e. the Radio-FIR correlation ([de Jong et al., 1985](#)) described in Section 1.2.4, but the relative luminosities of the synchrotron and free emissions is what matters. Taking $\log(\Delta S)/\log(\Delta \nu)$ yields the spectral index as a function of frequency and is presented in Figure 1.9, which illustrates its well behaved nature. In the domain of the emitted frequencies from star forming galaxies likely to be encountered in the *e*-MERGE survey, the spectral index is expected to change in a log-linear manner between about -0.8 and -0.1 if there is no other emission mechanism at work. In the domain of sources observed by *e*-MERLIN and the JVL A at L and C bands, the total SED of a star forming galaxy can be approximated by considering only the dominant contributors: synchrotron and free-free emission mechanisms

$$S_{<90GHz} = S_{sync} + S_{freefree} = a\nu^\alpha + b\nu^\beta . \quad (1.20)$$

The thermal dust contribution can be neglected within the limits of flux detection since we assume $z < 5$. If the source is placed at redshifts $z \sim 5$ having an emission frequency some six times higher than the observation frequency band, i.e. a C-band detection emits at about 35 GHz (K-Band), it is expected that thermal emission from dust would start to contribute and there is no unique redshift solution. (In these cases the Raleigh Jeans approximation would need incorporating into the model to represent the upper frequency regime in order to extend the redshift range further.) A similar technique was tested by [Carilli and Yun \(1999\)](#) who examined the flux density ratio between 1.4GHz and 350GHz of M82 and ARP220 and found that the change in spectral index would work up until $z \sim 7.5$, after which the 350GHz band was transformed 'over the top' of the thermal dust Planck curve, leading to two possible redshift solutions. Other problems they encountered included the inability to morphologically distinguish SFG from AGN, being limited to VLA resolution, and therefore not able to eliminate possible AGN contamination. The high resolution of *e*-MERLIN minimises this problem and allows more confidence in positively identifying SFGs. It is predicted that approximately 250 star-forming galaxies will be found in the *e*-MERGE survey between redshifts 2 and 3 ([Muxlow and McHardy, 2011](#)) and it is the ultimate intention of the survey that the luminosities be quantified where possible so that star formation rates can be deduced. If the relationship does not become invalid at high redshifts then it implies that the form of the SED of starburst galaxies is similar for local SFGs. To estimate redshifts of galaxies (classified as SFG by morphology) using measurements from both L and C bands requires solving the following relationship for z

$$\frac{S_{\nu_L}}{S_{\nu_C}} = \frac{a((1+z)\nu_L)^\alpha + b((1+z)\nu_L)^\beta}{a((1+z)\nu_C)^\alpha + b((1+z)\nu_C)^\beta} , \quad (1.21)$$

where a, b, α and β are assumed, ν_L and ν_C are known, S_{ν_L} and S_{ν_C} are measured. Making z the subject yields:

$$z = \left(\frac{a \left(\frac{S_L}{S_C} \nu_C^\alpha - \nu_L^\alpha \right)}{b \left(\nu_L^\beta - \frac{S_L}{S_C} \nu_C^\beta \right)} \right)^{\frac{1}{\beta-\alpha}} .$$

The values of a and b are relative emission luminosities of the synchrotron and free-free components at $z = 0$ which can be taken to be the fiducial luminosities $L_{sync\star}$ and $L_{ff\star}$ respectively as used in Equation 1.19 yielding:

$$z = \left(\frac{L_{sync\star} \left(\frac{\nu_L^\gamma}{\nu_C^\gamma} \nu_C^\alpha - \nu_L^\alpha \right)}{L_{ff\star} \left(\nu_L^\beta - \frac{\nu_L^\gamma}{\nu_C^\gamma} \nu_C^\beta \right)} \right)^{\frac{1}{\beta-\alpha}},$$

where γ is the measured spectral index. By inspection the limits on γ are between -0.1 and -0.8 , with the flatter index equivalent to the greatest redshift. Whether there is sufficient signal-to-noise to obtain redshift information from the data will be examined in Chapter 6.

1.3 Active Galactic Nuclei

The other broad category of galaxies lying within the GOODS-North field are those emissions are not dominated by star forming mechanisms, but rather by accretion, and are usually considerably more luminous objects than SFGs often exhibiting jet or lobe-like extended features. Their morphology is diverse and a complex taxonomy has emerged which includes numerous classifications; it was not immediately obvious that they belong to the same class of objects. Originally discovered in the optical bands as Quasi-Stellar Objects (QSO or quasars), their appearance was stellar-like and, due to their high luminosity, were originally thought to be objects within our own galaxy with highly unusual spectral energy distributions. Their extra-galactic reality was identified from the realisation that *broad emission lines* in the spectra were that of hydrogen (Lyman alpha 121.4nm) but redshifted by over 15%, making them cosmologically redshifted objects (Peterson, 1997). The explanation generally given for the presence of broad lines is accepted to be from highly energised regions that have a range of Doppler shifts due to differential velocities, i.e. revolving around a central nucleus. The mass of the nucleus could be estimated from the rotation velocities and typically derived figures were measured in millions of solar masses. However, other features are often noted in the SED; an increase in the IR region (known as the *IR bump*) and a peak in the optical (known as the *big blue bump*). Figure 1.10 illustrates a multi-wavelength assembled SED of one of the first discovered quasars, 3C273, which was found to be variable in luminosity on time periods ranging from days to years.

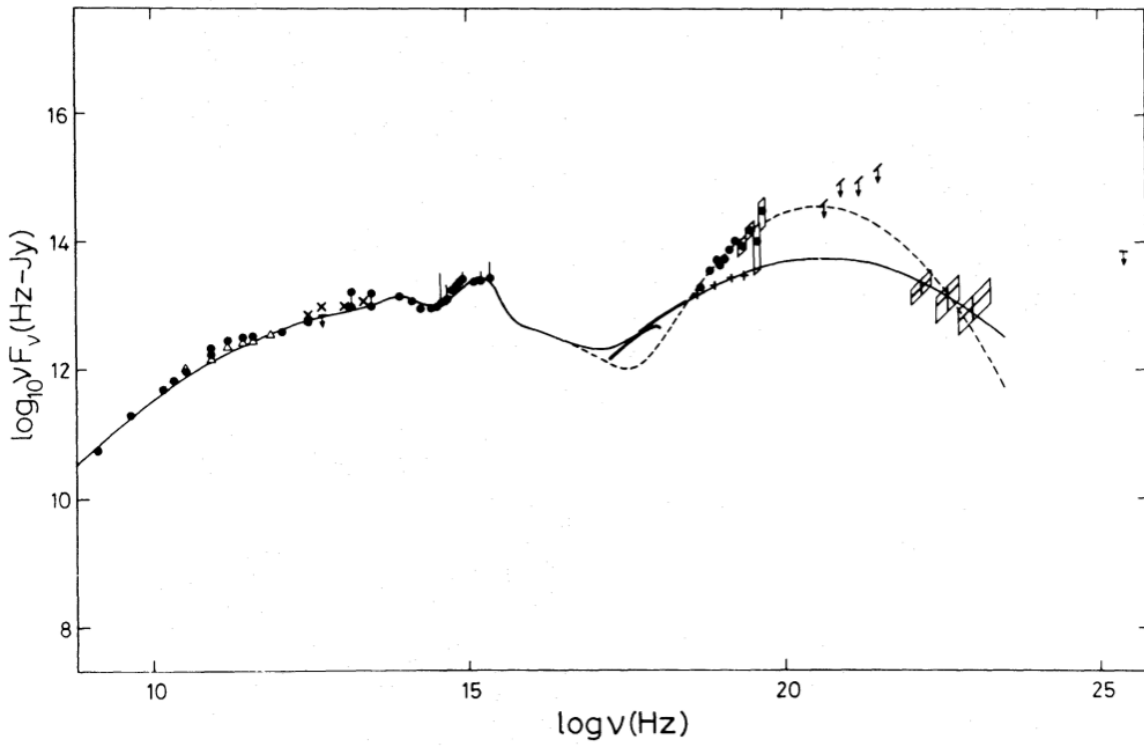


Figure 1.10: SED of 3C273 illustrating the 'IR bump' and the 'big blue bump' (Perry et al., 1987). The two curves refer to variability of emissions in 'high' and 'low' states.

Variability on such short timescales can only be reasonably explained if the source is relatively small i.e. the light travel time from one side of the emitting region to the other must be no larger than a few light days across, which strongly supports the compact object hypothesis. The modern model of these objects is therefore one of an accretion disk orbiting a *super-massive* compact object. Doppler broadening of emission lines, produced from the rotating material, yields estimates that constrain the compact size of the nucleus to densities only occupied by general relativistic physics. Unfortunately both the morphology and the SED of an AGN galaxy varies from object to object with some features being completely absent in many cases. Attempts to explain the diversity of observations, both in the SED and morphologically, include the unification scheme presented in Figure 1.11, whereby viewing the object from different orientations gives rise to different regions being visible (Antonucci, 1993; Urry and Padovani, 1995). For example, viewing the object along the jet axis predicts a Doppler brightened source, whereas viewing the same object side-on may obscure the core by the dusty disk or torus but allow a more favourable view of the lobes or jets. Spectral features such as the broad emission lines may also be absent as in the case of Seyfert 2 galaxies. However, the orientation hypothesis has been called into question in light of a recent angular size distribution analysis by Singal and Singh (2013). They observed that angular sizes of quasars did not appear to differ from those of radio galaxies in a flux limited case even though ‘one would expect a foreshortening of AGN angular size measurements’. For the purposes of this project, utilising the *e*-MERLIN array comparisons with observations made at other wavelengths shall be drawn upon where necessary. Radio galaxies were originally categorised by Fanaroff and Riley (1974) dividing them into two invented sub-classes known as FRI and FR II. FRI were morphologically characterised by their smooth jets emanating from their nucleus with brightness decreasing away from the core along the jets, whereas the label FR II was given in cases whereby the lobe ends were brighter than the core (Wold et al., 2007). In general, FR II objects appear to be more luminous objects than the FRI class but the reason for their difference in appearance is still not fully understood.

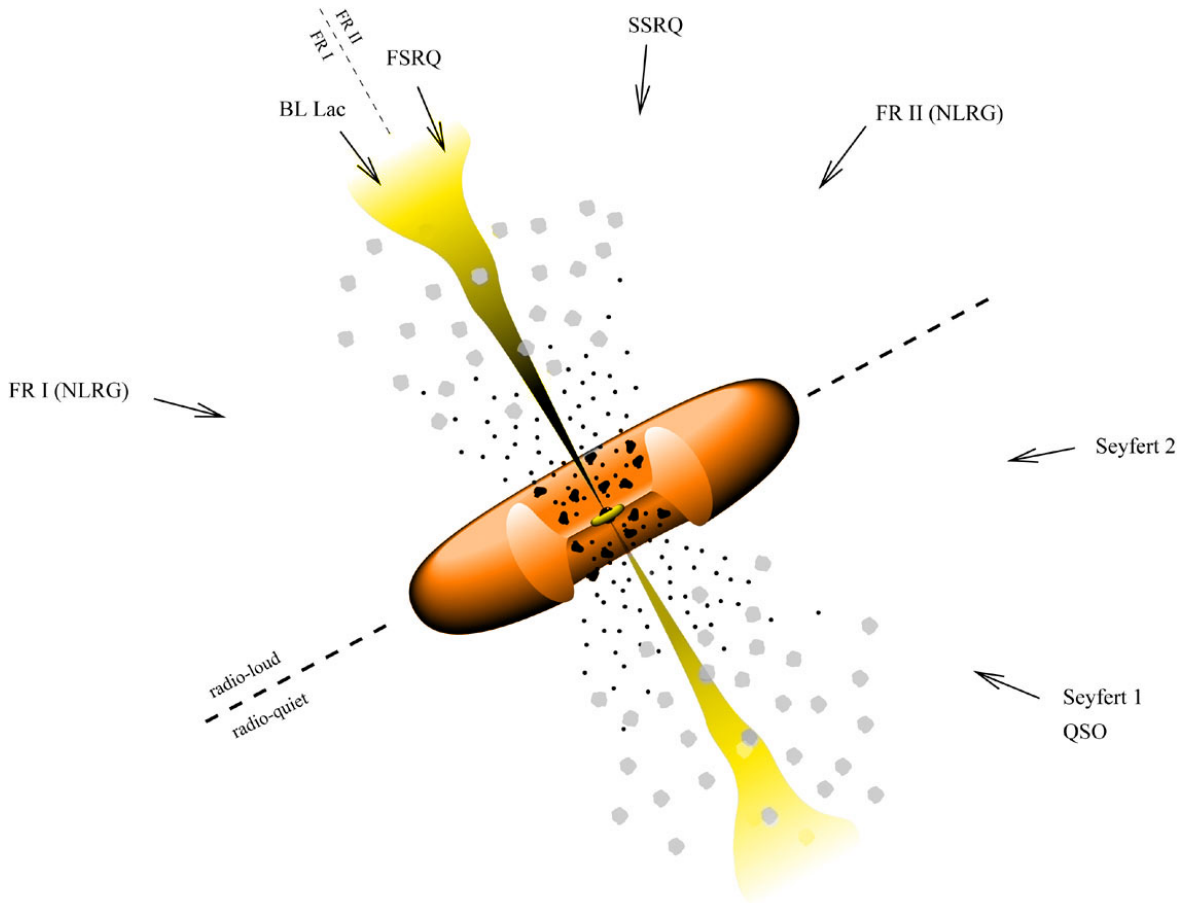


Figure 1.11: AGN unification schemes attempt to explain the diversity in observations by adopting an accretion disk model, surrounding a super massive compact object, viewed from a range of orientations ([Urry and Padovani, 1995](#)).

1.3.1 AGN Emission Mechanisms

Core emissions

AGN core emission mechanisms are thought to be powered by the accretion of material onto a super-massive compact object lying in the centre of the host galaxy. The in-falling material is heated to high temperatures within a toroidal disk-like region, surrounding the central engine, and consequently radiates energy via viscous dissipation from within the disk. The maximum luminosity generated by *spherical* accretion is given by the *Eddington Limit*:

$$L_{Edd} = 1.3 \times 10^{38} (M/M_{\odot}) \text{erg s}^{-1}, \quad (1.22)$$

([Juhan Frank, 2002](#)) although this luminosity can be circumvented (so called super-Eddington) for example by relativistic beaming effects. In reality the accretion is thought to take the form of a thin disk rather than a spherical cloud. Recent optical imaging of several AGN enhanced by gravitational lensing ([Muñoz et al., 2011](#)) enabled direct measurements of the temperature profile of a such disks which agreed with the form

$$T \propto R^{-1/p}, \quad (1.23)$$

where $p = 4/3$ and T is the disk temperature⁸. The SED of these core emissions from thin disks is predicted to have fairly flat spectral index as it derives from a broadened Planck function due to the sum of the variations in the temperature across the disk. Observations of AGN cores yield spectral indices that are not generally steep and lie in the range $0 < \alpha < 0.4$ ([Richards et al., 2007](#)).

Jet and lobe emissions

The generation of the jet is thought to arise from the existence of strong magnetic fields, that are semi-ordered and form a helical configuration ([Algaba, 2012](#)), in which particles become trapped and accelerated to relativistic velocities. The emissions are therefore predicted to be synchrotron, which is borne out by the evidence of steep spectral indices within the jets. The morphological appearance of a jet is reasonably presumed to depend on orientation to the observer with line-of-sight. Side-on views yield a Cygnus-A like appearance (see Figure 1.12) whereas direct alignment with the observer gives

⁸A full derivation of the *thin disk accretion model* is given in [Juhan Frank \(2002\)](#)

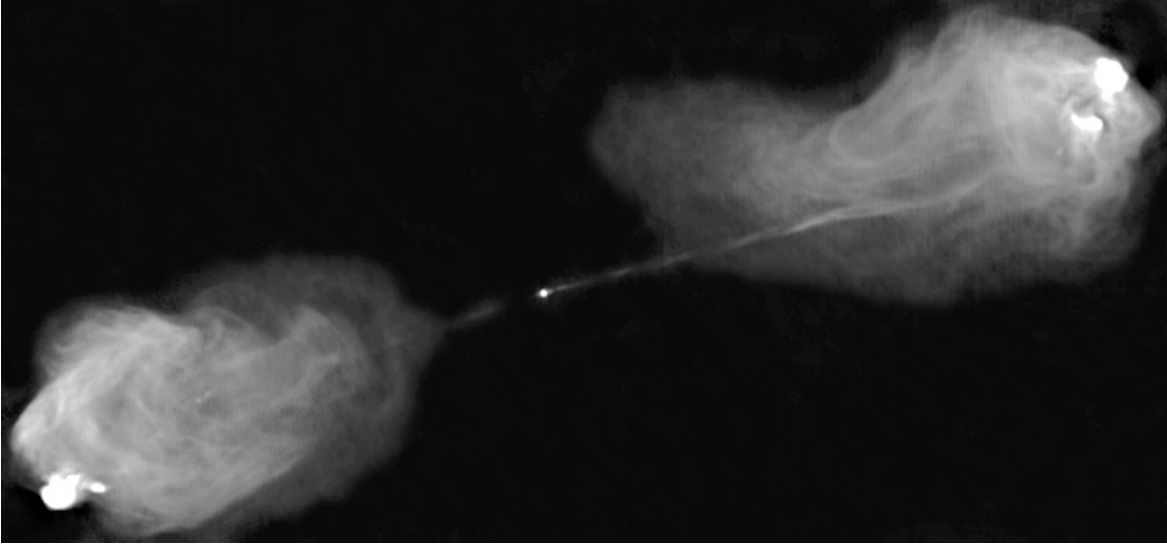


Figure 1.12: A 5GHz VLA image of nearby (230 Mpc) AGN 3C405 (Cygnus-A) illustrating core, jets, lobes and hotspot emissions ([Condon and Ransom, 2010](#)).

rise to Blazar phenomena in which relativistic beaming produces an intensely bright appearance. The lobes and hotspots are thought to be due to interaction of the jets with the intergalactic medium. In cases where there are no hotspots or prominent lobes, two hypotheses have been proposed to explain the differences between FRI and FRII appearances⁹:

- The presence or absence of lobes are due to differences in the intergalactic medium (extrinsic dependence).
- The presence or absence of lobes is due to differences in the core (intrinsic dependence).

Determining which view is correct appears to be problematic; indeed, considerable studies have been undertaken to predict whether FRI or FRII would emerge given various environmental conditions ([Gendre et al., 2011](#)) but no definitive conclusions have been reached and perhaps some combination of both intrinsic and extrinsic mechanisms are at work.

This synchrotron emission hypothesis is strengthened by the appearance of spectral steepening which occurs along the extended length of the jets (usually multiple times the optical size of the host galaxy). The populations of relativistic charged particles

⁹The unexplained differences between FRI and FRII is often called the *FRI/II dichotomy*.

tend to lose energy as they radiate and therefore this resultant lowering in energy of the whole population gives rise to a changing spectral index along the jet length (extending into the lobe). This measurement of spectral steepening can be quantified by the *spectral curvature parameter*:

$$SCP = \frac{\alpha_{\text{high}} - \alpha_{\text{low}}}{\alpha_{\text{high}} + \alpha_{\text{low}}} \quad (1.24)$$

where the α_{high} and α_{low} is the range of spectral indices within the region investigated (Sohn et al., 2003). The SCP can be a useful measure of the amount of intrinsic local acceleration of particles within jets or whether they follow simple synchrotron aging. Consequently, many AGN galaxies are reasonably modelled by a steep spectral index, at least in limited regions within the radio bands.

The spectral energy distributions of AGNs are, in general, more complicated than those associated with star forming galaxies, with spectral indices ranging from nearly flat ($\alpha \approx 0$) to very steep ($\alpha < -1$) depending on both the AGN orientation and the frequency within the SED that the flux density is measured (Richards et al., 2007).

1.4 Cosmological effects on deep field objects

So far this introduction has considered only the SEDs and morphologies of relatively *nearby* galaxies. In the GOODS-N field (and others) surveys of large populations of such galaxies are detected - indeed this is the principal reason for such studies - to determine the nature of the populations of these remote objects. Due to the finite speed of light, it is obvious that the distance to an object is directly related to its look-back-time, i.e. we observe more distant galaxies as they were at earlier epochs. The expansion of the Universe, first discovered in the 1930s by equating the redshifts to recession velocities, gives rise to several complications that alter both the flux and observed spectrum of remote galaxies including:

- The apparent angular size of a distant galaxy is related to the redshift z .
- The entire spectra (SED) of a distant galaxy is redshifted by a factor $1 + z$.
- The apparent brightness of a distant galaxy is related to its redshift z ,

where the redshift z is defined to equal $z = \frac{\lambda_{\text{observed}}}{\lambda_{\text{emitted}}} - 1$. The exact relationship between the redshift and the above properties depends upon the expansion rate of the Universe

as a function of cosmic time, and the geometry of the Universe; in other words they depend upon the cosmology¹⁰. Because of the expansion of Universe an observation of a single solid angle of sky, Ω , to some arbitrary redshift z , does not actually enclose a cone shaped volume (except at nearby redshifts $z \ll 1$), but rather a more complicated shape depending upon the cosmological expansion parameters (see Figure 1.13). Throughout this document Λ CDM cosmology is assumed with cosmological parameters: $\Omega_\Lambda = 0.7$, $\Omega_M = 0.3$ and $H_0 = 70$ km/s/Mpc. The accelerating expansion affects the expected number of sources per unit solid angle as a function of redshift, and hence the number of sources per unit volume. However, since the angular sizes of galaxies have a cosmological dependence as well as perhaps some intrinsic size evolution, then using them as standard rulers is problematic. If the ultimate objective is to determine how galaxies evolve from epoch to epoch, whether it is their spatial density or luminosity, then this important cosmological concept must be considered.

The situation is confused further because our surveys probe only a narrow band of the electromagnetic spectrum and, because the redshift of the galaxy transforms the SED frequency of the galaxy by a factor of $1+z$, a single survey samples different parts of the SED at different redshifts (epochs). This is illustrated in Figure 1.14 whereby a wide-band radio receiver (2 GHz bandwidth) is shown to record a different spectral index and flux density for the same hypothetical galaxy placed at different redshifts. In the case of star-forming galaxy, a 5 GHz radio observation would derive a lower intrinsic luminosity as the redshift increases, as the telescope probes the higher and higher frequencies in the rest-frame SED, moving away from the region dominated by synchrotron emission and into the free-free dominated region. Even more complicated is the case for AGN galaxies that may contain flat and/or steep spectral features depending upon orientation. Although core emissions are predicted to have fairly flat spectral indices, jet and lobe emissions are synchrotron based and exhibit steep spectra, so a similar situation exists in that successively increasing redshifts alter the apparent luminosity in any observed band. A more rigorous derivation for limited bandwidth observations can be obtained by representing the SED by a *source spectrum function* $\mathcal{S}(\nu)$ which, when integrated over all possible frequencies, is related to its bolometric luminosity L (Ribeiro, 2002). It can be shown that the flux observed in a frequency

¹⁰Angular diameter distance is defined to equal $d_A(z) = \frac{c}{H_0} \frac{1}{1+z} \int^z \frac{dz}{\sqrt{\Omega_M(1+z)^3 + \Omega_\Lambda}}$, the equivalent distance in a static Euclidean Universe.

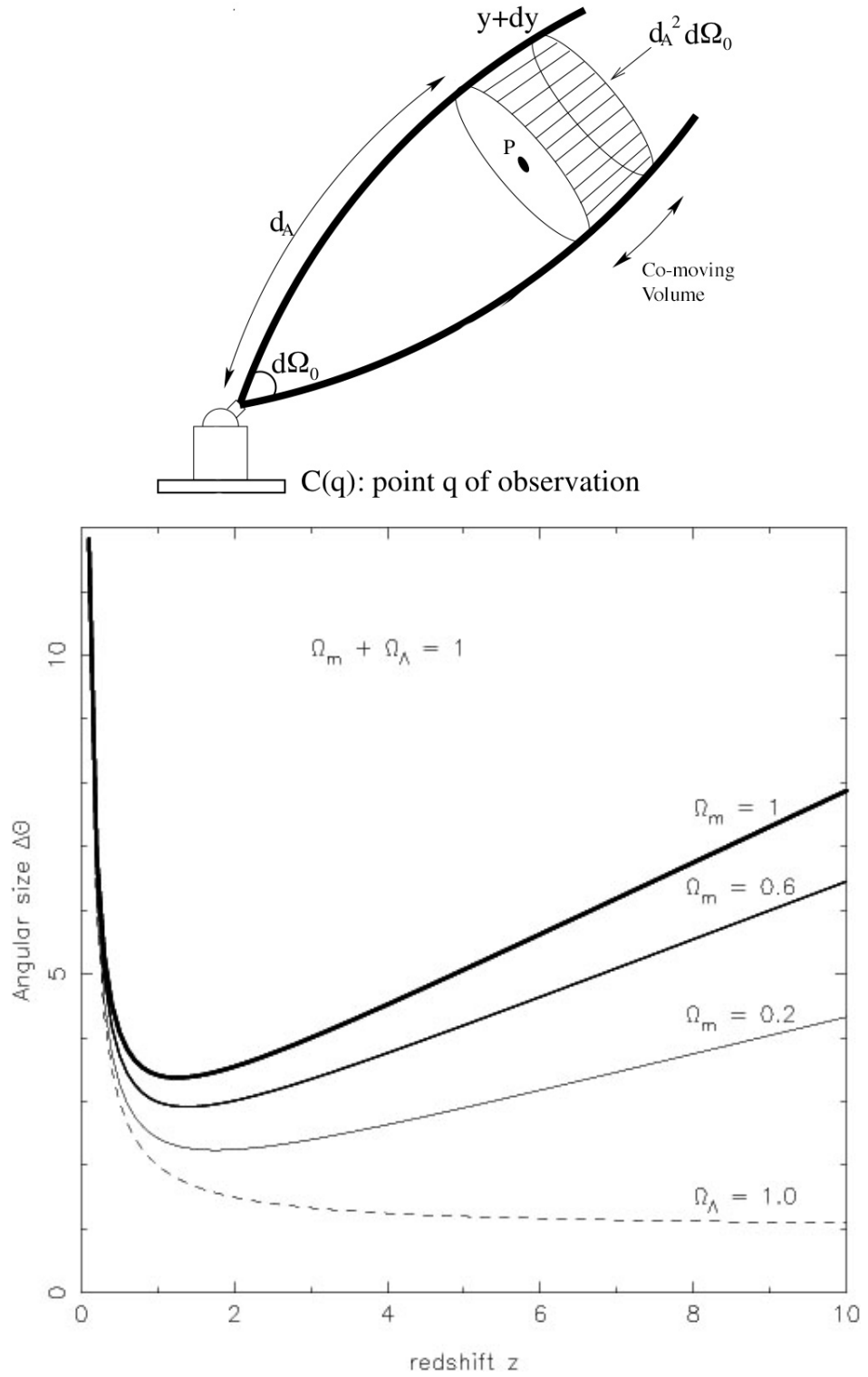


Figure 1.13: Past light 'cone' of an observer (top) is not a cone in an expanding (and accelerating) Universe (Ribeiro and Stoeger, 2003). The apparent brightness and angular size of an source depends on the angular diameter distance relationship which is a function of the cosmological parameters. Depending upon the value of the cosmological constant in Λ CDM cosmology, this deviation from $\theta \propto \frac{1}{z}$ is predicted (bottom) to yield minimum apparent size at around $z \approx 1.6$.

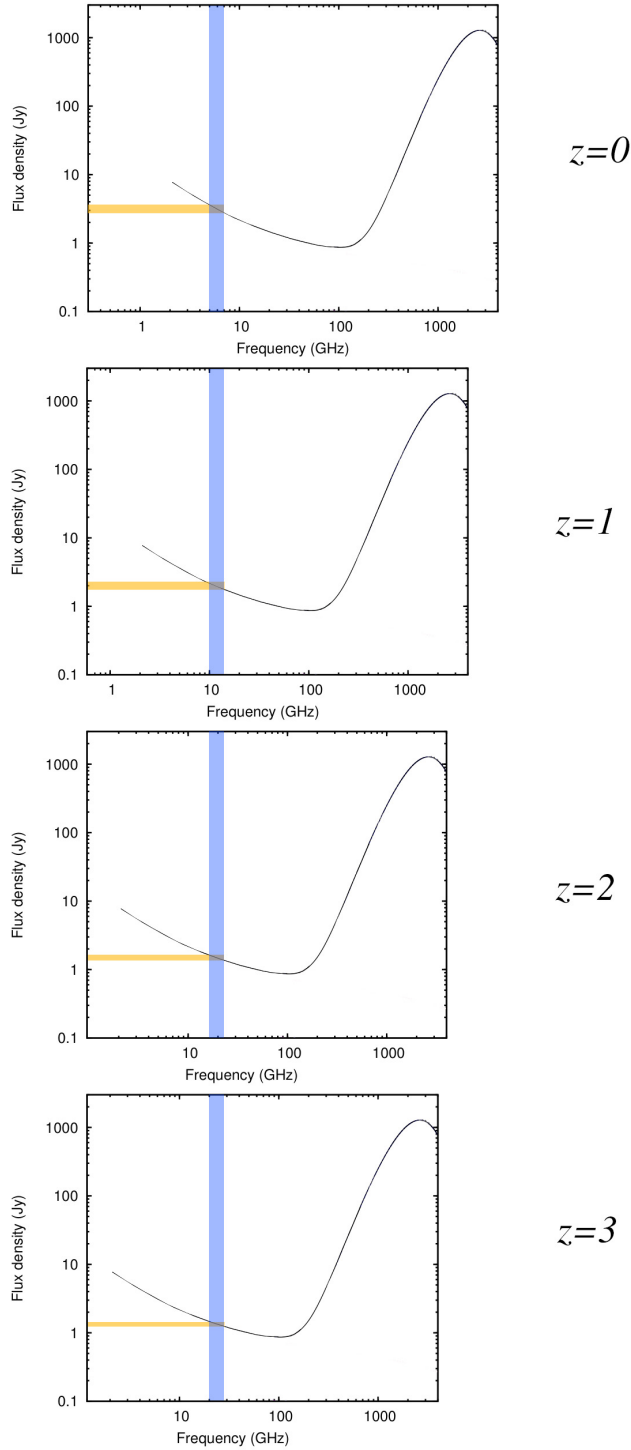


Figure 1.14: A wide-band radio telescope receiver that observes at the same hypothetical star forming galaxy, at 5 GHz, placed at increasing redshifts would measure different points in the SED and record different spectral indexes, different intrinsic luminosities and hence deduce different star formation rates if this cosmological effect was not considered. The vertical band indicates a 2GHz bandwidth of the receiver, the horizontal band illustrates that the spectral index appears relatively flatter at increasing redshift due to an increasing contribution from free-free emission. The observatory thus probes higher frequencies at higher redshifts. (SED taken from [Peel et al. \(2011\)](#))

interval $\nu, \nu + \delta\nu$ is equal to

$$S_\nu = \frac{L}{4\pi} \frac{\mathcal{S}[\nu(1+z)]}{r_0^2(1+z)^3}, \quad (1.25)$$

where $\mathcal{S}[\nu(1+z)]$ represents the change in the SED function at redshift z and $1/r_0^2$ is the ratio of the apparent solid angle subtended by the source to the angle measured in the source's rest frame, or $r_0 = \frac{d_L}{(1+z)^2}$ (Etherington, 1933), where d_L is the *luminosity distance*; $d_L(z) = (1+z)^2 d_A(z)$ (Hogg, 1999). The possible redshift dependence in the SED itself, which may include a modification in the bolometric luminosity of the source, presents significant problems in transforming observations at high redshifts to intrinsic quantities of the object. A full derivation reveals relationships that require more parameters than are observable. For example r_0 requires knowledge of the correct cosmology¹¹. Instead it is necessary to adopt a set of values to *define* the luminosity distance based on that particular cosmology to compensate for these angular size transformations. Results from the *WMAP* and *Planck* satellites have constrained the cosmological parameters and allow a tentative reduction in these unknowns. Another significant simplification can be made if it is assumed that the SED takes the same form at all epochs, which gives rise to the relationship (Ribeiro, 2002)

$$\mathcal{S}[\nu(1+z)]d\nu = \frac{\mathcal{S}(\nu)}{1+z}d\nu. \quad (1.26)$$

This simplification allows the transformation the flux observed to that emitted at redshift z to equal

$$K = \frac{\int_0^\infty \mathcal{S}(\nu)d\nu}{\int_0^\infty \mathcal{S}[\nu(1+z)]d\nu}, \quad (1.27)$$

where K has become known as the 'K-correction'.

1.4.1 Simplifying the Spectral Energy Distributions

A further simplification is generally adopted when investigating populations of galaxies in the deep field. If the SED can be represented as a power law *within a limited radio frequency range* then its intrinsic luminosity can be deduced provided that the redshift is known. This permits astronomers to investigate the luminosity of galaxies as a

¹¹AGN jet lengths or lobes sizes were once hoped to be provide a cosmological yardstick, but unfortunately this does not appear to be the case.

function of redshift. Applying this $S \propto \nu^\alpha$ relationship to the radio SED of a SFG yields a reasonable approximation for the rest frame flux S' :

$$S' = \frac{(1+z)^{1+\alpha}}{S}, \quad (1.28)$$

where the spectral index is assumed for a synchrotron dominated source defined earlier. The flux density can then be transformed into an intrinsic luminosity using

$$L(\nu) = \frac{4\pi S(\nu) d_L^2}{(1+z)^{1+\alpha}}, \quad (1.29)$$

where d_L is the luminosity distance with values depending on the assumed cosmological model.

Once luminosities have been derived for galaxies as a function of redshift it becomes possible for the star formation rate to be derived using the techniques outlined in Section 1.2.4 (Equation 1.19), provided that the FIR/radio correlation is valid at higher redshifts. The SFR per unit (co-moving) volume was first plotted for large samples of galaxies by (Madau et al., 1996; Lilly et al., 1996) in which a non-varying source SED was assumed in order to derive a luminosity to convert to a SFR for each galaxy. This was followed up more recently by Hopkins (2007); Seymour et al. (2008) who adopt a Λ CDM cosmology,¹² correcting for the expansion of the Universe, to obtain the SFR per co-moving volume measured in $\text{M}_\odot \text{yr}^{-1} \text{Mpc}^{-3}$. Given the uncertainties it is still useful to comment on the 'Madau-Lilly' plots in Figure 1.15. The radio-only derived star formation rate history of the Universe indicates that it appears to increase with increasing redshift until about $z \approx 2$, after which it could remain constant, continue to rise, or begin to fall again. Incorporating more recent measurements from the UV bands appear to agree that the peak is around $z = 2$. However, it includes derived obscuration factors based on column densities and redshifts. Obtaining deeper, more reliable obscuration-free radio derivations is desirable. Only more sensitive observations will be able to confirm at which epoch (the median redshift for SFGs is so far 'only' about 0.8) the peak SFR lies. The error bars in Figure 1.15 reflect the increasing possible errors in relating observed radio flux to star formation rate which include the following uncertainties:

¹²The Lambda Cold Dark Matter (Λ CDM) model of the Universe includes a cosmological constant to produce an accelerating expansion but is geometrically 'flat' i.e. $\Omega_\Lambda + \Omega_M + \Omega_k = 1$ where $\Omega_k = 0$.

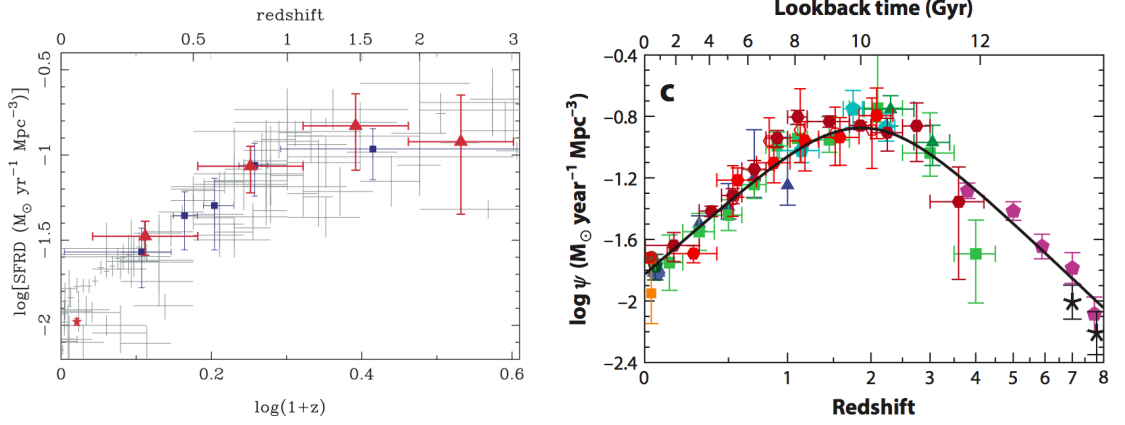


Figure 1.15: Star-Formation Rate per unit co-moving volume as a function of redshift (Seymour et al., 2008) derived from single band radio flux measurements (left). Uncertainties include Poisson, luminosity evolution uncertainties and sample variance ($<20\%$). Including multiband (UV) measurements (right), with derived obscuration factors, appear to rise to a peak at $z = 2.3$ (right) taken from (Madau and Dickinson, 2014).

SED not really approximated by power law This would affect luminosity measurements made at very high redshifts and at very high radio frequencies because the SED begins to flatten and the free-free emission component begins to dominate. The possibility that early SFG SEDs significantly differ from those of late type galaxies is difficult to test directly from single band data. The SFR is derived from the assumption that the SED is the same and any attempt to investigate otherwise is circular. Instead astronomers turn to mathematical computer simulations which model populations of galaxies with numerous variable physical parameters with the objective being to replicate the observable data.

Uncertainties in radio-flux to star-formation-rate This questions the validity that the radio traces the SFR rate, as was calibrated for local galaxies. However, if the SEDs are similar at deeper redshifts then evidence of this would be that the FIR radio correlation should still hold - a hypothesis tested by Garrett (2002) who found a good correlation within the GOODS-N region out to $z \sim 1.4$. This correlation was extended by Mao et al. (2011), using the VLA and Spitzer Space Telescope, to at least $z \sim 2$. Accepting that the SEDs are similar for SFGs at higher redshifts is of considerable use¹³ (Klamer et al., 2007; Bourne et al., 2011). This generates some confidence in

¹³The sub-mm band, which generally traces cooler dust, may show some signs of evolution in the correlation at significantly lower redshifts (Jarvis et al., 2010).

the hypothesis that the radio flux traces the SFR, but a slow evolution away from this correlation is suspected at higher redshifts.

Confusion in identifying SFG for AGN This third point arises because of errors in the selection of SFGs: AGN contamination must not be included in derived star formation rates. However, high redshift galaxies are often unresolved by the instrument (due to angular resolution limitations) so the morphology of the galaxy cannot be obtained directly for all the sources. Also, because the spectral indices of AGNs and SFGs overlap to some extent, so selecting by α is problematic and should rarely be used alone. High resolution radio observations that can resolve AGN cores embedded within SFGs will reduce uncertainties. Radio observations which do not suffer from extinction effects that plague IR, optical and UV bands are therefore of considerable advantage.

Difficulty in obtaining redshift data This would create an obvious barrier in determining the luminosity and lead to incomplete sampling and possible under-estimating of the number of galaxies per unit volume. Problems of extinction caused by intervening material would also lead to considerable contamination.

Cosmic Variance A limited survey size increases the possibility that the sample contains unrepresentative sources. Larger survey sizes minimise this effect.

Malmquist Bias Any survey preferentially selects against the higher redshift sources, which leads to an increasing underestimate of the number count of those objects and therefore any global star formation rates derived from them.

1.5 Observing the Deep Field at Radio Wavelengths

Examination of nearby galaxy SEDs, luminosity functions and deep field population counting has revealed a tangled picture of the evolution of galaxies. Due to uncertainties in the extent of evolution in density and spectral indices of the most distant galaxies, a significant range in predictions both in number counts of AGN and SFGs at the sub-mJy flux densities exists. The obvious method to constrain these parameters further is to observe populations at the sub-mJy region using a combination of

high sensitivity, high angular resolution and wide bandwidth imaging. Using evolution modelling, [Wilman et al. \(2008\)](#) produced a semi-empirical projection (called S-cubed) to determine the number of expected sources within any flux density interval in a virtual sky (to assist in design specifications for next generation radio telescope arrays such as the SKA). The predictions were in agreement with analytical models that the number of SFG sources should increase in relation to the AGN sources at the lowest flux densities. However, recent work by ([Prandoni, 2010](#)) suggests that many sub-mJy sources could be 'radio faint' AGN accounting for a significant fraction of these sources, and reduce the necessary amount of evolution in the SFG population. This can be investigated by the use of *differential source counting* (see Chapter 7, Section 7.2). The S-cubed model was used to produce an estimate of the number of sources that could be found within the GOODS-N region in the *e*-MERGE survey ([Muxlow and McHardy, 2011](#)) - the latest ultra deep radio survey of the field.

1.5.1 *e*-MERLIN Galaxy Evolution (*e*-MERGE) Survey

e-MERGE is high angular resolution L-band & C-band imaging survey using the *e*-MERLIN array, in which over 600 hours of observations will be combined at L-band and C-band observations taken by the Karl G. Jansky VLA array in New Mexico, USA. (Wide-band VLA observations are essential in recovering flux from diffuse sources that *e*-MERLIN is not sensitive to due to its lack of short baselines.) Previous studies involving MERLIN and VLA combination mapping ([Muxlow et al., 2005](#); [Beswick et al., 2006](#)) have demonstrated its effectiveness in distinguishing between starburst and AGN components, directly by morphology. The *e*-MERGE mapping will produce the deepest wide-field high angular resolution image of GOODS-North to date. The observations taken at 5 GHz will allow the spectral indexes of the sources to be determined. The observations should therefore gather data essential to untangling the evolution of galaxies and probe to a maximum redshift of $z \sim 5$. The high resolution imaging combined from the array's wide bandwidth will allow spectral features of bright sources to be examined in combination with their morphology raising the possibility of creating *spectral maps* of selected objects.¹⁴ The data will be used in conjunction with the latest results from other observatories such as *Spitzer* space observatory (FIR/sub-mm) but is a legacy project and will take many years to reduce the enormous amounts of data

¹⁴Spectral mapping uses multi-frequency synthesis techniques but requires sufficient signal to noise ratio such that sub-band imaging is greater than $\sim 10\sigma$.

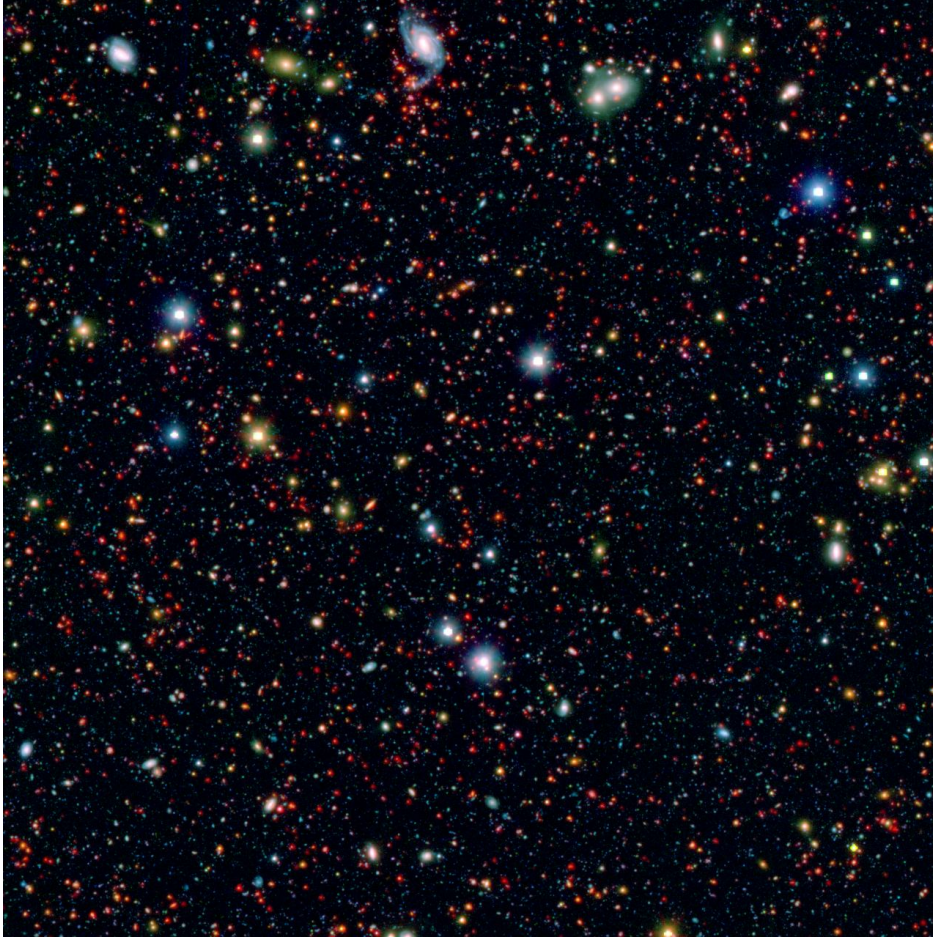


Figure 1.16: A GOODS-N image from the *Spitzer* Space Observatory will, amongst others, be used to investigate sources in the radio ultra deep field.

expected.

1.5.2 *e*-MERLIN and JVLA arrays

The *e*-MERLIN array consists of seven radio telescope spread across the UK countryside from Cheshire to Cambridgeshire¹⁵ and produces images by transmitting the data by optical fibre links, to its headquarters at Jodrell Bank Observatory, where the 76m Lovell telescope is situated. Observations are made at L-band (1.25 -1.75 GHz) and at C-band (4.5 - 6.5 GHz).

The JVLA consists of 27 radio telescopes situated in the desert of New Mexico with movable 25m dish antennas spread over a maximum separation distance of 36km. The

¹⁵The *e*-MERLIN array may ultimately be expanded to include a telescope at Goonhilly, Cornwall.



Figure 1.17: The observatories participating in the e -MERGE survey: the e -MERLIN array (top) and the JVLA (bottom).

telescopes are moved (along rails) every 6 months to form 4 different configurations. The 4 VLA configurations are as follows:

- A-array (highest angular resolution),
- B-array,
- C-array,
- D-array (lowest angular resolution).

The different configurations of the VLA sample different scale ranges on the sky, and when used in combination, create a more completely spatially sampled image.

1.5.3 Document Outline

This thesis focuses on deriving high resolution radio imaging of the GOODS-N field to include the full usable primary beam of the *e*-MERLIN array in L-band. The project represents the first results of the *e*-MERGE survey, which is still being actively observed at the time of writing, and sets a roadmap for data reduction and analysis. Techniques are developed to allow rapid imaging, particularly important due to the time constraints placed on the project, before the existing data are analysed to yield the first results.

- Chapter 2 introduces the techniques of radio interferometry involved in successfully obtaining radio images and pays particular attention to the limitations that are pertinent to wide-field and wide-band imaging. These include field-of-view effects such as bandwidth smearing, integration time smearing, curved sky distortions and crucially *primary beam* attenuations as a function of observing wavelength, which leads to induced spectral index effects.
- Chapter 3 describes the development of high speed imaging techniques including the development of a primary beam model for the *e*-MERLIN array. The primary beam correction model is described and calibrated using voltage maps obtained from the telescopes within the *e*-MERLIN array.
- Chapter 4 provides a brief review of legacy MERLIN + VLA imaging which is made contiguous for the first time, illustrating the dominance of extended objects.

These data will be used in combination with new *e*-MERGE observations to maximise sensitivity.

- Chapter 5 describes the *e*-MERGE observations including data reduction and a rigorous testing of the astrometry compared to legacy MERLIN data. The fast wide-field imaging technique is applied which is used to image the data before flux densities are primary beam corrected. Legacy data taken from the MERLIN array prior to its wide-band upgrade is incorporated to maximise the sensitivity, necessary as the *e*-MERGE survey is only partly observed.
- Chapter 6 describes how sources in the field are measured and develops a consistent methodology to determine the largest angular size distribution of *e*-MERGE sources.
- Chapter 7 discusses the classification of sources, with the aid of a machine learning algorithm. The first analysis of the *e*-MERGE survey expands on the discussion of evolution of galaxies, surmising an increase in the luminosity evolution of faint SFGs.
- Chapter 8 summarises and concludes the thesis with a view to continuing the observations and advancing methodologies as part of the *e*-MERGE survey.

Chapter 2

Radio Telescopes, Beams and Interferometry

This chapter summarises some fundamentals of radio interferometry, with a particular emphasis on issues that will affect wide-band and wide-field imaging in this project. The ultimate field-of-view restriction, that of the *primary beam*, of the *e*-MERLIN interferometer array, is introduced.

2.1 Principles of Radio Astronomy

A traditional radio telescope antenna converts incoming electromagnetic radiation, emitted from astronomical bodies, into a measurable voltage by use of a parabolic surface to focus electromagnetic waves onto a dipole placed at the end of a collecting feed horn at the focal plane. This voltage, which changes rapidly as function of time, is related to the instantaneous power received within the telescope's entire *field of view* or *beam* and provides a measure of the electromagnetic radiation received from all the astronomical bodies lying within it. It can be shown that for a source within the beam of *flux density* S_A produces a voltage rise V in the antenna, with impedance R , (Condon and Ransom, 2010) equal to

$$\langle V^2 \rangle^{1/2} = \sqrt{2\Delta S_A A_E R \Delta\nu}, \quad (2.1)$$

where A_E is the effective antenna collecting area and $\Delta\nu$ is the system bandwidth. A 1 mJy source generates a voltage increase of just a few nano-volts in a typical radio

telescope antenna; thus very sensitive low noise amplifiers are required, with high gain. The voltage at the receiver input can be increased by an increase in collecting area of the telescope, and hence more sensitive radio telescopes scale with size. A typical single dish radio telescope receiver employs a superheterodyne mixer to lower the frequency and a cooled high gain Low Noise Amplifier, to minimise thermal noise. More theoretical details about radio telescope hardware can be found in a variety of sources including [R. Thompson \(2001\)](#) and [Condon and Ransom \(2010\)](#).

2.2 Beam Functions

The angular resolution (ability to distinguish distant objects at angle θ apart) of a parabolic telescope can be shown to approximate $\theta_{\frac{1}{2}} \approx \lambda/D$, often known as the *Half Power Beam-Width* of the telescope, and crudely describes its directional response (see Figure 2.1). Incoming electromagnetic waves arriving at extreme ends of the aperture, when combined at the focal plane, give rise to constructive interference when the waves arrive on axis, but start to destructively interfere when the waves arrive at some incident angle from the normal axis. As the incident angle of waves is increased there comes a point where the wave interference reach half power (HPBW) before further canceling completely (the first null), and then begin to constructively interfere once more, to a lesser degree, in *side-lobes*. Hence flux is captured from directions outside the main lobe and in such side-lobes, albeit significantly reduced. It is more accurate to describe the beam as a *beam function* rather than a simple width.

The beam function is often measured directly using raster scanning methods and holography, but it can also be derived theoretically from directly modelling the *aperture illumination distribution* of the telescope. The aperture is defined as the projection of the reflecting surface of the parabolic dish on a plane immediately in front of the antenna. The relationship between the aperture size and the angular resolution is thus related to the number of wavelengths across that aperture. Using Huygen's principle (that the aperture can be broken down into an infinite number of small elements) it can be shown that the interference produced at the focus is equal to the sum of all the interference contributions from all points in the aperture. The interference of all these spatial frequencies is mathematically equivalent to taking the two-dimensional *Fourier Transform* (FT) of the telescope's aperture illumination distribution (the simplest of which being a uniformly illuminated circular aperture representing an ideal unobscured

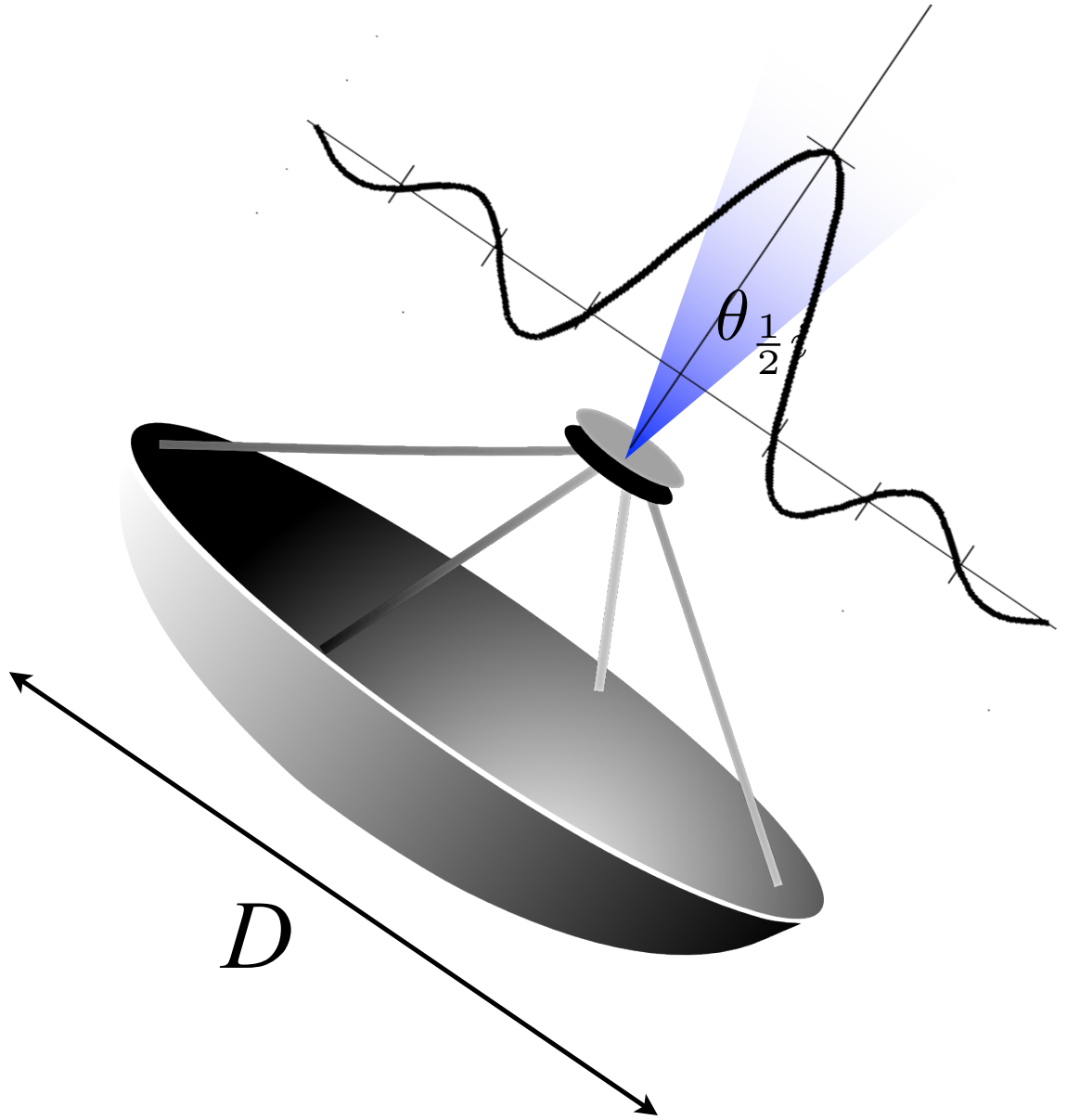


Figure 2.1: A single element radio telescope parabolic dish illustrating the Half Power Beam Width $\theta_{\frac{1}{2}}$.

parabolic dish antenna) and generates the beam function directly. The plane of the illumination function is known as the Fourier or uv plane and has dimensions measured in wavelengths. The associated beam function for such an aperture, derived from its FT, is the familiar *Airy Disk* with angular dimensions (l, m) referred to as the *sky-plane*. The resulting beams generated from these Fourier transforms are known as *voltage beams* - as this is the physical quantity generated at the antenna feed (Equation 2.1). The relationship can be described by;

$$J(l, m) = \int \int E(u, v) e^{2\pi i(ul+vm)} du dv, \quad (2.2)$$

(Rau et al., 2009) where $J(l, m)$ is the (complex) voltage pattern, $E(u, v)$ is the aperture illumination distribution, $u = \sin \theta \cos \phi$, $v = \sin \theta \sin \phi$, θ and ϕ are the polar coordinates from the centre. The intensity (or power) beam is proportional to the square of the voltage beam (Equation 2.1). (Note to generate a power beam directly, one could instead take the autocorrelation of the aperture distributions prior to Fourier transforming.) If a central obscuring region is introduced (say by a secondary receiver shadow), as is common in practical telescopes (illustrated in Figure 2.2), then the characteristics of the side-lobes are altered. These beams represent simplified cases, and in reality aperture distributions of real telescopes include features such as focal assembly struts which breaks axial symmetry by introducing additional shadows. Most importantly, the *receiving horn* introduces *illumination tapering* to deliberately under-illuminate the aperture edges in a effort to minimise side-lobes. Aperture tapering decreases the effective area of the telescope as well as increasing the width of the main lobe (primary beam), but this is an acceptable compromise if it results in fewer side-lobe artefacts receiving radiation from unwanted sky areas.

The telescope beam-widths are frequency dependent, hence flux from longer wavelengths is received over wider beams. This is of little consequence for monochromatic (narrow bandwidth) observations but becomes important for wide bandwidth instruments like *e-MERLIN* and will be considered in Chapter 3 in the development of a primary beam model for the *e-MERLIN* array. At L-band (20cm), the HPBW of a typical 25m diameter telescope is in the region of 30 arcmin; this is the maximum angular resolution for a large radio telescope when operating as a single dish and compares very poorly with optical telescopes a fraction of the size.

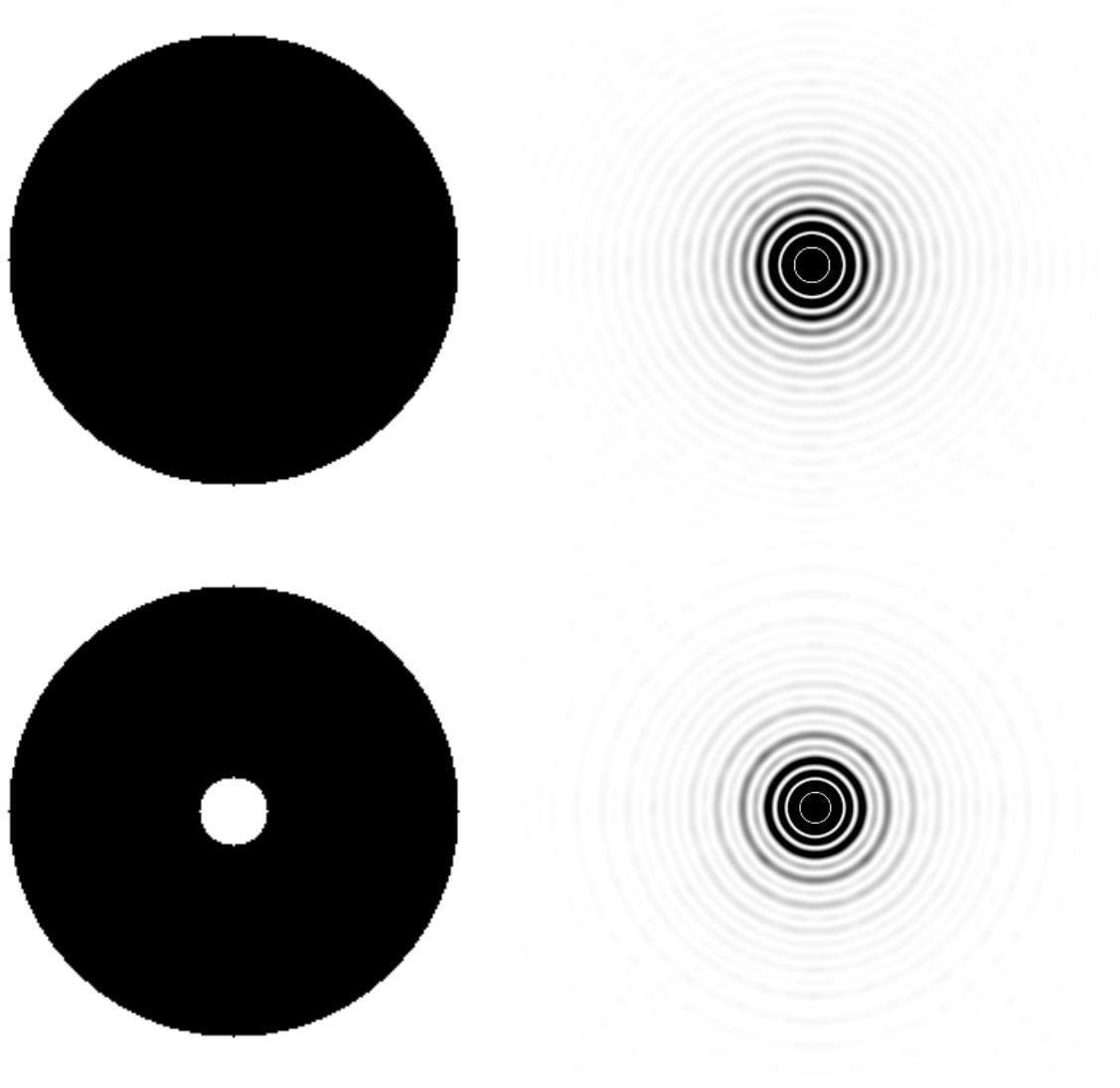


Figure 2.2: The solid (top left) aperture in uv plane produces a classic Airy disk beam-shape in the lm plane (top right) with the first null (total destructive interference) located at $\theta_{null1} \approx 1.22\lambda/D$, whereas the partly obscured aperture (bottom left) yields a beam with an altered side-lobe structure (bottom right).

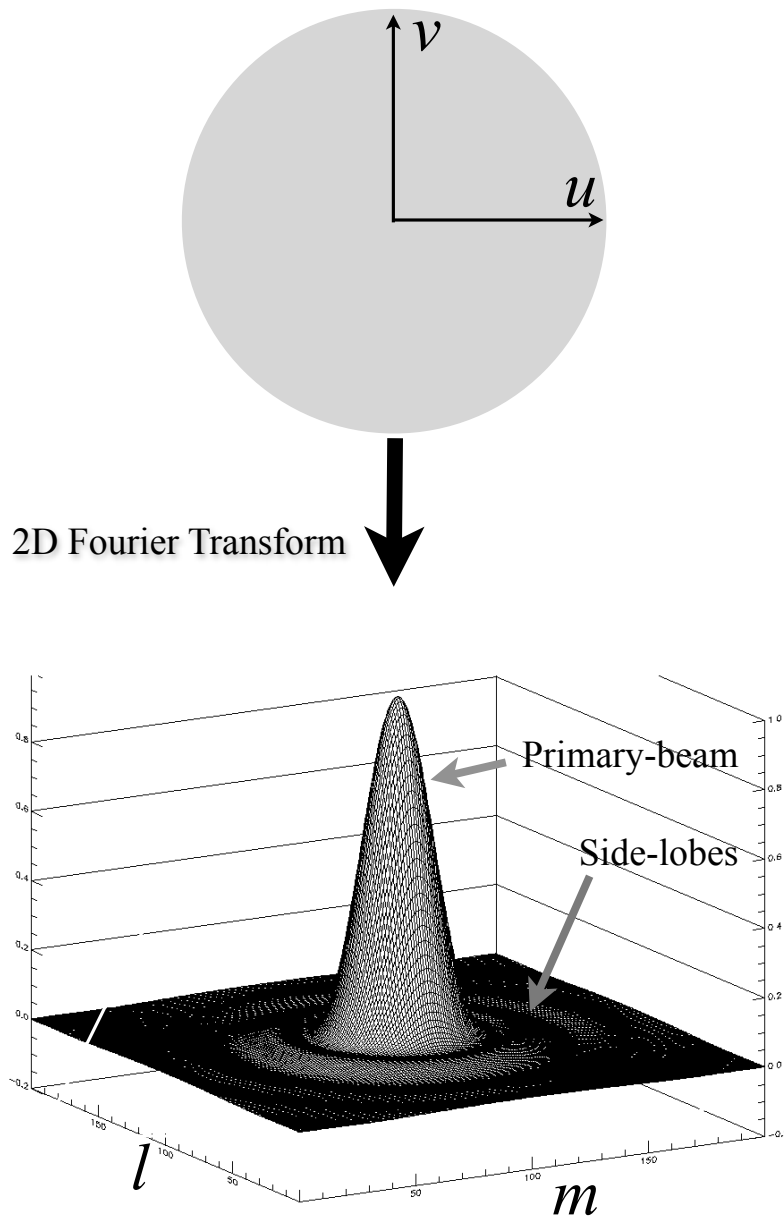


Figure 2.3: A simulated telescope beam derived by taking the Fast Fourier Transform of a circular aperture distribution. The (l, m) axes at the base are typically measured on scales of arcmin at radio frequencies for 25m diameter antennas. The vertical scale is a relative measure of the square of the voltage (i.e. power).

2.3 Radio Synthesis Imaging

Due to the large size of the HPBW of typical radio telescopes, they have low angular resolution when compared with their optical counterparts and consequently are unable to produce an image directly of remote galaxies on the required arcsec scales for deep field observations. Unless a radio telescope could be constructed with a diameter of many hundreds of kilometres it would be impossible to generate images on arc-second scales were it not for the development of *radio synthesis imaging* or *aperture synthesis*. In this method, several antennas, spread over a large area (many km apart), simulate a partially filled aperture. Rather than the electromagnetic waves being steered mechanically, i.e. by a parabolic dish focusing them onto a single plane, the signals from each antenna are combined electronically, with phase and amplitudes generated from interference fringes between baseline pairs of telescopes. The interference of source wavefronts at each antenna pair generate interference patterns and measurement of the amplitude and relative phases of the voltage signals allows the construction of the sky brightness distribution. The ‘steering’ of the waves is accomplished by a device known as the *correlator*, which compares the sampled voltages within time frames, for each baseline pair.

To better understand an interferometer, consider a single baseline pair of antenna elements of diameter D a distance L apart, as illustrated in Figure 2.4. Incoming plane waves arrive at the two antennas at differing times depending on their angle of incidence, hence the two signals received at the two antennas are not identical: a phase difference is induced. The varying voltages are sampled digitally and a time delay between the two bitstreams introduced to define a geometric phase centre, usually calculated to coincide with the pointing centre. A subsequent series of lags is introduced by the correlator which, when multiplied and Fourier transformed (Taylor et al., 1999), produces a large number of channels in the frequency domain. This type of correlator is known as an XF correlator. Another type of correlator reverses the order (FX), carrying out the Fourier transform first and then correlating. The WIDAR¹ correlator, used by *e*-MERLIN and the JVLA, adds an additional step to the XF process, prior to multiplication, which divides the frequency bands into separate sub-bands using a *polyphase filter-bank* by multiplying each antenna bitstream by a window function (which would yield a well defined pass-band if Fourier transformed at this stage). A

¹<https://science.nrao.edu/facilities/vla/docs/manuals/oss/widar>.

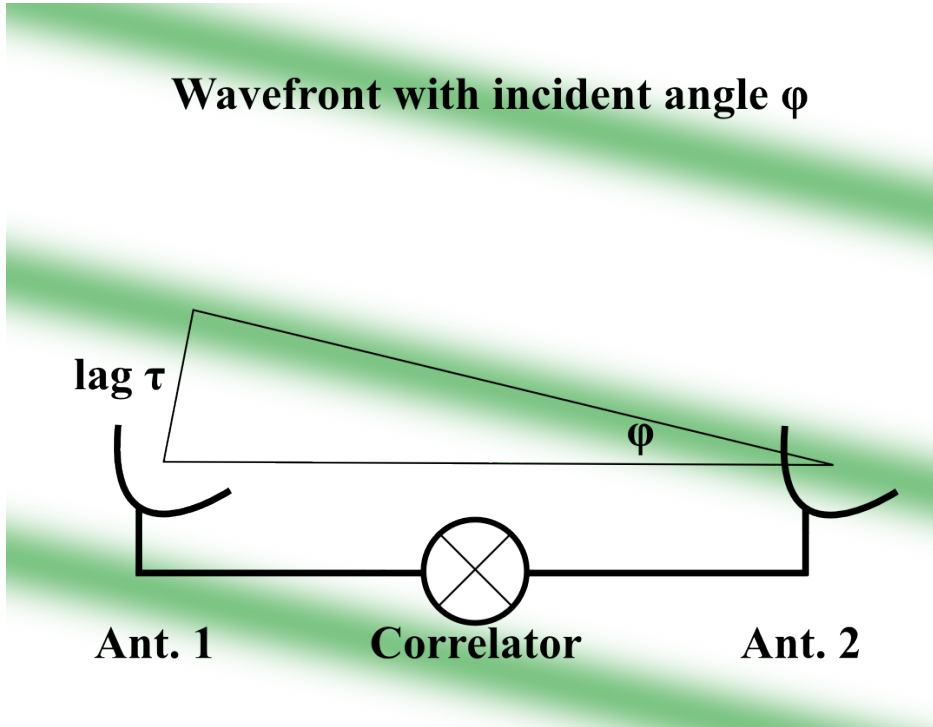


Figure 2.4: Illustrating how a single baseline pair of antennas collects visibilities. In the simplest (monochromatic) case, the two voltage signals are sampled using an Analogue to Digital convertor in real time and cross-correlated to effectively find the maximum correlation coefficient, corresponding to phase angle ϕ caused by the lag τ , before multiplying and integrating to find the amplitude. The result is a single complex visibility associated with each integration at a point uv determined by the position of the baseline at that ‘instant’.

series of time lags is then introduced between antennas for each spectral window, in all possible baseline combinations, with each lag associated with a desired channel. The delayed bitstreams are multiplied together and averaged before finally being Fourier transformed, yielding channelised amplitude and phase information. Thus a complex number at a corresponding uv coordinate with its associated phase and amplitude is derived for each channel, known as a *visibility*. The phase difference is related to the position of sources in the sky (i.e. in the lm plane), with signal amplitude proportional to the spatial sample of the sky brightness distribution. Each visibility is recorded and accumulates to populate the uv plane (here we redefine the uv plane to be equal the distance between two points in the aperture distribution referred to earlier). Provided that there are sufficient uv samples, the sky-plane image can be recovered by application of Equation 2.3 (i.e. the inverse Fourier Transform). The intensity $I(l,m)$ (which is proportional to the voltage squared) is known as the *sky intensity* distribution and is related to the visibilities $V(u,v)$ by (Clark, 1999);

$$V(u, v) = \iint I(l, m) \exp\{-2\pi i(ul + vm)\} dl dm \quad (2.3)$$

where (u, v) are now the coordinates of visibility $V(u,v)$ in a two dimensional plane with units in number of wavelengths ($k\lambda$). Note that although the relationship is identical to Equation 2.2, the resulting sky-plane distribution is a power distribution, not a voltage distribution as the correlation of points in the uv is collected in an interferometer. There are obvious implications for spatially extended structures in the l,m plane because of the reciprocal nature of Fourier transforms. Extended sources are associated with *small* components in the *Fourier* plane requiring sampling at short baselines.

In a similar way that the beam of a single telescope can be derived by Fourier inversion of the aperture distribution, the *array synthesised beam* can be derived by taking the inverse FT of its virtual aperture distribution, or *transfer function*, which extends out to the longest baseline. Hence the highest angular resolution (narrowest synthesised beam-width θ_s) of the array can be no better than greatest baseline separation - a longer baseline (L) means better angular resolution:

$$\theta_s \approx \frac{\lambda}{L} . \quad (2.4)$$

The choice of interferometer used should have baseline lengths which provide sensitivity at corresponding spatial scales of sources to be observed. Very long baseline interferometry (VLBI), for example, utilises baselines spread over thousands of kilometres and is therefore well suited to resolve sources on the smallest angular scales, but generally is poor at detecting larger spatial structure. When deciding on interferometer antenna locations, the rotation of the Earth is used to considerable advantage with the uv plane becoming increasingly filled as the uv coordinates describe arcs as the earth rotates. Additionally, taking measurements at different wavelengths corresponds to different uv coordinates in the same baseline and can act to fill out the uv plane almost completely. The sampled uv plane is also known as the *sampling function* or *transfer function*. The combination of numerous baselines, Earth rotation and multi-wavelength sampling produces good uv coverage, on which the e -MERLIN array relies to generate high fidelity imaging. e -MERLIN's sampling function is illustrated in Figure 2.5. Only the most extended sources are unsampled due to e -MERLIN's lack of very short baselines. This means that the e -MERLIN array cannot sample sources with a very large extended structure. The JVLA has many more antennas (twenty-seven) and consequently has superior instantaneous uv coverage but a longest baseline considerably shorter (36km) than e -MERLIN's 220km, yielding higher sensitivity at lower angular resolution.

Examination of Figure 2.5 reveals areas of incomplete sampling, causing the resulting image (the *dirty map*) produced on Fourier transformation to include undesirable side-lobe artefacts which manifest around each source. This synthesised beam (also known as the *dirty beam*) generated by FT of the sampling function deviates significantly from an Airy function. The synthesised beam is predicted for each observation by Fourier transform of the aperture distribution (sampling function) and it is found that its shape can be modified further by weighting the uv data recorded by the various baselines. The uv coordinates are binned into a regular cartesian grid of 'cells' such that Fourier inversion of the visibilities is possible using discrete Fourier transform techniques such as Fast Fourier Transforms (FFT). Each gridded cell can be individually attributed a relative weight to account for the fact that some cells contain numerous visibilities whilst others comparatively few. It is arguably more sensible to statistically weight well populated cells than sparsely populated ones, to minimise unwanted noise. Two extremes are conceivable - one scheme whereby all cells are weighted equally, regardless of number of visibility measurements they are comprised (uniform weighting) and another whereby the weighting is directly proportional to the number of observa-

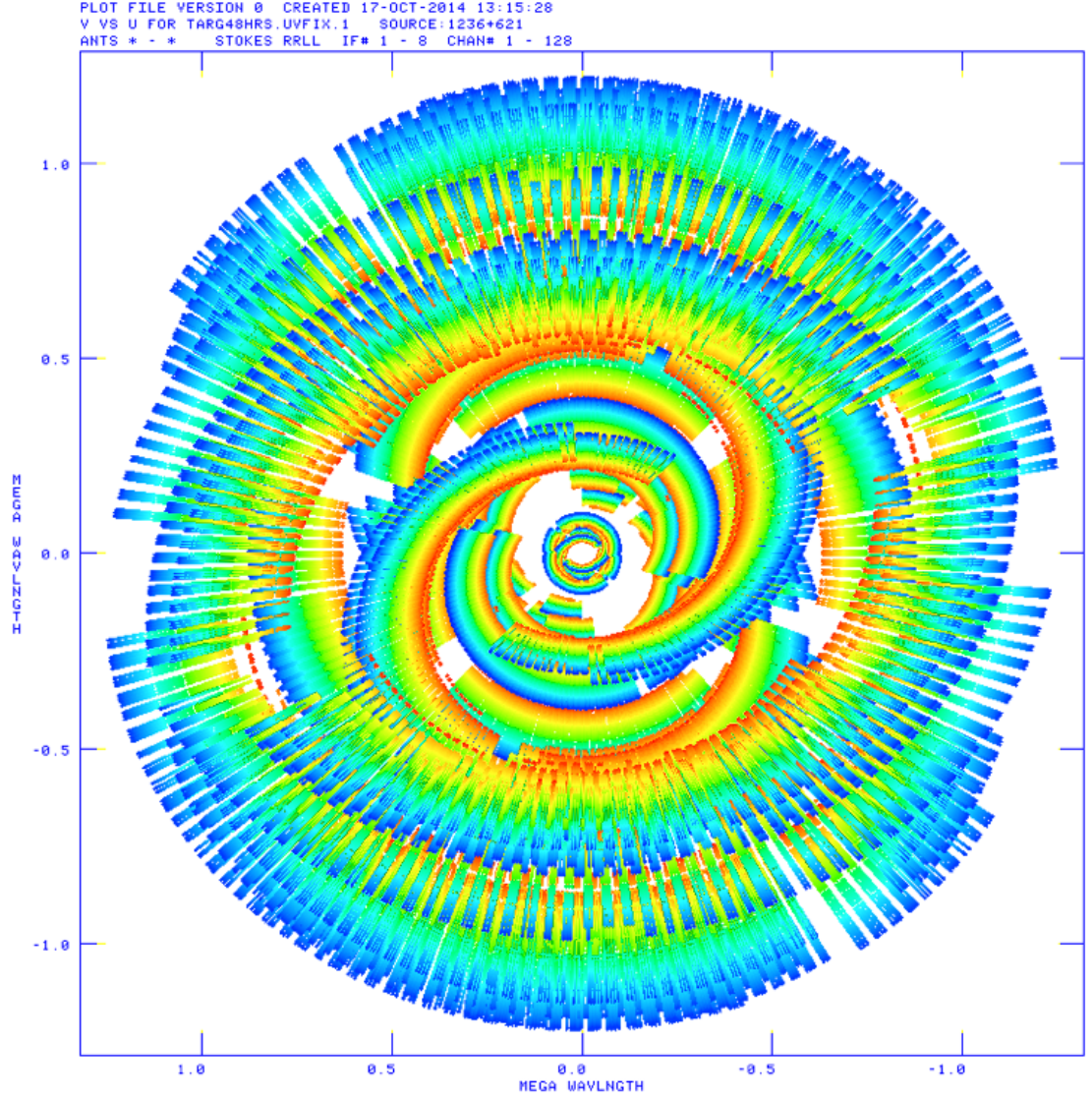


Figure 2.5: *uv* coverage or *sampling function* for a 12 hour track using the 7 antennas in the *e*-MERLIN array. Each coloured ellipsoid is a result of a single baseline pair (of which there are 20) and represent the different observing frequencies across L-band (1.25 - 1.75 GHz, red - blue). The coverage is incomplete, especially near the centre, caused by a lack of very short baselines.

tions taken per uv cell (natural weighting). Natural weighting favours sensitivity as it weights the cells proportionally with integration time, however uniform weighting gives equal weight to visibilities measured over the longer baselines, potentially maximising resolution at the cost of additional noise. Intermediate schemes are labelled using a *robustness* parameter ranging from -7 (uniform) to +7 (natural) (Briggs, 1998). A tapered weighting scheme can also be adopted to modify the shape of the synthesised beam in a similar fashion to aperture tapering within a single antenna. This may have an effect of reducing side-lobe amplitudes at the cost of angular resolution². Inverse Fourier transforming the visibilities by a discrete DFT or FFT, as per Equation 2.3, yields (as least theoretically) the synthesised image or *dirty map*.

2.3.1 Sensitivity of an Interferometer

The total integration time τ comprises many visibilities each of integration time δt which, because of the hardware specifications for the array (such as effective aperture A_{eff} , system temperature T_{sys} and number of baselines n_b), determines the expected rms noise (R. Thompson, 2001):

$$\sigma = \frac{\sqrt{2}kT_{\text{sys}}}{\sqrt{\tau\Delta\nu}A_{\text{eff}}\sqrt{n_b}} \quad , \quad (2.5)$$

where $n_b = \frac{N(N-1)}{2}$ baselines and T_{sys} is the equivalent system temperature of the entire radiometer system comprising cosmic microwave background, atmospheric contribution and thermal noise from the receiver:

$$T_{\text{sys}} = T_{\text{cmb}} + \Delta T_{\text{source}} + T_{\text{atm}} + T_{\text{receiver}} \quad . \quad (2.6)$$

However, for a non-homogeneous array the sensitivity is based upon the combination of each telescope, each with a slightly different T_{sys} which is related to the System Equivalent Flux Density (SEFD) of each telescope by

$$SEFD = \frac{2kT_{\text{sys}}}{A_{\text{eff}}} \quad . \quad (2.7)$$

²The array can be thought of as an incompletely filled aperture, an optical telescope with parts of the aperture missing would similarly produce artefacts significantly deviating from the Airy pattern.

The sensitivity of each baseline composed of antennas i and j is therefore:

$$\sigma_{\text{baseline}}(\theta, \phi) = \frac{1}{\eta\sqrt{2\Delta\nu\tau}} \frac{\sqrt{SEFD_i \times SEFD_j}}{P_i(\theta, \phi)P_j(\theta, \phi)} . \quad (2.8)$$

where $P_i(\theta, \phi)$ is the power beam function (see Chapter 3) normalised to unity in the centre. The total rms noise σ_{array} is simply given by

$$\frac{1}{\sigma_{\text{array}}^2} = \sum \frac{1}{\sigma_{\text{baseline}}^2} , \quad (2.9)$$

where σ_{array} is also a function of the offset position from the pointing centre. The derivation of the primary beam of the e -MERLIN array is described in detail in Chapter 3.

2.3.2 Högbom Cleaning

Each point source in the image generates an amplitude-scaled version of the synthesised beam within the map and it is mathematically equivalent to state that all point sources in the dirty map have been *convolved* with the dirty beam. Therefore, a reasonable recovery of the original sky intensity function is achieved by the inverse process of *deconvolution*. However, whereas convolution has an exact mathematical prescription, deconvolution does not and must be performed as an iterative process. Deconvolution of point-like sources utilises an algorithm, devised by Clark and Högbom, known as *clean*. The process of deconvolution via the clean algorithm attempts to remove the side-lobe artefacts caused by incomplete sampling. This is the most widely used deconvolution algorithm incorporated into the Astronomical Image Processing computer suite (AIPS) and is particularly suited to deconvolving compact sources such as those found in the deep field and utilised in this project. Cleaning requires that an amplitude-scaled version of the dirty beam, based on the Fourier transform of the sampling function for the set of observations, is partially subtracted from the brightest point in the dirty map. With position and intensity recorded, the location and magnitude of each subtraction is known as a *clean component*. The process is repeated for the next brightest point in the map, and then the next etc. until the resulting *residual map* becomes indistinguishable from the local RMS noise. The clean components, i.e. positions and amplitudes, are replaced with an idealised representation of the resolution of the array - usually a

Gaussian beam or point spread function (PSF) that is similar to an Airy function but lacks undesirable side-lobes. Thus the resulting cleaned map is a reasonable representation of the sampled sky intensity distribution convolved with a Gaussian beam. In the case of some observations of sources, the array projects a smaller baseline in one orientation compared to an orthogonal orientation, yielding a non-circular beam. This effect is minimal for high declination targets like the HDF where the beam is near circular.

2.4 Calibration

The above description omits to consider numerous errors and interference introduced by Earth's atmosphere, receiver and amplifier gains, and also timing errors in the instruments themselves. A most significant problem is that the amount of perturbation or *gain correction* required of a signal amplitude and phase varies temporally and geographically throughout a sufficiently long observation. Widely spaced antennas are subject to differing atmospheric phase perturbations which may vary typically on timescales of approximately 15 minutes (a problem thought at first to be intractable even by Martin Ryle who pioneered synthesis imaging at Cambridge). However, it was realised that if a well defined point source phase calibrator is observed at regular intervals during the observation of the target (for phase at least every 15 minutes at GHz frequencies) then the variations can be corrected by construction of simultaneous equations incorporating at least three baselines that include common antenna, i.e. any set of measured visibilities \tilde{V}_{ij} in a baseline pair of antennas ij can be described in relation to their corrected visibilities V_{ij} by (Fomalont and Perley, 1999) $\tilde{V}_{ij}(t) = V_{ij}(t)G_{ij}(t)$ where the complex gain correction is $G_{ij}(t) = g_i(t)g_j^*(t)g_{ij}(t)$ and g_i and g_j are complex corrections associated with each baseline. (The final combined term is a residual called *closure error*, which should be close to unity in amplitude and zero in phase, and is a measure of the goodness-of-fit for solutions.) A flux calibrator often used in the northern hemisphere is 3C286, which has a well behaved flux density, but resolved by *e*-MERLIN (i.e. has some significant extended structure) hence flux will be attenuated at longer baselines. To overcome this to allow it to be used as an amplitude calibrator, it is usual to *bootstrap* the flux from the primary flux calibrator using only the inner baselines (where the calibrator is unresolved) to some bright point source to act as a flux calibrator for all baselines. Phase calibrators are chosen such that they are

unresolved across all baselines and are near to the target (within the same isoplanatic patch). Phase reference sources usually do not generally have a well defined flux density over years as they are likely to be compact AGN objects, but are useful in that they contain considerable flux density as seen by the instrument. Because both *e*-MERLIN and the JVLA have a wide bandwidth (with multiple channels) it is likely that the calibrators have some intrinsic spectral index or curvature within the bandwidth and this is incorporated into the calibration, given the known flux density per spectral window. The channels will have their own complex gains per channel and therefore a further bandpass calibration is usually performed to correct for systematic errors in frequency channel gains across the band. Several rounds of self-calibration, in which models of individual sources are assumed, are performed. This stage is particularly important in wide-field radio data to correct localised phase errors, and at least several dozen bright source models are used to refine solutions. Calibration of the *e*-MERGE data is described further in Chapter 5.

2.4.1 Radio Frequency Interference

During observations it is usual to encounter radio frequency interference (RFI) from local radio sources (television transmitters, mobile phones, artificial satellites etc.) which has the potential to distort the calibration and/or overwhelm the data entirely making imaging the target source impossible. Therefore the visibilities must be examined baseline by baseline for obviously excessive flux and marked for deletion. This process is called *flagging* and can in most cases is the most time consuming step in data reduction, particularly if the RFI is present at relatively low amplitudes and difficult to spot. Automatic flagging tools exist (e.g. SERPENT), however, these can be difficult to adjust to yield optimal results in some cases and ultimately the human touch is still necessary for the time being. Flagging is described in Chapter 5.

2.5 Wide-Field Wide-Band Imaging

In addition to the techniques described above, both *e*-MERLIN and the JVLA incorporate a large number of radio frequency channels. The *e*-MERGE project also demands that a wide field of view be mapped (15 arcmin diameter), which also complicates image processing. In particular the following subtle effects require consideration when

constructing wide-field and wide-band maps:

- Sky curvature, i.e. Isoplanatic sky function $I(l, m)$ violated in equation 2.3.
- Finite integration time per uv visibility (integration time smearing).
- The image should cover as large a sky area as possible i.e. should extend throughout the primary beam of the array.
- The wide bandwidth of the e -MERLIN/JVLA array (bandwidth smearing).
- Computing power is limited.

A innovative solution to image in the wide-field wide-band of e -MERLIN, described in more detail below, is derived in Chapter 3.

2.5.1 Curved Sky (w -term)

The visibility equation (2.3) describing the transformation between the uv and lm coordinates assumes that the sky is a flat plane (with coordinates lm) and that incoming rays are parallel. This approximation is acceptable for sources close to the phase centre but becomes increasingly invalid for sources whose incident waves arrive from a non-parallel direction. Positions derived from larger phases become increasingly invalid as a function of distance from the phase centre, as the flat sky assumption is violated. A more thorough treatment incorporates a correction within the visibility equation by introducing an extra dimension normal to the uv plane, the w -term (Thompson, 1999), yielding

$$V(u, v, w) = \int \int \frac{I(l, m)}{\sqrt{1 - l^2 - m^2}} \exp\{-2\pi i(ul + vm + w(\sqrt{1 - l^2 - m^2} - 1))\} dl dm \quad . \quad (2.10)$$

The w term represents the phase difference between the flat and curved sky path displacements. The additional phase correction reveals that a phase error present in the simpler 2D version only becomes significant when the w term becomes a moderate fraction of the sum of u & v terms. Therefore the addition of the w vector will only deviate significantly from the sum of the u or v vectors if it is of the order of a radian or so, below this value the region contains insignificant directionally dependent errors and is known as an isoplanatic patch. Hence, provided that $2\pi w\{\sqrt{1 - l^2 - m^2} - 1\} < 1$,

then w can be ignored and the 2D transform can be used. The above expression can be simplified to one dimension, say m , yielding; $m \sim \theta_w < \frac{1}{\sqrt{\pi w}}$. The largest value of u or v approximates L/λ and because this is the maximum value of w , errors are insignificant provided $\theta_{w_{max}} < \sqrt{\frac{\lambda}{L}}$ (Perley, 1999a), where L is the longest baseline in the array (the factor of π has been ignored in this approximation). Provided that the facet size is much smaller than θ_w , the resulting synthesised image will not contain significant w -projection errors and the 2D transform can be used in transforming the visibilities to the image plane. This facet size is said to be an isoplanatic patch for which directionally dependent phase errors are not significant.

An alternative method was devised by Cornwell et al. (2008) and Bhatnagar (2012) in which an additional convolution step is used to effectively transform the w -term component such that 2D deconvolution can still be used. This is incorporated into the CASA software suite, but is not yet suited to e -MERLIN data due to computational demands. Imaging software like AIPS does not include the w -term in its Fourier inversion algorithms and therefore large fields must be broken down into smaller facets covering a polyhedral-like isoplanes representing the sky. For typical e -MERLIN data at L-band each facet should be smaller than about 3.3 arc-minutes across to avoid significant w -term distortion, as the array has a maximum baseline of 217 km. Facets are in fact usually smaller than this due to computational limitations. However, for wide field imaging this approximation becomes important. For example, to obtain an image 15 arc-minutes wide using the above array would require separating the field into at least five facets (in one dimension) to avoid significant distortions. The w -term correction is considered in Chapter 3 in the development of a Fast Wide-field Imaging technique.

2.5.2 Bandwidth Smearing

Each frequency channel, with its own bandwidth $\Delta\nu$, can be considered to be its own interferometer, producing fringes with other telescopes in the array. The fringes associated with each wavelength within this channel bandwidth differ slightly from those of other channels but when integrated, like the Young's slit experiment, interfere in superposition. At the phase centre of the array, the interference is entirely constructive. However for sources at some significant angular displacement from the phase centre, the superposition becomes increasingly destructive and fringes begin to smear out. The extent of smearing is analogous to the double slit experiment whereby light

is projected through two narrow slits onto a screen. The double slit is analogous to a single baseline with each slit representing an antenna. The fringes produced on our hypothetical screen correspond to the set of visibilities, with the displacement from the screen centre corresponding to the range of *delays* in the radio interferometer, from its phase centre. For this reason the usable field of view is often called the *delay beam* and is defined by an acceptable amount of smearing, i.e. some chosen fraction of the synthesised beam for example. For a single frequency the amplitude of the interference fringe on the screen is constant, but as the bandwidth is increased the interference pattern becomes increasingly smeared as a function of displacement from the centre. In general, the 'fringe visibility' (amplitude difference from peak to trough) *decreases* as the angle from the phase centre *increases* and it can be shown that this is proportional to $\sin \theta / \theta$ or $\text{sinc}(\theta)$. Expanding the treatment into 2-dimensions puts imaging limits the usable field of view as it acts to introduce *radial* smearing which is proportional from the phase centre (Thompson, 1999):

$$R\Delta\nu/\nu, \quad (2.11)$$

where $\Delta\nu$ is the channel width, ν is the lowest frequency and R is the radius from the phase centre. Since channel widths are generally fixed across the observing band, the relative smearing is slightly larger for channels at the lower end of the spectral window, and is therefore slightly different across the range of frequencies. The smearing effect causes a reduction in the peak amplitude of a source as the peak flux density is smeared over a larger apparent area. Radial smearing is unavoidable but is generally acceptable if it affects the image by less than about 10% in amplitude. The size of the delay beam therefore depends upon acceptability of bandwidth smearing in comparison with other effects, e.g. integration time smearing (see below).

2.5.3 Integration Time Smearing

Each visibility is derived from correlated and integrated data taken over a finite time period; with an integration time t of usually about 1 second for wide field imaging. The rotation of the earth causes the baseline projection within the uv plane to rotate and therefore the integration time must be kept short enough for those uv coordinates to remain approximately the same for the duration of that visibility. Generally, the

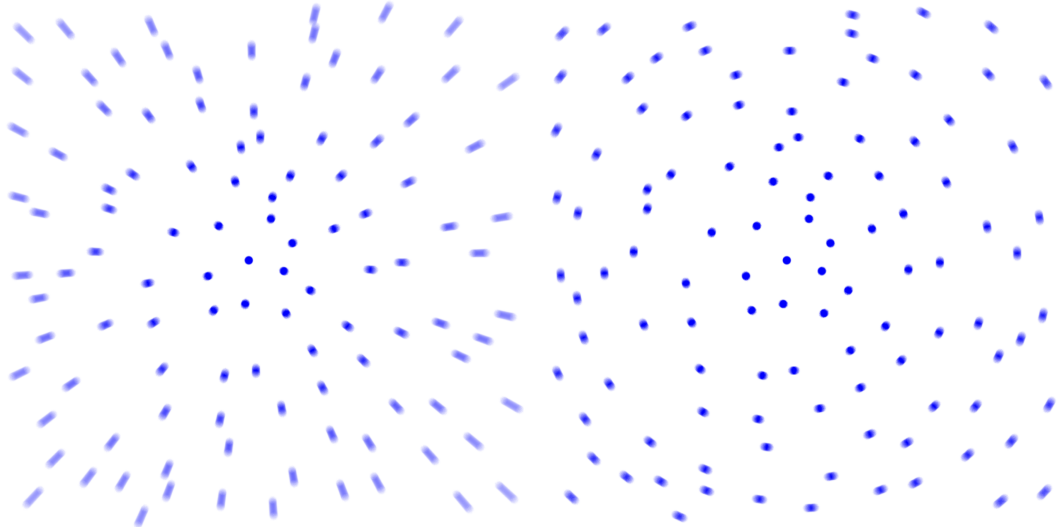


Figure 2.6: Illustration of Bandwidth Smearing (left) and Integration Time Smearing (right) acting on sources as a function of distance from the phase centre. The effects act together to reduce the image resolution and peak flux densities, although integrated flux densities are conserved.

integration time should be no larger than

$$t \sim \frac{86400\lambda}{2\pi L\Delta\theta}, \quad (2.12)$$

where 86400 is the number of RA seconds in an one earth rotation, λ is the shortest observing wavelength and $\Delta\theta$ is the distance from the phase centre in arcsec. Hence optimum integration time and distance from phase centre are inversely related; mapping a wide field necessitates short integration times. Cell dimensions allocated to the uv grid should be selected such that longest baseline visibilities are not under-sampled. Integration time smearing causes source elongation around the phase centre (orthogonal to the bandwidth smearing) and is proportional to distance from the phase centre (see Figure 2.6).

2.5.4 The Primary Beam of an Interferometer

A radio interferometer observes visibilities of all sources that lie within the beams of all the antennas in the array and represents the ultimate restriction in wide-field imaging. The synthesised image brightness of sources is therefore not the true sky brightness but is reduced as a function of angular displacement from the pointing centre depending

on the antenna directivity and can be transformed by

$$\tilde{I}(\Theta) = A(\Theta)I(\Theta) , \quad (2.13)$$

where $A(\Theta)$ is the beam function of the array, $I(\Theta)$ is the true sky brightness distribution and $\tilde{I}(\Theta)$ represents the synthesised image. If all the antennas are identical (i.e. the array is homogeneous) then $A(\Theta)$ is theoretically identical to that of any single antenna. However, for an interferometer with dissimilar antennas, i.e. a non-homogeneous interferometer, the resulting beam-shape is some weighted combination of them all. The primary beam of an inhomogeneous interferometer is described in detail in Chapter 3 in which tools are developed specifically to facilitate wide-field and wide-band imaging.

Chapter 3

Development of wide-field & wide-band imaging techniques

The *e*-MERLIN datasets for the *e*-MERGE project are observed at various epochs according to scheduling opportunities and, consequently, are delivered in blocks. Each block, which is at least a full track observation, measures over 1 TB. A motivation exists, due to computational constraints, to generate a rapid method to generate wide-field maps for each epoch. *e*-MERLIN data is optimally processed with the AIPS suite, which includes all the necessary tools for calibration and imaging and is well understood. Consequently the *e*-MERLIN pipeline ([Argo, 2015](#)) written in ParselTongue ([Kettenis et al., 2006](#)), a python-like interface designed to control AIPS and in effect replacing the old POPS user interface, is used to develop customised tools to allow production of maps within a reasonable timeframe (days). Standard imaging methodologies have proved to be impractical, although these will be used in the years to come as computers advance. This chapter describes the methodologies developed to generate the images, overcoming the following issues:

- The primary beam of the array causes attenuation across the field.
- The primary beam causes an induced spectral index across the band.
- The curved sky *w*-projection effect restricts imaging size.
- The dataset is large and imaging takes excessive amount of time even on modern workstations.
- Confusing sources cause a reduction in dynamic range.

Each of these problems was solved in a combined methodology, modified from a technique originally devised for imaging VLBI data (Wucknitz, 2010). The process, called fast wide-field wide-band imaging, involves a hierarchical approach to averaging the uv data in both time and frequency to create smaller facets which locally overcome the w -projection problem, and reduce the amplitude of confusing bright outlying sources. Synthesised beam modification compensates for the induced spectral index caused by the primary beam. The result is a technique that produces images up to two orders of magnitude faster than the standard AIPS cleaning method, with a caveat of increased smearing. The imaging techniques are used in the production of maps for each epoch of e -MERGE data as it becomes available.

3.1 Primary Beam Correction

Mapping the wide-field of GOODS-North out to the maximum usable field of view requires consideration of the effect of the array’s primary beam on source amplitudes. Whilst calibration flux density scales are derived for the pointing centre, the effect of the beam of each telescope in the array will contribute an increasing amount of reduction in observed flux as a function of angular displacement from the centre, with each telescope having a different beam. Flux density calibration is usually the least accurate of the attributes of any radio interferometrically derived map due to the incomplete sampling which depends on the nature of the source being observed. Therefore, any beam correction at present needs to be accurate to the order of a few percent.

3.1.1 Holography

The concept of telescope beams was introduced in Chapter 2. In an effort to model the beams of the telescopes comprising the e -MERLIN array as accurately as possible, voltage patterns from telescopes within the e -MERLIN array were obtained from holographic scans. The scanning method employed a single baseline formed from the *scanning telescope* to be investigated and a second telescope or *auxiliary telescope* to form a single interferometer pair. The auxiliary telescope is directed at a bright point source (in this case 3C84), while the scanning telescope is scanned across the same point source in a raster-like manner, nodding in elevation and azimuth and covering the expected main beam. High resolution holographic scans require very large angular

sweeps to cover multiple side-lobes so that Fourier inversion of the data produces an accurate aperture distribution. However, due to time constraints, only the primary beams and first side-lobes for telescopes in *e*-MERLIN were obtained. This means that aperture distributions cannot be obtained directly by transforming the data and instead the result of these low resolution scans is a complex voltage pattern (modulus) for each telescope (see Figure 3.1). The 76m diameter Lovell telescope scans are pending at the time of writing. The holographic scans provide a method of calibrating theoretical beam models which can be used to simulate any baseline combination in any telescope weighting scheme.

Theoretical beam-shape of a telescope

Recall from Chapter 2 that the beam-width of a single radio telescope antenna is inversely proportional to its aperture diameter. For homogeneous arrays, like the JVLA, a description of the beam of a single telescope is usually sufficient to correct the fluxes in images produced from the whole array, regardless of the relative sensitivities of the individual telescopes, as they are assumed to be effectively identical. Most field studies require only the central lobe (primary beam) to be well determined, which is approximated by either a Gaussian or simple polynomial function of θ . The primary beam model is based on a monochromatic case which is then extended to the wide-band array to include complications caused by integration of visibilities from all spectral windows (Intermediate Frequencies or IFs). The beam-widths associated with observations at the high frequency end of the band will be considerably narrower than those of the lower frequencies (if the bandwidth is wide enough then the side-lobes of the former may partly overlap the primary lobes of the latter). This has consequences when integrating multiple channels together in an integrated wide-band image (which is how modern interferometers have increased their sensitivities). The relative sensitivity weighting for each antenna must also be considered, and is likely to vary as a function of the frequency due to the following factors:

- Surface accuracy of the telescope.
- Feed horn sensitivity frequency variation.
- Standing waves between surface and focal point ([Popping and Braun, 2008](#)).

These third order effects are not incorporated into the modelling as they are considered to be best determined experimentally. The aim of the model is in producing a beam

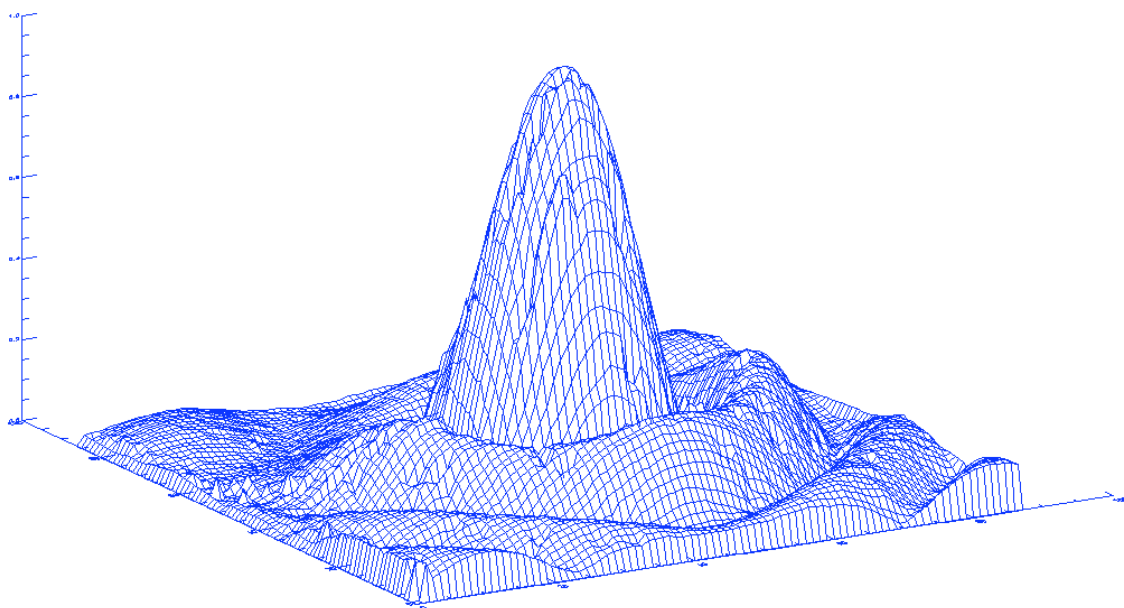
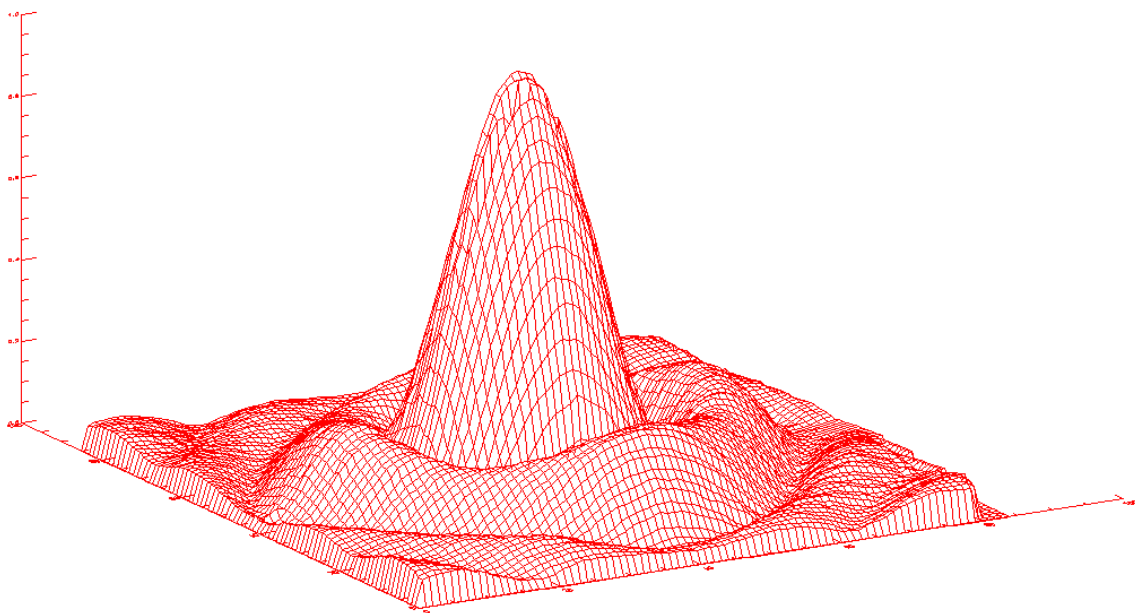


Figure 3.1: Magnitude of voltage pattern of the Darnhall (top) and Pickmere (bottom) telescopes obtained from holographic scanning techniques (private communication P. Harrison).

correction algorithm that can be used to produce results for the *e*-MERLIN pipeline incorporating relative telescope sensitivities and beam functions.

Modelling the *e*-MERLIN telescopes

The antennas comprising the *e*-MERLIN array can be approximated as being equal to 25m diameter apertures with two exceptions - the Cambridge telescope (32m) and the Lovell telescope at Jodrell Bank (76m). Four of the telescopes are Cassegrain systems with secondary reflectors supported by four pylon struts. Defford and MKII telescopes are prime focus but also have four pylon struts. The Lovell telescope however has the receiver supported by a single pylon (see Figure 3.2). The receivers are designed to include moderate amounts of aperture tapering which has the effect of under-illuminating the edges of primary reflector in an attempt to reduce the amplitude of secondary side-lobes. If the aperture tapering is Gaussian, then the beam function will be more Gaussian-like (recall that the FT of Gaussian is another Gaussian). A model is hence constructed with the above characteristics in addition to the central secondary reflector shadow (see Figure 3.3). The *e*-MERLIN aperture model is generated within gridded matrices (within IDL/GDL) and allows each telescope aperture to be adjusted in the following:

- Diameter.
- Gaussian tapering.
- Focal assembly shadow.
- Pylon shadowing including spherical shadows caused by obscuration of the outer part of the dish.

Each aperture distribution is designed in a Cartesian matrix so that it could be converted into an array, i.e. gridded, such that the Fast Fourier Transform (FFT) can be used. The 2-dimensional array has pixel dimensions N by N depending on the desired resolution of the beam model (IDL implements an FFT such that the output array has the same dimensions as the input array). The Fourier transform relationship is an inverse one and the dimensions must be chosen such that the aperture is small in relation to the array size in order to avoid additional harmonics, but not too large such that the memory footprint exceeds the capabilities of the computer. Additionally,

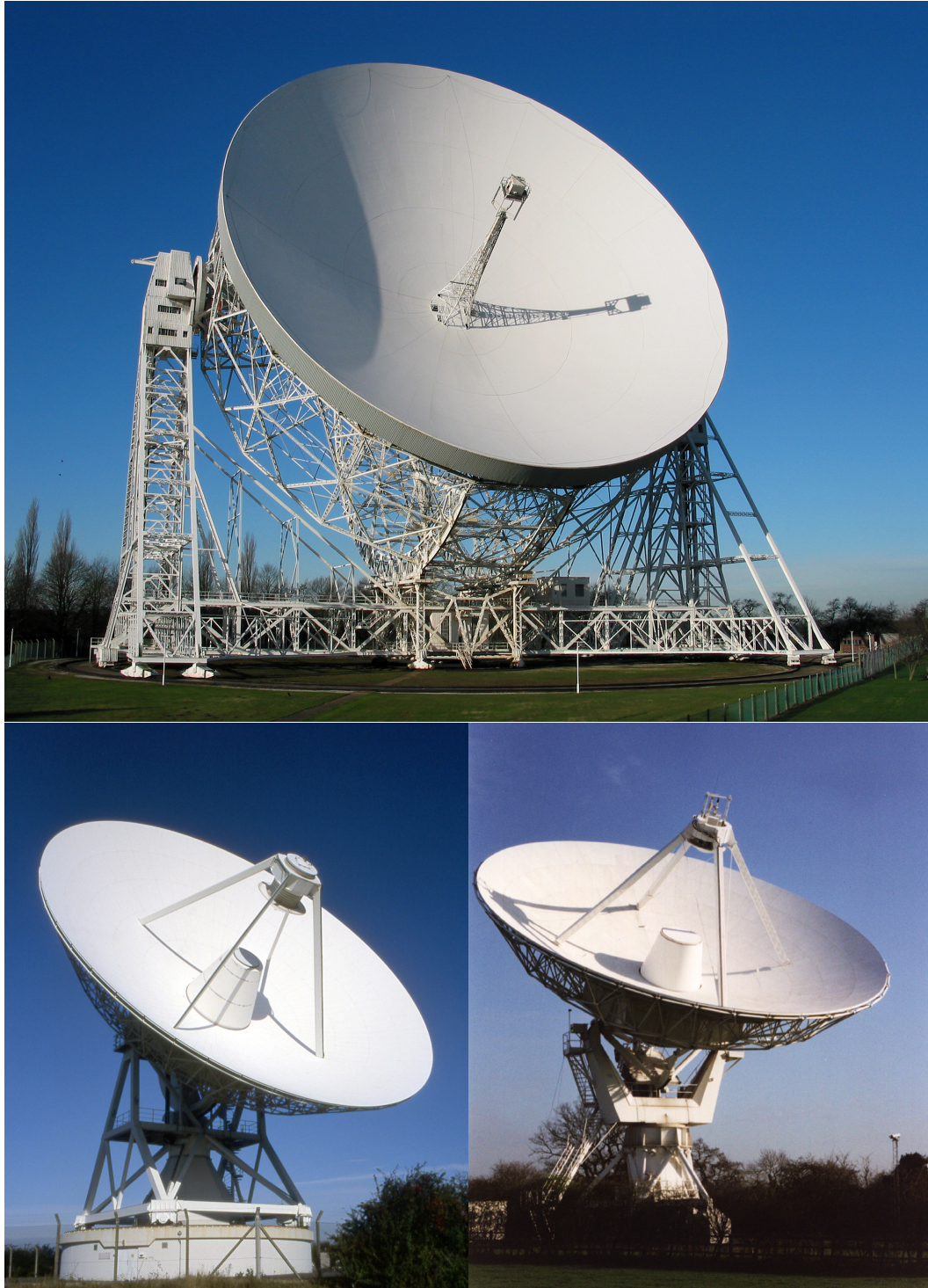


Figure 3.2: The 3 sizes of telescope in the *e*-MERLIN array. The 76m diameter Lovell telescope with a single primary focus pylon (top), the 32m diameter telescope at Cambridge (bottom left) and 25m diameter telescope at Darnhall (bottom right) both have secondary receiver assemblies with 4 pylon struts.

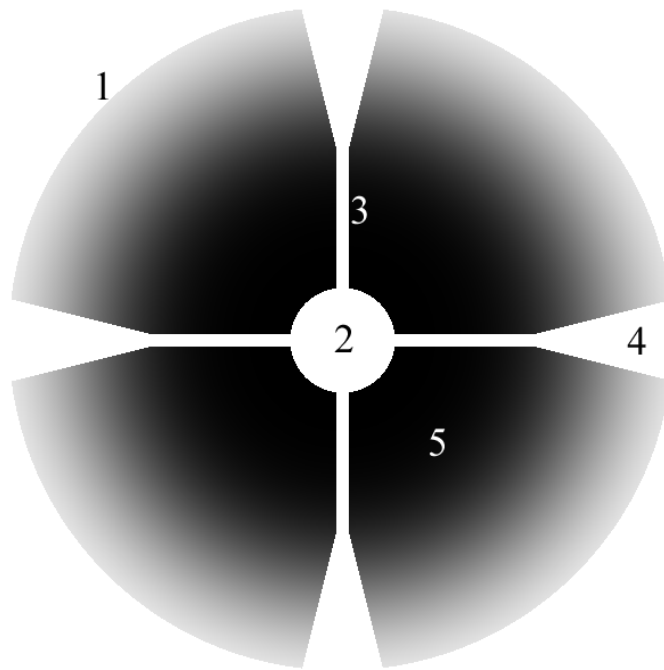


Figure 3.3: A realistic model telescope aperture illumination distribution consists of 5 basic components. (1) The circular aperture. (2) The secondary reflector shadow. (3) The support strut shadows. (4) The secondary spherical shadowing caused by the support struts. (5) The aperture tapering.

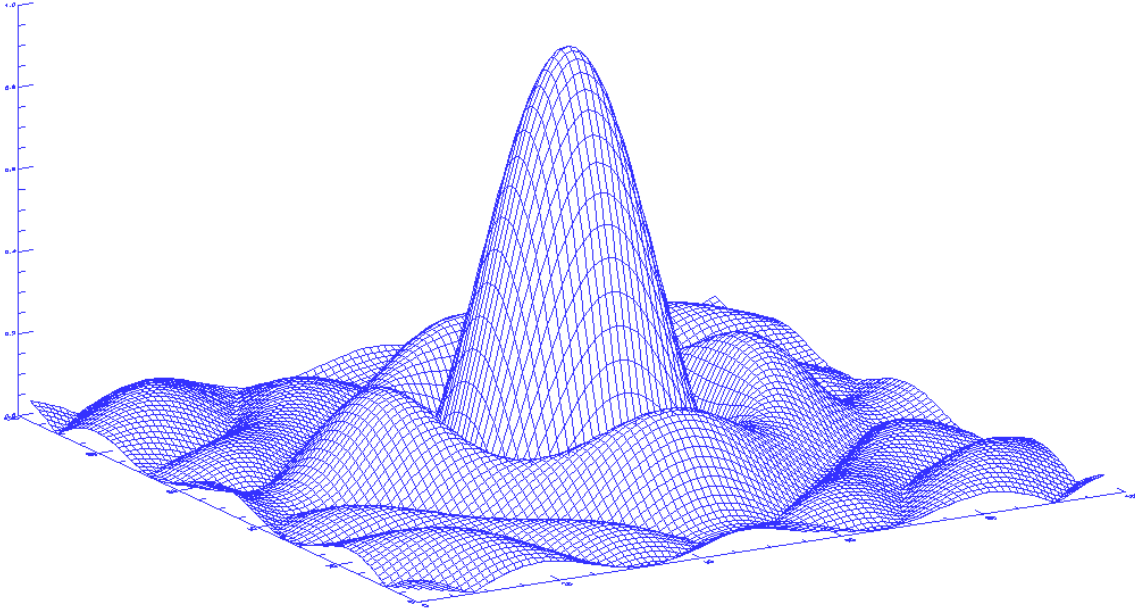


Figure 3.4: Voltage beam derived from FFT of the gridded aperture distribution in Figure 3.3.

apertures must be split and moved to the four corners of the array, otherwise additional harmonics are generated during the transform. For p_λ pixels per wavelength, and $\theta_{px(rad)}$ radians per pixel in the output array, each array dimension N must equal

$$N = \frac{p_\lambda}{\theta_{px(rad)}} \quad (3.1)$$

or, for θ in arcsec

$$N = \frac{p_\lambda \times (\frac{360}{2\pi} \times 60 \times 60)}{\theta_{px(arcsec)}} \quad (3.2)$$

Hence, for a resolution of 30 arcsec per pixel, an array of size 6856×6856 is required (approximately 47 megapixels). To achieve a resolution of one arcsec per pixel requires array dimensions over 42.5 gigapixels, which far exceeds the random access memory capacity of desktop computers at the time of writing. This is not considered a major obstacle because beam-shapes are continuous functions and are easily interpolated from lower resolutions. Implementing the above methodology within a GDL script generates a voltage beam illustrated in Figure 3.4. The voltage beams are generated for each

telescope, which when compared to the holographic scans, can produce very close approximations. Several additional subtleties exist that may cause further departure from reality which include the following:

- Inaccuracies in the parabolic surface of each antenna.
- Off-axis path differences between focal receiver and parabola (non-isoplanicity).
- Standing waves between the surface and the receiver.
- Asymmetries caused by bowl sagging which may be elevation dependent,

but these are not modelled here. The simulated beams are compared to holographically derived voltage patterns, and aperture distributions refined until the resulting beam function is a close approximation. The power beam pattern of 25m telescopes, obtained by squaring the voltage pattern, also has a profile in good agreement with the polynomial fits obtained by raster scans carried out by Rick Perley on the VLA antennas (Perley, 2000). However, the 25m *E-Systems*¹ telescopes fitted to the VLA differ slightly from those within *e-MERLIN* due to differences in receiver mountings; VLA telescopes have offset carousels to allow rapid changing of receivers giving rise to a slightly asymmetric beam, but the models here assume on-axis feeds. All available holographic scans were normalised and plotted for comparison, with the one notable exception of the Lovell telescope. Instead, an approximate aperture distribution was generated, which was refined using derived data from legacy MERLIN data (which was taken as being quasi-monochromatic). The method of differential flux-fitting was used and involves the measurement of point sources both with and without the Lovell baselines (see Chapter 5). This provides an estimate of the half power beam width which is matched by adjusting the amount of aperture tapering. With aperture distribution models constructed for each telescope in the *e-MERLIN* array, they could be Fourier transformed to produce complex voltage patterns and then transformed to power beam pairs by gridded multiplication.

Assembling baseline power beam pairs

Baseline beam-pairs ij are formed for each baseline combination of the array by multiplication of the complex voltage patterns with appropriate with scaling factors; the

¹*E-Systems manufactured these telescopes for both the VLA and MERLIN in the early 1980s.*

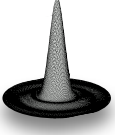
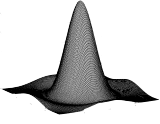
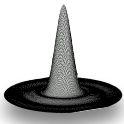
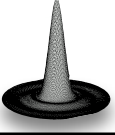
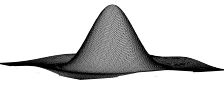

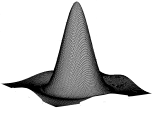

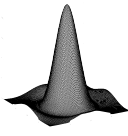
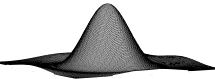
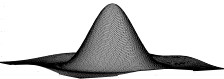
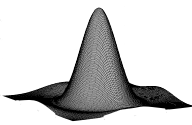
J_i	J_j	Diameters (m)	No. of base- lines	Resulting Power Beam	HPBW @ 1.5 GHz
		76 by 32	1		12'
		76 by 25	5		14'
		32 by 25	5		25'
		25 by 25	10		29'

Figure 3.5: Illustration of the complex multiplication of voltage beams J_i and J_j resulting in 4 types of power-beam baseline-pairs.

geometric weightings W_i and W_j are introduced to incorporate the relative sensitivities of each antenna;

$$P_{ij}(\theta, \phi, \nu) = \frac{1}{2} [J_i J_j^* + J_i^* J_j] \sqrt{W_i(\nu) W_j(\nu)} \quad (3.3)$$

where P_{ij} is the power beam, θ is the angle from the beam centre in radians and W is the relative antenna weighting, as used in AIPS' WTMOD task for example. Theoretical derivations of individual telescope weights can be derived from the square roots of ratios of System Equivalent Flux Density measurements (see EVLA memo No. 152).

Each voltage beam is hence multiplied as per Equation 3.3, which first normalises, such that the value of the central peak of the primary lobe has amplitude unity, before being weighted appropriately. The resulting power beams, 20 in total (excluding the MK-LO baseline), are weighted according to Table 3.1, based on derived sensitivities used within the *e*-MERLIN pipeline.

	Sensitivity W_i :	5.0	50.0	1.0	1.0	1.0	1.0
Sensitivity W_j	Antenna Name	Cambridge (CA)	LO (1)	Mark II (2)	DA (8)	KN (5)	PI (7)
1.0	<i>Defford (DE)(6)</i>	2.24	7.07	1	1	1	1
1.0	<i>Pickmere (PI)</i>	2.24	7.07	1	1	1	-
1.0	<i>Knockin (KN)</i>	2.24	7.07	1	1	-	-
1.0	<i>Darnhall (DA)</i>	2.24	7.07	1	-	-	-
2.0	<i>Mark II (MK)</i>	2.24	7.07	-	-	-	-
50.0	<i>Lovell (LO)</i>	15.81	-	-	-	-	-

Table 3.1: Geometrically averaged weightings $\sqrt{W_i W_j}$ for all baseline-pair combinations in the *e*-MERLIN array based on WTMOD parameters used within the pipeline.

The power beam for the array is then calculated using

$$P_T = \sum P_{ij} , \quad (3.4)$$

which generates a 2-dimensional array per frequency. Since *e*-MERLIN observations for the *e*-MERGE survey are all full-track scans (i.e. at least 24 hours), the beams must be rotationally averaged around the pointing centre. The averaging is achieved within the model using built-in IDL functions, and allows a 2D slice through the beam to be represented as a function of radius from the pointing centre. This facilitates the fitting of a polynomial expression that can be used within the AIPS task PBCOR. Fitting the polynomial expression (similar to a Perley fit) to five orders required the use of the evolutionary algorithm, *Pikaia* (Charbonneau, 1995). The advantage of evolutionary fitting is that no initial parameters are required, unlike other fitting routines which can easily get caught in local minima given a poor starting set. Therefore, the tool can be run completely 'blind' for any weighting scheme and frequency range and makes the software completely generic. Once the best solution set has been determined, the polynomial parameters are generated for various weighting schemes and frequencies, for later use in beam correction.

These resulting parameterised fits are frequency dependent and hence, for wide-band imaging, produce differing beam widths depending on the radio frequency of the observation (see Figure 3.6), the consequences of which when imaging are discussed below. The HPBW for the *e*-MERLIN array, using recommended sensitivity weighting ($WT_{LO} = 50$), is predicted to be approximately 15 arcmin at L-Band.

Amplitude Correction Parameters

The beam correction model presented here for the *e*-MERLIN array yields point source flux density corrections as a function of spectral window, whilst providing the framework for a derivation of an optimal sensitivity weighting scheme as a function of frequency. Various standard weighting schemes are possible, some of which are presented in Table 3.2.

The beam correction is checked by re-imaging an *e*-MERLIN field without the Lovell telescope and measuring point-like sources within the field. Comparing fluxes between the two was found to reveal that flux densities for point sources agree to within 3% within the HPBW of the *e*-MERLIN array. This is expected as differential flux

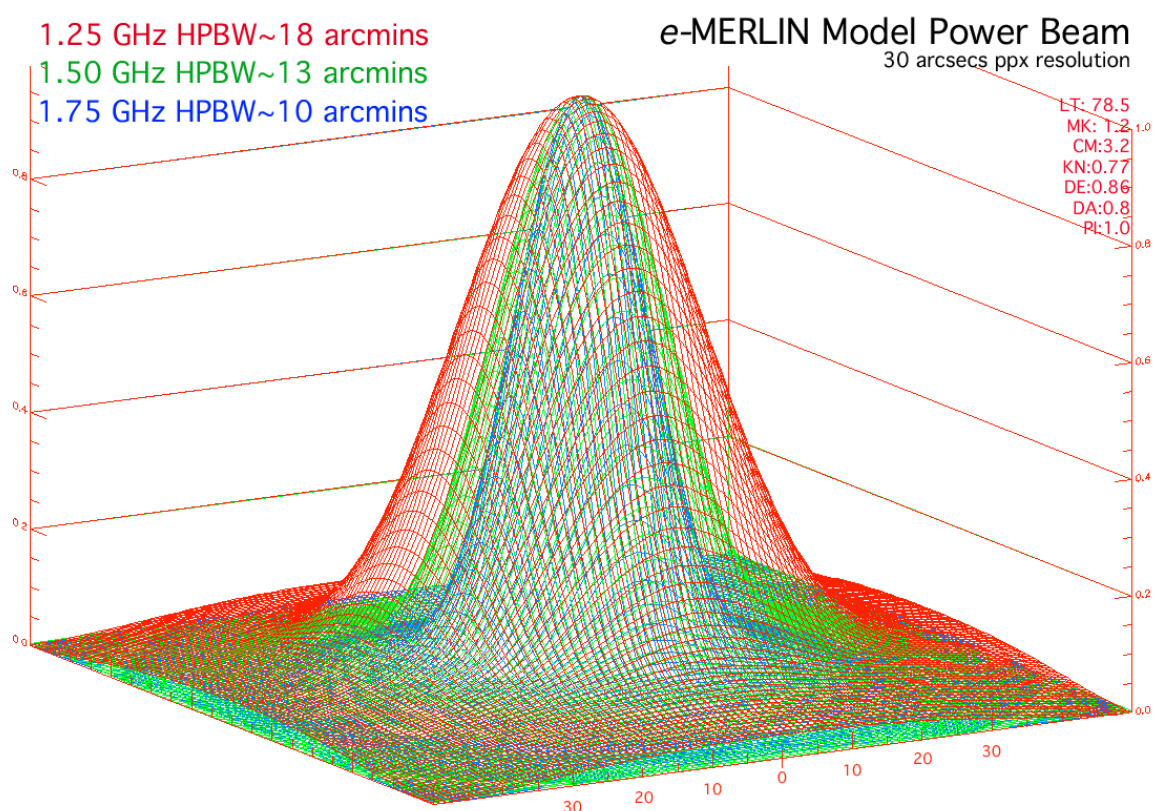


Figure 3.6: Predicted primary beam of the *e*-MERLIN array as a function of frequency for particular weighting scheme. High radio frequency observations offer a narrower field of view than do lower RF observations.

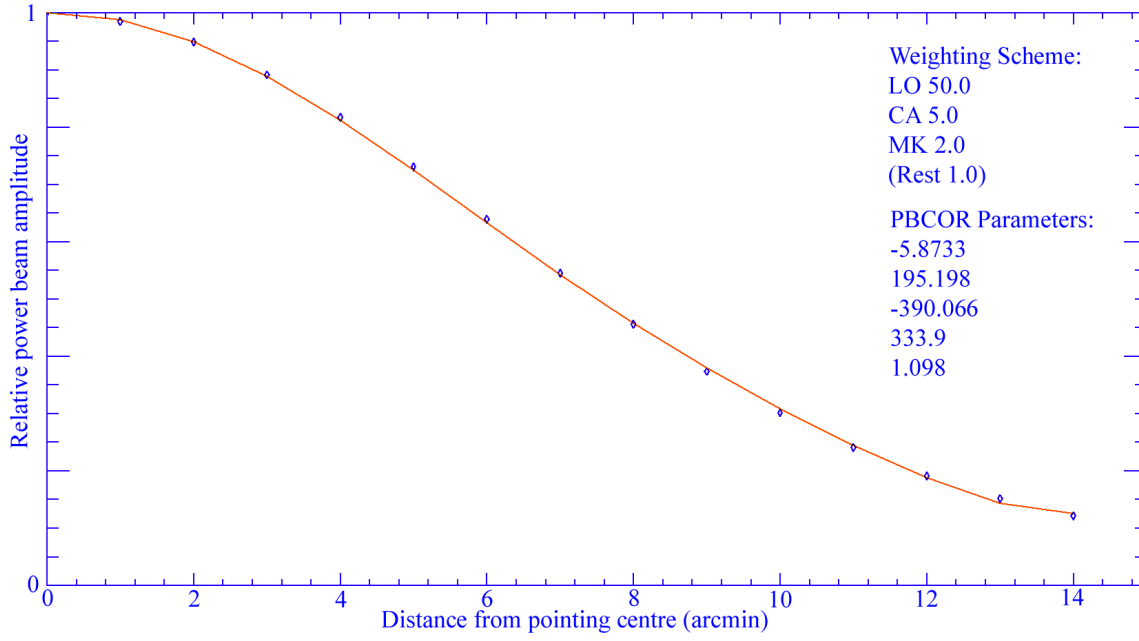


Figure 3.7: Derived beam correction for an *e*-MERLIN full track run with weighting scheme described in the plot. The points are the sampled result of the beam model, the curve is the fitted parameter set for use within the pipeline. The bandwidth was taken to be 0.5 GHz, with a mid-band frequency at 1.5 GHz.

Lovell Weighting	a_1	a_2	a_3	a_4	a_5	Gaussian 2σ width (arcmin)	HPBW (arcmin)
30	-5.6712	191.82	-378.306	303.408	0.186	14.6	17.2
50	-5.8722	195.198	-390.066	333.9	1.098	13.7	16.0
80	-6.3174	242.64	-600.162	597.27	100.026	13.0	15.2

Table 3.2: Beam correction PBCOR parameters for various Lovell weighting schemes at L-band. The fit is given by $P(\theta) = 1 + a_1\theta \times 10^{-3} + a_2\theta^2 \times 10^{-7} + a_3\theta^3 \times 10^{-10} + a_4\theta^4 \times 10^{-13} + a_5\theta^5 \times 10^{-16}$ where the displacement from the pointing centre θ is measured in arcmin.

measurements using the legacy MERLIN data also found a scatter in the comparison, although the reasons are not yet obvious. It is also found that approximately 68% of the sensitivity is derived from Lovell baselines at the pointing centre. Further afield, the influence of the Lovell telescope diminishes as the primary beam causes increasing attenuation on Lovell baselines in comparison to the non-Lovell baselines. The widest field of view, beyond which sensitivity would be comparatively greater by discarding the Lovell baselines, can now be established. The results of the calculation (which is determined within the beam model by computing the sum of non-Lovell baseline beams and comparing it to the sum of the total) is illustrated in Figure 3.8. The sensitivity of non-Lovell baselines becomes equal to the full array including the Lovell only beyond about 12.5 arcmin at 1.5 GHz. This calculation does not, however, take into account any off-axis phase errors associated with the Lovell telescope that would be likely to become significant at this angle, due to the non-isoplanicity given its short focal length. Given that the GOODS-N field is smaller than this region, it is unnecessary to utilise the array without the Lovell telescope at L-band. C-band data to be taken in the future will need to explore the usable extent of the beam, taking into account possible phase errors induced by the non-isoplanicity of the Lovell telescope. Given derivation of the extent of the primary beam of the array, the challenge of wide-field imaging out to the HPBW is explored.

3.2 Fast Wide-Field Imaging

To compensate for the induced spectral index, whilst at the same time reducing the image processing time considerably, and avoiding the well known w -projection problem (Perley, 1999b), fast-wide-field wide-band imaging techniques, originally conceived for VLBI imaging (Wucknitz, 2010), are incorporated into a single method and implemented in a ParselTongue script. The method is procedural with minimal input from the user, so that it could be incorporated into the *e*-MERLIN pipeline. A calibrated target uv dataset is first phase rotated (using UVFIX) to four new phase centres, pre-determined by the required field of view. Each of the new visibility sets is then averaged in time by a factor of two (i.e. 1 second averaging becomes 2 seconds etc) and also in frequency (i.e. 512 channels become 256 channels within each spectral window). The resulting uv files are each 1/4 of the size of the original, but time and bandwidth smearing at the extremities have increased correspondingly. This has the

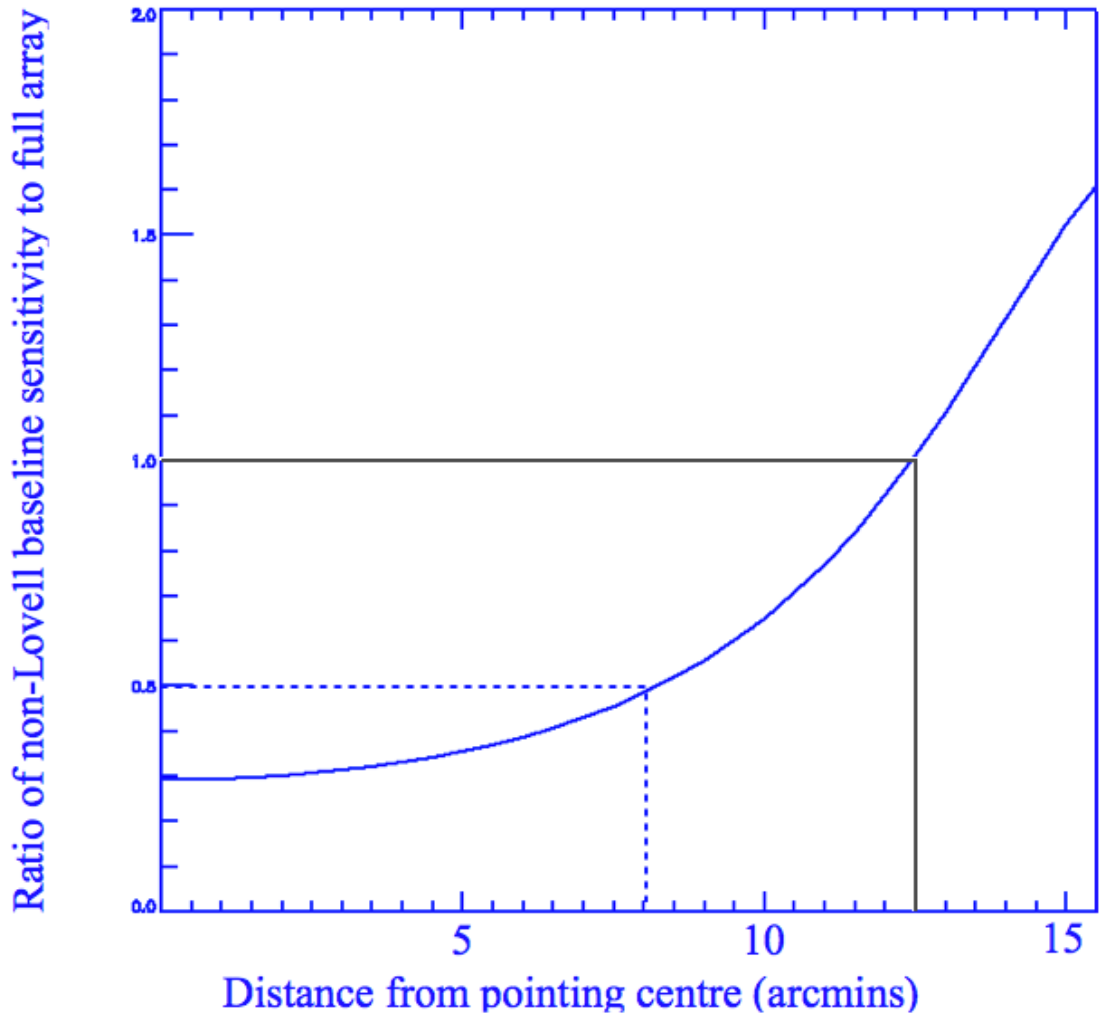


Figure 3.8: The ratio of the sensitivity of the *e*-MERLIN array including the Lovell to that without the Lovell as a function of angular displacement from the pointing centre at 1.5 GHz.

effect of slightly broadening the sources as well a small reduction in peak flux; however the integrated flux remains unaltered. The effect is mitigated by an equal amount because the field-of-view is reduced by an identical factor. The procedure is repeated for the newly averaged file by phase rotating each one four times again and re-averaging. The process is illustrated in Figures 3.9 and 3.10.

The process continues until each facet is small enough to be considered locally 'flat' such that 2D deconvolution is applicable, i.e. w -term effects are negligible within the imaging area. For typical *e*-MERLIN data at L-band, with a desired field-of-view diameter of 15 arcmin, a total of 64 tiles is required. The bandwidth smearing is

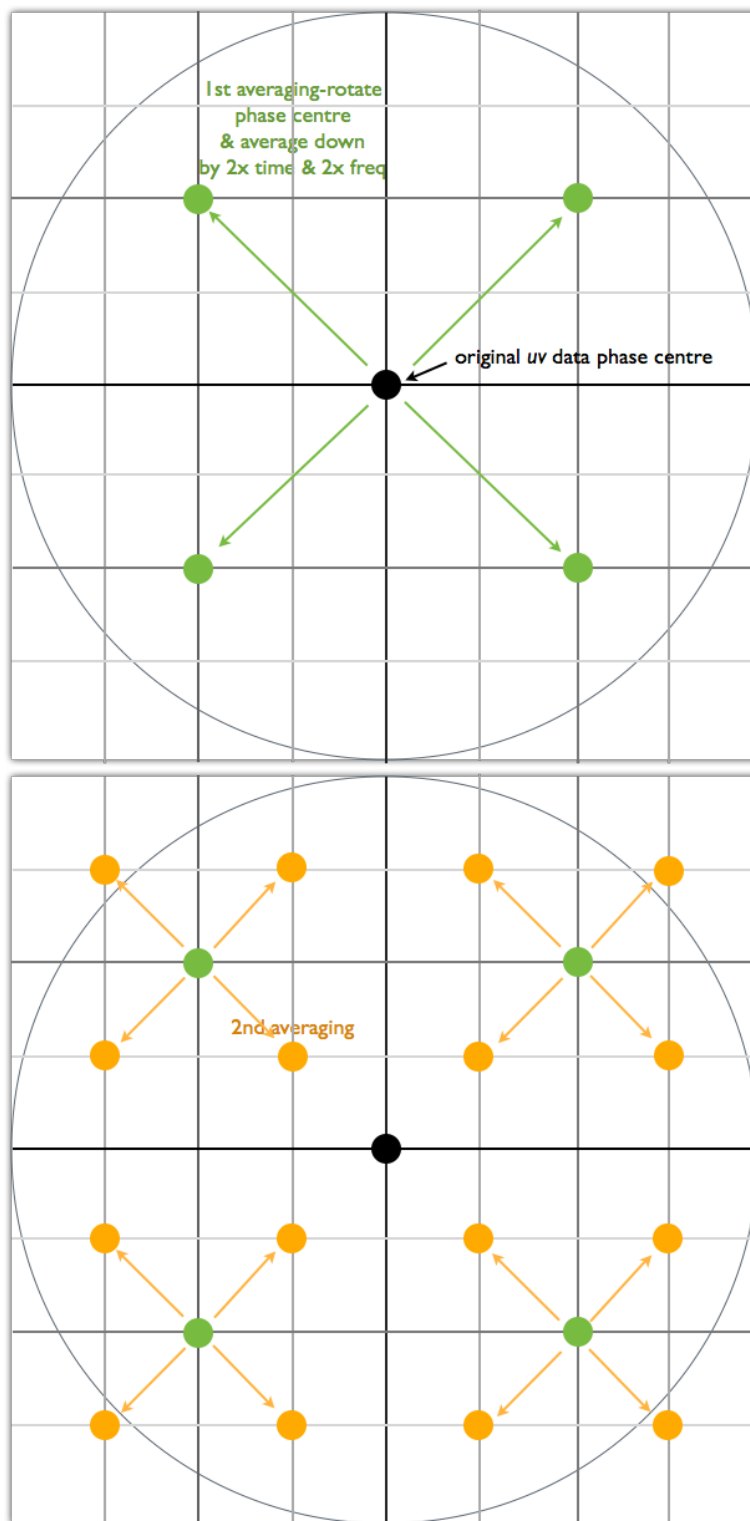


Figure 3.9: Fast Wide-field Imaging - first and second rotation and averaging.

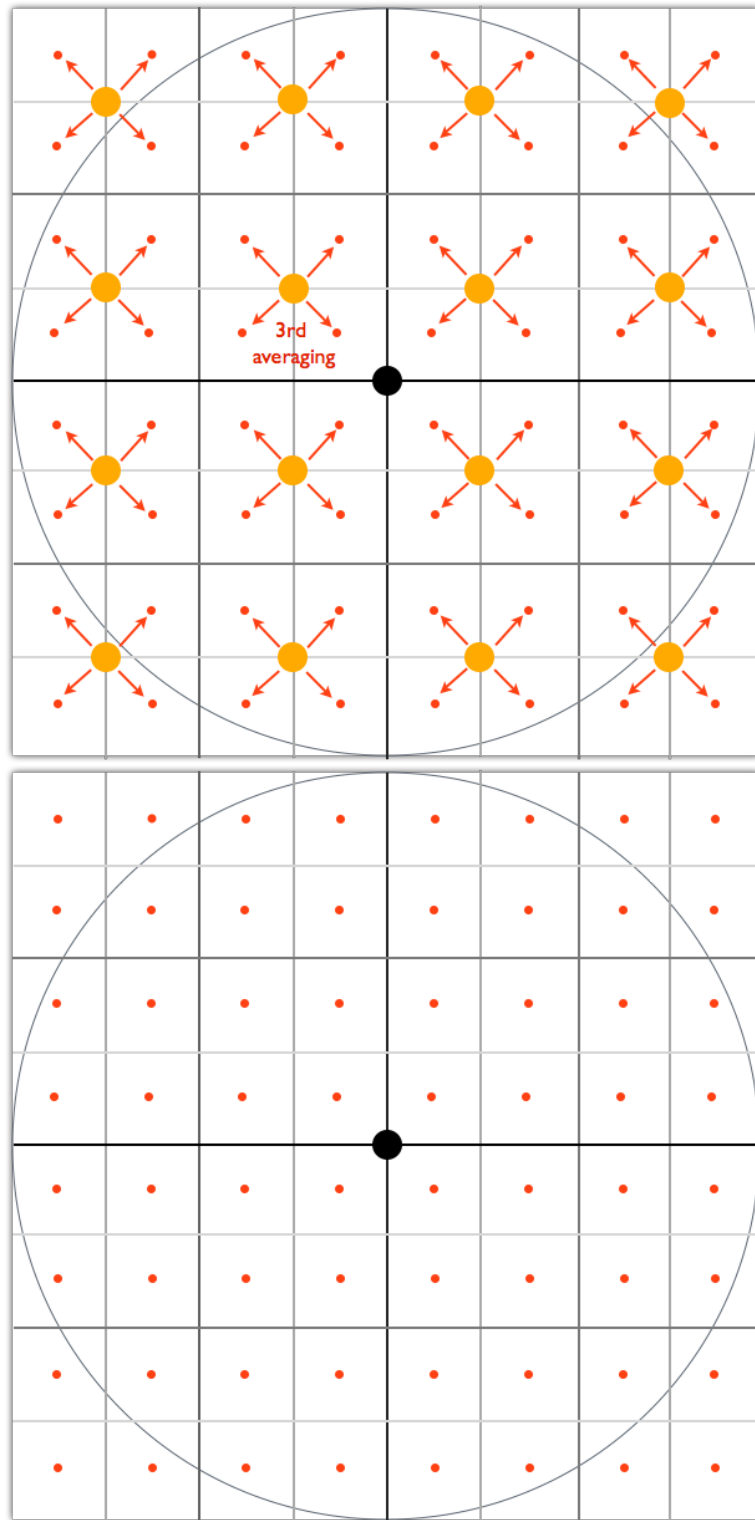


Figure 3.10: Fast Wide-field Imaging - final rotation & averaging with resulting facets. Each of the new uv datasets can be imaged at high speed.

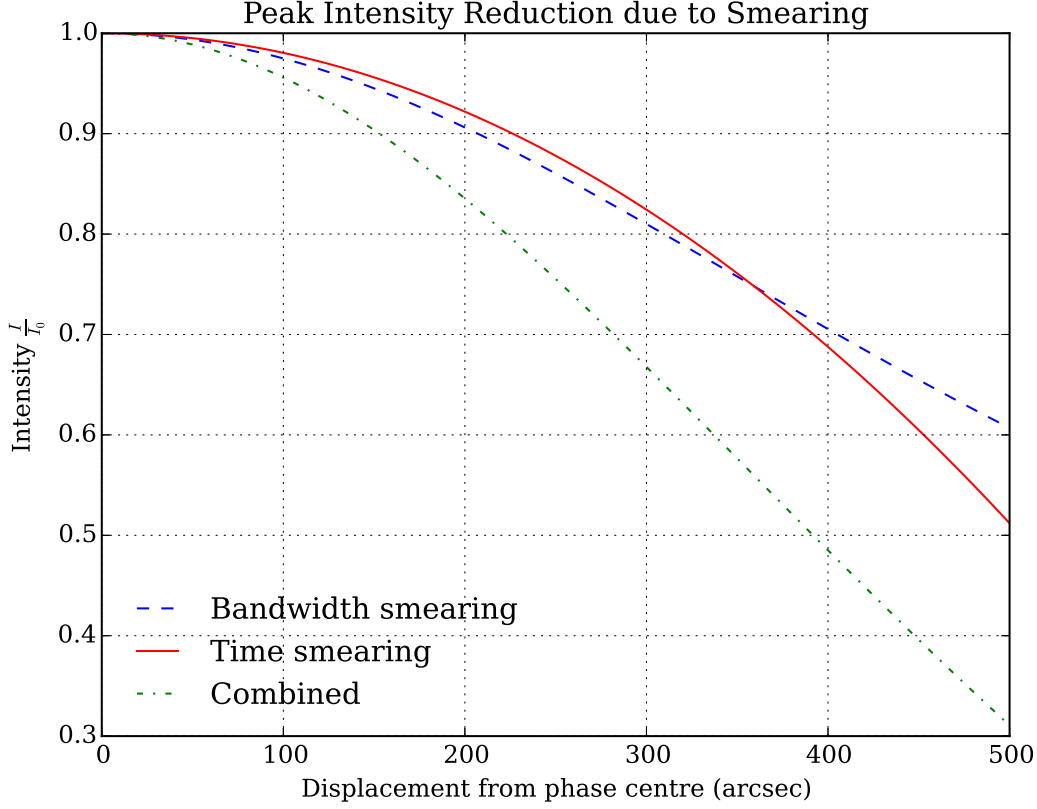


Figure 3.11: Bandwidth and time smearing outside a single tile within the fast wide-field-imaging routine for 1MHz channels and 8 second averaging. The tile radius at its corner is 76.9 arcsec resulting in acceptable smearing within each image.

approximated by (Bridle and Schwab, 1989):

$$R_{\Delta\nu} = \frac{I}{I_0} = \frac{\sqrt{\pi}}{2\sqrt{\ln 2}\beta} \operatorname{erf} \frac{2\sqrt{\ln 2}\beta}{2}, \quad \beta = \frac{\Delta\nu}{\nu_0} \frac{\theta_0}{\theta_{\text{HPBW}}}, \quad (3.5)$$

assuming Gaussian uv tapering and a square bandpass, where β is a dimensionless parameter equal to the product of the fractional bandwidth and the radius from the phase centre in multiples of synthesised beam-widths. Assuming the original calibrated data has a bandwidth at L-band of 512 MHz, a channel width of 125kHz, and a 15 arcmin diameter field with 0.2 arcsec resolution, each of the final 64 averaged uv datasets has a channel width of 1MHz. Thus for each facet at a maximum radius of 79.6 arcsec, smearing of the order of a few percent is expected (see Figure 3.11). Some sources may appear enlarged by up to a few percent of the beam (approximately

0.01 arcsec). The procedure also increases the level of time smearing, orthogonal in direction to bandwidth smearing, due to the integration time increasing from 1 to 8 seconds. Time smearing manifests as ellipsoidal arcing around the phase tracking centre, and has a similar effect as bandwidth smearing, that is a reduction in the peak flux of a source and a slight broadening of its size. Determining this, however, is not general and requires computation of the tracking of each source on the sky and its projection onto each baseline. However, because most deep surveys are full track observations (>12 hours), an average reduction in flux density can be calculated using (Bridle and Schwab, 1989):

$$R_\tau = 1 - 1.22 \times 10^{-9} \left(\frac{\theta}{\theta_{\text{HPBW}}} \right)^2 \tau_a^2, \quad (3.6)$$

which for the above integration times yields a value of over 98%, i.e. not significant. Further afield, however, this value reduces to a significant fraction of the original intensity. The effect is leveraged to reduce confusion (ripple noise) induced by bright sources further afield. A bright confusing source, at the edge of the 15 arcmin field, is reduced in intensity by over 50% when both smearing effects are considered.

Each facet must be deconvolved with the synthesised beams, created by AIPS, to yield a locally cleaned region. In practice, a region some four times larger in area is cleaned around each facet to reduce confusion from nearby sources, ensuring that even moderately bright in-field sources do not cause additional ripple noise over the expected rms noise associated with the sensitivity of the map. Following deconvolution, a single map can be generated by flattening the facets together before amplitude beam correction is executed according to the beam model. However, for wide-band cleaning, required by modern arrays like *e*-MERLIN, the varying primary beam width as a function of frequency must be considered in this deconvolution process.

3.2.1 Spectral Cleaning

The HPBW and first side lobe occur at different angular displacements from the beam centre depending on frequency illustrated in Figure 3.6. This effect must be considered and compensated. The radio bands (L-band and C-band) available within *e*-MERLIN (and the JVLA) are divided into separate *spectral windows* or *Intermediate Frequencies* (usually 8 or 16) which are defined during the scheduling of the observations. Each

of these spectral windows is again divided into spectral channels to avoid bandwidth smearing. Any number of these spectral channels can be integrated together. The signal-to-noise ratio (S/N) for sources observed within the beam increases as sub-bands and spectral windows are integrated. It is expected, for the faint-source population to be investigated by *e*-MERGE, that only sufficient S/N will be attained on integration of the entire bandwidth (512MHz for L-band or 2GHz in C-band). In these cases the spectral index cannot be derived from a single band (i.e. from L-band) but will require the use of the observations made at another to attain this information, i.e. L & C. There is an exception in the case of *very* steep spectrum sources whereby most of the flux is received in the lower part of the band, L-band for example, in which case the higher band, C-band, would be unlikely to detect such a source. Such steep spectral sources may indicate the detection of an AGN lobe or jet as starburst SEDs appear to be consistent (Condon, 1992; Condon and Ransom, 2010; Peel et al., 2011) and are expected to be shallow at higher redshifts. However AGN cores would remain flat even at high redshift so morphological discrimination is important in all cases.

The changing primary beam-width as a function of radio frequency has undesirable effects when utilising the standard Högbom algorithm within AIPS, leading to amplitude errors. Sources at the centre of the field (i.e. at the pointing centre) remain unaffected by the primary beam effects. However, those some displacement from the pointing centre will experience significantly more reduction in amplitude at the higher frequency end of the band than at the lower end. Consequently, sources will appear fainter in higher IFs than in lower IFs. This is often called an *induced spectral index* because it emulates the amplitude error artefacts caused by a source of very high spectral index. The effect increases as a function of the angular displacement from the pointing centre. The ratio of the amplitude (i.e. induced spectral index) at either ends of L-band is illustrated in Figure 3.12, which visually demonstrates that the spectral index varies slowly within the primary beam, but becomes excessively steep near the first side-lobes. To understand how standard deconvolution is incomplete without modification of the synthesised beam, consider the point spread function of an unresolved source near to the edge of the primary beam (here, edge means usable extent, perhaps 7.5 arcmin at L-band). The visibilities associated with such a source contribute more flux density at the low frequency end of the band than in the higher spectral windows, and AIPS, unaware of the primary beam, constructs a synthesised beam comprising equal contributions from all parts of the band. A first approach, attempted in the past,

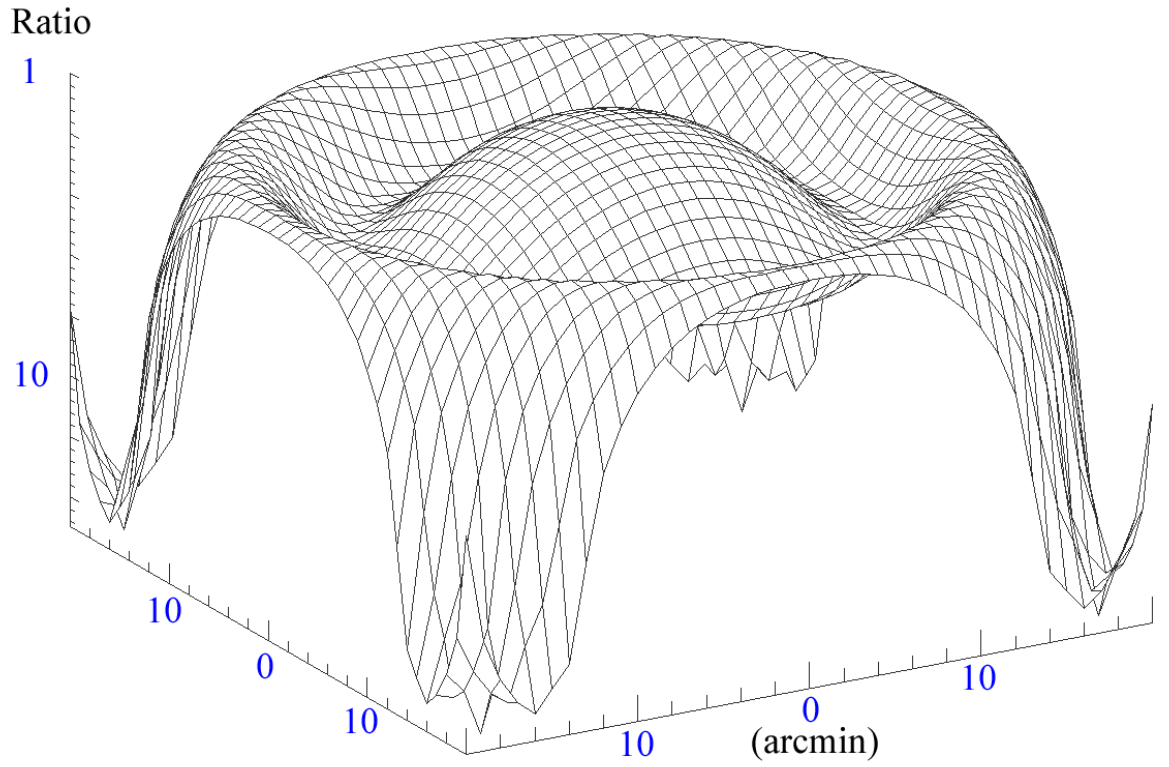


Figure 3.12: An diagrammatic illustration of the ratio of beams at extreme frequency ranges across a very wide field using *e*-MERLIN. The total width is 20 arcmin but it is observed that the ratio (related to the spectral index) is relatively well behaved within about 10 arcmin of the pointing centre.

is to clean each spectral window separately, but this can only be successful if the S/N ratio of sources is sufficient in each spectral window in isolation. This is often not the case, sources are only deconvolvable if they can be detected by the clean algorithm, which for the majority of faint sources requires integration of the whole band. A more efficient way to clean sources towards the edge of the primary beam is to *modify* the dirty synthesised beams such that they likely *more accurately represent* the integrated point spread function artefacts of sources at any position within the primary beam. This is achieved by instructing AIPS (via ParselTongue) to generate dirty beams for each spectral window separately, at each tile position in the grid. The synthesised beams are then *scaled in amplitude* per spectral window, based upon their position in the primary beam and on their centre frequency. Once scaled, the dirty beams are then averaged together in position and normalised to unity to yield a localised dirty beam, applicable to deconvolve with a fully integrated dirty map for that particular region of the grid. Deconvolution is thus said to be directionally dependent and this new methodology is implemented in a ParselTongue script. The deconvolution task used is APCLN, which implements the Högbom-Clark algorithm using user defined beams and maps. The methodologies described here have been merged together into a integrated procedure and utilised within the *e*-MERLIN pipeline. Testing was performed on a 15 arcmin field at L-band as part of the *e*-MERGE survey and used to contiguously image sources in the field. The total time to produce a map using a calibrated 0.5 TB *e*-MERLIN *uv* data file was less than 48 hours utilising a single Intel Xeon CPU core on a 128 GB RAM machine with a RAID 5 array. Approximately half of the time involves the phase rotation and averaging procedures which are IO limited. However, cleaning with 1 million iterations

(for example) in APCLN took less than 24 hours; this is compared with an estimated time of 1000 days using IMAGR with its built-in amplitude scaling invoked. A comparison of the technique is illustrated using JVLA data in Figure 5.12.

The above correction makes the assumption that sources are *point sources*. However, there is an additional subtlety that would cause an error in the correction if the sources are very extended. The correction should be baseline dependent because there may be instances whereby the short baselines, that do not involve the Lovell telescope, dominate the source signal. In these cases the synthesised beam correction would be better represented by assuming a wider primary beam. If, instead, sources are partly detected by the long baselines, then the synthesised beam scaling correction lies some-

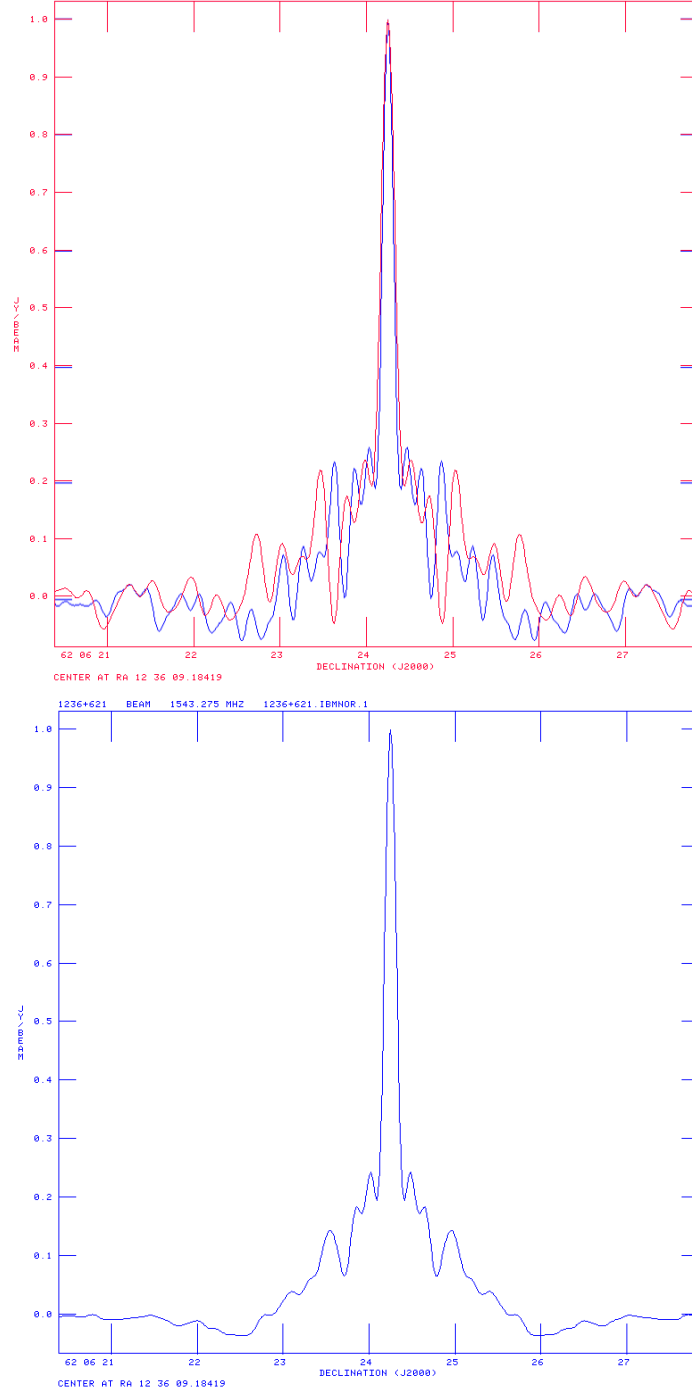


Figure 3.13: Synthesised resolution beam for two single IFs (top) and an integrated synthesised resolution beam (bottom) for a combination of all 8 IFs (1.25 - 1.75 GHz) in the *e*-MERLIN array. Point sources further from the field centre are attenuated by a greater amount in the higher frequency spectral windows than in the lower frequencies because the primary beam is narrower at higher radio frequencies. To compensate for this undesirable effect, synthesised beams are scaled in relative amplitude (weighted) according to the results of the primary beam correction model before being averaged into a single synthesised beam more appropriate for that location in the primary beam.

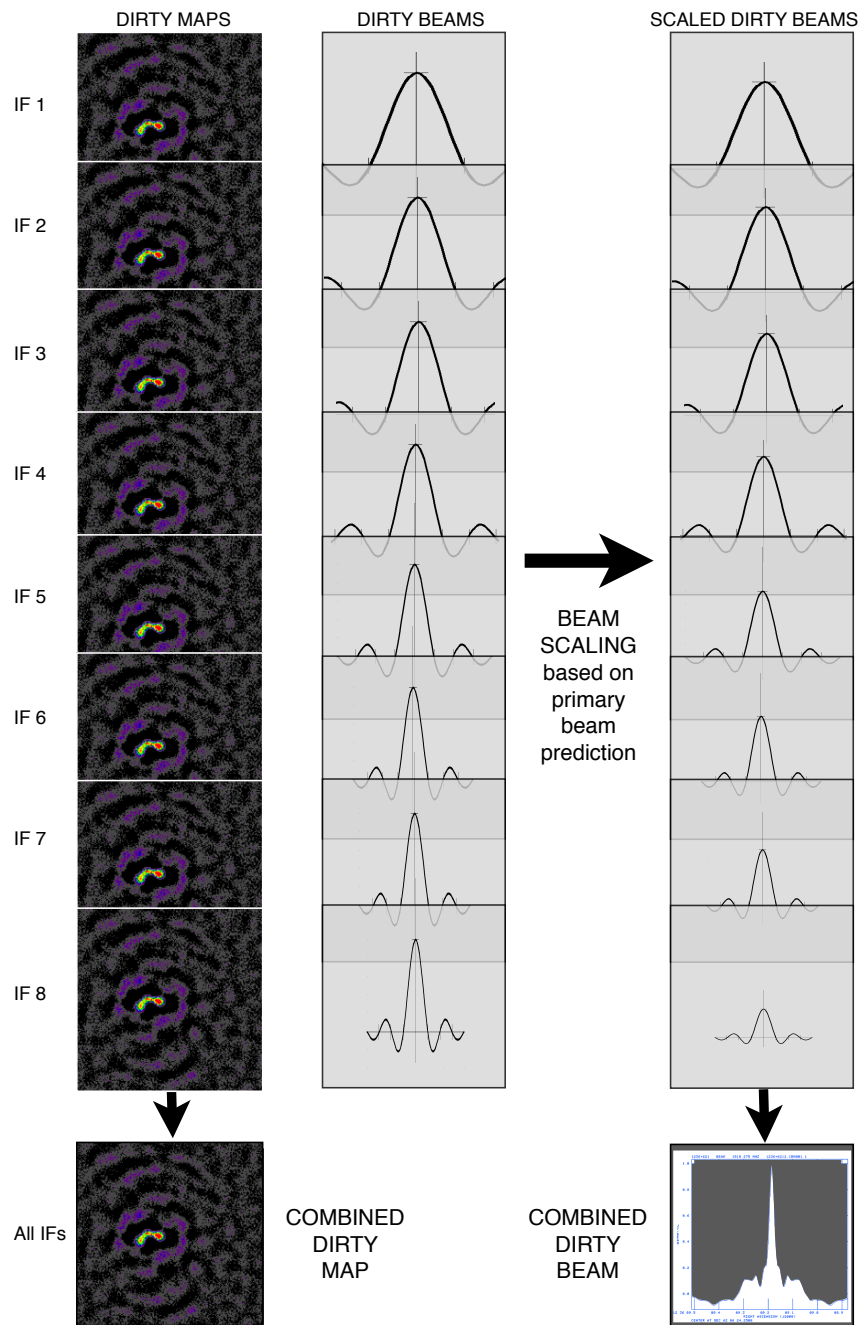


Figure 3.14: To compensate for the primary beam induced spectral index, the synthesised pairs of dirty maps and beams for each position in the wide-field image and at each spectral window must be generated. Each frequency produces a pair for each position in the wide-field based on its displacement from the pointing centre.

where between the 25m and 76m beams, and is actually *source dependent*. However, for sources in the GOODS-North field this effect is likely to be small.

3.3 Summary

The development of the techniques in this chapter was motivated by the necessity to image as wide a field as possible, on as short a timescale as possible, whilst mitigating some of the problems inherent in wide-field and wide-band imaging. The fast wide-field wide-band imaging method uses phase rotation and averaging to reduce the effects of bright outliers. The methodologies are applicable to inhomogeneous arrays in general, for example the European VLBI Network (EVN), as well as other *e*-MERLIN projects where wide-field imaging is required. This includes the SuperCLASS project, whereby the method is being used to catalogue sources in the field.

The *e*-MERLIN primary beam, being dependent upon the weighting of each telescope, is the limiting factor for the field-of-view of the *e*-MERGE project. A customised tool derives a axially symmetric polynomial fit, compatible with AIPS tasks, for band-integrated continuum observations and successfully corrects amplitude beam effects to within 3% of the HPBW. A full-track observation is predicted to have a HPBW of approximately 15 arcmin at mid L-band using the scheme adopted for the project, but is greatly dependent upon the beam-width of the Lovell telescope, which is derived from legacy MERLIN+VLA data, described in Chapter 4.

Chapter 4

Legacy MERLIN + VLA HDF-N imaging

The original GOODS-N data, taken (in 1996) from both the VLA and MERLIN arrays at 1.42 GHz were the precursor for the *e*-MERGE project with a sensitivity of $3.5\mu\text{Jy/bm}$ at the pointing centre ([Wrigley, 2011](#)). This legacy data is, in comparison to the modern *e*-MERLIN data, quasi-monochromatic and hence did not require wide-band beam models. The data are used here for three reasons: to investigate the angular size distribution using Gaussian fitting and visual inspection techniques, to determine the Lovell beam size, and to be used in combination with the new *e*-MERGE data to improve sensitivity. The legacy data were faceted in 19 separate regions to overcome w-projection errors, and 26 bright sources were subtracted from the data to avoid excessive confusion or *ripple noise*. These sources are now restored to assemble a fully contiguous wide-field image for the first time. The chapter introduces the Largest Angular Size (LAS), Gaussian fitting and presents an LAS distribution based on visual inspection techniques.

4.1 Restoration of Contiguous Image

To create a completely contiguous image from the original data, 26 bright sources, subtracted because they caused significant confusion or ripple noise, needed to be restored. These confusing sources were recovered from the *uv* plane combination datasets and restored to the incomplete sky-plane map by transferring clean components. The new map consists of over 300 megapixels and, with a resolution of 0.2 arcsec, is the widest

high-resolution image ever derived from a single pointing of the legacy MERLIN array (see Figure 4.1). Postage stamp sub-images were extracted for each of the 339 sources catalogued in the very deep VLA catalogue (Morrison et al., 2010) within the 15 arcmin diameter field. Of those, 178 appear above the 5σ threshold which almost doubles the 92 found in the 10 arcmin field by Muxlow et al., 2005 (see Figure 4.2). The peak flux density distribution is presented in Figure 4.2, which illustrates that the minimum flux threshold appears to rise as a function of the distance from the pointing centre caused by the primary beam.

When the sources, binned according to peak flux density per beam, are compared with peak flux densities in the Deep VLA catalogue, a difference in the distributions is exhibited (see Figure 4.3). It illustrates that the number of detections below $30\ \mu\text{Jy}$, across the entire field within the MERLIN+VLA observations, is approximately double compared with those falling below $30\ \mu\text{Jy}$ within the VLA only data (Morrison et al., 2010). It can be inferred that there must exist a large fraction of sources with structures that extend beyond the 0.2 arcsec resolution of MERLIN (Muxlow et al., 2005) and have been partly resolved away; i.e. this is consistent with the view that the lower flux density sources are dominated by spatially extended emission regions (SFG-like) rather than by point-like (AGN-like) objects.

4.2 Measuring Sources

To investigate the angular sizes of the population, each of the 178 sources were examined using a combination of techniques to derive the LAS, peak flux densities, integral flux densities and local rms noise. Two methods were used based on those adopted in Muxlow et al. (2005):

- Gaussian Fitting,
- Largest Angular Size.

4.2.1 Gaussian fitting

Gaussian fitting using 2D ellipses is the de-facto method for measuring source attributes and assumes that a source has a Gaussian profile. The spatial extent of each source, with position identified using the Morrison et al. 2010 catalogue, was initially measured

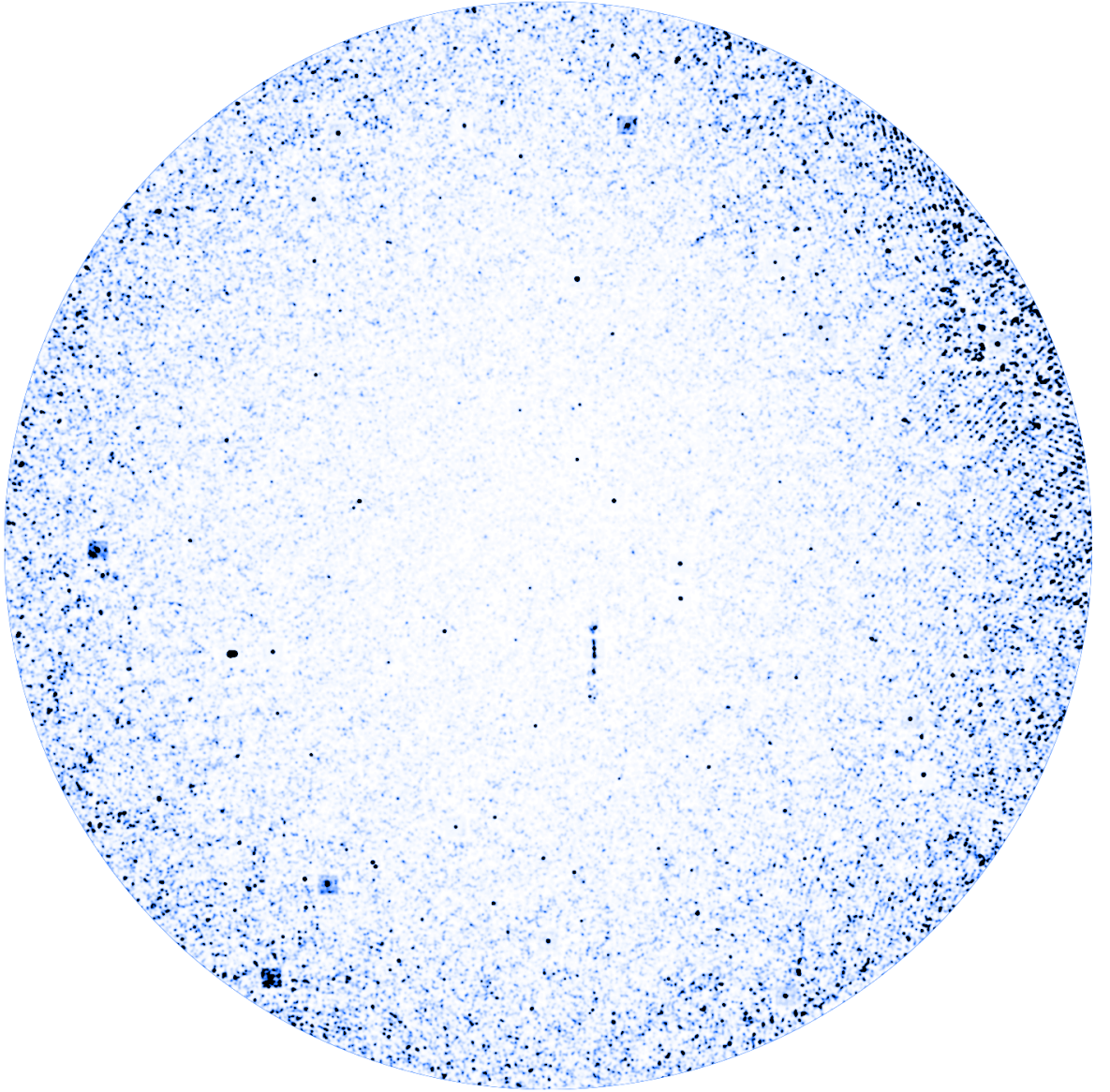


Figure 4.1: The restored 15 arcmin diameter wide-field image of GOODS-N derived using MERLIN+VLA arrays in L-band. The image has been resampled to a low resolution for display in this figure. The North-westerly region (top-right) exhibits a considerable amount of 'ripple noise' due to bright outliers.

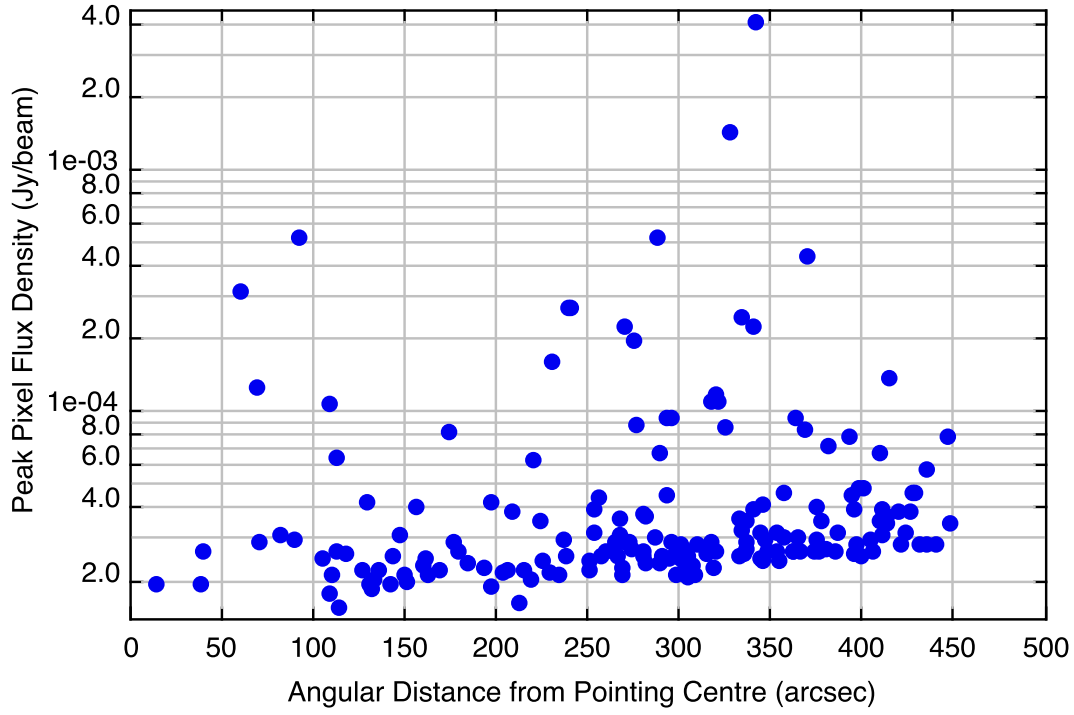


Figure 4.2: Peak flux densities of the 178 sources $> 5\sigma$ vs angular distance from pointing centre. There are naturally a greater number of sources towards the edge of the field. The 5σ detection threshold rises as a function of angular distance from the pointing centre due to primary beam effects.

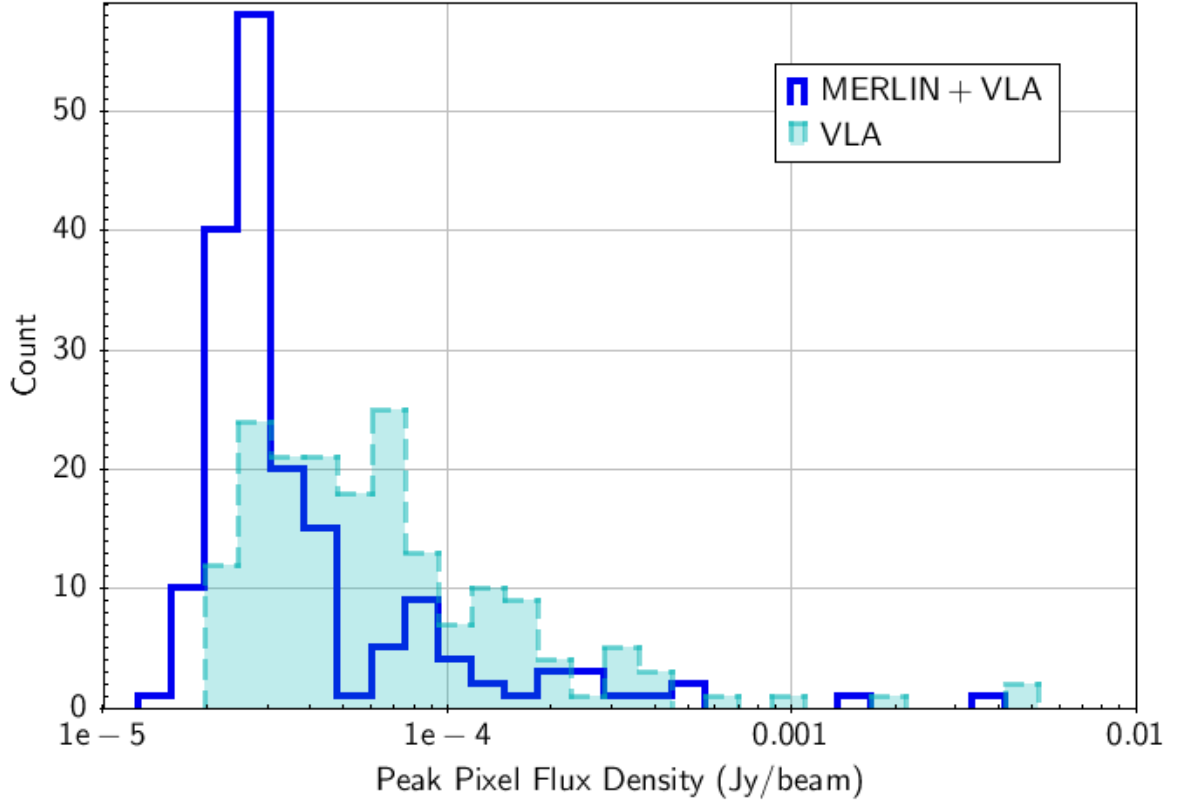


Figure 4.3: Number counts of peak pixel flux densities of the MERLIN+VLA observations and those obtained solely from the VLA [Morrison et al. \(2010\)](#) for 178 sources detected over 5σ . A large proportion of objects are heavily resolved away by long MERLIN baselines.

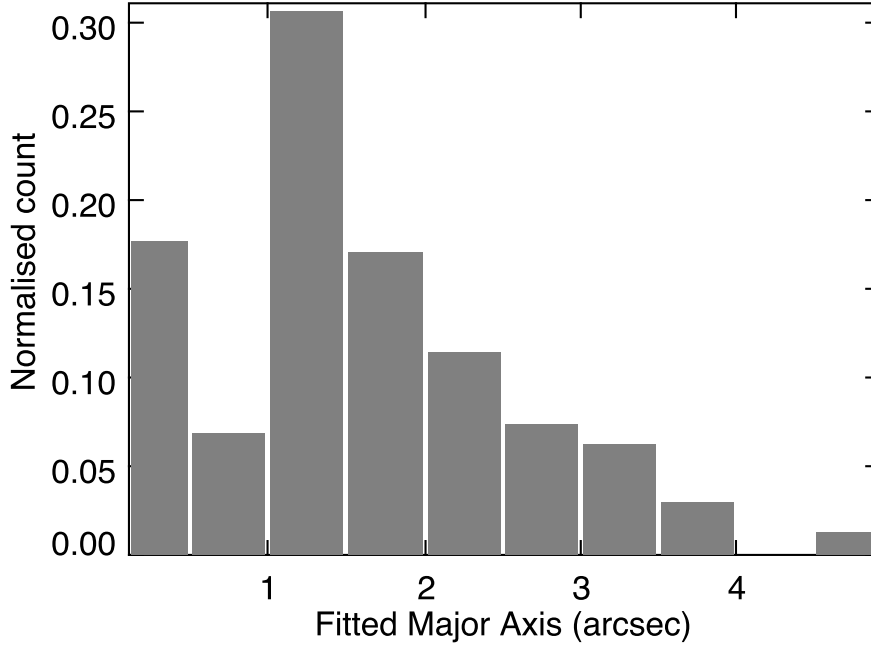


Figure 4.4: Gaussian fitted angular size measurement of 178 elliptically fitted sources (arcsec) generates a clear bimodal distribution.

using this method. A 2-dimensional Gaussian was fitted to each source, assigning parameters to major and minor axes of an ellipse, and deriving a new peak flux density (consistent with the calculated integrated flux) as well as a major axis position angle. Integral flux densities are derived from the area of the ellipse. This process yields a crude but consistent measurement for the apparent size of each source as it removes user bias. However, because most sources exhibit a complicated morphology, Gaussian fitting tends to 'flatten' the source profile (derived peak fluxes differ more in spatially extended sources than in point-like sources) to maintain an integrated flux density that is consistent with that of the source. The elliptically fitted angular dimensions exhibit a clear bimodal distribution (see Figure 4.4), with one peak placed between 1.0 - 1.5 arcsec and another between 0 - 0.5 arcsec. A median size of 1.4 arcsec is a result of an extended tail. It was observed that if a compact substructure of a source is sufficiently brighter than its extended emission then only the compact source is recorded, the primary cause of the first peak. If the data is subdivided in terms of peak flux density, say an arbitrary break at $50\mu\text{Jy/bm}$, then the data exhibits correlation with the brightest

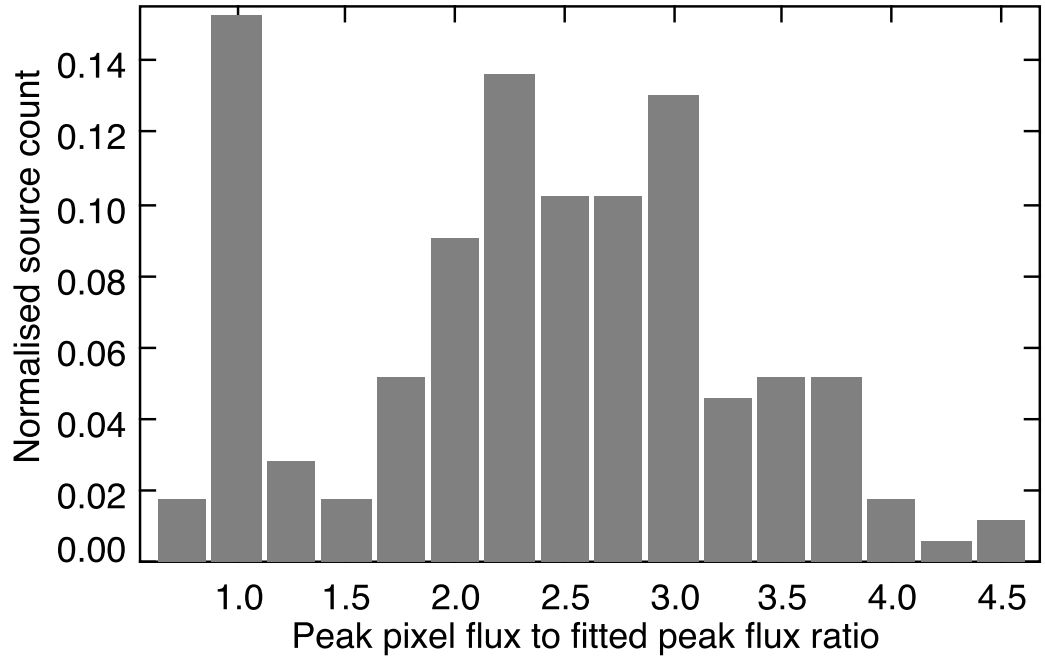


Figure 4.5: Ratio of Gaussian fitted flux density measurements of the peak pixel to the fitted peak illustrate that over 15% of sources have a value near unity indicating the presence of a compact source.

peaks associated with the smallest fitted angular sizes: evidence that blind Gaussian fitting cannot determine the largest size of a source, but only the size of the dominant component *within* the source. However, a useful result can be derived by taking the ratio of the peak pixel to the fitted Gaussian peak, the flattened peak. The amount of flattening can be used as a rudimentary measure of the morphological complexity of a source; a ratio of unity indicates a well-defined, simple shape, whilst a high ratio indicates more complicated morphological structure. The result of this is presented in Figure 4.5 in which approximately 15% of sources are observed to have a ratio near unity, implying a compact core. The remaining sources clearly contain spatially extended structure and require an alternative measuring technique over Gaussian fitting.

Image Artefacts

Low-level ripple noise across the entire field has the effect of producing periodic peaks and troughs across an extended source, which causes difficulty in measurement of the attributes of any source. Additionally, if sources lie close to subtracted outliers, additional ripple artifacts may be present, leading to errors in flux density measurements. Of concern is whether these artefacts significantly distort the statistics of the size and shape of sources, thus affecting the reliability of the maps. To investigate this, a technique usually applied to the detection of weak lensing ([Brown and Battye, 2011](#); [Chang et al., 2004](#)) was applied to the results obtained by from Gaussian fitting. The methodology involves selecting coordinates in a grid-like manner throughout the field and examining the orientation of sources relative to each other in within annuli of increasing radii. If there is no local systematic effect then all galaxy orientations will appear statistically random¹. However, any systematic distortion effect would cause a bias in their relative position angle in relation to the epicentre of the source of the artefact. The algorithm was implemented in IDL² and the list of source detections, minus any obviously poor Gaussian fits due to non-elliptical galaxy shapes (i.e. major axis $> 4''$ and position angle error > 20 degrees), was examined methodically. The result (using 178 sources) revealed no such bias. Previous studies by [Patel et al. \(2009\)](#) revealed no weak lensing detection within the central inner region using these data, and it can be concluded that systematic shape distortion effects are not significant in legacy MERLIN+VLA imaging.

Primary Beam

The compact cores identified above permit differential flux fitting of these sources to establish the difference in primary beam with the Lovell, and was used in defining the Lovell beam-width for the model in Chapter 3. This involved observing the same sources without the Lovell telescope. The difference in flux, given knowledge of all other beams in the array, yields information about the width of the Lovell beam. Using this method it was found that the best fit for the beam-width of the telescope is equivalent to $\theta = 1.13\lambda/D$ where $D = 76\text{m}$. The appropriate amount of aperture tapering was increased in the beam model to simulate this beam-width. The difference between the

¹This assumes that no significant weak lensing phenomena exists in the HDF-N and that intrinsic alignments are negligible ([Patel et al., 2009](#)).

²C. Demetroullas, private communication.

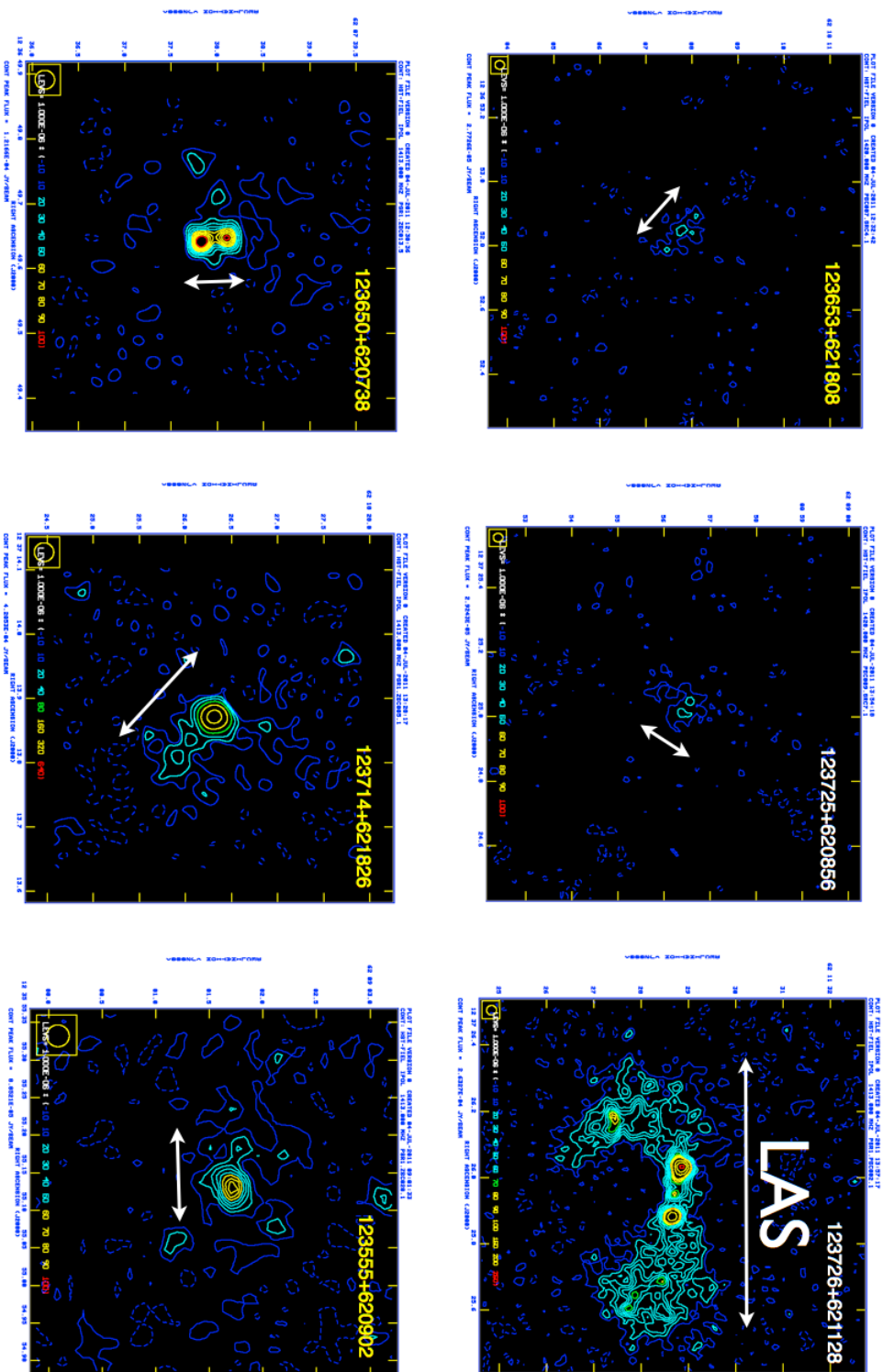
flux density measurements with the beam applied varies by approximately $\pm 3\%$ across the field.

4.2.2 Largest Angular Size

The *Largest Angular Size* (LAS) attempts to overcome the problem of the core component dominating the measurement but is a technique that relies heavily on visual inspection. It also avoids the assumption that the source has a Gaussian profile. AGN cores are unaffected but the angular extent of jets does depend on their projection angle. Unresolved sources have equal major and minor LAS lengths, with AGN jets exhibiting an extension in one axis. Cores can be identified by comparison of the integral flux with the peak flux density. Several sources exhibit multiple peaks, thus the LAS yields a more realistic measure of an object's size, a technique favoured in [Muxlow et al. \(2005\)](#), which yields a double peaked LAS distribution (see Figure 4.7). The method involves measuring the largest axis of a source out to its lowest contour visible in the image. In the case of a naked core, a Gaussian fitter is used. It does, however, introduce user biases and a less subjective measure is sought in Chapter 5 that is less reliant on human intervention. Some examples are illustrated in Figure 4.6.

4.3 Angular Size Distribution of MERLIN+VLA Legacy Data

To overcome the lack of extended emission by MERLIN, size data taken from the Morrison catalogue, which utilises data from the VLA in all four main array configurations (A, B, C & D), was used in compiling the LAS dimensions for sources *resolved* by the VLA. For objects unresolved by the VLA (i.e. deconvolve to zero width) the MERLIN+VLA images are able to reveal the angular size of the emission. The combined LAS sizes for all sources were binned yielding the histogram of which is presented in Figure 4.8 exhibiting a peak under 1 arcsec, and a median size of 1.2 arcsec. The distribution is similar to that presented in ([Muxlow et al., 2005](#)) in that the median lies less than the 1 arcsec scale, however any bi-modality is no longer exhibited, which is likely to be attributed to insufficient population sampling. *e*-MERLIN sampling will not be directly equivalent because the *uv* coverage for the wide-band array samples more *uv* space and will be more complete than MERLIN. Furthermore if only sources previously



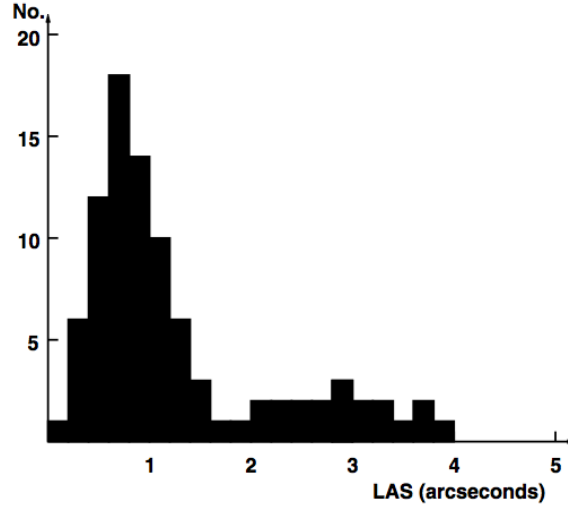


Figure 4.7: Previously measured Largest Angular Sizes of 92 brightest sources in the 10 arcmin field (Muxlow et al., 2005) using the MERLIN and VLA arrays. A tentative bimodal distribution was exhibited.

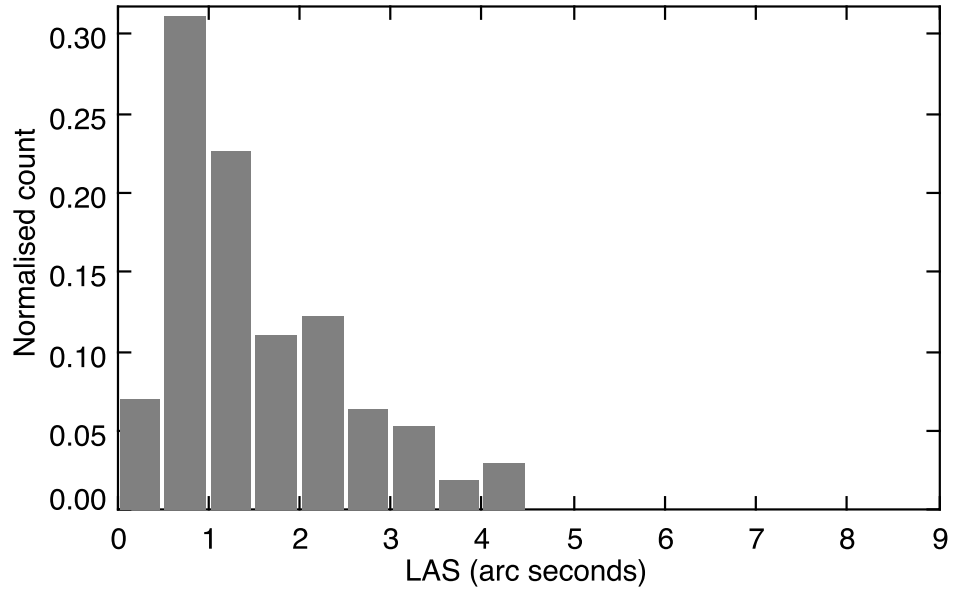


Figure 4.8: Largest Angular Size (LAS) Distribution of 178 Sources in the MERLIN+VLA (A,B,C,D arrays), 1.4 GHz GOODS-N field, < 9 arcsec. with a median of 1.2 arcsec.

classified as either starburst or AGN candidates are separated then a weak correlation is apparent with AGNs favouring smaller angular sizes. This unsurprising feature simply reflects the morphological discrimination technique used in classification, a topic examined in Chapter 6. Spectroscopic or photometric redshifts were cross matched where available (Barger et al., 2008) by searching for optical sources lying within 1.0 arcsec, resulting in a median redshift of 0.936.

4.4 Summary

The restoration of the original MERLIN+VLA observations, taken in the late 1990s, has been used for three purposes: generating a contiguous map that can be combined with the *e*-MERGE observations, anchoring the beam of the Lovell telescope, and generating some source statistics for comparative use. The production of the map yields the largest and deepest single wide-field image ever derived from the MERLIN array. The Largest Angular Size of sources, a measurement important when considering the design of future telescope arrays, was completed using a combination of MERLIN+VLA data, with the VLA data including all 4 main array configurations. The analyses were carried out by visual inspection of all 178 detectable sources ($> 5\sigma$) in the field. Almost all sources were found to be resolved by the MERLIN array, with 15% of sources dominated by a compact component. The presence of ripple noise meant that standard Gaussian fitting was not reliable and used only in compact cases, but spatially extended emission could be observed in most sources. The peak LAS lies between 0.5 and 1.0 arcsec with a median of 1.2 arcsec. These data will be used in Chapter 6 to refine measurement techniques for sources in the *e*-MERGE data. It will also serve as an astrometric check and will be used in combination with the first release of *e*-MERGE data.

Chapter 5

e-MERGE Observations and Imaging

This chapter describes the collection and imaging of data for the *e*-MERLIN Galaxy Evolution survey using the *e*-MERLIN and JVLA arrays at L-band (centre frequency 1.5 GHz) and C-band (centre frequency 5.5 GHz). The fast wide-field wide-band imaging method and primary beam model developed earlier are utilised to correct for the attenuations in flux density and induced spectral index as a function of angular displacement from the pointing centre. The chapter concludes with a summary of the data products, many of which have been uploaded to the *e*-MERGE project wiki for other analyses by the consortium.

5.1 *e*-MERGE Observation Strategy

The *e*-MERGE observations are taken using a combination of the *e*-MERLIN array and the JVLA, at L-band and C-band, the spatial coverage being defined by the primary beam of the *e*-MERLIN array at L-band. Both arrays are used in order to maximise *uv* coverage, with *e*-MERLIN providing the long baselines and the highest angular resolution. Because the width of the primary beam is frequency dependent, C-band observations require mosaicing to achieve the same spatial coverage as the L-band observations. A total of seven pointings for C-band were devised, such that the *e*-MERLIN array yields similar coverage as the single L-band pointing (see Figure 5.1). This maintains good overlap of the Lovell beam within the *e*-MERLIN array and results in significant oversampling of the JVLA. Both the *e*-MERLIN and JVLA observations use the same correlator configurations when possible, with frequencies and channel widths detailed in Table 5.1. At the time of writing, the only *e*-MERLIN

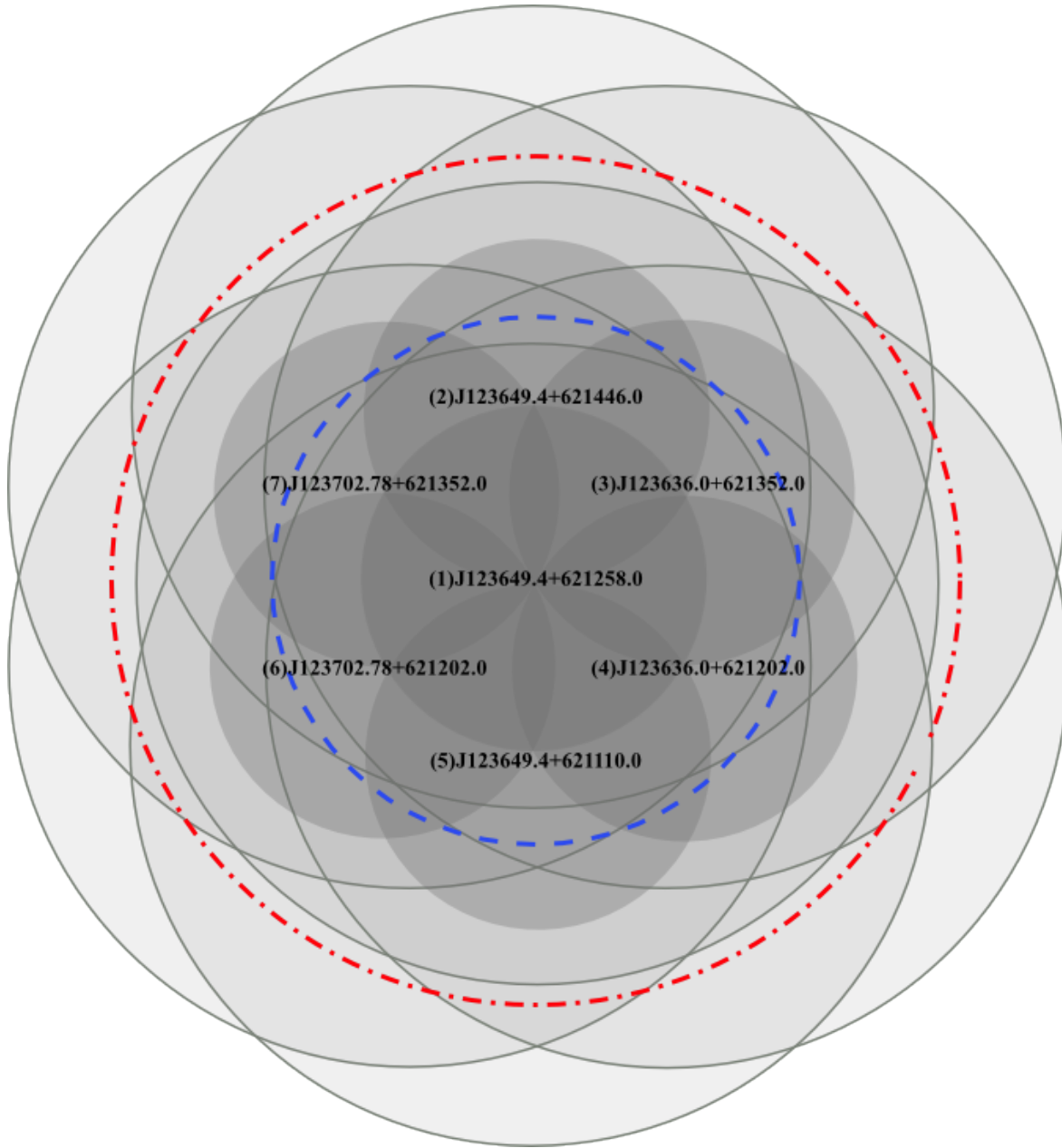


Figure 5.1: The 7 pointing mosaic strategy at C-band (5.5GHz) utilises primary-beam overlap to acquire sufficient coverage, the extent of which varies with the observing radio frequency. Each small circle represents the estimated HPBW of the Lovell telescope in C-band, with the larger circles representing the HPBW coverage of the 25m (VLA) telescopes. The blue dashed and red dot-dashed circles represent the beams of the Lovell and VLA respectively at L-band for comparison.

observations currently taken are at L-band, and only a minor fraction of the projected 360 hours. No C-band data has yet been taken from *e*-MERLIN aside from preliminary test observations previously published by [Guidetti et al. \(2013\)](#). Conversely, the JVLA observations are nearly complete, although the C-array C-band data is of considerably lower quality than the A-array and B-array data, and arguably requires observing again.

5.2 *e*-MERLIN L-band data reduction

e-MERLIN observations discussed in this thesis were taken at three epochs (March, April & December of 2013), centred on the GOODS-N field, and represents less than 25% of the total *e*-MERLIN observations for the *e*-MERGE survey. These relatively short observations still provide sufficient depth to be comparable with the deepest observations made at high resolution by the relatively narrow-band MERLIN array described in Chapter 4, and will therefore enhance the sensitivity of those data when used in combination. The obvious difference between the new *e*-MERLIN observations and their legacy MERLIN counterparts is in bandwidth, with the *e*-MERLIN data some 512 MHz wide (cf. 32 MHz). A total of 8 spectral windows, ranging from 1.25 GHz to 1.75 GHz required considerable preparation due to Radio Frequency Interference (RFI) at L-band. The first IF, divided into 512 channels, suffered from a large amount of man-made interference. The time consuming task of *flagging* these bad data, which otherwise have the effect reducing the sensitivity of the observations considerably, was carried out in manageable blocks. Basic flagging was first performed by the automatic flagging tool SERPENT ([Peck and Fenech, 2013](#)) using the AIPS Pipeline. The pipeline automates some of the more mundane tasks involved in the preparation of interferometric data. ParselTongue provides considerable flexibility, incorporating freely available python modules. The pipeline is controlled using an input file, which passes parameters and tells AIPS which tasks to run, and in which order. The preliminary tasks involve procedures to the following:

- Sort and concatenate the data.
- SPLIT out the target into a single file.
- Apply the *flag mask* (a list of flags of known bad channels caused by local RFI).

Band	Array	Centre ν	Pointings	IFs	Channels/IF	Channel $\Delta\nu$	Total $\Delta\nu$	τ	Target τ	Complete
C	JVLA A-array	5.5GHz	7	16	64	2 MHz	2048 MHz	1s	14 hrs	100%
C	JVLA B-array	5.5GHz	7	16	64	2 MHz	2048 MHz	1s	2.5 hrs	100%
C	JVLA C-array ^a	5.5GHz	7	2	64	2 MHz	256 MHz	1s	1.25 hrs	100%
L	<i>e</i> -MERLIN	1.5 GHz	1	8	512	125 kHz	512 MHz	1s	360 hrs	20%
L	JVLA A-array	1.5 GHz	1	8	64	1 MHz	512 MHz	1s	7 hrs	100%
C	<i>e</i> -MERLIN	5.5 GHz	7	16	256	0.5 MHz	2048 MHz	1s	378 hrs	0%

Table 5.1: *e*-MERLIN and JVLA correlator configurations.

^aThese were preliminary observations with non-matching IFs due to correlator limitations at the time of the observations..

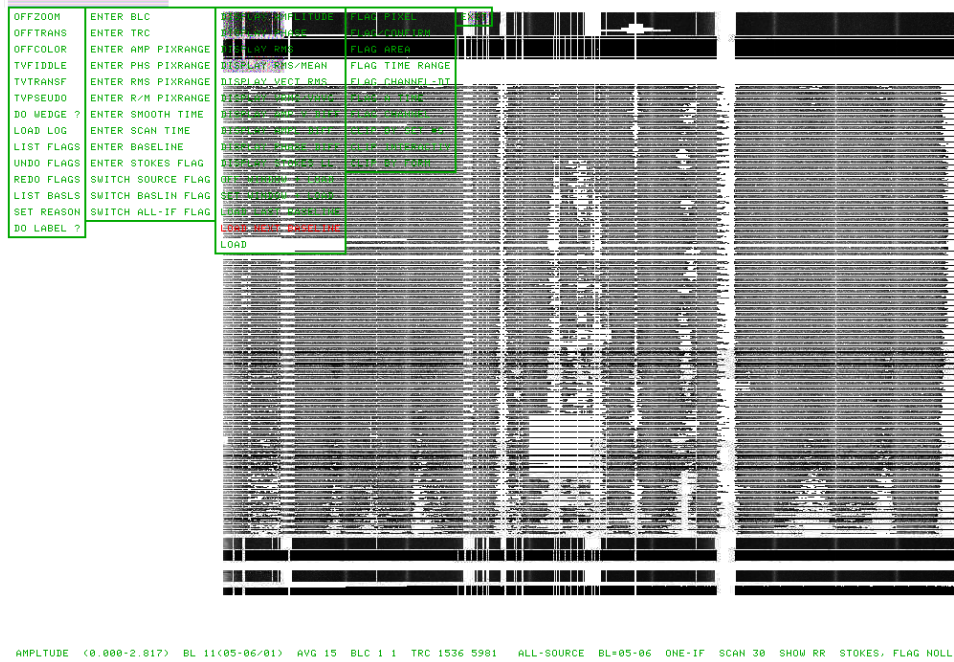


Figure 5.2: A screenshot showing the aftermath of the application of the SERPENT auto-flagger used within the *e*-MERLIN pipeline. Auto-flagging tools are very sensitive to the input parameters that control the σ thresholds. It successfully removes some of the worst RFI.

- Run SERPENT and apply flags using UVCOP.
- Remove timestamps with telescopes that were off-source.

Once the SERPENT flags are applied, an extended process of manual flagging begins. The editing process is important when handling sensitive data as even relatively modest levels of RFI can degrade the data quality.

The SPFLG task, for example, provides the user with an interactive editing tool, which visualises the radio data into a time vs frequency matrix of pixels that vary in brightness, indicating the relative amplitude or phases of the correlated radio data (see Figure 5.2). When the bad data are selected, a table of flags is written as an addendum to the AIPSuvdata file. Due to the enormous number of flags required, these could only be applied using the UVCOP task, which writes a new AIPSuvdata file. Consequently, the flagging and copying procedure was carried out in stages, gradually creating and applying successive flag tables. As each dataset measures some significant fraction of a terabyte, this is demanding on a standard workstation. It was found that the bottleneck is mainly due to I/O constraints but could be alleviated considerably by increasing the

amount of available RAM in the system to reduce disk swap files. Once the first full round of flagging was complete, the target, phase, flux and bandpass calibrator files were assembled together using into a single multi-source file.

Basic calibration begins by fringe-fitting the calibrators. This fits for the delays in a set of observations assuming that the calibrators are bright and relatively unresolved. These delays, resulting from both atmospheric and instrumental effects, are fit over all spectral windows simultaneously. The resulting offsets to correct for these phase displacements are written into a *Solution Table* (SN) and are interpolated into a *Calibration Table* (CL) using the CLCAL task. The calibrator sources used within the observations were:

- 3C286 (J133108.3+303032.96): A bright Seyfert 1 galaxy of well determined flux density used for flux calibration, and
- 1241+602 (J124129.59+602041.32): an unresolved, point like AGN source (<10 mas), used for phase calibration.
- OQ208 (1407+284): : an unresolved, point like AGN source (<10 mas), used for bandpass calibration and bootstrapped flux calibration.

The flux densities of 3C286 are known to AIPS and can be used to set the flux scale of visibilities. However, because 3C286 is an extended source, its total flux density can only be measured using the shortest baselines of the *e*-MERLIN array, and can only set the flux scale of those baselines. Three inner telescopes (Mark II, Pickmere & Darnhall) of the total seven are calibrated using 3C286 and then used to measure the flux of the phase reference calibrator (1241+602) and point source calibrator (OQ208), which are unresolved across *all* baselines. The reference source thus becomes the primary flux calibrator with values presented in Table 5.2. Application of this preliminary flux density calibration scale was followed by bandpass calibration using OQ208. Bandpass calibration assumes that there is little time-dependent change within each channel, and corrects for variation in channel sensitivity within each IF by comparison to the bandpass calibrator spectral index. The phase calibrator was imaged using all calibration tables before performing phase reference self-calibration, reducing the averaging time on each iteration. The final calibration was applied to the GOODS-North target observation, for subsequent postage stamp imaging and self-calibration. 26 sources were imaged as postage stamps, with a box-file specifying coordinates derived from the

IF bottom channel ν (GHz)	3C286 flux (Jy)	1241+602 flux (Jy)	OQ208 flux (Jy)
1.25465	<i>15.57</i>	0.37	0.76
1.31865	<i>15.21</i>	0.40	0.83
1.38265	<i>14.87</i>	0.42	0.93
1.44665	<i>14.55</i>	0.43	0.98
1.51065	<i>14.25</i>	0.43	1.05
1.57465	<i>13.96</i>	0.42	1.10
1.63865	<i>13.68</i>	0.41	1.18
1.70265	<i>13.42</i>	0.40	1.24

Table 5.2: Flux densities of calibrator sources derived from 3C286 bootstrapping.

legacy MERLIN+VLA imaging detailed in Chapter 4. Once imaged, the sources were used as models to self-calibrate the data using, i.e. determining complex gains as a function of time and baselines until solutions produce images comparable to the models. Following application of the self-calibration solutions, the images were inspected and a further round of flagging embarked upon. Some further bad data were found, caused by the calibration boosting the amplitude on noisy time-ranges on certain baselines. Once this reflagging was complete, the target pointing centre was imaged to reveal an rms noise of $6.5 \mu\text{Jy bm}^{-1}$ (cf. 18 days legacy MERLIN $6.6 \mu\text{Jy bm}^{-1}$). Splitting the target out, with calibration applied, completed the calibration process and the first epoch was ready for final imaging.

5.3 Imaging the *e*-MERLIN GOODS-N Field

5.3.1 Astrometric accuracy

Previous observations of GOODS-N from the legacy MERLIN array data were known to have an average astrometric accuracy better than 0.1 arcsec by comparison to VLBI data (Chi et al., 2013). A test to examine the positional accuracy of those same sources imaged by *e*-MERLIN was devised and compared to these legacy data. 48 of the brightest sources were selected from the MERLIN+VLA results, for examination to determine location of the source peak in each case. These were imaged as small (256x256 pixel) postage stamps. The same feature within each source (e.g. the core) was identified in both the legacy MERLIN and new *e*-MERLIN observations and its position determined by Gaussian fitting. Of the 48 imaged sources, 28 had compact features that could be identified reliably; other ambiguous or noisy sources with prob-

able artefacts were rejected. A small offset was also corrected due to differences in the assumed reference source position at 0.001485 seconds of RA and 0.00202 arc-seconds between these *e*-MERLIN and original MERLIN positions. A summary of the key measurements is described in Table 5.3.

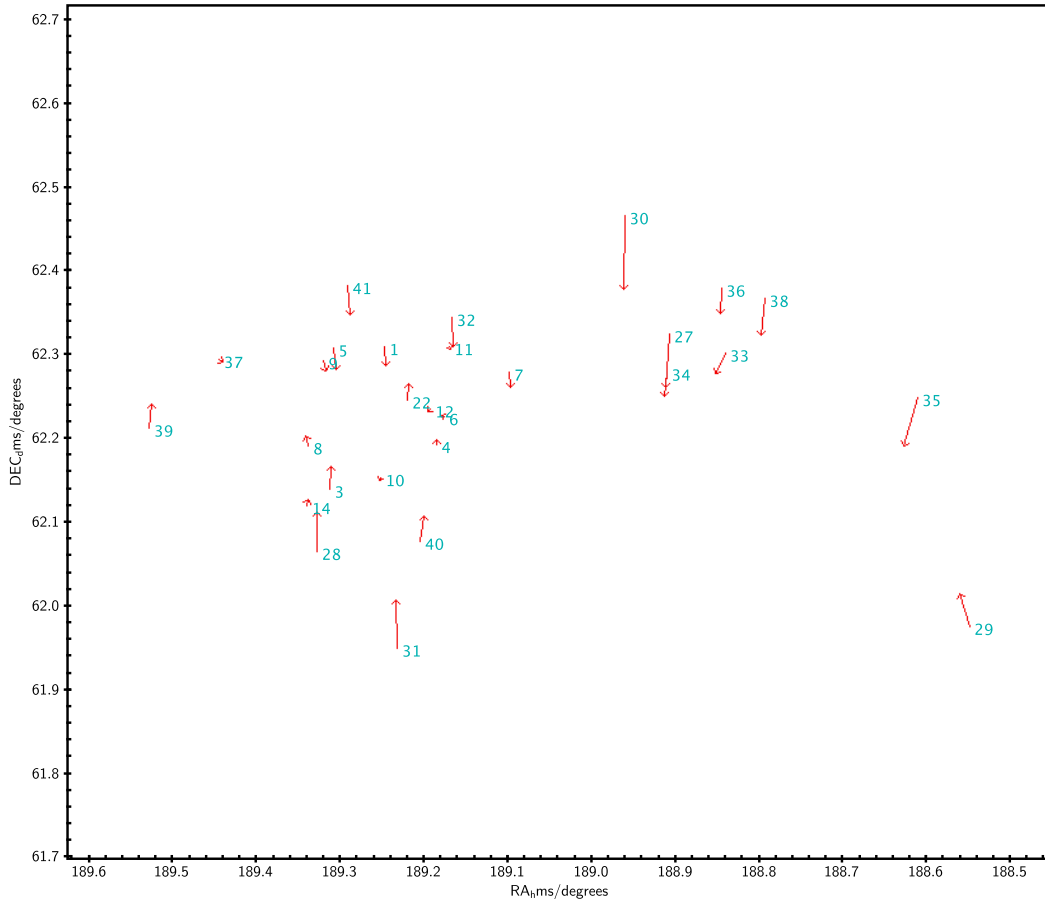


Figure 5.3: Displacement vectors between MERLIN and *e*-MERLIN source locations. The vector origins represent the sources derived from the legacy MERLIN imaging, the vectors towards the source location derived from the new *e*-MERLIN data are grossly exaggerated for clarity. The pointing centre is located at $189.2 + 62.21$ decimal degrees.

A comparison of MERLIN and *e*-MERLIN source positions is shown in Figures 5.4. It became apparent that the larger the displacement from from the pointing centre, the greater the difference between *e*-MERLIN and MERLIN positions become, as demonstrated by the vectors in Figure 5.3. On average, sources observed with

ID	MERLIN RA	MERLIN Dec	e-MER RA offset(sec)	e-MER RA offset(asec)	e-MER Dec offset (asec)
1	12:36:59.33417	+62:18:32.57540	-0.001865	-0.0130000444	-0.0288799997
3	12:37:14.94179	+62:08:23.21150	-0.001445	-0.0101290764	0.0360200018
4	12:36:44.38709	+62:11:33.14360	6.35E-4	0.0044434303	0.00752
5	12:37:13.87079	+62:18:26.31040	-0.002765	-0.0192746394	-0.0327800005
6	12:36:42.09120	+62:13:31.42320	0.0029549998	0.0206552058	0.00142
7	12:36:23.54402	+62:16:42.75800	-0.001155	-0.0080591321	-0.0235799994
8	12:37:21.25286	+62:11:29.95110	0.002555	0.0178792068	0.0166200003
9	12:37:16.68208	+62:17:33.32620	-0.002615	-0.0182379202	-0.0169799994
10	12:37:00.24733	+62:09:09.78750	0.0027650002	0.0193736564	-0.0040799999
11	12:36:40.56687	+62:18:33.08260	-6.0499E-4	-0.0042171527	-0.0025800001
12	12:36:46.32908	+62:14:04.69960	0.003715	0.0259595901	-0.0047800001
14	12:37:21.38364	+62:07:08.28140	-2.8499E-4	-0.0019991488	0.0117200003
22	12:36:52.88649	+62:14:44.03370	-0.002055	-0.014354679	0.0254199994
27	12:35:37.55999	+62:19:31.51680	0.0068949995	0.0480356516	-0.0838800012
28	12:37:18.70262	+62:03:55.71640	-4.44999E-4	-0.0031269854	0.06012
29	12:34:11.73924	+61:58:32.43330	0.0156850008	0.1105431088	0.0510199987
30	12:35:50.63812	+62:27:58.02670	0.001295	0.0089796541	-0.1156800031
31	12:36:55.82627	+61:56:58.92660	0.0012750001	0.0089934646	0.0736199976
32	12:36:40.14775	+62:20:37.64000	-0.001935	-0.013472396	-0.0441799997
33	12:35:21.61361	+62:18:07.40440	0.0154549995	0.1077546357	-0.0313799991
34	12:35:38.48835	+62:16:43.30790	0.003835	0.0267589741	-0.0375799998
35	12:34:26.79462	+62:14:54.84070	0.0205449996	0.1434975741	-0.0735799982
36	12:35:22.61224	+62:22:48.03690	0.0015349999	0.0106745092	-0.0394799984
37	12:37:46.67270	+62:17:38.60640	-0.0066149999	-0.0461330634	-0.0030800002
38	12:35:10.26647	+62:22:02.06950	0.006285	0.0437249941	-0.0584799997
39	12:38:06.77111	+62:12:42.19050	-0.0035849999	-0.0250702107	0.0386200012
40	12:36:48.99494	+62:04:38.84300	-0.006075	-0.0426717878	0.0396199995
41	12:37:09.95829	+62:22:58.99140	-0.002785	-0.0193651411	-0.0455800011

Table 5.3: Legacy MERLIN source positions with e-MERLIN differences.

e-MERLIN appear to lie slightly closer to the pointing centre than the same source observed using MERLIN. The spread in offsets as a function of RA or DEC can be quantified by plotting the differences in their respective angular distances from a normal meridian bisecting the pointing centre. This is carried out for both DEC and RA, and also in combination by taking the magnitude of the offset vector vs the radial distance from the pointing centre. The results are plotted in figures 5.4.

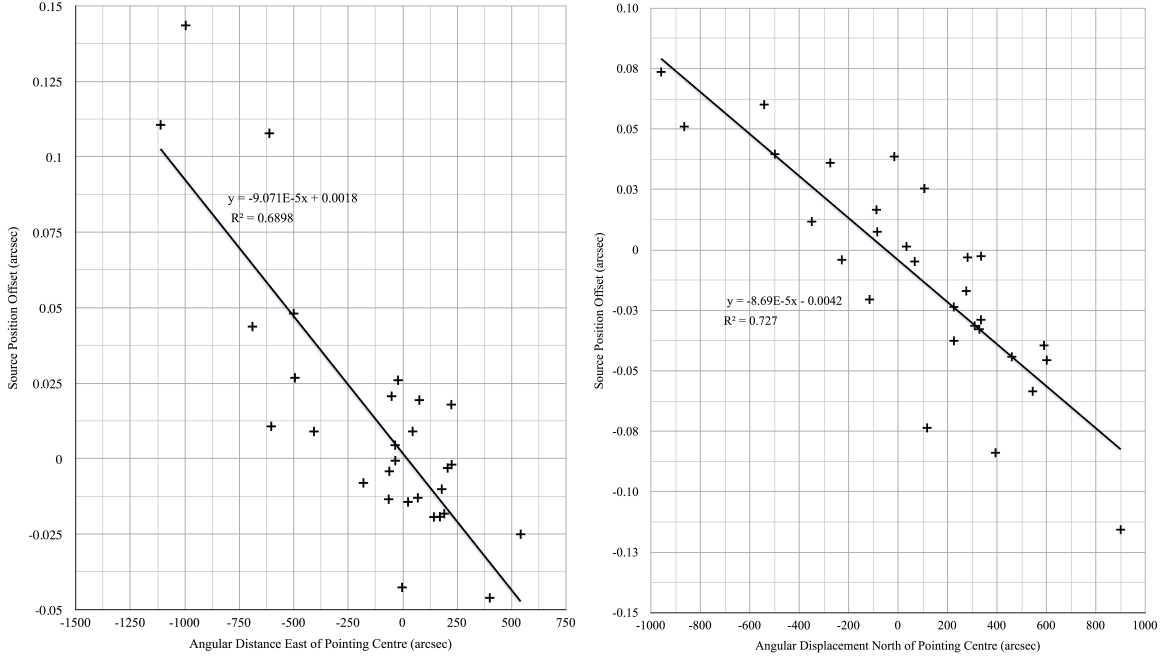


Figure 5.4: Right Ascension Offsets East of Pointing Centre (left) and Declination Offsets North of Pointing Centre (right)

All three plots include least-squares-fit linear regressions which pass through the origin to within 4 milli-arcseconds. An additional measurement, obtained from another set of calibrated *e*-MERLIN data containing source SN1986J, indicates an offset of 20.501 arcsec at a radius of 120.89 arcsec (from VLBI measurements), which is entirely consistent with the above displacements. When this is added to the HDF-N data then the resulting best fit for radial stretching is

$$\Delta r = 1.0 \times 10^{-4} r + 0.001, \quad (5.1)$$

where r is the angular distance from the pointing centre in arcsec and Δr is the '*e*-MERLIN - legacy MERLIN' difference (in arcsec); the fractional stretching is determined to be 10^{-4} . Note that the direction of the offset is lost in the magnitude plot

(Figure 5.5), but the trend can be confirmed by plotting the scalar product of the vector from the pointing centre to each source by its *e*-MERLIN - MERLIN offset vector.

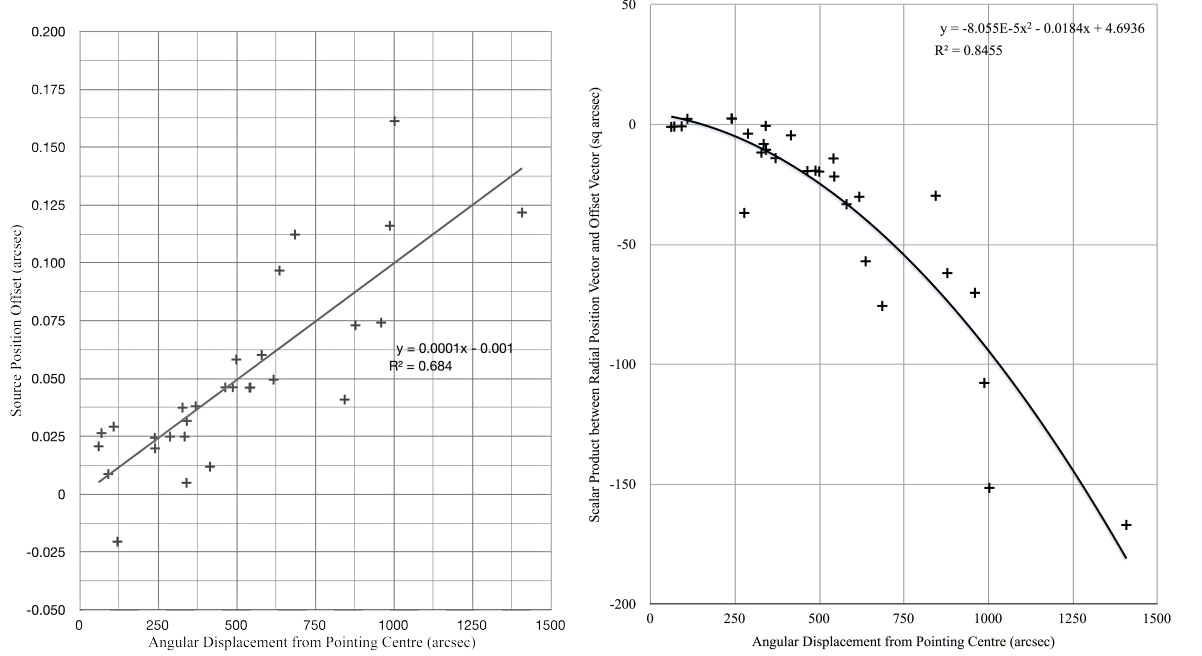


Figure 5.5: Magnitude of offsets as a function of angular displacement from the PC including source SN1986J from an independent *e*-MERLIN dataset (left). Displacement vector away from the pointing centre calculated from the scalar product between position and offset vectors demonstrates the consistently negative trend (opposing vectors), confirming a radial contraction (right).

The scalar product diagnostic is also used to determine the angle between the position and offset vectors, and therefore the perpendicular vector can be resolved. This allows rotation with respect to the pointing centre to be calculated by division of the magnitude of the position vector (small angle approximation) with the rotation direction, derived by determining the polarity of the cross product. Using the fractional stretch ratio (10^{-4}) derived above, it is possible to determine the equivalent frequency offset that would be required to cause the stretch (assuming that this is the reason). The reference base frequency used for the data was 1.254650 GHz (with each channel band being 125kHz wide). Multiplying the fractional ratio by this value yields an equivalent offset frequency 125.5 kHz, which is suspiciously close to a single channel width. The supposition is that the reference frequency is being incorrectly labelled as it is being transferred from the correlator to AIPS. AIPS labels the reference frequency

at 'pixel 1', i.e. the top of the first channel. The correlator, however, outputs the reference frequency at the centre of channel 1. AIPS takes the reference frequency and adds 1 channel width to the value.

Correcting the data

It was important to ensure that the *e*-MERGE data are astrometrically compatible with the legacy image derived in Chapter 4. The *uv* dataset was transformed by the equivalent of 1 un-averaged channel to a new (lower) reference frequency of 1.254525 GHz. A smaller sample of sources scattered across the inner and outer field were re-imaged and position attributes measured.

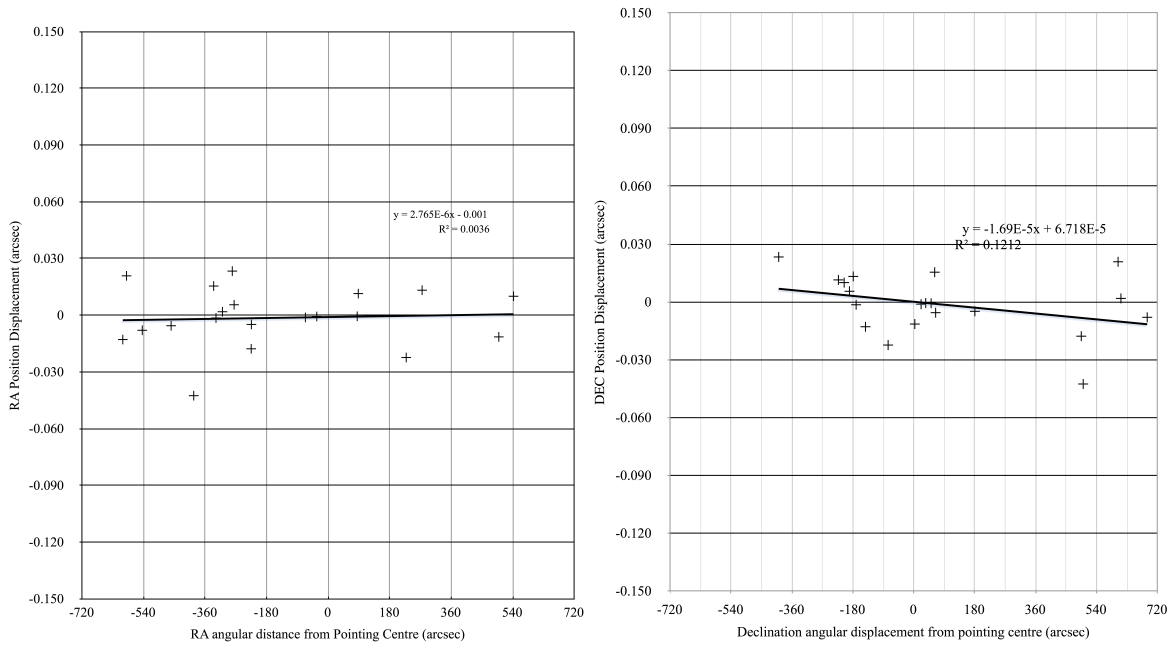


Figure 5.6: RA and DEC position offset plots for the corrected data illustrates no systematic correlation between the MERLIN and frequency shifted *e*-MERLIN source positions.

Figure 5.6 illustrates that no correlation between source displacement from the pointing centre and position difference is detected following the correction of the dataset reference frequency; the Pearson coefficient is less than 1%. The plot of the scalar product illustrates that the compression towards the centre of the field is no longer apparent.

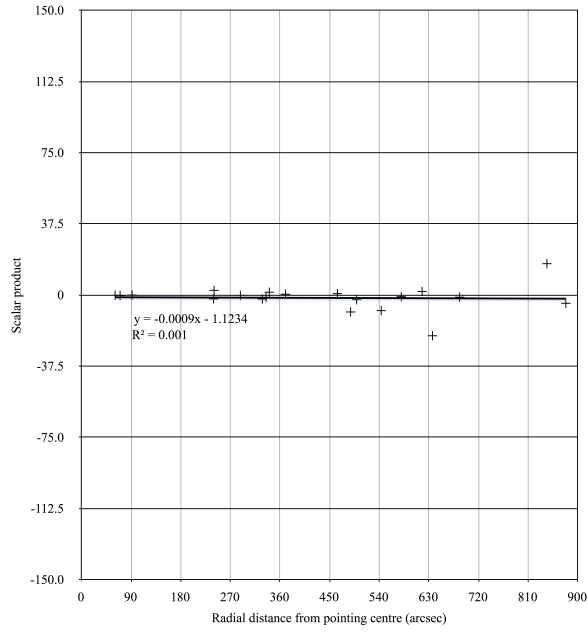


Figure 5.7: Scalar product related to the displacement vector away from pointing centre for source positions compared with the corrected *e*-MERLIN data. Neither a compression nor a stretch is observed.

Figure 5.8 illustrates that no significant rotation exceeding 10^{-3} arc-seconds is detected between the MERLIN and *e*-MERLIN source positions.

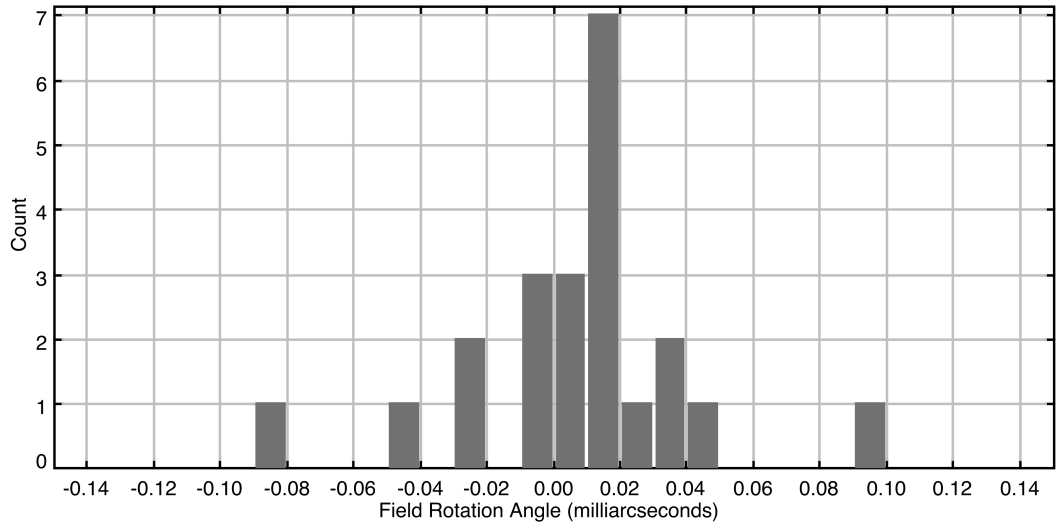


Figure 5.8: Relative rotation of the field is less than 0.02 milliarcsec.

To summarise, an incorrect frequency label had been introduced, which had the effect of causing a radial compression in source positions with respect to the pointing centre. This is attributed to misinterpreting the top end of the lowest channel for its bottom end (pixel 0 vs pixel 1) within the header. To avoid this in future it is recommended that the software at the back end of the correlator is modified accordingly. Alternatively, datasets must be corrected during data processing stages. The astrometry of the new *e*-MERLIN data, once this frequency error is corrected, is suitable for imaging, combining with the legacy data, and for general mapping purposes with high repeatable astrometric accuracy (± 0.03 arcsec). The other two epochs were calibrated, reduced and astrometrically corrected in the same way.

5.3.2 Imaging the *e*-MERLIN data using Fast Wide Field Imaging

Following the application of successful calibration and astrometric correction, all three available epochs of *e*-MERLIN data (March - December 2013) were ready to be imaged using the newly developed fast wide field imaging tool (see Chapter 3). Two combination methods are conceivable for combining the 3 datasets: *uv*-plane combination or *sky-plane* combination. With *uv*-plane (or Fourier plane) combination methods, the *uv* coordinates are gridded onto the same plane becoming a single set of visibilities. Sky-plane combination techniques, which have been demonstrated to give equivalent results to Fourier plane combination (Wrigley, 2011), sum the data in the image plane, prior to deconvolution. It was decided in this case that sky-plane combination methods are preferable due to ease of dataset manipulation. This required a modification to the fast imaging routines. The 3 *uv*-files are transformed into 192 separate tiles using the cascade-like methodology (see Chapter 3). These are converted to oversized dirty maps and beams for each spectral window, yielding a total of 1536 beams and 1536 dirty maps. The beams are each scaled as per the primary beam prediction (depending on frequency and displacement from the pointing centre) and then averaged together at common coordinates.

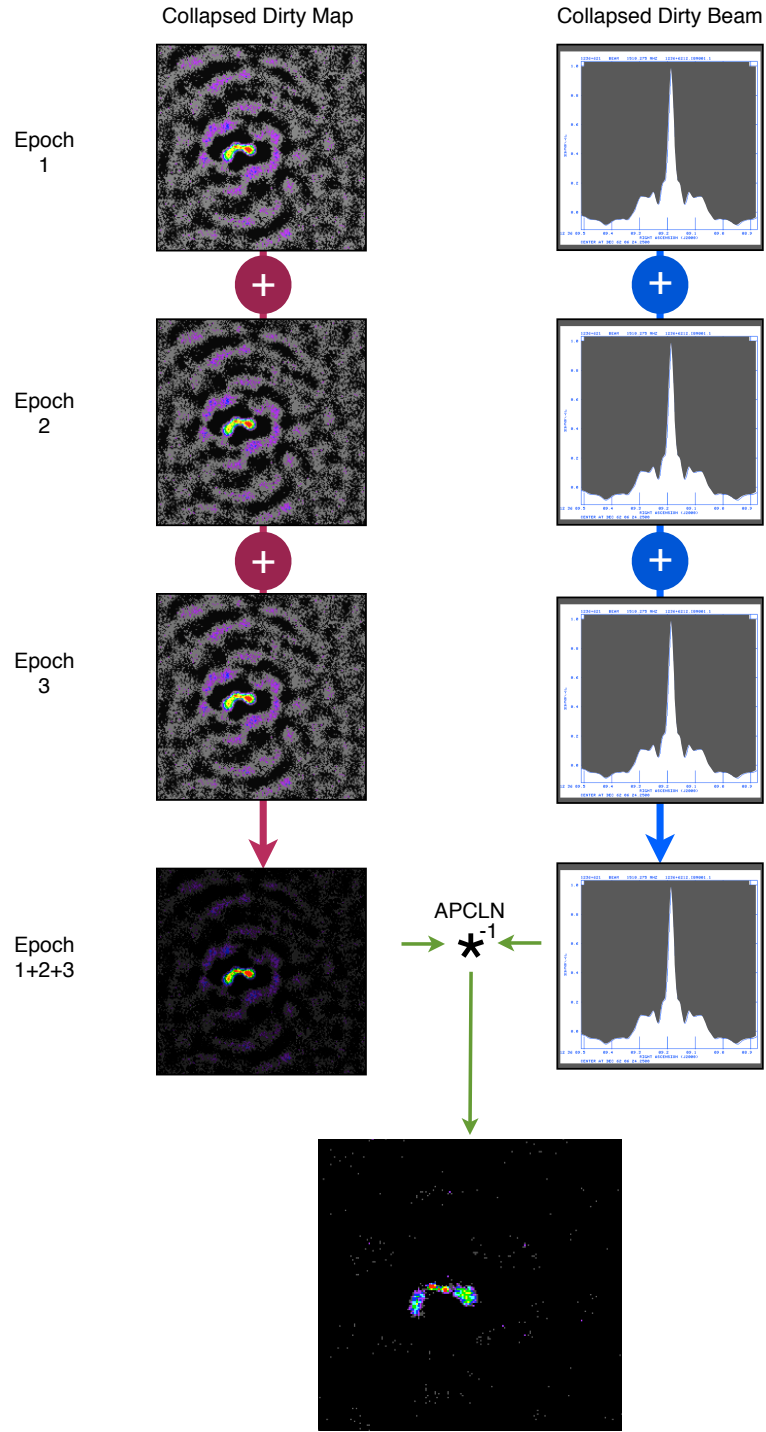


Figure 5.9: Combining the dirty map/beam pairs for each epoch generates a single map/beam pair for each facet within the wide-field. They can then be cleaned together using APCLN before being reassembled and primary beam corrected using the model parameters derived in Chapter 3.

The beams and maps are then combined in a further step illustrated in Figure 5.9 and deconvolved together. The result is a set of 64 maps that are cleaned using the modified synthesised beams. Deconvolution at a gain of 0.1 were executed and restored with a Gaussian beam with a HPBW of 200 mas until residuals were indistinguishable from noise. These facets overlap to ensure that nearby confusing sources are cleaned to reduce ripple noise (those further afield are significantly reduced by the averaging explained in Chapter 3). Consequently the number of clean iterations were increased resulting in an effective 250,000 iterations across the usable 15 arcmin field. *e*-MERLIN is relatively insensitive to clean bias, which can cause some loss of flux due to its well sampled *uv* plane, so cleaning was performed thoroughly. The 64 overlapping facets are then re-assembled to produce a single wide-field map by trimming and flattening. Once the primary beam correction, predicted from the *e*-MERLIN beam model (Chapter 3), was applied, the resulting fully contiguous map represents the first dataset for the *e*-MERGE consortium.

5.4 Imaging the JVLA GOODS-N field

Data obtained from the Karl G. Jansky Very Large Array (JVLA or VLA) provides a critical contribution to the *e*-MERGE project. *e*-MERGE observations have been made with the three highest resolution configurations at C-band (A, B & C) and at A-configuration at L-band. The spatial scales probed at C-band by each JVLA array configuration range from sub-arcsec (A-array), approximately 1 arcsec (B-array) to over 5 arcsec (C-array). At the time of the start of this PhD, only JVLA C-array data had been observed at C-band for *e*-MERGE, and then only at a reduced bandwidth because the upgraded array was not yet fully operational. An A-array proposal had been successfully submitted, which would produce images of comparable angular resolution to the *e*-MERLIN L-band images. The following paragraphs describe the data reduction from the JVLA, starting with the lowest angular resolution.

5.4.1 JVLA C-band data reduction

The JVLA’s C-array configuration has relatively short baselines and samples sources with the largest spatially extended emission. Since the primary beam of the 25m telescopes is proportionally smaller at C-band than at L-band, the observations used seven

pointings (see Figure 5.1) each of 33 minutes integration (in three sessions), to produce a single wide-band image to cover a 15 arc-minute diameter field of interest. The 256 MHz bandwidth, divided into two Intermediate Frequencies based at 4.896 GHz and 5.024 GHz, represents the narrowest total bandwidth of all *e*-MERGE observations. Each channel being only 2 MHz wide avoids significant bandwidth smearing problems within the primary beam, as does the 1 second per visibility integration time. The following section describes the C-array calibration, but in general describes the reduction of any JVLA data using AIPS.

Calibration

These observations were divided into three observing blocks, each of which were imported into the AIPS suite. To account for possible positional errors in the VLA antennas, the task VLANT was also executed to update the CL table directly. The data were examined and bad data were flagged resulting in the loss of one antenna in each of the three observation sessions in both IFs, and the loss of some channels across several baselines due to RFI. The large bandwidth per IF in the JVLA inevitably exhibits some phase rotation across the range. To combat this undesirable effect, a multi-band delay solution was derived and applied to the data. In addition to delay variations across the bands, the receiver gains also vary from channel to channel and must also be normalised via bandpass calibration using a calibrator source with a well defined SED, in this case 3C286 (observed for 11 minutes in each of the 3 sessions). The remainder of the gain and phase calibration followed standard cookbook techniques resulting in a total of 21 separate *uv* fits files.

Concatenating and Imaging

The resulting set of calibrated *uv* data comprises three sessions, each of seven pointings. To combine the data, the three epochs were combined at each pointing centre to create seven *uv* FITS files. The resulting seven files could now be used for imaging. The relatively small size of the files means that the fast wide-field wide-band imaging tool was not needed and each pointing could be imaged and cleaned directly using the IMAGR task.

Wide Band Imaging & Mosaicing

The fast wide-field imaging technique (Chapter 3) was not considered necessary because (1) the fractional bandwidth is not sufficiently large and (2) multi-faceting is unnecessary due to the mosaicing scheme and narrow fields of view at C-band. The IMAGR task was therefore used over the average of the middle channels (6 to 59 inclusive) associated with each IF to produce a map for each of the seven pointings. The Clark and Högbom iterative technique was used with a cell-size of 1.3 per pixel, 10,000 iterations per pointing and a robustness of 0 to achieve a synthesised beam of 5". This low resolution image detects structure on the largest of scales so is likely only to be useful for determining integrated flux for most objects that could be detected using these observations. However, because of the mosaicing technique, each pointing must be primary beam corrected prior to combining into a single image.

Primary Beam Correction

The primary beam correction used for the VLA data is based upon polynomial fits derived from holographic scans of telescopes

$$P(\theta) = 1 + G_1(\theta f)^2 + G_2(\theta f)^4 + G_3(\theta f)^6, \quad (5.2)$$

(Perley, 2000) where f is the observing frequency in GHz, θ is the off-axis angle from pointing centre (arc-minutes) and the best (least squares minimisation) fit parameters are given in Table 5.4 on page 146.

Parameter	Value
G_1	-1.372 E-3
G_2	6.940 E-7
G_3	-1.309 E-10

Table 5.4: C-Band VLA Perley fit parameters for θ in arc minutes.

Since the beam-shape is a function of frequency, the beam correction applicable at one end of the band is, strictly speaking, incorrect for the other end of the band. However, because the fractional bandwidth is less than 5% for these data, then the error will be negligible.

Combining the de-convolved images

The images were beam corrected and mosaiced into a single image. The resulting map is presented in Figure 5.10. The rms noise at the centre of the mosaic measures

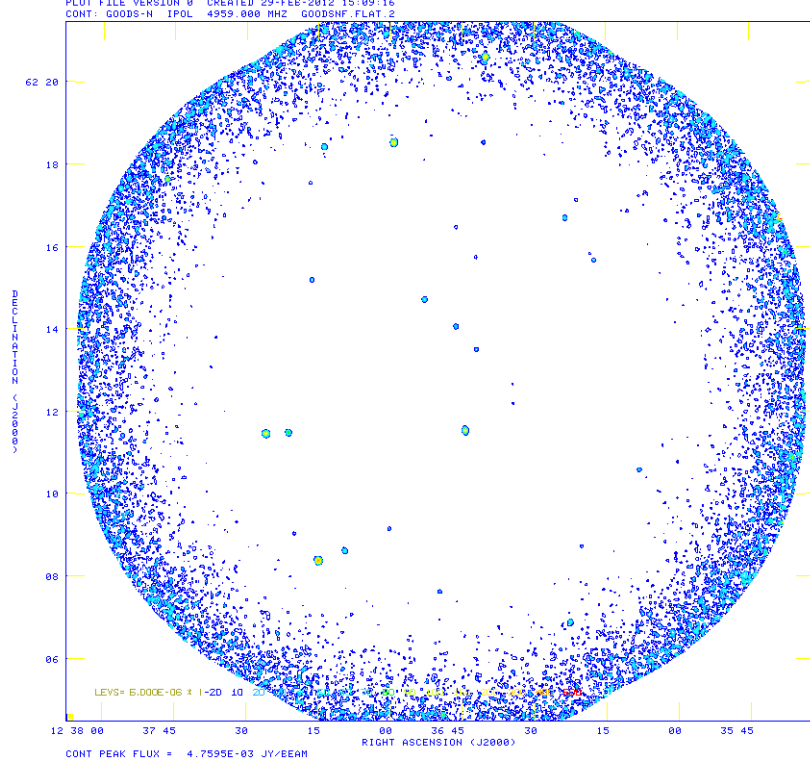


Figure 5.10: The resulting beam-corrected and averaged imaging from the 7 pointings in JVLA C-band C-array.

$5.8\mu\text{Jy}/\text{beam}$. The theoretical RMS noise per pointing is derived using

$$RMS = \frac{SEFD}{\eta_c \sqrt{n_{pol} N(N-1) t_{int} \Delta\nu}}, \quad (5.3)$$

where $SEFD$ is the System Equivalent Flux Density (≈ 330 Jy), N is the number of antennas (26), t_{int} is the integration time (1980 seconds), $\Delta\nu$ is the bandwidth (256×10^6 Hz), n_{pol} is the number of polarisations (2) and η_c is the correlator efficiency (0.92), yielding a value of approximately $14\mu\text{Jy}$ per beam. The mosaic is constructed such that the six adjacent beams (to the central beam) contribute approximately $1/0.9$ of this value at the centre of the mosaic. The theoretical noise level at the centre is

therefore:

$$RMS = \frac{14\mu\text{Jy}}{\sqrt{(0.9 \times 6) + 1}} = 5.5\mu\text{Jy/beam} \quad (5.4)$$

which is marginally better than the measured rms. The difference can be partially accounted for by the robustness (0) used in imaging as well as the fact that the observations were taken in the afternoon - a time known to increase the SEFD of the array. The rms noise increases as function of angle from the pointing centre until the image becomes unusable beyond about seven arc-minutes radius.¹

5.4.2 C-Array Source Detections

Due to the low angular resolution of the imaging, bright sources are immediately visible (see Figure 5.10) and can be compared to existing catalogues at L-band. Source locations can be matched using the AIPS task Search And Destroy (SAD), which measures the value at each pixel and compares it with the local rms (computed using the RMSD task) to determine whether a source is present based on S/N thresholds. Excluding obvious out of range pixels, 54 locations satisfied the search criteria and had common locations in L-band. These points were then cross-matched with the *Very Deep VLA field* (Morrison et al., 2010) database built from L-band observations of the GOODS-N region to determine which points were likely to be genuine detections, and which could be rejected as statistical noise.

¹These effects will also occur in the *e*-MERLIN observations, however because of the smaller primary beam-width of the *e*-MERLIN array, the middle of the central pointing is near the *edge* of the primary beams of the 6 outer pointings of the mosaic which will lead to additional confusion and smearing effects.

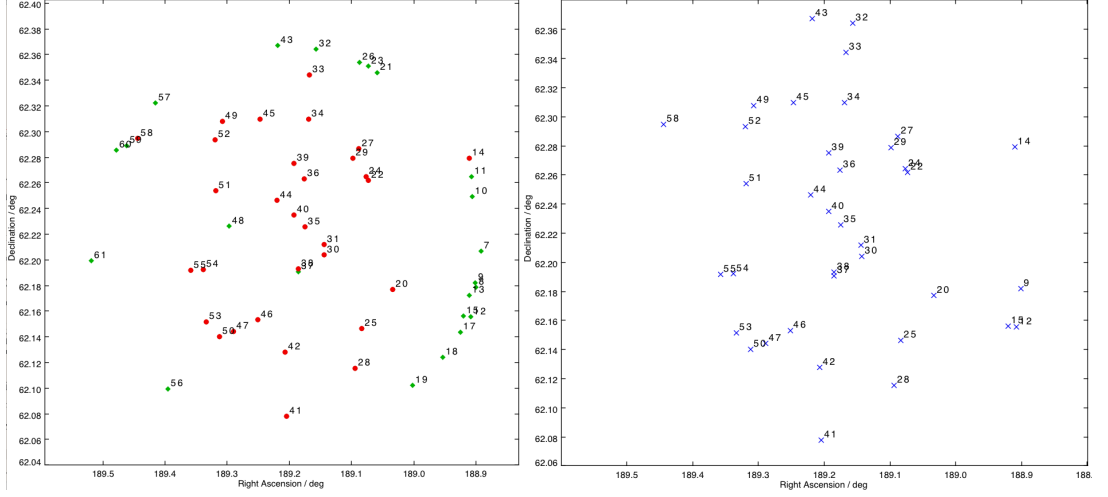


Figure 5.11: Left: Cross-matching the JVLA C-band observations with deep VLA L-band observations. Red-circle=match, green diamond=no match. Right: JVLA C-band C-array sources $> 5\sigma$

A total of 32 C-band detections correspond, within 2 arc-seconds, to sources included in VLA L-band observations. The number of cross-references is presented in 5.11 (points labelled 30 and 31 are the two jets of an FRI that have in fact been detected as separate objects) and illustrate that sources around the edge of the field (the noisy outer region) were almost certainly erroneously counted as sources (it is conceivable that they simply have no emission in L-band but this is thought unlikely due to the depth of the Morrison Catalogue). These detections were all less than 5σ over the local rms noise. A map illustrating detections for sources greater than 5σ is presented in 5.11 and corresponds to all points, with the exception of five points (labelled 9, 12, 25, 32 & 43), all of which are located in the noisy outer edge of the primary beams of the mosaic. Therefore, restricting the search to exclude the outer-most points and including only sources $> 5\sigma$, the methodology for source detection is established. The following contour plots, tabulated in 5.5, represent the 31 sources with detections $> 5\sigma$ within the mosaic. The C-array observations demonstrate that tight mosaicing (based on *e*-MERLIN throws) creates JVLA imaging with rms noise almost as low as a single, but longer-integration, JVLA pointing. The majority of all sources, except the FRI (30 & 31) and the Wide Angled Tail (source 55), were unresolved since the peak and integrated flux densities are equal. The results from the C-array data are only used to provide integrated flux densities for the brightest sources at C-band.

Source #	RA (HMS)	Dec (DMS)	Detection σ	radius (arcmin)	Peak flux density (Jy/bm)	Integrated flux density (Jy)
14	12:35:38.48	62:16:43.40	65.2	9.028	4.8001	5.08
20	12:36:08.14	62:10:35.60	10.4	5.323	0.146	0.146
22	12:36:17.55	62:15:40.80	10.4	4.558	0.114	0.159
24	12:36:18.34	62:15:50.50	5.6	4.584	0.061	0.078
25	12:36:20.18	62:08:44.40	6.9	5.400	0.092	0.092
27	12:36:21.27	62:17:09.00	5.9	5.283	0.087	0.103
28	12:36:22.54	62:06:53.90	9.9	6.809	0.260	0.284
29	12:36:23.57	62:16:42.50	17.3	4.771	0.204	0.219
30	12:36:34.44	62:12:12.70	10.2	1.857	0.0628	0.0628
31	12:36:34.51	62:12:40.80	8.9	1.712	0.0541	0.0541
33	12:36:40.13	62:20:37.50	29.1	7.726	1.316	1.316
34	12:36:40.56	62:18:33.00	6.8	5.669	0.111	0.119
35	12:36:42.07	62:13:31.30	22.3	0.980	0.131	0.134
36	12:36:42.18	62:15:45.70	11.0	2.905	0.080	0.080
38	12:36:44.40	62:11:33.10	121.3	1.513	0.700	0.808
39	12:36:46.32	62:16:29.20	9.7	3.534	0.0797	0.093
40	12:36:46.32	62:14:04.70	29.6	1.154	0.174	0.188
41	12:36:48.97	62:04:38.70	7.8	8.322	0.404	0.419
42	12:36:49.70	62:07:38.30	8.6	5.329	0.116	0.119
44	12:36:52.87	62:14:44.00	39.5	1.823	0.247	0.247
45	12:36:59.33	62:18:32.50	74.2	5.702	1.146	1.174
46	12:37:00.22	62:09:09.80	11.7	4.022	0.106	0.106
47	12:37:09.46	62:08:37.80	25.6	4.950	0.302	0.310
49	12:37:13.85	62:18:26.10	15.8	6.185	0.308	0.324
50	12:37:14.94	62:08:23.20	173.2	5.489	2.382	2.423
51	12:37:16.38	62:15:12.20	16.4	3.894	0.146	0.150
52	12:37:16.77	62:17:33.70	5.8	5.617	0.091	0.091
53	12:37:19.99	62:09:03.00	6.5	5.330	0.087	0.088
54	12:37:21.25	62:11:30.00	49.7	4.036	0.455	0.455
55	12:37:25.91	62:11:28.40	70.1	4.555	0.753	0.994
58	12:37:46.61	62:17:38.30	9.8	8.171	0.544	0.544

Table 5.5: Bright sources detected in GOODS-N by the JVLA C-Array at 5 GHz.

5.5 A & B-array Data

The data obtained in C-array configuration contain information on the largest of scales, and most sources were unresolved (the peak flux being near-identical to the integral flux). The *e*-MERGE project was originally devised such that JVLAs data would be used as a combination of A and C array JVLAs data, with A-array yielding the small scale structure and C-array the larger scales. The results of these would be combined into a single image before subsequent analysis. However, because of the incompatible data structure of the C-array data, it was considered that an excessive discrepancy in resolution between A & C would create very poor sky-combination imaging (see Figure 5.12). For this reason, an additional proposal was formulated for a mosaic B-array observation of the HDF-N. The C-array data would be used for integrated flux measurements, as well as determining those handful of sources that were considerably spatially extended. The B-array proposal was successful and a seven pointing B-Array dataset was observed in October 2013, which could be added to the *e*-MERGE survey.

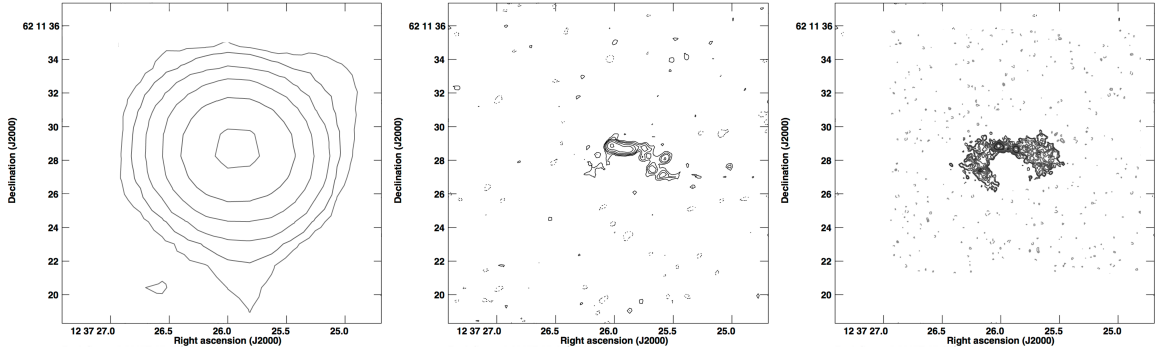


Figure 5.12: Comparison of the wide-angle-tailed source J123726+621128 at C-band JVLAs, in C-array (left) and A-array (middle) illustrating the large resolution mismatch. Intermediate *uv* coverage was deemed essential to provide a more completely sampled image - critical to determine reliable identification of extended sources on arc-second scales. The Legacy L-Band MERLIN+VLA image is pictured for comparison (right).

B-Array Data

The B-array data (proposed, scheduled and reduced by the author) was observed in a single session of 2.5 hours with each of the seven pointing targets observed for 10 minutes. A standard WIDAR correlator setup spread the 2 GHz bandwidth over 16 IFs with 2 MHz channels, with 1 second correlation time. Perhaps because it was the first

observation of the B-array season, it was found that one of the sixteen spectral windows (IF 14) contained no useful data and regrettably needed to be completely flagged. The data were clipped and flagged in a manner described earlier. The reduction of the data followed a standard calibration technique, similar to that used for the C-array observations above, bootstrapping the flux from 3C286 to OQ208 to be used as secondary flux calibration as well as for bandpass calibration. Once calibrated, each pointing was primary beam corrected using the VLA beam model built into AIPS. The data were ready to be combined with the highest resolution JVL A data from A-array. This involved other members of the *e*-MERGE consortium which required the author to travel to INAF in Bologna, Italy.

A-Array Data

The largest baseline configuration of the JVL A spans 36km, yielding an angular resolution of 0.4 arcsec at best. The data were obtained from the JVL A in four observation blocks (three on sequential days), with the full WIDAR bandwidth available at the time (from 4.5 to 6.5 GHz). Due to the larger amount of data, the author reduced one block with the other members of the *e*-MERGE consortium reducing the other three blocks (D. Guidetti, M. Bondi & I. Prandoni). The flagging and calibration was carried out in AIPS using the methods detailed earlier. Once the seven pointings were calibrated, they were ready for combination imaging.

Combining and Imaging A & B array observations

Both A-array and B-array data were observed at identical frequencies and channel numbers to facilitate combination imaging. Following some experimentation it was decided that the addition of the incompatible C-array data yielded little advantage over the addition of the new B-array data. Three possible methods were available which take into account the wide bandwidth of the data:

- Fast wide-field wide-band imaging as used for *e*-MERLIN.
- Imaging each IF separately.
- Imaging using multi frequency synthesis imaging in CASA.

The first option uses the methodology developed for *e*-MERLIN to facilitate high-speed imaging of the data. It would produce a beam-corrected image whilst optimally

cleaning sources, by considering the induced spectral index of the beam (see Chapter 3). This would be carried out 14 times in total (once for each pointing and once for each array configuration). The dirty maps and beams for each array are combined before deconvolution using APCLN. The second option is to deconvolve each IF separately to account for induced spectral index across the beam. However, for reasons already discussed in Chapter 3, this option is rejected because low flux sources are remain undeconvolved. The final option is to import both data sets into CASA and use the wide-field wide-band tool there, since the array is homogeneous. This is the preferred method for imaging JVLA data for which CASA was designed. Ultimately, both methods were carried out, with the author executing the fast wide-field method in ParselTongue. Comparing the results reveals little difference between the maps (see Figure 5.13).

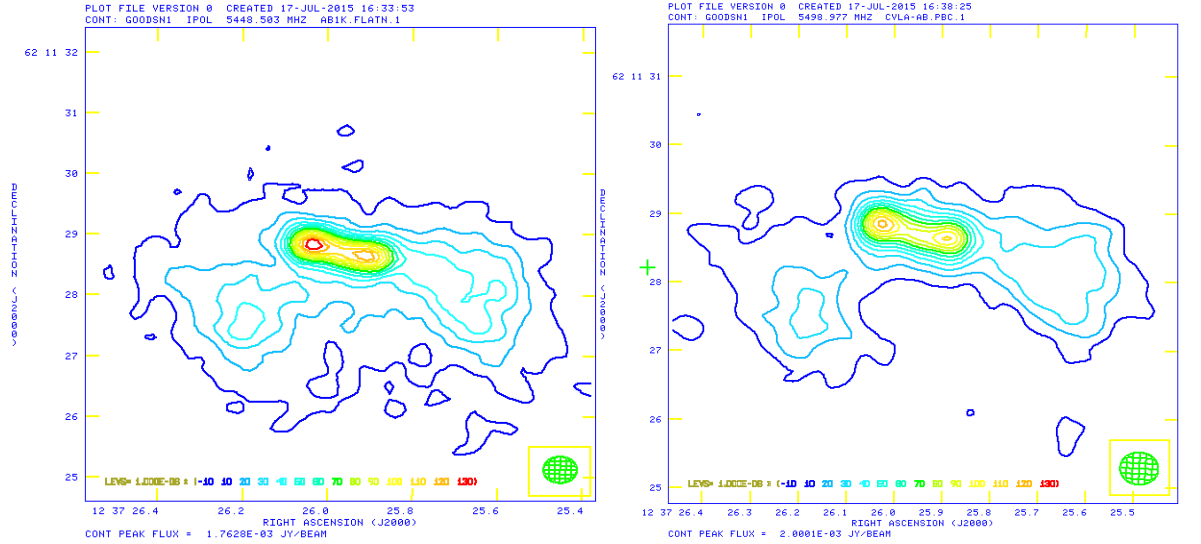


Figure 5.13: Comparison between A+B array JVLA C-band images. The Wide Angled Tail source on the left is imaged using the fast wide-field method, and on the right using CASA.

The slight difference in flux density scales is attributed to the different weightings applied to the A & B datasets within DBCON, yielding a different sized beam (0.4 mas vs 0.5 mas) with the fast wide-field method favouring a weighting ratio of A:B = 1000:1 to minimise the noise.

5.6 L-band Data

L-band data (1.25 - 1.75 GHz) were obtained² as a fully calibrated and pre-averaged *uv* dataset. The data had been averaged such that several baselines were merged to reduce the file-size, but this had a consequence that the visibilities could not be concatenated with the *e*-MERLIN data. Sky-plane combination techniques also proved unfruitful here due to a UVFIX problem resulting in positional mis-matches causing incomplete deconvolution when used in combination with *e*-MERLIN data. Instead, it was decided that this dataset should be imaged separately and measurements taken from it to record any extended emission resolved away by *e*-MERLIN. High speed imaging, with spectral beam correction (described in Chapter 3), was employed to generate a 0.4 arcsec map which showed significant confusion from a number of bright outliers (see Figure 5.14). The bright sources were identified, cleaned and subtracted IF by IF. It was important to subtract spectrally as each source may have some intrinsic spectral index and would consequently have differing clean component amplitudes within each spectral window. The subtraction routine has been integrated into the *e*-MERLIN pipeline to remove bright sources identified from the FIRST (Faint Images of the Radio Sky at Twenty-one centimeters) database (private communication N. Jackson). Once the two confusing sources were removed, re-mapping using the fast wide-field wide-band imaging tool produced a completely contiguous image over 15 arcmin in diameter (see Figure 5.14) which was primary beam corrected using optimal VLA best fit values at the centre frequency of 1.492 GHz. The JVLA L-band imaging completed the first wave of data for the *e*-MERGE project, with datasets uploaded to the *e*-MERGE website to allow all members of the consortium access to the data products so far.

5.7 Summary of *e*-MERGE observations

The 3 L-band *e*-MERLIN epochs, taken in March, April and December of 2013 yield central rms noise levels of 6.6, 5.1 & 5.2 $\mu\text{Jy/bm}$ respectively. These were combined with the legacy MERLIN+VLA observations of 1996 (rms 3.5 $\mu\text{Jy/bm}$) with appropriate amplitude weights based on their sensitivities. The final high resolution combination map has a noise profile shown in Figure 5.15 with a minimum measured rms noise at the centre equal to 2.34 $\mu\text{Jy/bm}$ using a 200 mas beam. The JVLA L-band

²Private communication F. Owen.

data, used for flux density measurement and large scale emission identification, has a minimum measured rms noise equal to $2.7\mu\text{Jy/bm}$ with a 400 mas beam.

The JVLA C-band A+B array combination imaging has a minimum measured rms noise at the centre of the mosaic of $1.4\mu\text{Jy/bm}$ using a 500 mas beam. The JVLA C-array data, not combined because of the enormous resolution mismatch, but useful to obtain integrated flux densities, has a minimum rms at the centre equal to $5.6\mu\text{Jy/bm}$ with a 5 arcsec beam.

Band	Observation	PC rms noise ($\mu\text{Jy/beam}$)	Beam (arcsec)
L	Legacy MERLIN+VLA	3.5	0.2
L	<i>e</i> -MERLIN 1	6.6	0.2
L	<i>e</i> -MERLIN 2	5.1	0.2
L	<i>e</i> -MERLIN 3	5.3	0.2
L	All of above	2.34	0.2
L	JVLA (A array)	2.7	0.4
C	JVLA (A+B array)	1.4	0.5
C	JVLA (C array)	5.6	5.0

Table 5.6: *e*-MERGE Data Products Sensitivity Summary.

These data complete the first stage of the *e*-MERGE data products (summarised in Table 5.6) and have been uploaded to the consortium website, to be used in future analyses. The increased signal to noise ratio over the previous legacy data increases the usable source counts. The original MERLIN+VLA study (Muxlow et al., 2005) permitted the examination of 92 (peak flux density $> 40\mu\text{Jy}$) sources over the central 10 arc-minute field, which was increased to 178 ($> 5\sigma$ peak flux density) by expanding the field width to 15 arcmin (Wrigley, 2011). With the incorporation of the first tranche of *e*-MERGE data, the number of usable source-counts used for analysis increases to 248. As the *e*-MERGE survey matures, a blind search will be undertaken using a combination of JVLA and *e*-MERLIN data, but at this time the VLA survey (Morrison et al., 2010) yields the most reliable radio catalogue of the GOODS-North region. The 248 measurable sources (from a total of 340 by VLA extraction from the Morrison database) represent those sources for which there exists either extended flux density information for extended objects above 2.5σ , or with peak detections above $20\mu\text{Jy}$. Fainter sources are discarded as size measurements are likely underestimated. The selection methodology for sources is described in the following chapter along with size and flux density measurements.

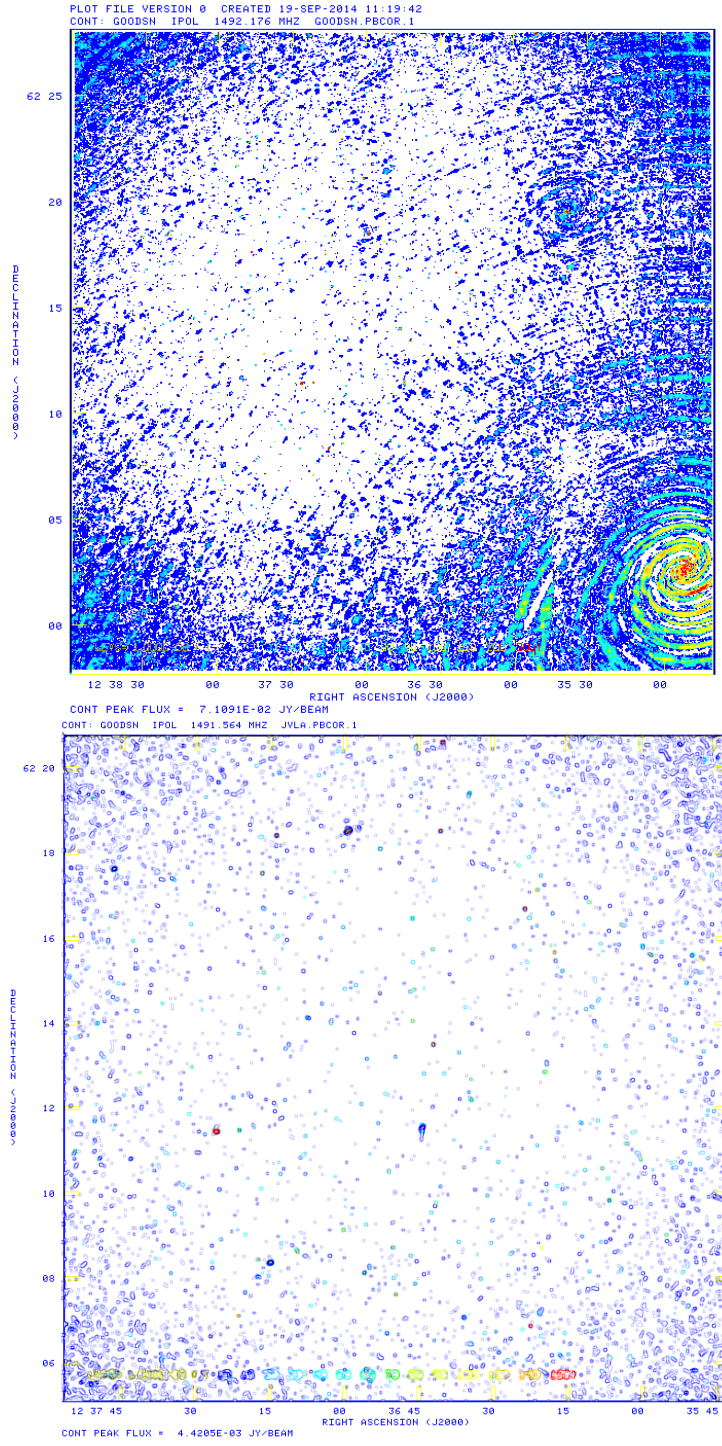


Figure 5.14: JVL A L-Band map produced using high-speed imaging technique prior to subtraction of bright sources (top) and following subtraction of the bright sources (bottom).

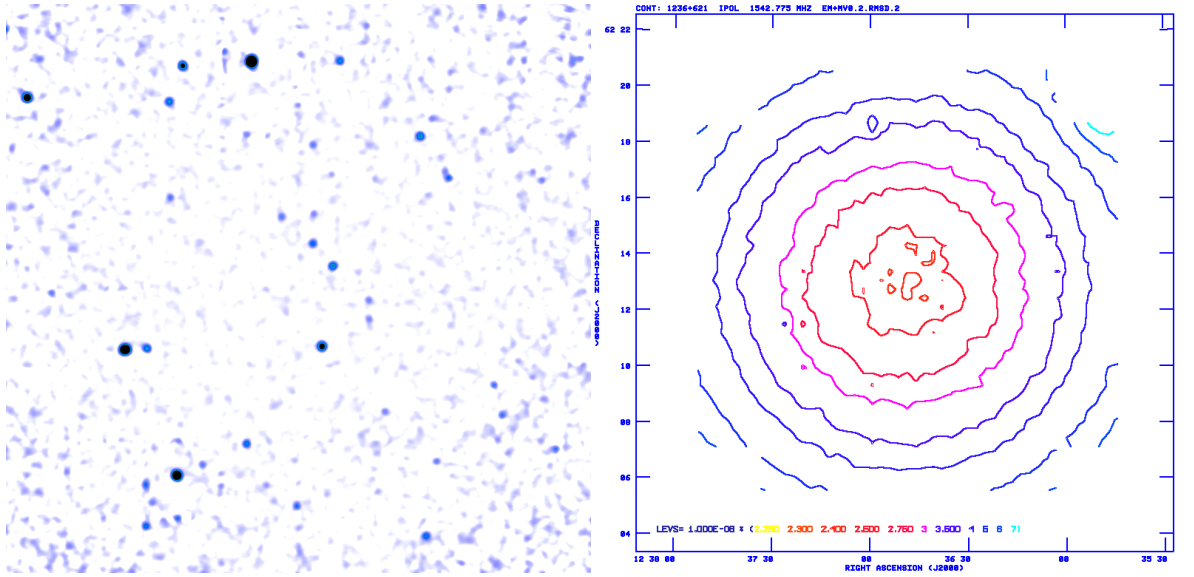


Figure 5.15: A low angular resolution version of the highest resolution *e*-MERGE map showing the brightest sources (left). The rms map (right), with minimum noise at $2.34\mu\text{Jy/bm}$ at 200 mas, has a profile that reflects the primary beam correction applied.

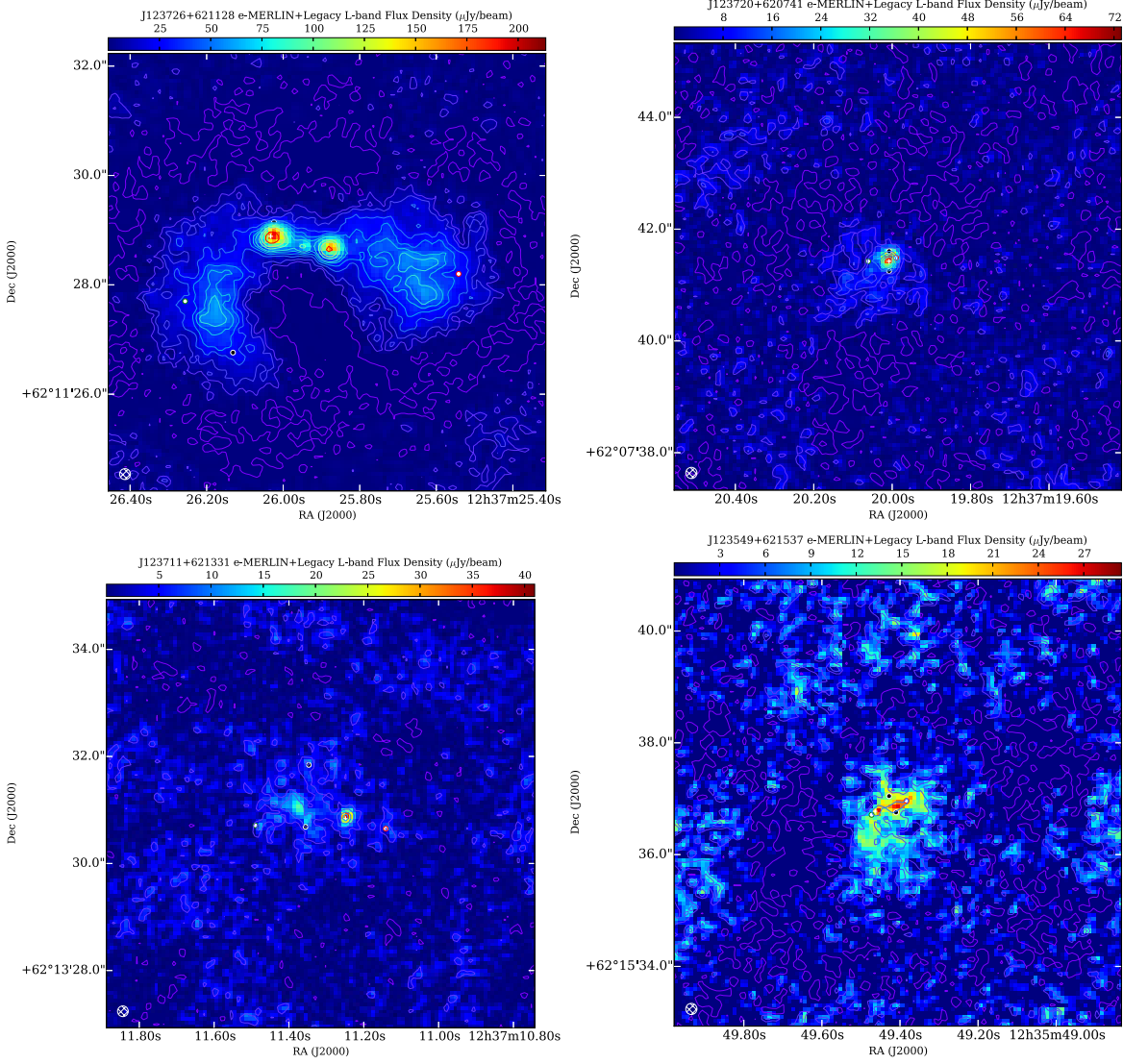


Figure 5.16: A selection of *e*-MERGE sources derived from *e*-MERLIN & Legacy Data. Top left: Wide Angled Tail exhibiting excellent image fidelity. Top right: An AGN embedded within a spatially extended region. Bottom left: A source with two components. Bottom right: A source at the edge of the field exhibiting extended spatial features.

Chapter 6

Characterising Angular Sizes of Sources in *e*-MERGE Data

The combination of the *e*-MERGE and legacy MERLIN+VLA data described in Chapter 5 is analysed in this section to yield distribution information for sources within the GOODS-North field in the radio bands, including size and subsequently flux density. The high angular resolution of the *e*-MERLIN array allows, for the first time, source sizes to be quantified at L-band and assists in the classification of galaxies, a key objective of the *e*-MERGE project. Although most of the observations from the *e*-MERGE survey are yet to be observed, the methodologies and innovations developed here will be applied to the entire *e*-MERGE survey.

6.1 Measuring the angular extent of sources

Determining the angular extent of a source is an important morphological characteristic along with its flux density. If the source size is overestimated then so too are integrated flux densities. Conversely, too small and fluxes are underestimated. In an attempt to create a consistent technique for defining the extent of a galaxy, several methods have been developed over the years including the following:

- Sersic index.
- Gaussian fitting.
- Largest Angular Size (LAS).

- Petrosian radius, half-light or effective radius.

The Sersic index (Sersic, 1968) characterises the morphology of well defined elliptically shaped galaxies which are commonly assumed profiles encountered in optical surveys. This is achieved by fitting two power law profiles in superposition, representing bulge and disk components. These cannot, however, well describe the size of a source if the profile is fragmented, a feature often exhibited in radio images. The *Petrosian Radius* (Petrosian, 1976) is arguably better able to estimate the overall size of a source that does not fit a well behaved profile and can be used to gauge the maximum likely spatial extent of the source. Optical surveys, like SDSS, also characterise the size of sources using a several metrics, including a modified Petrosian radius. At radio wavelengths the galaxies have varying morphologies which are, in general, more diverse and depend significantly on whether the source contains AGN cores, jets, lobes or star-forming components. Many radio catalogues simply use 2D Gaussian elliptical fitting tools to characterise their sizes, as described in Chapter 4. *e*-MERLIN data suffers from a non-Gaussian ripple noise which was found to cause significant problems with standard search algorithms. Legacy MERLIN analyses (Muxlow et al., 2005) used a combination of Gaussian fitting and Largest Angular Size which is applicable to most sources. Such a combination of techniques can produce results that are unconsciously biased due to human factors. Gaussian fitting and Largest angular size measurement methodologies have already been described in Chapter 4 and further elaboration is unnecessary other than to reiterate that Gaussian fitting is often a poor representation of source dimensions, particularly if the source appears fragmented. A bespoke combination of the methods listed above were developed to provide a quantification of the useful attributes of each source, including largest angular size and hence integrated flux density.

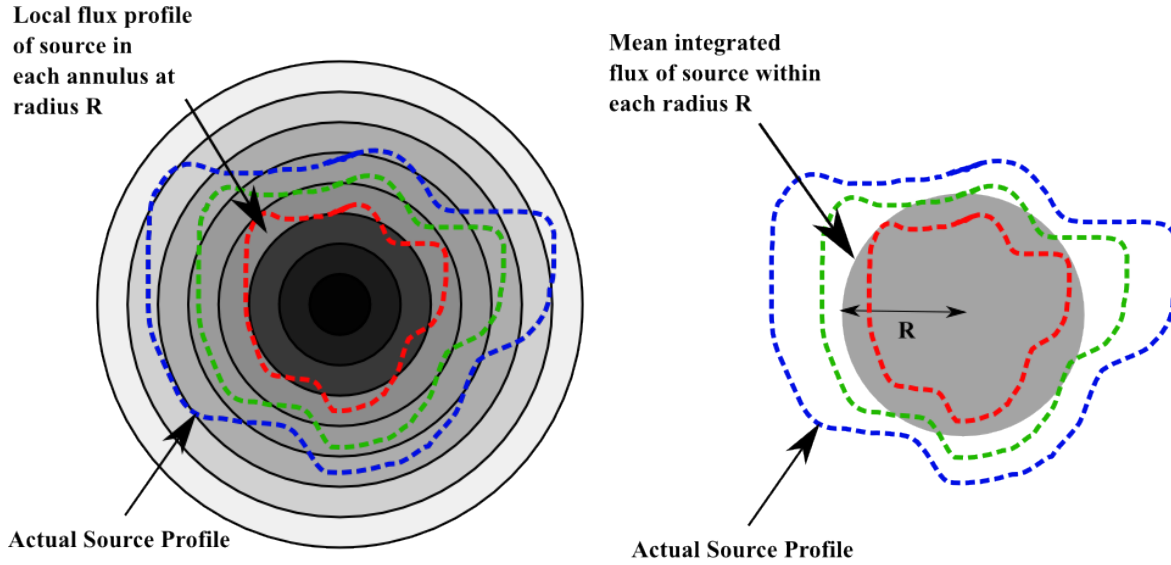
Defining the source size can often become a choice of definition as galaxies do not have sharp boundaries. The methodology developed here utilises both the Petrosian aperture, to eliminate neighbouring sources, followed by a LAS measurement to derive the angular extent of the galaxy whilst attempting to compensate for biases caused by ripple noise. The LAS has an advantage over the Petrosian radius in that, by assuming that galaxies are disk-like in nature, their projection angle is irrelevant and the angular size is same same regardless of the projection angle. The technique is executed by machine to minimise subjective biases, but checked by a comparison with the visual inspection technique used in Chapter 4.

6.1.1 Petrosian Aperture

The Petrosian Radius, R_P , is defined as the radius at which the average of the integrated flux within that radius is equal to the profile flux at the same angular distance from the galaxy's centre. The flux ratio can be quantified as the Petrosian index η :

$$\eta(R) = \frac{\int_0^R I(R') R' dR'}{R^2 I(R)} = \frac{\langle I \rangle_R}{I(R)} \quad (6.1)$$

where $I(R)$ is the intensity of the source at radius R and $\langle I \rangle_R$ is the mean intensity within radius R . In practice it is necessary to adopt a Petrosian aperture deviating from a ratio of $\eta = 1$ because the mean intensity is usually much lower than the local intensity, ultimately generating a very small value of R_P which fails to include the majority of the source. Hence, to integrate most of the flux of any given object, the value of the inverted Petrosian index $1/\eta$ is modified, i.e. typically $1/\eta(R_P) = 0.2 \rightarrow 0.4$. The photometry aperture is then extended to some multiple of R_P , i.e. between 1.5 and 2 as demonstrated in [Graham et al. \(2008\)](#). So long as all measurements use the same definition then the quantity provides a useful method of limiting the aperture for angular size measurement, without the human subjectivity inherent in visual inspection. A significant advantage of the use of the Petrosian radius is its comparative insensitivity to irregular morphologies and distance independence. A python program was written to measure the Petrosian aperture of each source. The aperture is divided into discrete annuli (see Figure 6.1) with each annulus width chosen such that it is comparable with the synthesised beam-width, but not so large that the profile of extended sources is smeared away. A running integral of the flux within each annulus is performed and compared with the average flux within that radius. The radius at which the integral drops below the running mean is noted and used as the defined value of R_P for that source. A factor 1.6 is applied to this value and defines an oversized region within which the source is assumed to be confined. An example plot of axially integrated flux density, how it compares to the running mean and the resulting Petrosian radius R_P , is illustrated in Figure 6.2. It was found that the value of η could be adjusted to scale the Petrosian aperture by an arbitrary amount and hence required some 'calibration' to determine the extent over which the 'size' is quantified i.e. the proportion of flux enveloped. Studies by [Graham et al. \(2008\)](#) indicate that the Petrosian method can capture $>80\%$ of the flux depending upon η but it may include some additional contamination beyond that. The Petrosian aperture is therefore only used for scop-



Standard Petrosian Radius when Local Flux at R = Mean Flux Within R

Figure 6.1: An illustration of the technique used to define the Petrosian Aperture. The profile flux density in each annulus r is compared with the running mean of the integrated flux within radius r . The source need not be a regular shape to determine R_P which mitigates the problem of detecting neighbouring contaminants.

ing purposes, within which the LAS is determined. Consequently, the LAS is always smaller than the Petrosian aperture.

6.1.2 Fitting LAS major and minor axis sizes

To identify the size of a galaxy, the LAS was identified as the most reasonable method of ignoring the projection angle for SFGs. If a galaxy can be detected out to some consistent isophote, then the size of a source can be defined by its largest dimension. In an attempt to recover the LAS of every detectable source in the field, a methodology was developed to search for isophote contours within the Petrosian aperture. However, the non-Gaussian noise profile must also be considered, exhibited by the characteristic ripple noise illustrated in Figure 6.3.

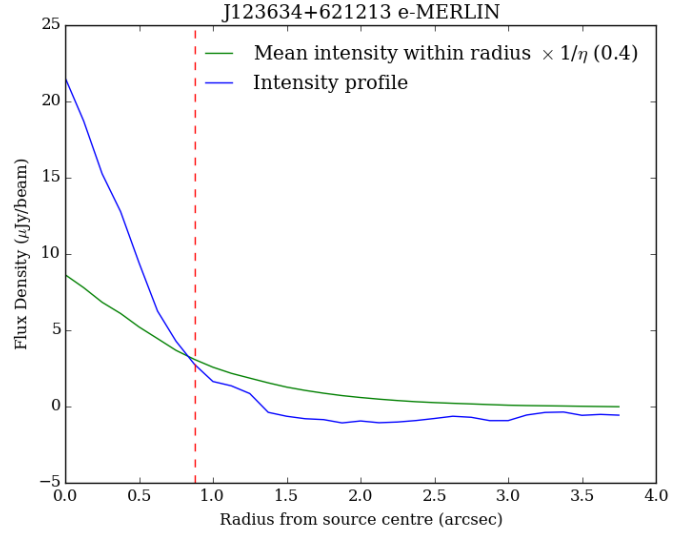


Figure 6.2: The modified Petrosian aperture (of radius R_p represented by the vertical dashed line) is computed and used to constrain the field size to avoid including neighbouring sources that may be present the field edge. The slight negative bowl is caused by a lack of inner baselines.

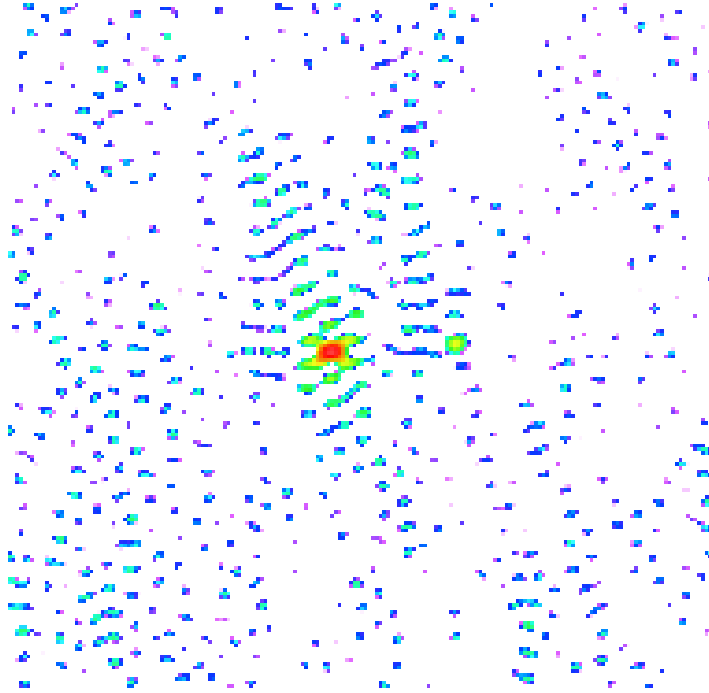


Figure 6.3: Exaggerated ripple noise surrounding a source within *e*-MERLIN data.

The non-Gaussianity causes the brightness of a source to vary due to its position

amongst the ripples. This is illustrated in Figure 6.4 in which the amplitude S_p of a Gaussian profile has been modified, by some factor λ , by the ripple noise σ , to yield an observed flux S_p^{OBS} .

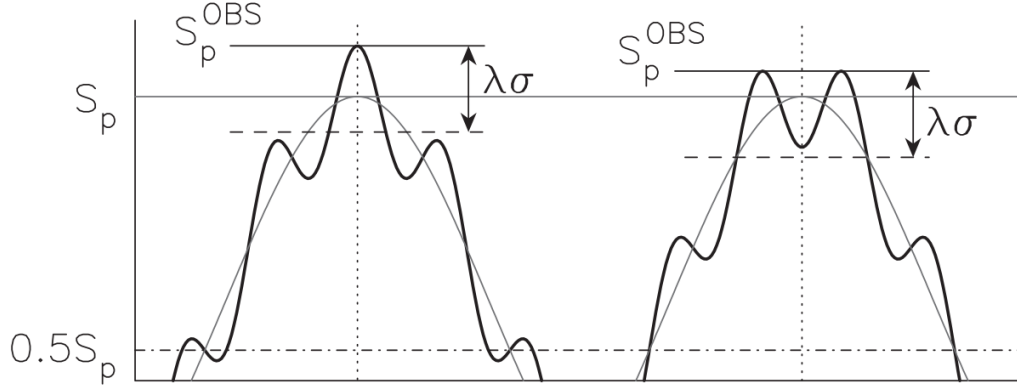


Figure 6.4: An idealised representation of a source of true peak flux density, S_p , with a Gaussian profile observed amongst ripple noise. On the left the source is coincident with the peak of a ripple, whereas the source on the right falls into a ripple trough. Both cause an overestimate in the peak flux density S_p^{OBS} , related to a factor $\lambda\sigma$ (Hales et al., 2012).

Consequently, to avoid spurious noise being incorporated into the integrated flux density of the source, the outer isophote threshold needs to be modified according to the S/N ratio of the source. The reason for this variation in the outer contour threshold was investigated by Hales et al. (2012) in the building the flood-fill algorithm software 'BlobCAT'. Their simulations revealed that the outer contour threshold, T_f , varied between a signal-to-noise ratio of 2.6 and 4.0 to recover real flux and minimise contamination and was proportional to the signal-to-noise ratio of the peak amplitude of the source. A similar approach is adopted here, with a varying σ threshold related to the peak flux density of the source. The background noise is derived by measuring the pixels in the region immediately surrounding the Petrosian aperture. A contouring algorithm is then applied, searching for the extent of the source based upon the S/N. Studies were required to set the correct thresholds. Numerous tests on sources, previously identified by eye, refine the S/N threshold at which the extent of the galaxy is judged to end and noise begin. In the case of this data, the outer contour threshold was limited to 3.8σ for bright sources and to a minimum of 2.5σ for the faintest detected. These are close to those values adopted in the BlobCAT software, and differ only due to the specific noise profile. After careful trials on all 340 sources in the *e*-MERLIN field

(already identified from the deep VLA catalogue compiled by [Morrison et al. \(2010\)](#)), over 90 sources had to be rejected entirely as being over-sensitive to this threshold variation and hence too unreliable. The methodology is illustrated in Figure 6.5.

As a test, the technique was refined using the legacy MERLIN+VLA map (described in Chapter 4) which was measured by visual inspection, and reveals an automated LAS distribution that closely resembled the one in Chapter 4 (see Figures 4.7 and 6.6). A python program was written which reads the contiguous *e*-MERGE wide-field maps, along with a list of coordinates, and measures, without user intervention or human subjectivity, the following attributes of each source:

- LAS Major Axis (θ_{LAS}).
- LAS Minor Axis (θ_{LASmin}).
- Position angle (PA).
- Integral Flux Density (S_ν).
- Peak Flux Density (S_{Peak}).
- Half-light radius (R_{eff}), Petrosian aperture (R_P), Compactness parameter.

The definition of the LAS of each source as well as the position angle is illustrated in Figure 6.5. The greatest distance between pixels identified in outermost contour T_f at the chosen sigma threshold is computed, and the width is defined as the sum of the two vectors normal to the LAS length axis. It was found that the contours associated with some of the lower flux sources become fragmented and contain little contiguous emission. Only the islands within the ripple are usually identified, although a visual inspection reveals that the source merely varies in intensity due to noise structure. To determine the most complete integrated flux density for each source, an ellipse is constructed from the LAS major and minor axes which envelope the source. The area within the ellipse hence determines the integrated flux density of the source and is computed by summation of all pixels enveloped, followed by division by the number of pixels per synthesised beam (each pixel is measured in Jy/beam). The position of the peak flux density is also located for comparison with the integral intensity, to provide a measure of the amount of resolved flux per source. The stand-alone JVLA L-band data was analysed simultaneously with the *e*-MERLIN map which was useful to provide a more complete estimate of the LAS and integral flux. In cases where

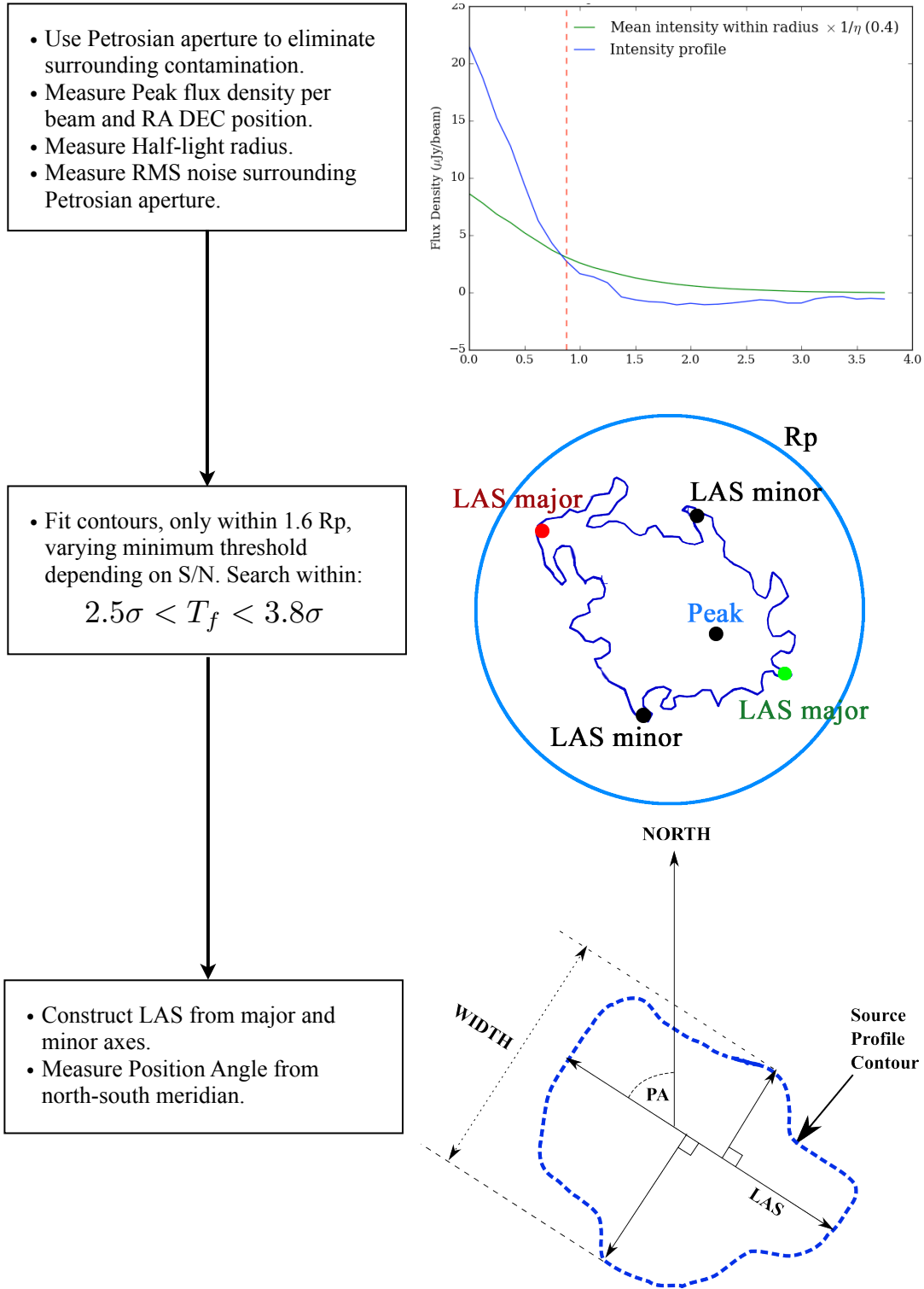


Figure 6.5: Angular size measurement methodology.

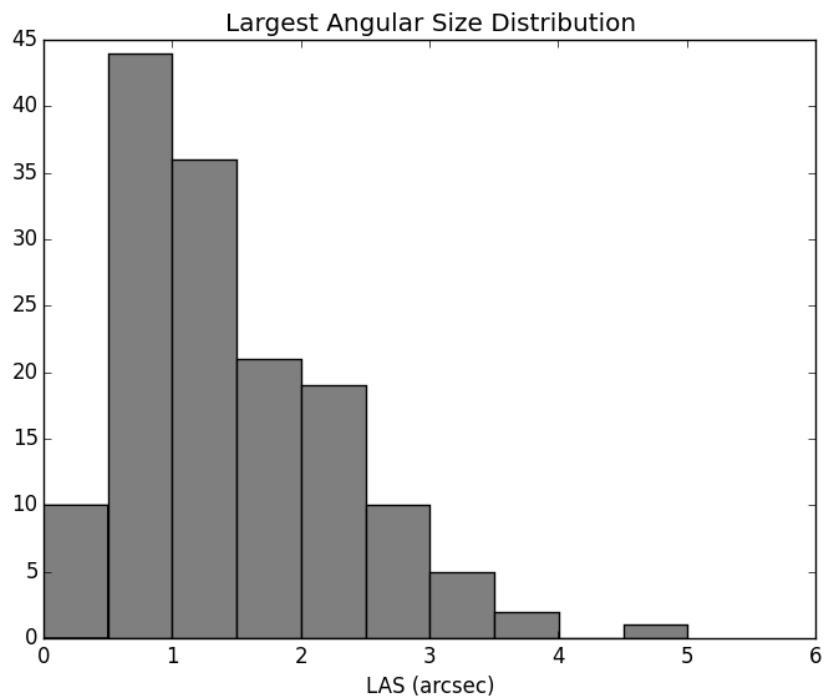


Figure 6.6: Petrosian aperture constrained contour fitting of the Legacy MERLIN+VLA data for 169 sources reveals a distribution with a median size of 1.2 arcmin, peaking near 0.75 arcsec. An expanded Petrosian aperture (1.6X) is used to minimise contamination from neighbouring sources. The distribution is similar to the one obtained by rigorous visual inspection in Figure 4.7 .

the LAS is smaller than the JVL A L-band beam (i.e. unresolved by the JVL A), the *e*-MERLIN+Legacy dimensions are used. The analysis was expanded to include the JVL A C-band data which measures integral flux densities for spectral index determination. A list of source attributes was in this way assembled for the latest *e*-MERLIN + legacy observations (presented in Appendix 1). Statistical findings for this first data release from the *e*-MERGE survey are discussed in Section 6.3 following a brief description of uncertainties.

6.2 Uncertainties

Quantification of the uncertainties in each measurement of flux density, which propagates throughout derived values, is established using aperture photometry to determine the rms noise profile surrounding each source. Measurement of the uncertainty of the flux density depends largely on the noise structure of the surrounding region. The presence of the characteristic ‘ripple noise’ could mean that a source lies anywhere between a noise peak or trough and hence slightly modify the flux density measurement as explained in section 6.1.2. Aperture photometry techniques attempt to mitigate this effect by sampling the noise surrounding each source to determine the likely error in measurement. The standard deviation of the sampled pixels surrounding the source ellipse, defined by θ_{LAS} and θ_{LASminor} , is divided by the square root of the number of beam samples within the ellipse, yielding the uncertainty σ_S on its flux density measurement S . This method extends to all JVL A measurements as well as the *e*-MERLIN+Legacy observations to provide a quantitative estimate of the error attached to each source. The uncertainty in spectral index α is

$$\sigma_\alpha = \frac{1}{\ln(\nu_L/\nu_C)} \sqrt{\left(\frac{\sigma_{S_L}}{S_L}\right)^2 + \left(\frac{\sigma_{S_C}}{S_C}\right)^2}, \quad (6.2)$$

where ν_L and ν_C are the observing frequencies at L and C bands respectively and σ_L is the measured rms noise surrounding the source being examined. Besides the error in flux density measurement (σ_S), there are several systematic errors to consider including the following:

- Flux calibration errors.
- Beam-shape calibration error.

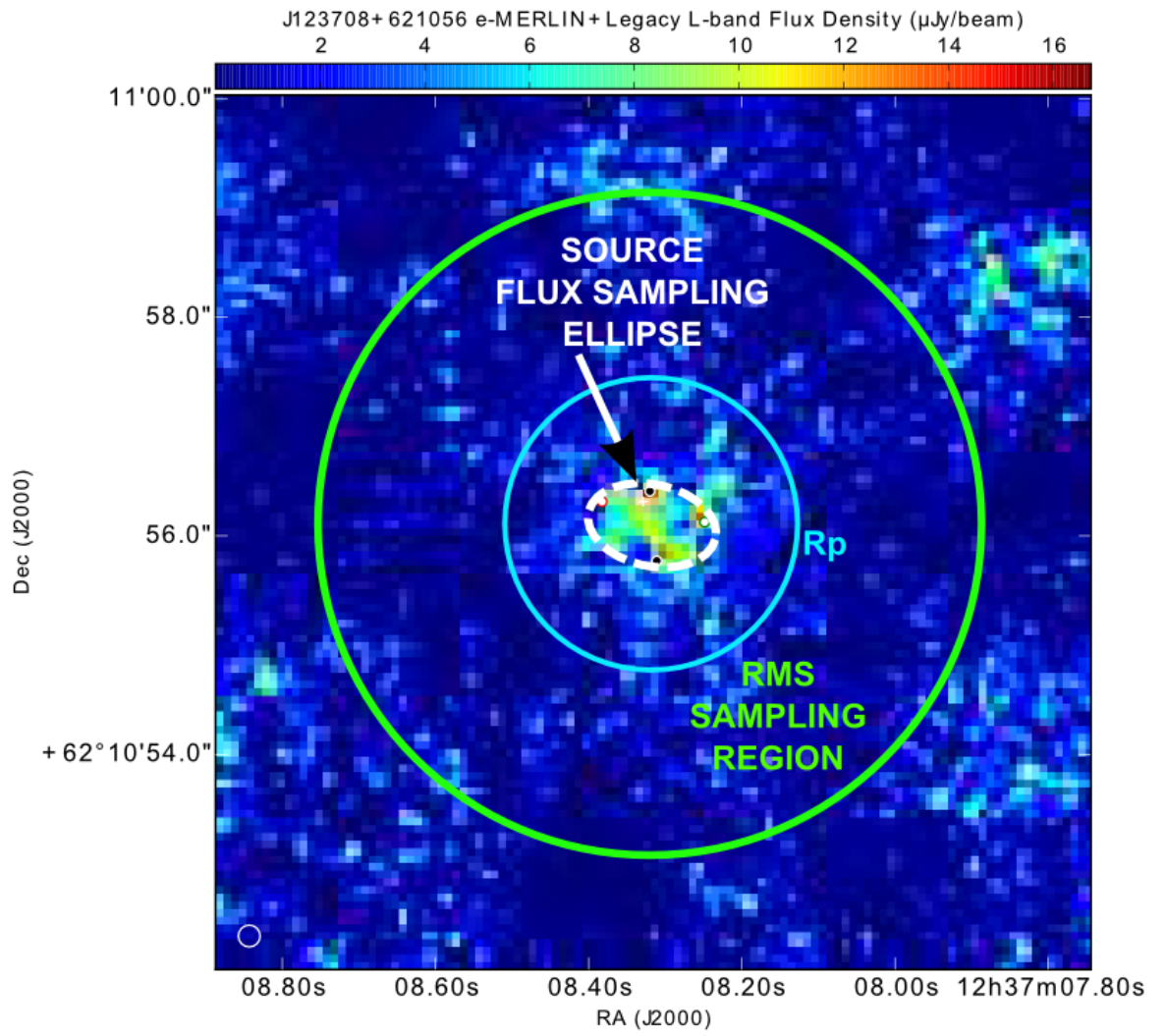


Figure 6.7: Measurement of flux density using aperture photometry (not to scale). The ellipse is determined using the LAS major and minor axes.

Calibration errors are difficult to quantify in interferometric deep field datasets due to differences in uv sampling and variability of sources themselves and is usually taken statistically. A 3% error in amplitude calibration is considered typical and is assumed within this study. The beam correction will also act to exaggerate the error for those sources significantly displaced from the pointing centre. To account for these uncertainties the error (σ_{PB}) was observed to be 3%, so the total flux error is assumed to rise to 6% at the HPBW of the e -MERLIN array.

6.3 Size Distributions of e -MERGE galaxies

6.3.1 Angular Size Distributions

The new e -MERLIN observations represent the highest resolution wide-band data yet obtained of the GOODS-North region at radio wavelengths and, in combination with the now contiguous legacy MERLIN+VLA data, the most sensitive to date. The increased sensitivity allows a greater number of sources to be recorded with increased statistical reliability due to the greater signal to noise ratios. It was argued that LAS yields the most appropriate method of describing the size of the source for this sort of radio data, assuming that each galaxy is disk-like. This assumption fails for AGN type galaxies whose apparent size depends critically on the projection angle but if sources can be segregated into SFG and AGN groups then the linear size of SFGs can be estimated, provided redshifts are also available. The LAS distribution for 248 measurable ($T_f > 2.5\sigma$) L-band galaxies is presented in Figure 6.8. The median LAS of all 248 usable sources was measured to be 1.04 arcsec and the mean 1.25 arcsec, whereas the peak falls between 0.5 and 0.75 arcsec. The Petrosian aperture is a different metric from the LAS, and depends greatly upon its parameters, but had a median diameter of 2.00 arcsec and a mean of 2.1 arcsec, as it intentionally includes more flux surrounding the source.

Measurements of the angular size of galaxies in the deep field have been studied at various wavelengths including optical/UV and in the radio bands, albeit at comparatively low resolution (the highest resolution of the VLA at L-band). The *HST* ACS data arguably provides the highest resolution study to date and, because the angular sizes of galaxies are expected to correlate at some level, then the size distribution trend from that survey is also expected to be similar. [Ferguson et al. \(2004\)](#) used the *HST*

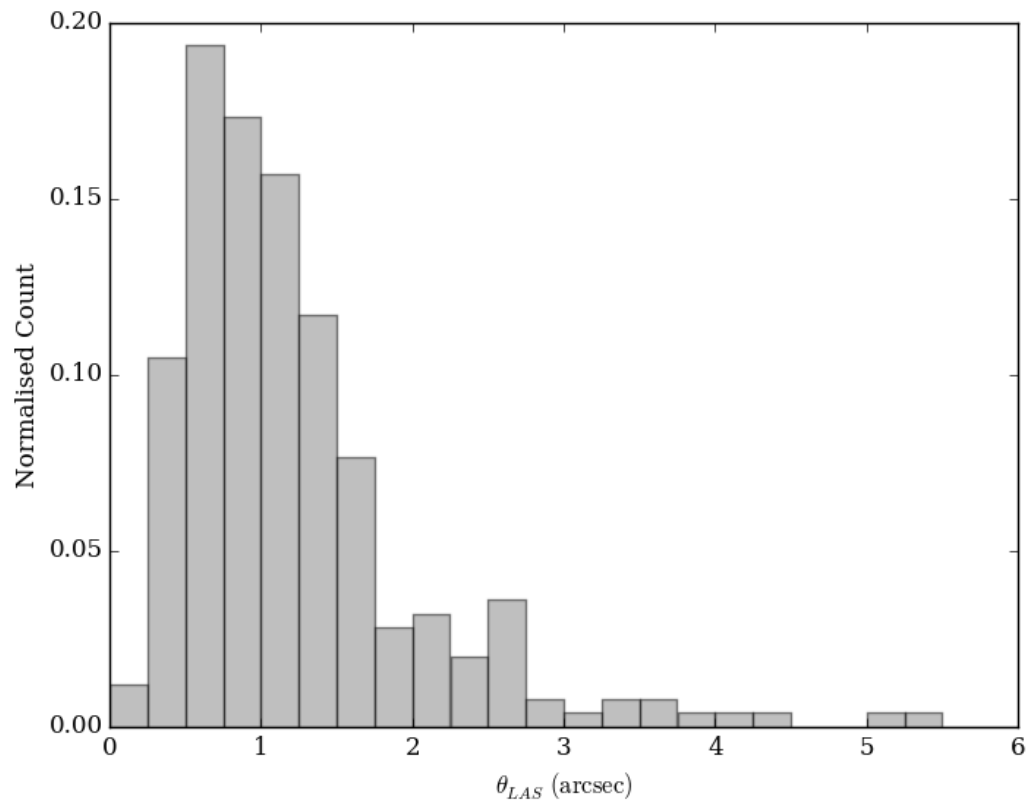


Figure 6.8: The 1.49 GHz LAS source size distribution compiled from 248 sources of *e*-MERLIN and JVLA L-band data.

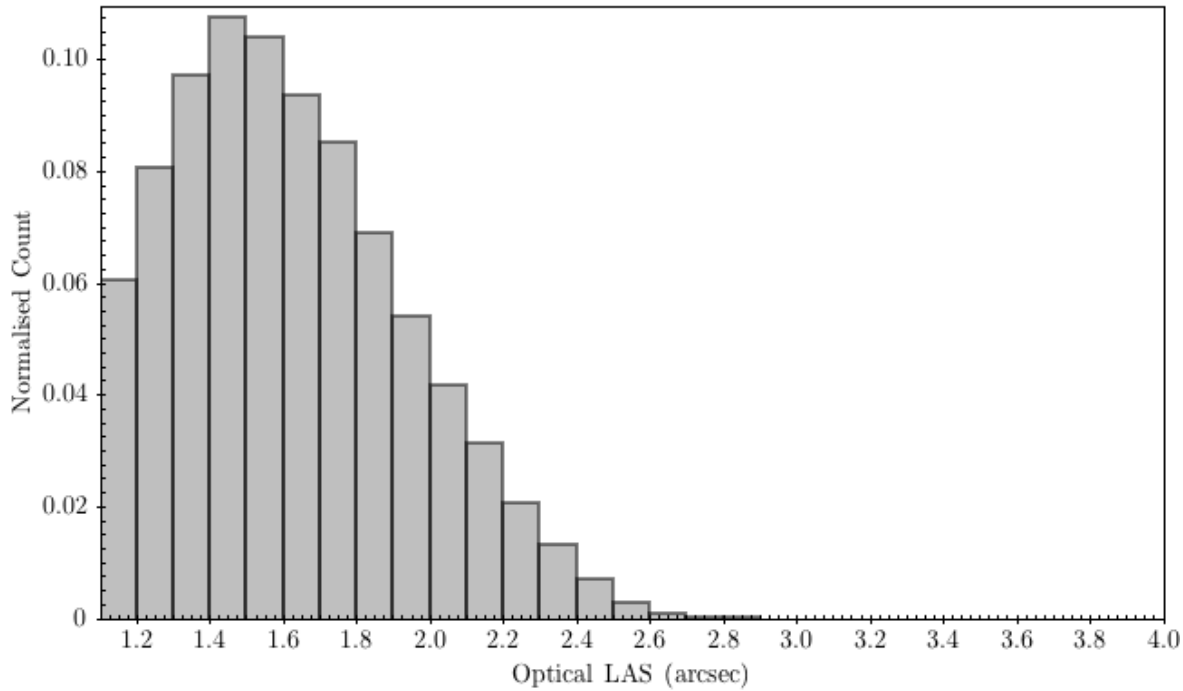


Figure 6.9: Optical largest angular size taken from the STAGES *HST* ACS Survey (Gray et al., 2009). The optical size is assumed to approximate $2 \times 5R_{eff}$.

ACS data to measure the sizes of galaxies in the GOODS fields as part of the STAGES survey. They use the half-light radius R_e to measure the sizes of sources, which assumes a Sersic profile. This can be extrapolated to include the likely extent of the visible disk, generally accepted to be about $5R_e$. Doubling this to yield a diameter results in the distribution shown in Figure 6.9. The optical distribution has a similar shape to that of the radio distribution, although the radio distribution exhibits an extended tail, but not as extended as the radio LAS distribution. This is expected because the jets of AGN are more prominent at radio wavelengths.

A key advantage of the *e*-MERGE survey is its high angular resolution and ability to morphologically distinguish galaxies and divide them into two main groups: one whereby emissions are dominated by accretion and another in which emissions are dominated by star formation processes. This is not a straightforward task and is usually accompanied by an unquantifiable subjective error, but was carried out by Muxlow et al. (2005), who divided them based on morphology as well as multi-band comparisons. They found that at least 35% of sources were AGN dominated. A technique for classifying sources in a systematic way is formulated in Chapter 7, and using those

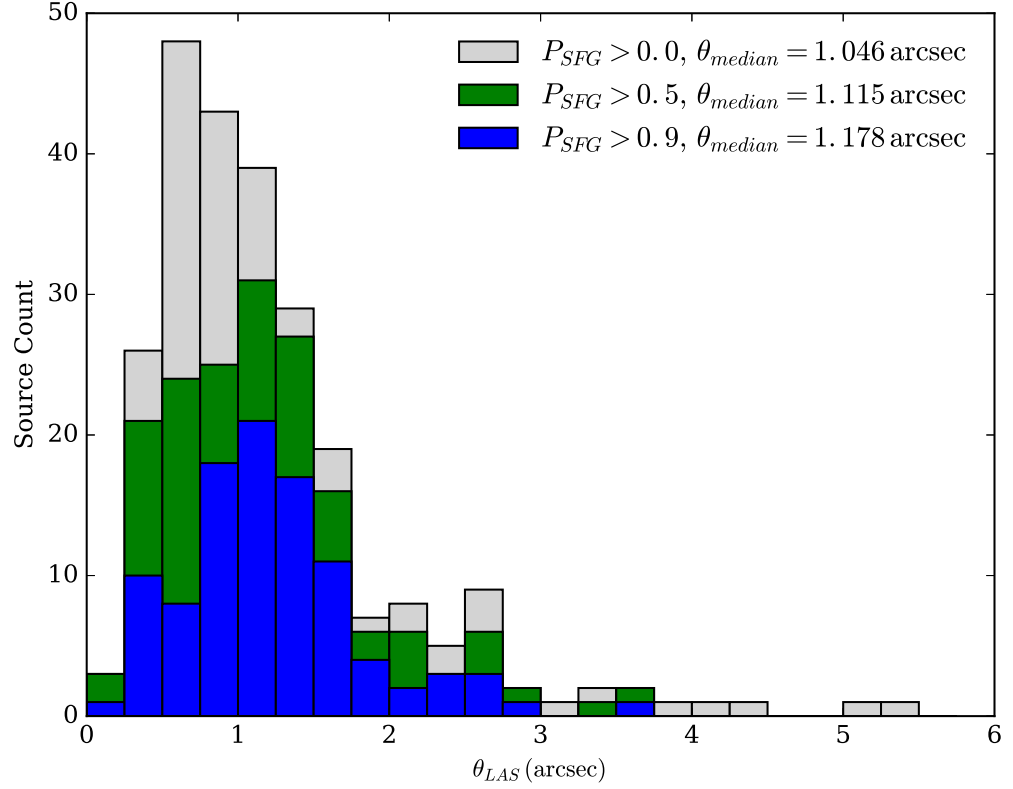


Figure 6.10: Largest Angular Distributions resampled by the population probability of AGN.

techniques the population has been assigned probabilities being either AGN or SFG. Sampling the population by probability of AGN or SFG (P_{AGN} or P_{SFG}), as described in Chapter 7, reveals a change in the median angular size (θ_{median}) as illustrated in Figure 6.10. Once dubious source detections ($T_f < 2.5$) have been removed and the probability of AGN sources above 50% have also been omitted, the median LAS of the remaining 173 sources increases to 1.12 arcsec. Removing yet more of the AGN, leaving just 100 sources, increases the median LAS to 1.18 arcsec. Although the median size increases with increasing SFG probability, the tail of the distribution shortens as long AGN jets are eliminated.

6.3.2 Linear sizes of sources

The linear size of radio emitting regions and their absolute luminosities can be determined only if their distances are established. Redshifts obtained from [Barger et al.](#)

(2008), who compiled a catalogue of all available spectroscopic redshifts of the Hubble Deep Field, can be used to determine the linear size and luminosity of galaxies in the field. Many galaxies have no optically detected counterpart and therefore no optical emission lines to study, neither are there photometric estimates. The number of redshifts recorded within the HDF (that crossmatch within 1 arcsec of those detected in this study) are therefore only a subset. Once the SFG dominant galaxies are selected from this subset (see Chapter 7), the number of sources reduces to a mere 70, and of those only 61 have sufficient S/N to be usable. This represents only one third of all those galaxies identified as SFG and, furthermore, it is expected that these omissions will disproportionately discriminate against those of higher redshifts due to Malmquist bias. An effort to obtain more redshifts was attempted using radiometric SED fitting, comparison of integral flux densities at L and C bands as outlined in Chapter 1. However a major problem encountered was directly related to the measurement inaccuracy in this method due to the relatively closely spaced frequencies between L and C bands and hence a large error in the spectral index. The result included many sources that appear to exhibit spectral indices outside the sensible range. Additional contributions may also include:

- A proportion of SFGs containing AGN contamination.
- Systematic flux calibration errors in either the JVLA L-band or C-band data.
- Insufficient S/N.

The JVLA C-band datasets were reduced in separate blocks and hence the amplitude calibration was replicated. Even if there were calibration errors in one block, the total contribution to the error in integrated datasets would have been reduced. The L-band data compare well with the legacy flux densities, although variability between a few sources has been noted. Many of the sources lie near to the 5σ detection limit in L-band but dip well below this for C-band measurements. This produces an reduction of the flux density within the C-band measurements due to the likely spectral index of sources. It must be concluded that the measurement of the C-band data is too noisy to yield sufficiently robust spectral indices for the weak sources. For example one source, J123654+620745, categorised as SFG by morphology, has a measured spectral index of -0.31 and yields a predicted redshift of $z = 0.26$, whereas Barger et al. (2008) records it at $z = 0.2022$. However, since the spectral index errors lie within the $\pm 25\%$ (due to

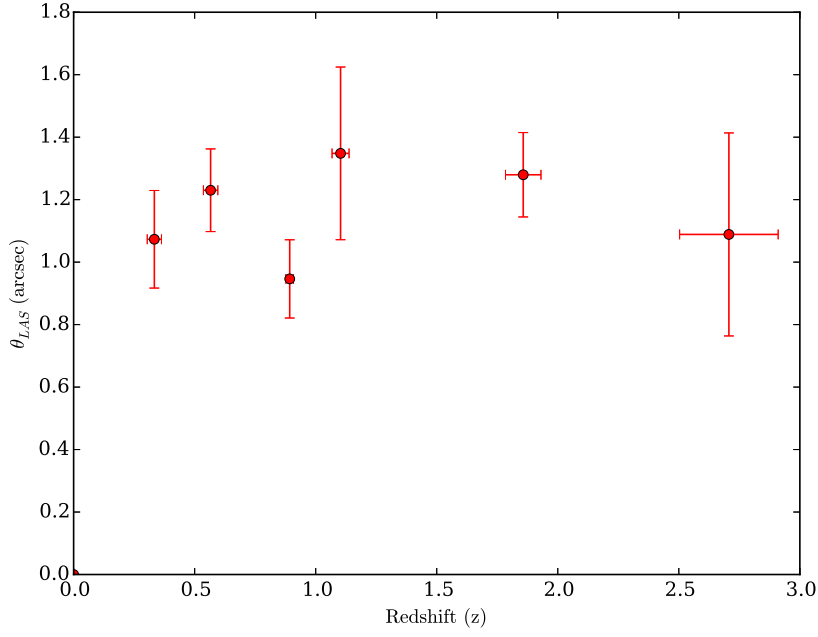


Figure 6.12: The binned mean largest angular sizes of SFGs plotted against available redshifts. The LAS varies around 1 arcsec. The error bars describe the scatter within each redshift bin.

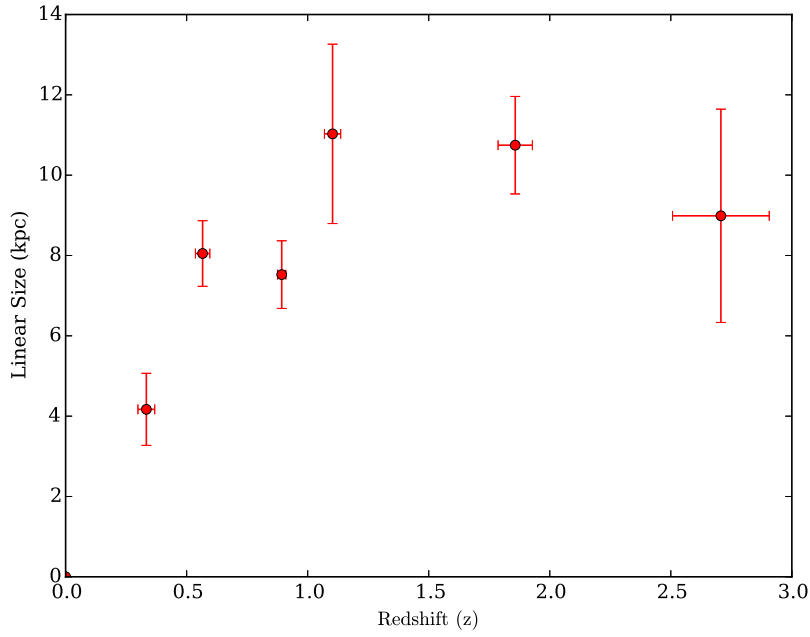


Figure 6.13: The linear sizes of binned SFG sources ($P_{SFG} > 0.5$) plotted against available redshifts.

galaxy sizes appear to rise until approximately $z \approx 1$ and then remain nearly constant thereafter (see Figure 6.13). The trend is true for both LAS and Petrosian radius size measurements.

The size of sources constrains the integral flux densities which, when combined with redshift information, provide an estimate of the intrinsic luminosity of sources. The evolution in luminosity is expected to be coupled with an evolution in the size of galaxies, and, therefore, the angular size distribution of galaxies as seen by us. The popular theory is one whereby the existence of a dark matter halo attracts normal baryonic matter, and the infall of surrounding matter gains sufficient angular momentum to produce a disk - a theory which appears to replicate the emergence of spiral galaxies using N-body simulations. As cosmic time elapses, the absolute size of luminous galaxies increases, thus it is expected that high redshift galaxies are locally smaller. However, in the case of the radio observations, the size of the emitting region is smaller than the optical size of the galaxy as only the components involved in active star formation are detected. An added complication is due to the cosmological distance redshift relationship which alters the perceived angular size and hence galaxy angular size and evolution and cosmology are intertwined, leading to a frustrating degeneracy. The estimate of luminosity evolution and other derived quantities are presented in Chapter 7.

6.4 Summary of Angular Size Distribution

The high resolution imaging of the GOODS-N field using *e*-MERGE data has, for the first time, generated a sub-arcsec sub-mJy description of the angular size distribution of galaxies. The largest angular size distribution for all detected ($T_f > 2.5\sigma$) *e*-MERGE sources was detected to peak under 1 arcsec at $\theta_{LAS} \leq 0.75$, with a median placed at $\theta_{LAS} = 1.04$ arcsec. This is broadly in agreement with Muxlow et al. (2005). Comparison with optical data yields a similarly shaped angular size distribution, and is consistent with the view that the radio-emitting regions lie within the disk of galaxies. The linear sizes of SFG dominated galaxies, calculated from available redshifts and a Λ CDM cosmology ($\Omega_M = 0.3, \Omega_\Lambda = 0.7, h_0 = 0.7$), appears to verify this conjecture, lying between 4 - 10 kpc. There is perhaps a weak dependence on redshift with smaller sources placed nearby ($z < 0.5$) rising to a linear size approaching 11 kpc for $z \gtrsim 1$.

The measured angular size of sources in this study has implications when consider-

ing the optimisation of future radio telescope projects if morphological characteristics are to be usefully resolved. For at the present time only *e*-MERLIN has baseline lengths sufficiently large to yield the necessary angular resolution at L-band. The Square Kilometer Array Phase II, having long baselines, would theoretically be equipped to delve deeper with the angular resolution in order to morphologically distinguish between AGN and SFR characteristics. The high angular resolution, a key diagnostic in discriminating SFGs and AGN is explored further in the next chapter.

Chapter 7

Source Classification and Flux Density Distributions

One of the main objectives of the *e*-MERGE survey is to be able to identify galaxy components to determine the amount of star formation occurring in the micro-Jy population of sources. Accomplishing this requires the ability to distinguish between the two broad classes of galaxy. This chapter describes a technique based upon *Support Vector Machines*. The results are utilised to determine relative prevalence of SFGs and AGN in the field and are presented in the form of differential source counts. Derived attributes include luminosities and star formation rates.

7.1 Classifying Galaxies

Discriminating between AGN and SFG components takes advantage of the emission characteristics described in Chapter 1. These include the following:

- Component shape and size.
- Compactness.
- Spectral index.
- Evidence of IR or X-ray emissions.

These metrics were used in [Muxlow et al. \(2005\)](#) to classify sources into two categories: AGN and SFG, which were also sub-divided based on a judgement of the ambiguity

in the final classification adopted. The first and second points relate to morphology, the principal discrimination advantage of high angular resolution *e*-MERLIN imaging. The spectral index of sources is determined by comparing integral flux densities of sources retrieved from the *e*-MERGE JVLA L-band and C-band data. The final point takes advantage of the Radio/FIR correlation or the presence of extreme energies from compact sources. The legacy data were analysed originally by [Muxlow et al. \(2005\)](#) and [Richards et al. \(2007\)](#) who classified over 90% of the 92 detected sources and found that approximately 70% of those identified as SFG also exhibited some X-ray emission. This suggests that the X-ray discrimination technique is of poor reliability when used alone and so the majority of source classifications utilised morphology. Compact components are strongly suggestive of AGN activity, whereas a lumpy extended structure on galactic scales indicates star forming regions. However, there exists a subset that may contain both components. Some of these attributes are exhibited in the example sources shown in Figures 7.1 and 7.2 with the principal type of emission characterised.

e-MERLIN images are of sufficiently angular high resolution to permit such morphological discrimination. For fainter sources with lower S/N ratios, a reduced certainty arises. It is necessary to use all measurements available, including LAS, Petrosian radius, compactness and spectral index collectively, to establish the character of a galaxy. A significant problem is that human judgement is brought to bear on each source individually, potentially introducing subjective bias, making it difficult to attribute a quantification of the certainty of any classification. The judgement is usually given a label similar to ‘AGN candidate’ or ‘SFG candidate’ for example. Where considerable uncertainty exists the source is usually designated as simply ‘Unclassified’. It is also unknown whether biases towards particular attributes sway the ultimate classification. It must also be questioned if definite classifications are appropriate at all, or whether a continuum of AGN/SFG component ratios should instead be adopted for each object. To test the robustness of the different parameters used to identify the classification of galaxies more objectively, and to minimise human bias, the employment of *machine learning* is used here.

7.1.1 Machine Learning

Machine learning has been utilised on previous occasions and compared within large surveys ([Gauci et al., 2010](#); [Hocking et al., 2015](#)), with many originally classified by eye ([Lintott et al., 2008](#)), and appears to have a similar rate of success in correctly

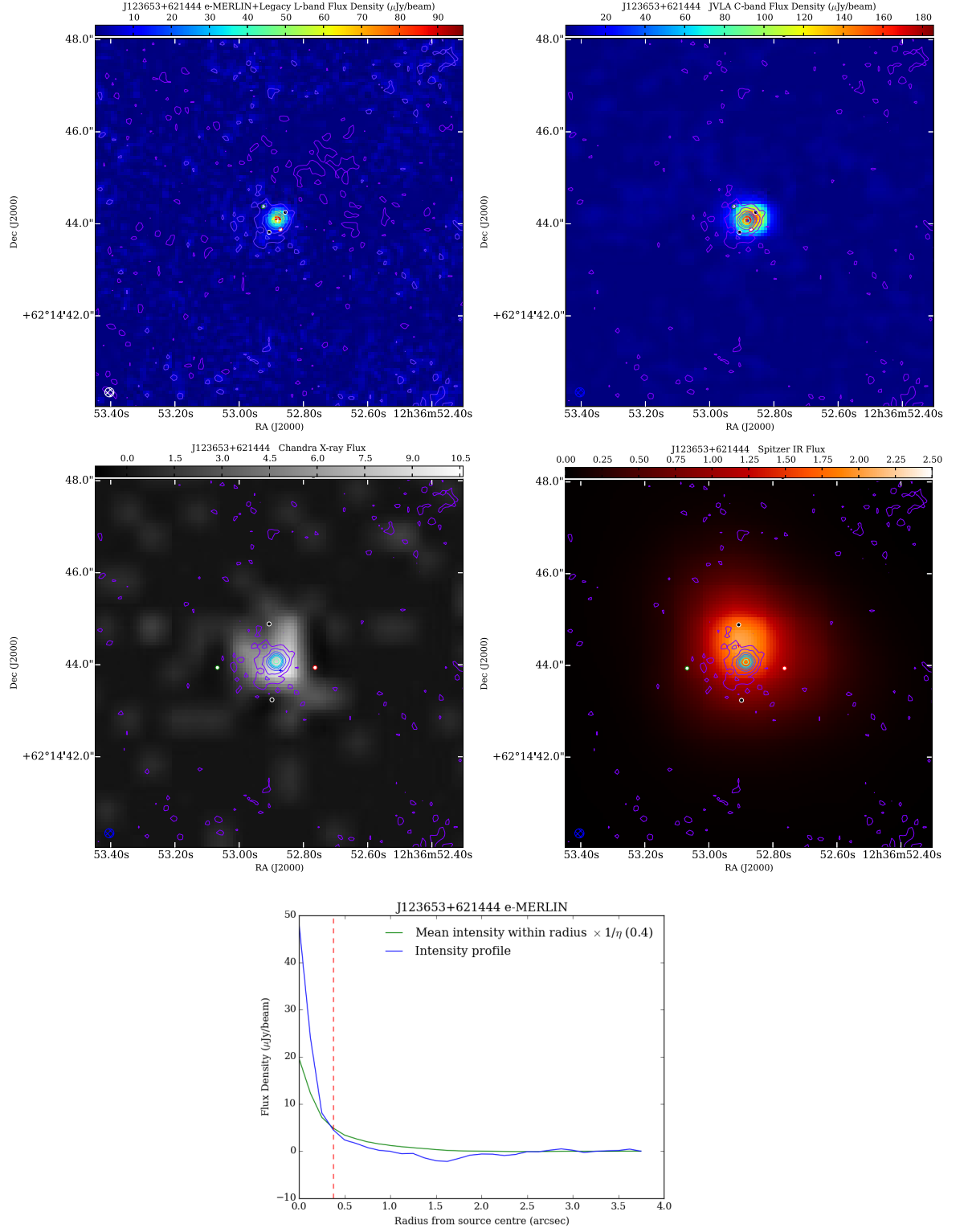


Figure 7.1: A source with an AGN character as classified by [Muxlow et al. \(2005\)](#). From top left to bottom: *e*-MERLIN L-band image showing compact core, JVL A C-band also showing compact component, X-ray emission, IR emission, the radially integrated source profile.

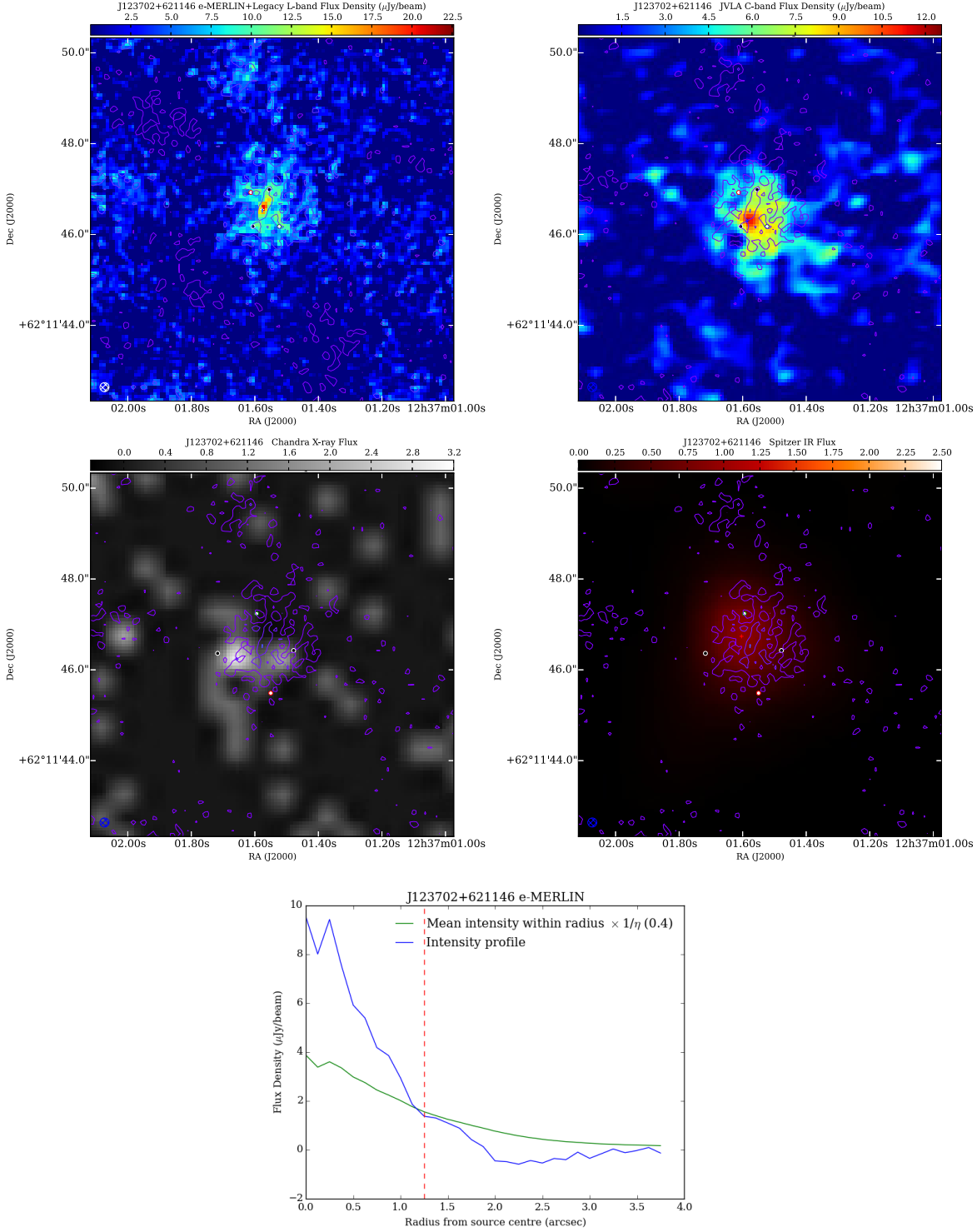


Figure 7.2: A source with an starburst component classified by [Muxlow et al. \(2005\)](#). At first this source appears to have similar attributes to the previously classified AGN source, with one exception: the Petrosian profile is shallow even though there is a sharp component. This ‘lumpiness’ as well as the extended structure is suggestive of star-forming activity. This is reflected in the compactness parameter and Petrosian Radius.

identifying galaxy morphologies as visual inspection techniques. Authors are careful to highlight that the success can only be as good as the set of data used to train the machine - the *training set*. This is a robust set of data that has well determined and relatively uncontaminated classifications.

Various methods for teaching a computer to learn diagnostic techniques have been theorised but a full investigation of artificial intelligence methodologies is beyond the scope of this thesis. For example, neural networking relies on mimicking the way the brain learns to identify visual patterns by strengthening complex pathways of feature detectors by a system of weighting. These can become quite robust given a large amount of data. Drawbacks include the amount of computing power required to act on each image, their non-mathematical nature and erroneous conclusions due to falling into local minima. An alternative method, and the one used here, is the *Support Vector Machine* (SVM), which instead utilises a multi-dimensional parameter space ($n - 1$) of n types of the collected attributes (i.e. in this case angular size, spectral index and infrared flux) and attempts to find the *decision hyperplane* that divides the two sets. This is achieved by constructing a system of *support vectors* between the attributes in each hyperspace dimension (see Figure 7.3). Only a single solution is possible: the hyperplane within the parameter space maximising the distance between the support vectors of the two characteristic sets. Once the hyperplane is calculated, placing previously unclassified sources in the parameter space automatically assigns a category, theoretically the category that their attributes most closely resemble. A scoring system is then used to determine their displacement from the hyperplane and is used to provide a measure of the certainty of the classification. The great advantage in this technique is that multiple attributes of the source can be used in combination to arrive at a conclusion about its likely classification, as well as testing whether some measured attributes add any significant value at all. The SVM module used in this project is implemented in python: *SciKit Learn* (Pedregosa et al., 2011). The module allows integration within the existing python scripts and permits rapid studies to be conducted. Because multiple variables are used, which alone may not yield an obvious correlation other than some clumping, but together create a more powerful correlation in a higher dimension.

A subset of the data is selected, based on the sources classified previously (by Muxlow et al., Richards et al. and expanded by Guidetti et al.), which have good detections, to be used as the training set. The training set is used by the machine learning

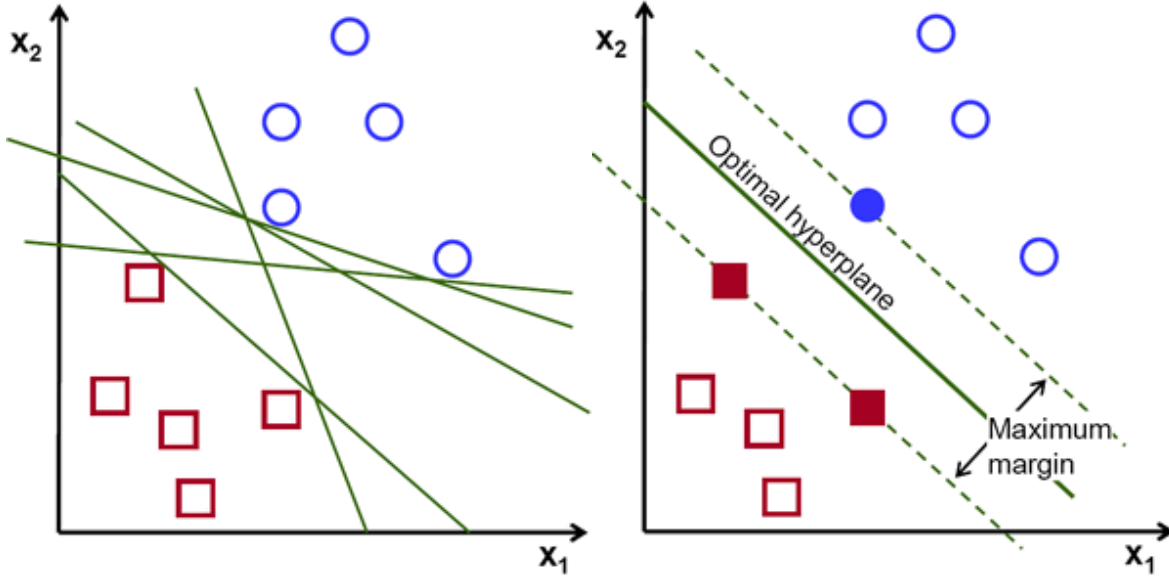


Figure 7.3: Support vectors (left) with decision optimal hyperplane (right) within an example 2D parameter space. The dimensionality x_n of the space depends upon the number of source attributes.

algorithm to identify common attributes from the full gamut of measurements. Training the SVM to identify an AGN or a SFG involves identifying the most appropriate set of measured attributes from the training set of classified sources. There is no limit on the number of attributes that can be used, but too many can cause over-fitting so it is better to contract them prior to use. The number and selection of attributes to most effectively produce the most reliable classification were selected by trials. The SVM was trained on the previously outlined robust training set by selecting from the following attributes:

- Largest angular size.
- Petrosian radius.
- Compactness parameter.
- IR flux.
- X-ray flux.
- Peak flux density.
- Integrated flux density.

For the process to work, there must be some correlation between the various attributes, although it need not of course be a linear correlation, else a straightforward association between attributes could be used as a discriminator directly. Figure 7.4 illustrates that some correlation between the various measurements (such as LAS and Petrosian aperture) exists but is insufficient alone. Only in ensemble do they produce a multi-correlated delineated partition. A total of 61 sources were considered sufficiently robust to train the machine and an array was constructed with the above attributes for each source, as well as the a binary label representing whether it is an AGN or SFG dominant galaxy. All sources have outermost contours that lie at the highest threshold (T_f) and all were assigned a classification of either SFG (+ve) or AGN (-ve) dominated based on the classifications assigned by Muxlow et al. (2005); Richards et al. (2007); Guidetti et al. (2013). These are inputted into the SVM to determine the hyperplane that best separates the two groups, which takes just seconds on a modern personal computer. Once the decision hyperplane had been determined, the same training set is then fed back into the SVM again, i.e. placed into the parameter space, to gauge how well the hyperplane correctly separated the source designations. The outcome of this is a scoring system with SFGs having a positive label and AGN a negative label, with the scoring system quantifying the amount of 'starburstness' or 'SFG-like' properties of each source. The resulting histograms in Figure 7.5 illustrate how the decision function responds to the training set, given various input attributes with the hyperplane located at starburstness score zero. As well as observing a large fraction of true positives and true negatives, it can be seen that a smaller fraction of sources are deemed to be SFGs when they were previously judged in the training set as AGN (false positives) and vice versa. The number of *interlopers* can be used to determine the *True Positive Rate* (TRP) using:

$$\text{TPR} = \frac{\text{true positives}}{\text{true positives} + \text{false negatives}} \quad (7.1)$$

and the *False Positive Rate* (FPR) using:

$$\text{FPR} = \frac{\text{false positives}}{\text{false positives} + \text{true negatives}} \quad (7.2)$$

With these definitions, whereby each correctly identified source is given its appropriate label, the TPR and FPR can be plotted against each other, with respect to a running threshold, to produce the *Receiver Operating Characteristic* or ROC curve. These are presented in Figure 7.6 as cumulative distributions. The area underneath the ROC

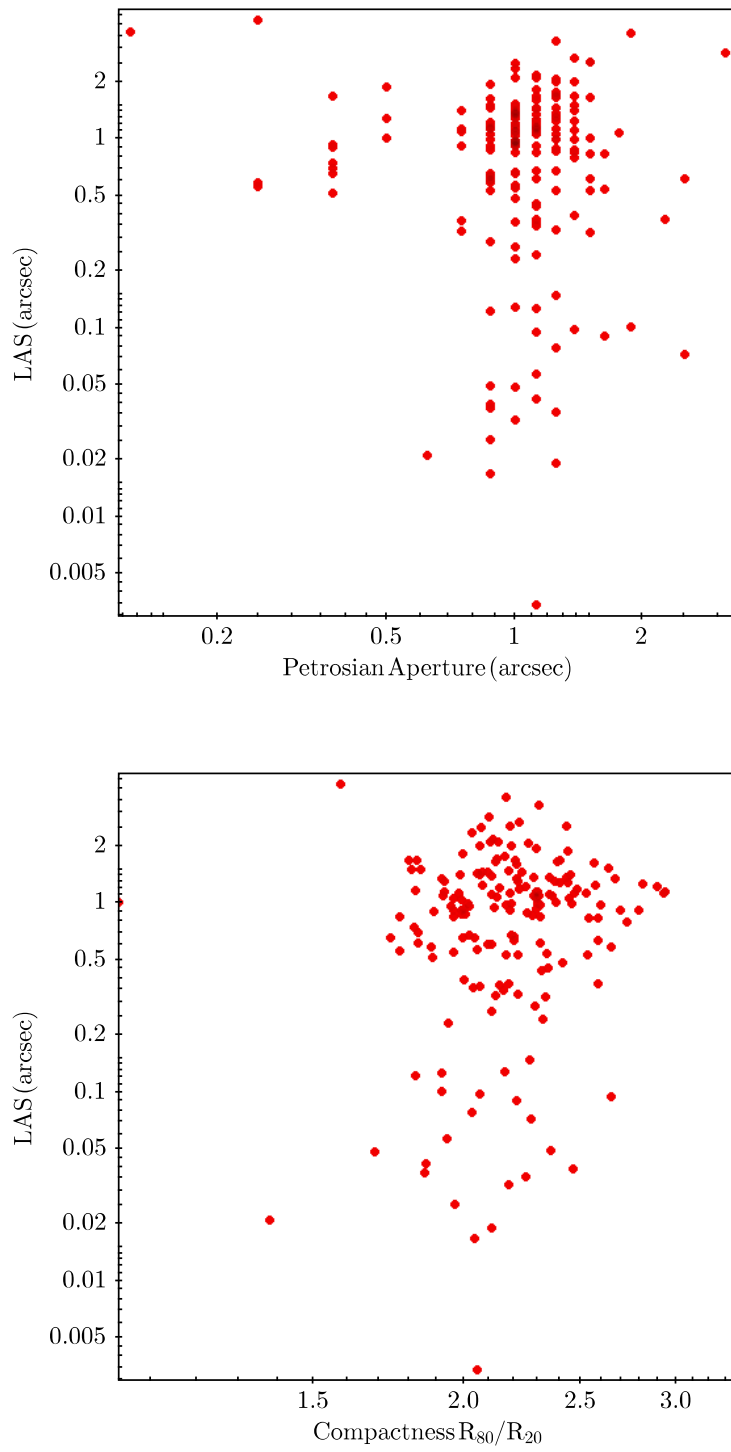


Figure 7.4: Plotting attributes against each other reveals clumping, used by the SVM to determine a higher dimensional hyperplane.

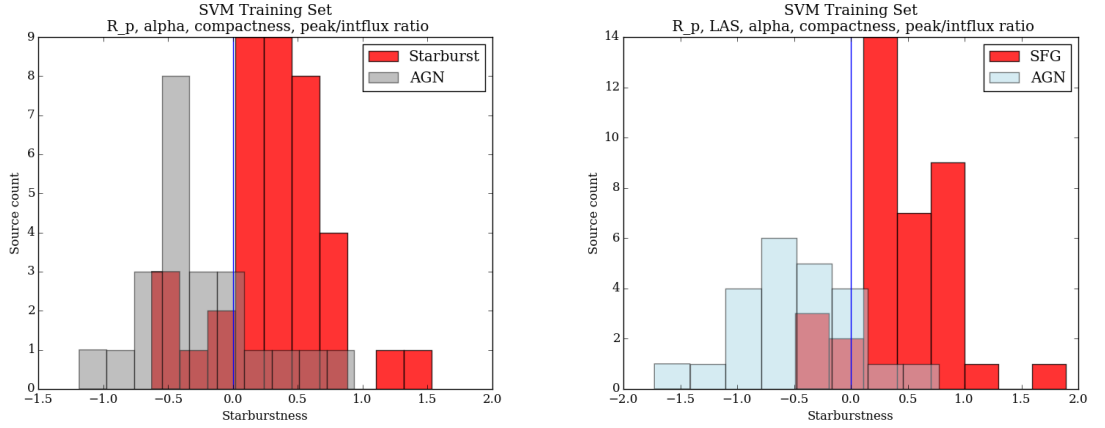


Figure 7.5: Histograms illustrating how the SVM decision function responds to the 61 source training set given different selection attributes, in this case in inclusion or not of the LAS. Sources positive of the decision bisect (zero on the abscissa) are likely to have more Starburst-SFG-like multi-parameter features than the more AGN-like (negative score values) to the left.

curve provides a useful measure of the number of true positives given that set of input attributes, and hence the reliability of the trained machine. The attributes could be included or not based upon studies. By examining the output of numerous such ROC curves given the varying combinations of input attributes, it was observed that the most dominant classifiers included:

- Compactness Parameter.
- Spectral index.
- Peak/Integral Flux Ratio.
- Petrosian Radius and LAS.

Those attributes with the least influence on classification included:

- X-ray flux.
- IR flux.

The latter two were at first surprising, but given the large overlap in multi-band flux detections in both categories of galaxy (Richards et al., 2007) and the fact that most of the galaxies identified by Muxlow et al. (2005) were categorised by morphology, their influence on the SVM decision was smaller. It may also reflect the suspicion that many

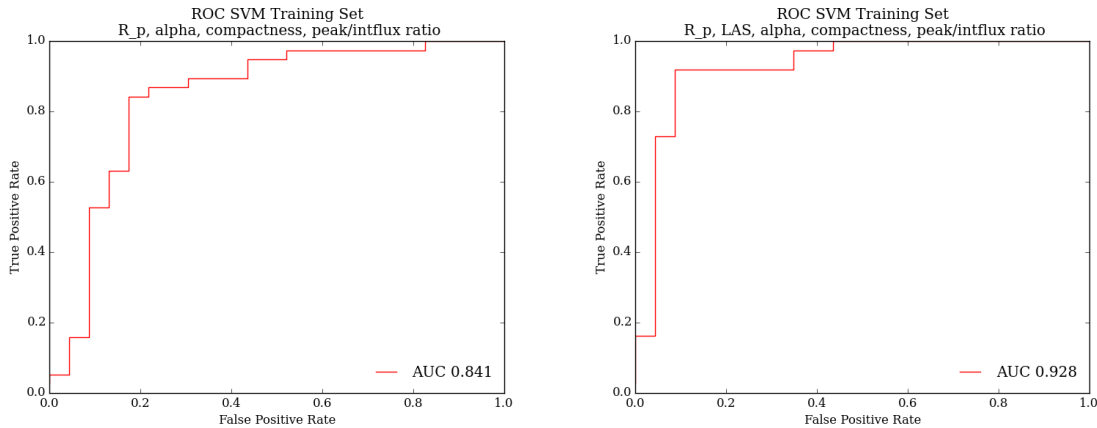


Figure 7.6: ROC Curves for SVM Training Set.

sources contain components from both types of emission, which is why IR and X-ray are detected in both at varying intensities and that in this implementation only a crude multi-band input is supplied, which does not include for example characteristics such as IR colour or X-ray hardness values.

The absolute flux densities were found to have the tendency to bias the machine learning algorithm by preferentially associating all bright sources as AGN and all dim sources as SFG. However, it was important to make the trained set flux independent so it can be applied to sources at any flux density. Consequently, the results of the best trained machine include only morphological attributes and flux *ratios* between L-band and C-band. The associated ROC curve for the best combination of attributes yields an area of 92%. This equates to a large fraction of True Positives and minimises the number false classifications. The decision bisect, located at starburstness zero, represents the best fit division between the two classes, but it is noted from the training set that a number of interlopers maybe spread over scores up to ± 0.5 whereas the entire range extends to ± 2 .

Using the best trained machine it was possible to reliably categorise the majority of sources in the field, even many that appeared to be too difficult to classify by visual inspection. A total of 248 sources (i.e. $>70\%$) could be classified (or reclassified) robustly using the SVM with 173 falling into the SFG dominated category and 75 falling into the AGN dominated category. This ratio of 2.3:1 is larger than the 61 source training set ratio of 1.65:1, but may reflect the suspicion that the number of SFGs becomes more prevalent at lower flux densities which are probed more by the deeper full data set ($S_{min} \sim 20\mu\text{Jy}$) than the training set ($S_{min} \sim 40\mu\text{Jy}$).

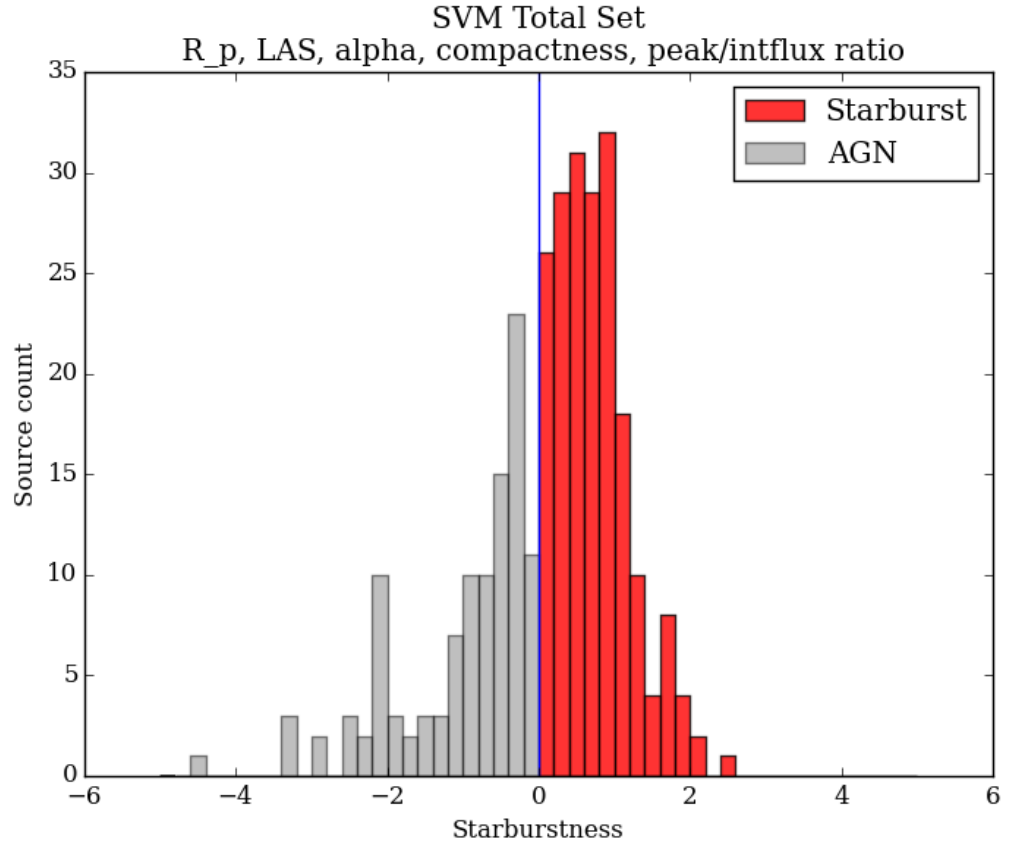


Figure 7.7: The 248 SVM scored sources based upon the training set. The distribution is bimodal as expected with a greater number of SFGs identified than AGNs. 92 sources could not be classified reliably because of low signal to noise ratios of outer contours fell below $T_f = 2.5\sigma$.

The separation of the dataset into two broad classes will have errors attached to them, as there is evidently an overlap in the bimodal distributions, investigated later in this chapter. All sources were examined by visual inspection but no sources appeared to be falling obviously into the wrong category. Some of the SVM decisions are presented in Figures 7.8 and 7.9. One conspicuously bright source (J123642+621331) was identified as AGN by the SVM when originally classified as SFG dominated by Waddington et al. (1999) using a spectroscopic analysis. The SVM score of -0.599, however, places the source far enough away from the decision hyperplane to question the initial classification. Recent VLBI observations¹ appear to confirm that this source does indeed harbour an AGN component due the appearance of bright radio jets. The redshift was also questionable for an SFG, being placed at $z = 4.424$, forcing it into ultra-luminous ULIRG territory, although ambiguities in the line identification (OIII or Ly α) may place this source closer ($z \approx 2$). This source is henceforth reclassified as AGN dominated for the remainder. The *e*-MERGE sources have been re-classified using the SVM with results presented in Appendix I and the distribution of these classifications plotted in Figure 7.7. Whether the relative proportions of SFG and AGN appear credible can be investigated by examining the *differential source counts* and comparing them to previous studies within the flux density limits.

7.2 Differential Source Counts

Differential source counting is employed in the measurement of populations of galaxies, like the *e*-MERGE survey, to reveal information regarding the evolution of sources over cosmological scales. It involves binning populations of galaxies by their flux densities. Taking $\Delta N/\Delta S$ and normalising to a Euclidean Universe by multiplication of $S^{2.5}$, yields a simple method for presenting population change *independent* of the cosmology (i.e. essentially assuming a classically flat non-expanding Universe). A full description of relativistic number densities and the cosmological effect on source counting, independent of any particular model, is given in Iribarrem et al. (2012). The differential source counts presented in Figure 7.11, taken from Seymour et al. (2004) (who compiled an ensemble of studies as well as measuring sources obtained from the VLA), illustrate that there appear to be two distinct 'humps' or peaks in the distribution and indicate that two broad populations of object may be involved. These are hypothesised to be

¹J. Radcliffe (private communication).

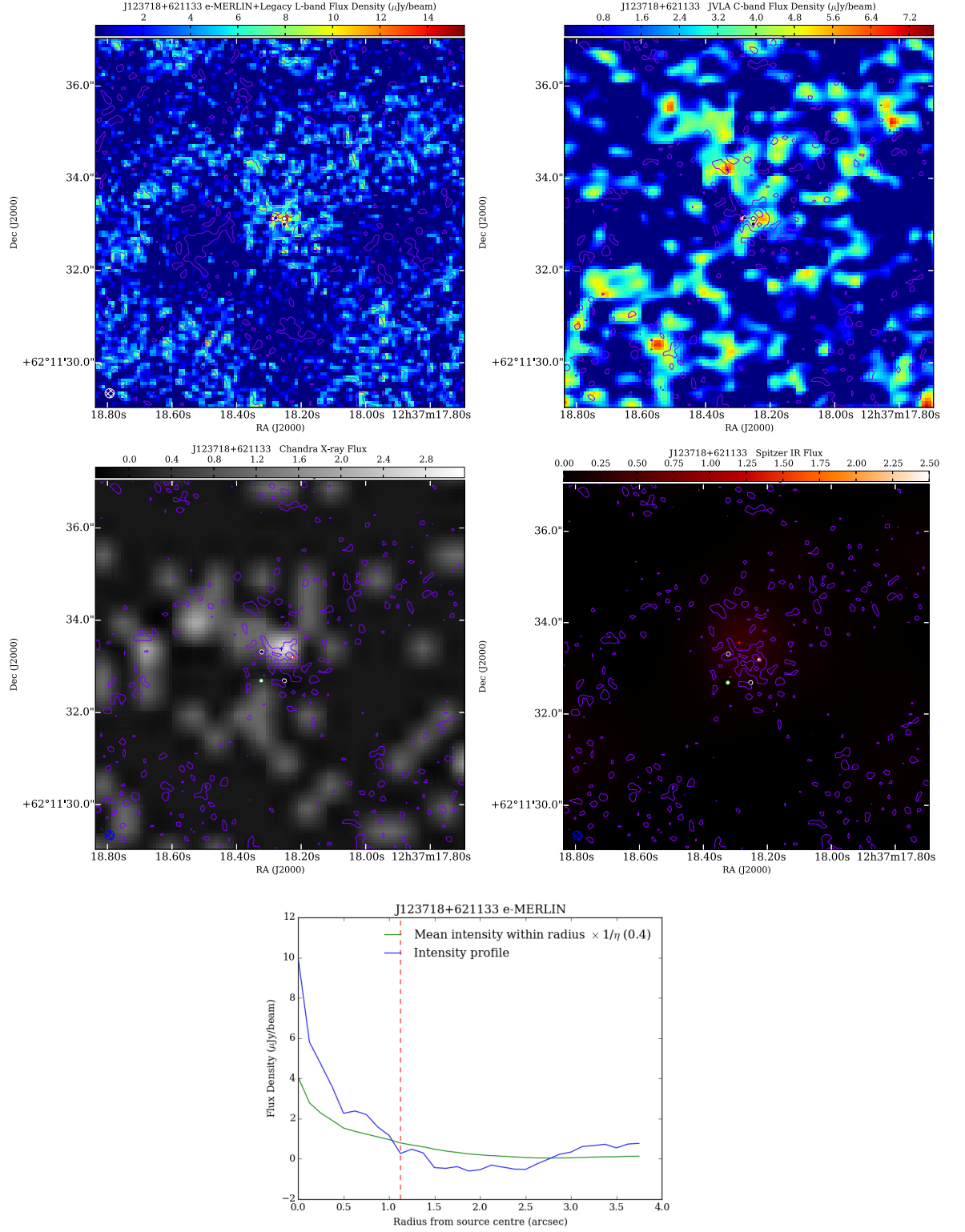


Figure 7.8: Previously unclassified source J123718+ 621133 narrowly categorised by the SVM as weakly SFG dominated but with a score of just 0.264. It lies close to the decision bisect and could arguable contain some AGN contamination, given the very faint X-ray and IR flux detections.

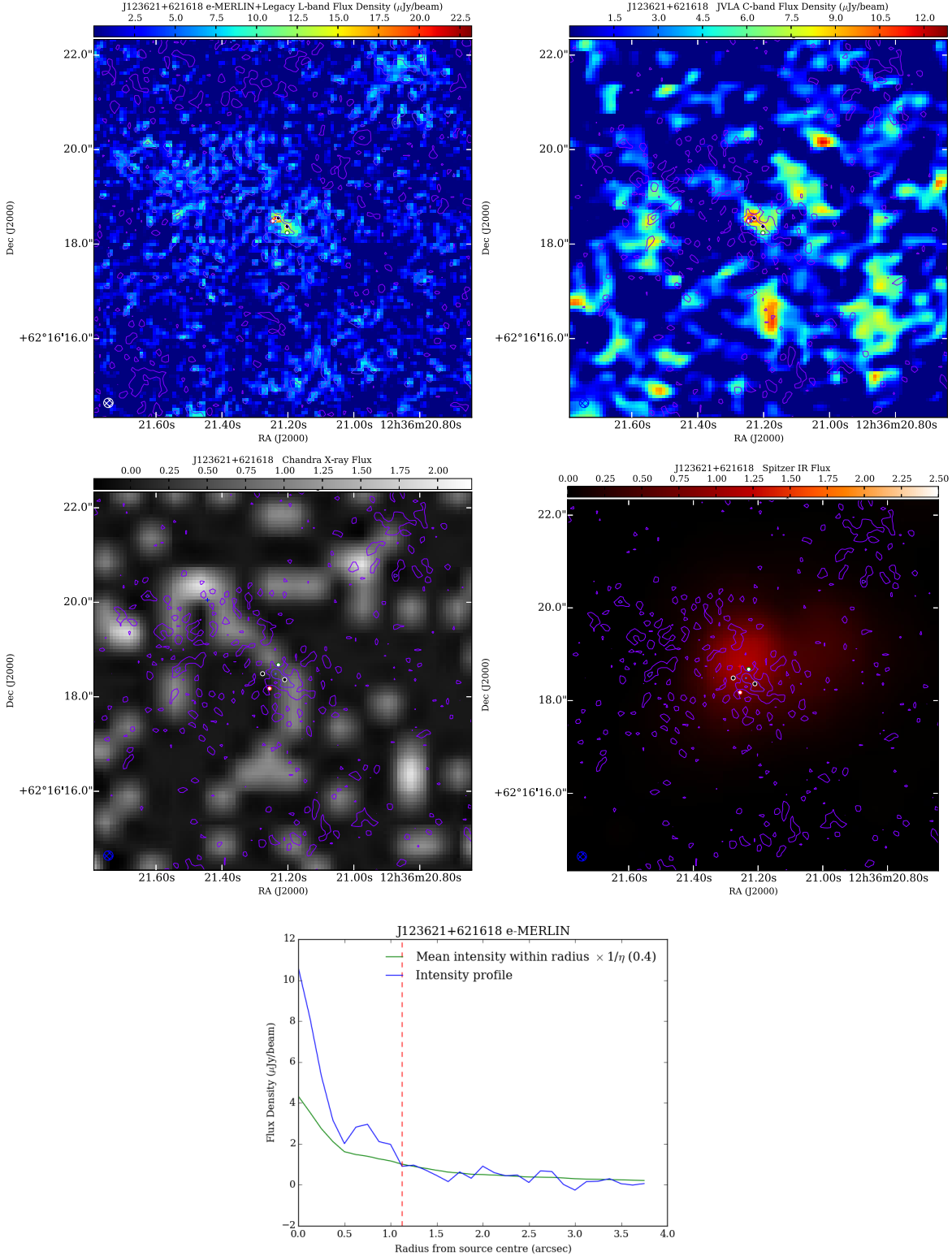


Figure 7.9: Source J123621+621618 classified by the SVM as an SFG with a score 0.887. A lack of X-ray flux appears to confirm the more positive starburst score.

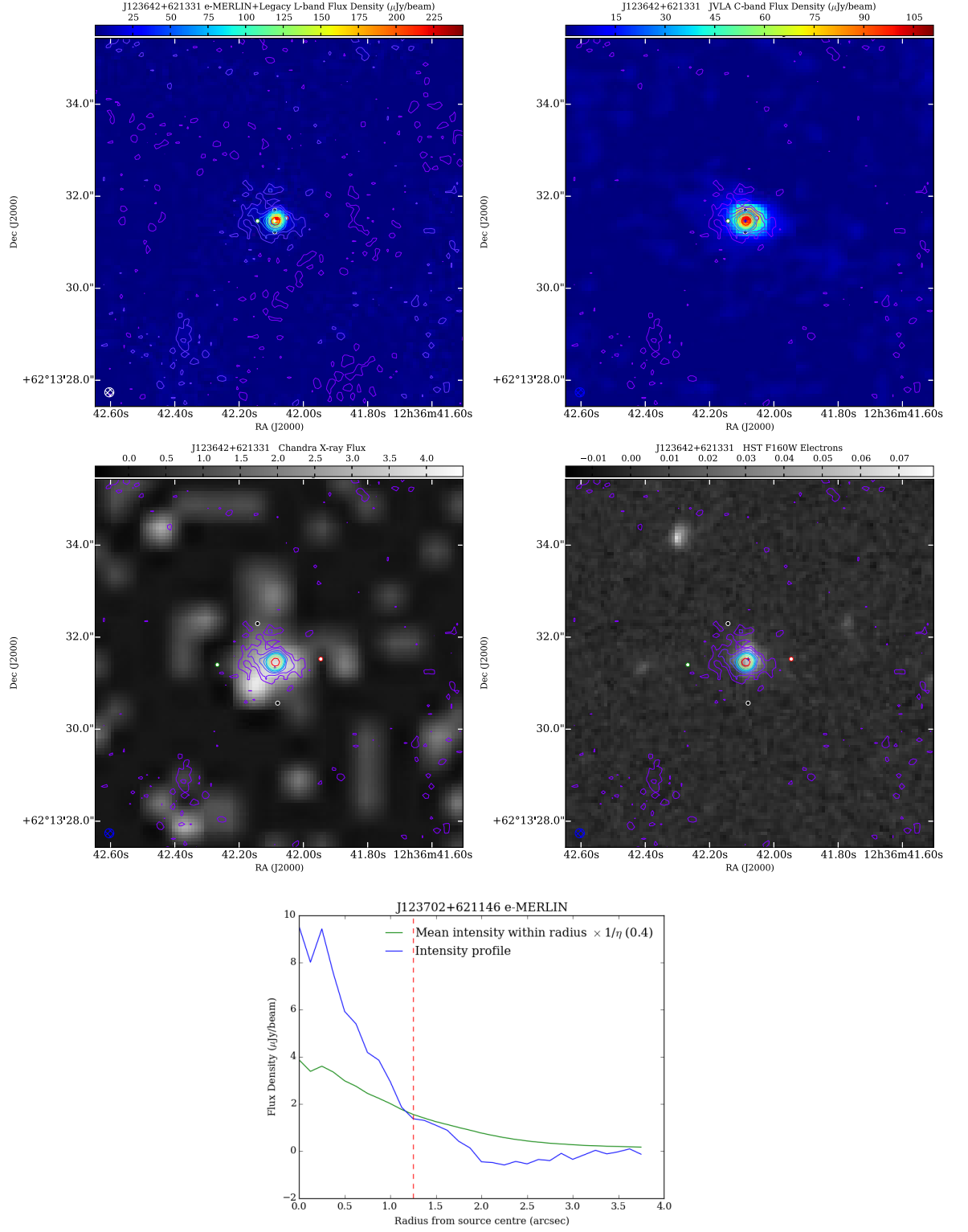


Figure 7.10: Source J123642+621331 re-classified by the SVM as an AGN dominant galaxy. Top Left: L-band *e*-MERLIN+Legacy map. Top right: JVLA C-band map. Mid left: X-ray with *e*-MERLIN contours. Mid right: *HST* image with *e*-MERLIN contours. Bottom: Radially integrated profile.

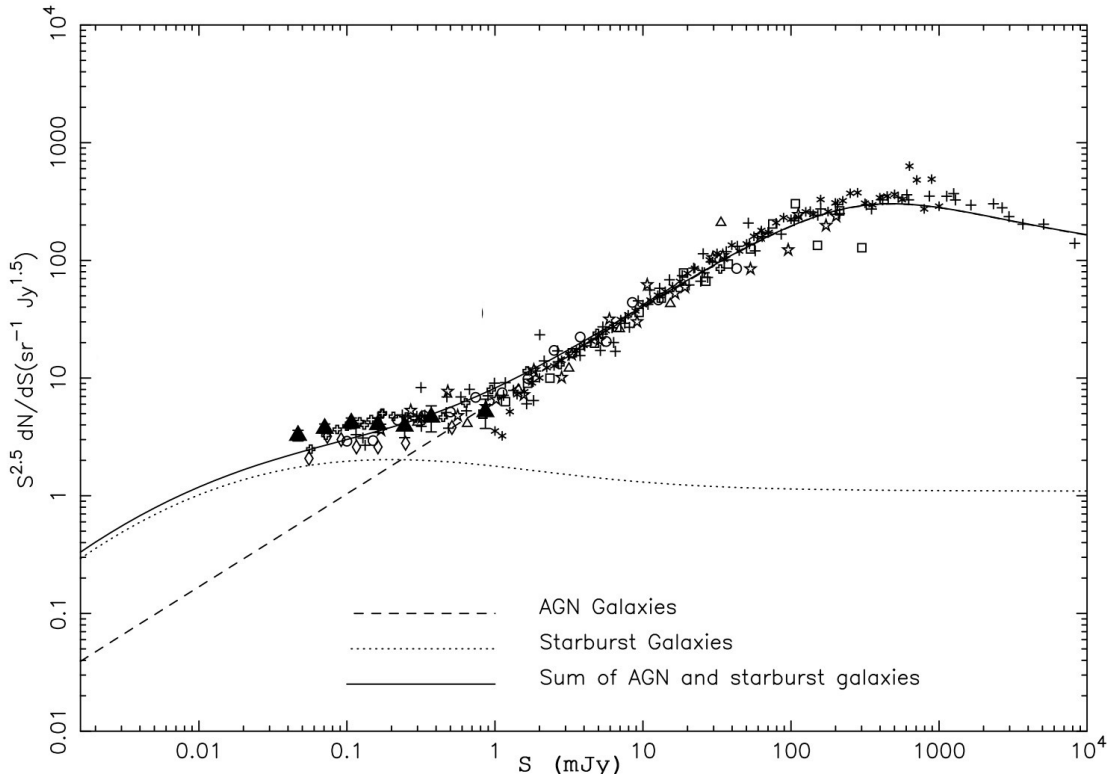


Figure 7.11: Differential source counts appear to demonstrate two distinct populations of objects (Seymour et al., 2004). In the compilation of observations here the number of sources per flux density interval has been normalised such that a horizontal (zero gradient) represents no change in the number density of sources through in time for a non-expanding Universe. The two 'humps' that appear to make up the total distribution are believed to arise from evolution in populations of SFG and AGN dominated emission mechanisms.

AGN and SFG dominated populations, which when added together produce the characteristic shape of the differential source count plot (see Figure 7.11). The sloping nature of the function also implies that a change in the luminosities or number densities, or both, have occurred (part of the slope will be due to cosmological expansion effects but this will apply equally to both populations). Reproducing the differential source count distributions in Figure 7.11 involves perturbing the *local luminosity functions*, representing the relative abundances of intrinsic luminosities of populations of each type of galaxy, as a function of redshift. The modification in the luminosity function can change the population in two possible ways:

- Modifying the number density per unit co-volume as a function of redshift (density evolution).

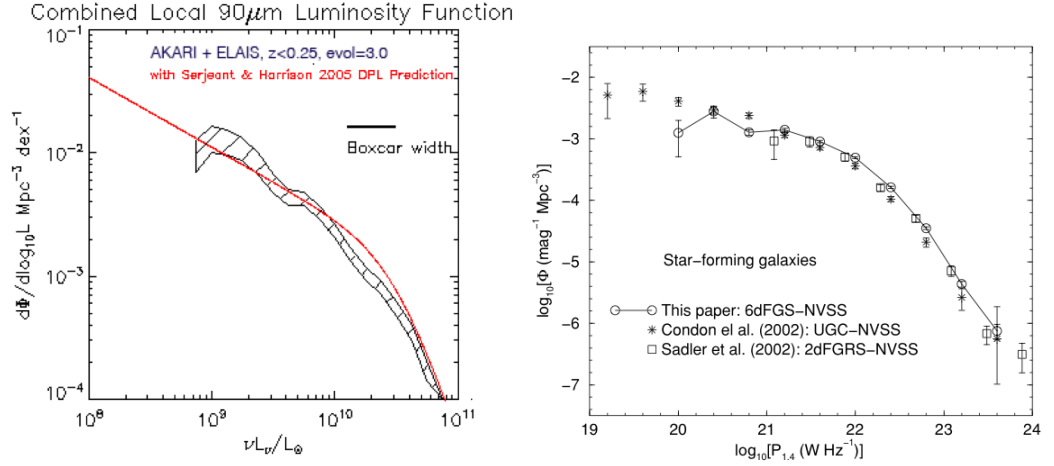


Figure 7.12: Local luminosity functions for SFGs in the FIR (left [Sedgwick et al. \(2011\)](#)) and the Radio (right [Mauch and Sadler \(2007\)](#)).

- Modifying the luminosity of the population as a function of redshift (luminosity evolution).

To do achieve this it is first necessary to probe large populations of morphologically identifiable nearby galaxies (i.e. near $z \sim 0$) to form a local luminosity distribution for the two classes. Distance measurements for each galaxy can be found by 'standard candle' methods (Cepheid variables for instance) and luminosities computed. The result for normal (i.e. SFG) galaxies is observed to follow

$$\phi(L) \propto L^\alpha e^{-L},$$

([Schechter, 1976](#); [Saunders et al., 1990](#)), which describes the number of galaxies per unit volume per luminosity interval (i.e. falling between L and $L + dL$) and was originally based on optical observations. Luminosity functions have since been determined across the electromagnetic spectrum. In the radio domain these are called *Radio Luminosity Functions* (ϕ_0) which are band-specific (i.e. they sample a single part of the SED). Nearby luminosity functions presented in Figure 7.12 illustrate that in both the FIR and the radio bands, there exist far more low luminosity galaxies than high luminosity galaxies. The similarity in the shape of the functions reflects the FIR/radio correlation discussed in Chapter 1. The same is true within the AGN local luminosity functions: an abundance of lower luminosity objects (see Figure 7.13). However, the luminosity functions for AGN take a different form as they are composed of two char-

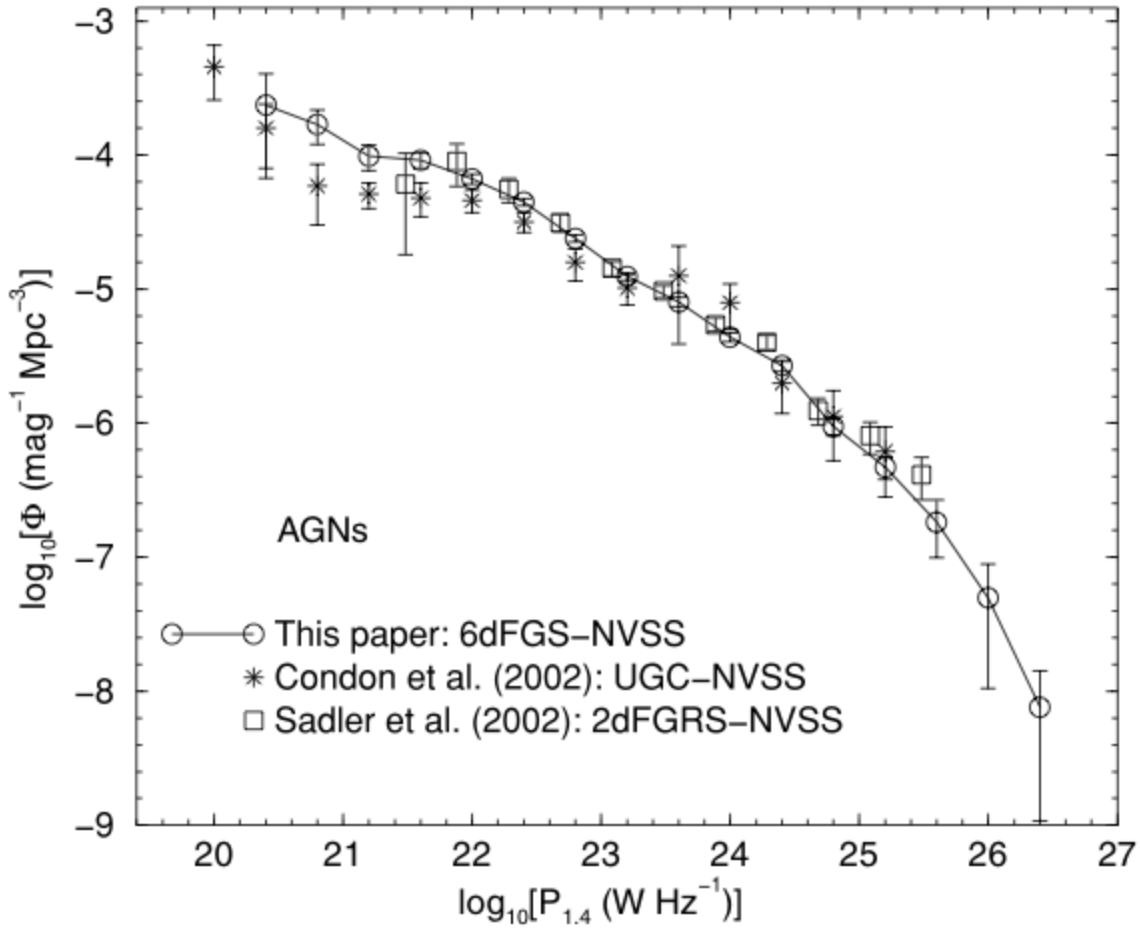


Figure 7.13: Local Radio luminosity function for AGN ([Mauch and Sadler, 2007](#))

acters: core and lobes/jets. . To determine the luminosity functions of more distant galaxies directly requires redshift estimates, obtained spectroscopically or photometrically. Instead, radio luminosity functions are sought as a function of redshift by fitting observed differential source counts.

Evolution modelling carried out by [Hopkins et al. \(1998\)](#) and [Seymour et al. \(2004\)](#), and later summarised by [de Zotti et al. \(2010\)](#) attempted to simulate the differential source count distributions by altering the luminosity (or number density) of AGN and SFG sources as a function of redshift. This is represented mathematically by dividing ϕ by $(1+z)^Q$ for perturbing the luminosity of the population of galaxies, with Q parameterising the extent of the evolution. A more sophisticated perturbation parameterises the function as a polynomial (see Equation 7.6). This is typically carried out for at least three galaxy subsets: SFG, AGN flat-spectrum and AGN steep-spectrum. The SFGs

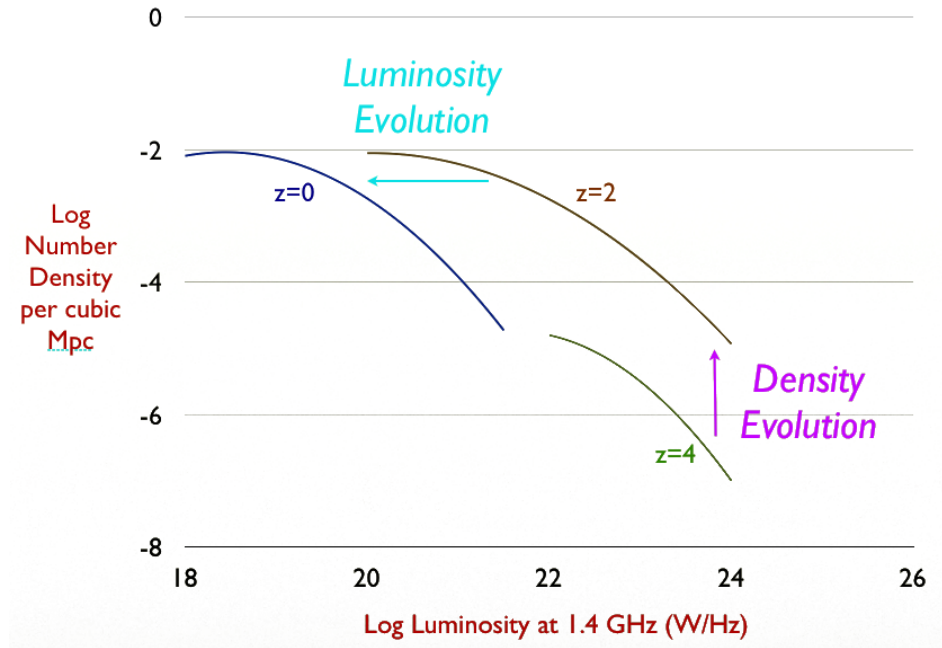


Figure 7.14: Perturbing a local RLF as a function of redshift causes evolution in the populations of galaxies (assuming the SED remains the same) [Carole Haswell \(2002\)](#).

can themselves be split into subsets with the higher luminosity galaxies, or starbursts, represented by a power law. When differential source counts are generated from these models it is found that strong density evolution followed by strong luminosity evolution in the AGN populations is required to simulate AGN number counts ([Simpson et al., 2012](#)), with a peak at about $z \sim 2$. For this reason a more complicated evolution is usually used which combines the effects of both. Luminosity evolution in the SFG population of $Q \sim > 2.5$ ([Smolčić et al., 2008](#)) is required to reproduce the SFG number counts but, because of the large amount of scatter near the present flux limit, there exists considerable uncertainty, causing problems in extrapolating predictions into the micro-Jansky flux density regime. Additionally, the SEDs of each category of object have been represented as simple power laws, an assumption that must, beyond some redshift, become invalid. As an extreme example, a 5 (+2) GHz observation observing a source placed at a redshift of $z = 9$, would actually be probing a 50 (+18) GHz emission and lead to erroneous predictions for SFG population luminosities due to the spectral curvature exhibited by the galaxy's SED over that range. Although it is unlikely that such redshifts are encountered at present surveys (including the *e*-MERGE survey), a lesser effect will still exist for moderately high redshifts ($z \sim 5$) and care

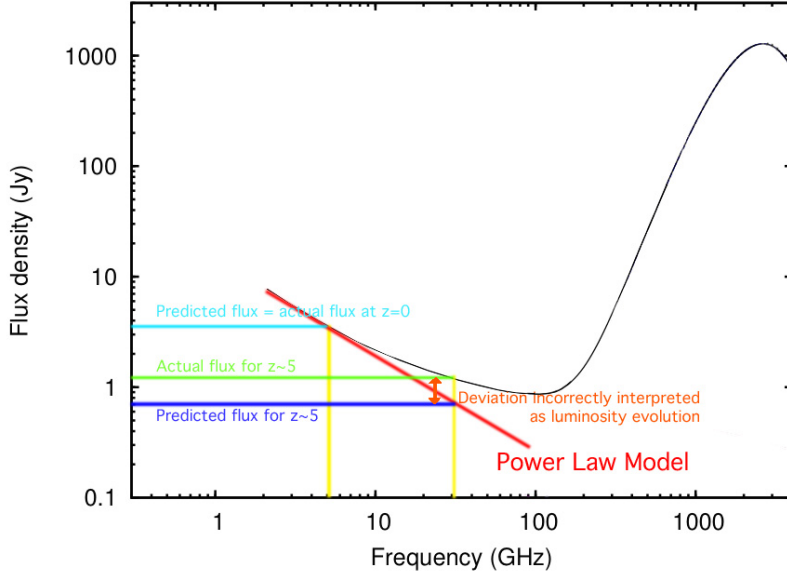


Figure 7.15: Exaggerated illustration using an SED power law approximation in source count modelling which incorrectly attributes a recorded increase in flux to a luminosity evolution. The error increases as a function of redshift - here a 5GHz observation causes a 2-fold under-prediction in flux at a redshift of $z \sim 5$.

must be taken in defining the scope of the evolution model (see Figure 7.15). Once appropriate evolution models have been formulated, they can be used to extrapolate deeper and used to create numerical simulations of the deep radio sky, such as the S-Cubed database (Wilman et al., 2008). Changes in population density are usually explained by merger scenarios and/or active or inactive emission states.

7.2.1 Generating Differential Source Counts from *e*-MERGE data

The flux densities obtained from each of the sources detected in the *e*-MERGE data are binned into several flux intervals covering the full range of integral flux densities measured. These are usually arranged logarithmically. In the *e*-MERGE survey the flux densities are obtained from the JVLA L-band measurements to minimise uv sampling losses as *e*-MERLIN tends to resolve away the most extended of sources. The number of sources in each flux bin is divided by the flux density interval before being multiplied by the representative flux density raised to the power of $5/2$ to normalise the plot to a Euclidean Universe. The representative flux density of each bin is calculated by finding

the arithmetic mean of the flux densities for sources within the bin, with an spread error bar representing the standard deviation of the fluxes. A normalised differential source count distribution is generated and presented in Figure 7.16.

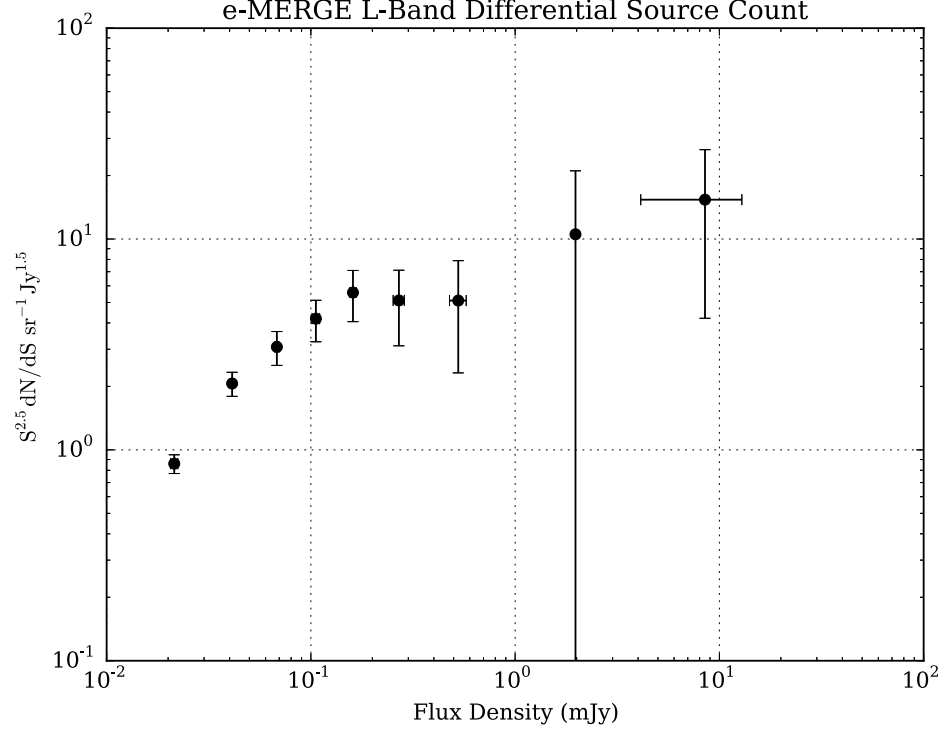


Figure 7.16: Differential Source Count for *e*-MERGE galaxies. Integral fluxes are derived from the ellipse LAS constraints. 1σ error bars are derived from measurement flux density uncertainties from each source and from poisson statistics added in quadrature.

If the sources are crudely separated into SFG and AGN classifications along the SVM bisect ($SFG = \{Score > 0.0\}$, $AGN = \{Score < 0.0\}$) then then two source counts can be plotted independently (see Figure 7.17) already clearly demonstrates a diverging evolution between the two selections. Errors were estimated and arise from two dominating factors:

- Errors in the flux density measurements.
- Errors due to low number count statistics and cosmic variance.

The flux density measurement error is dominated by the noise, as many sources are of low S/N ($T_f < 3.8\sigma$). The rms noise was determined by measuring the region immediately surrounding each source using aperture photometry methods. Low number count

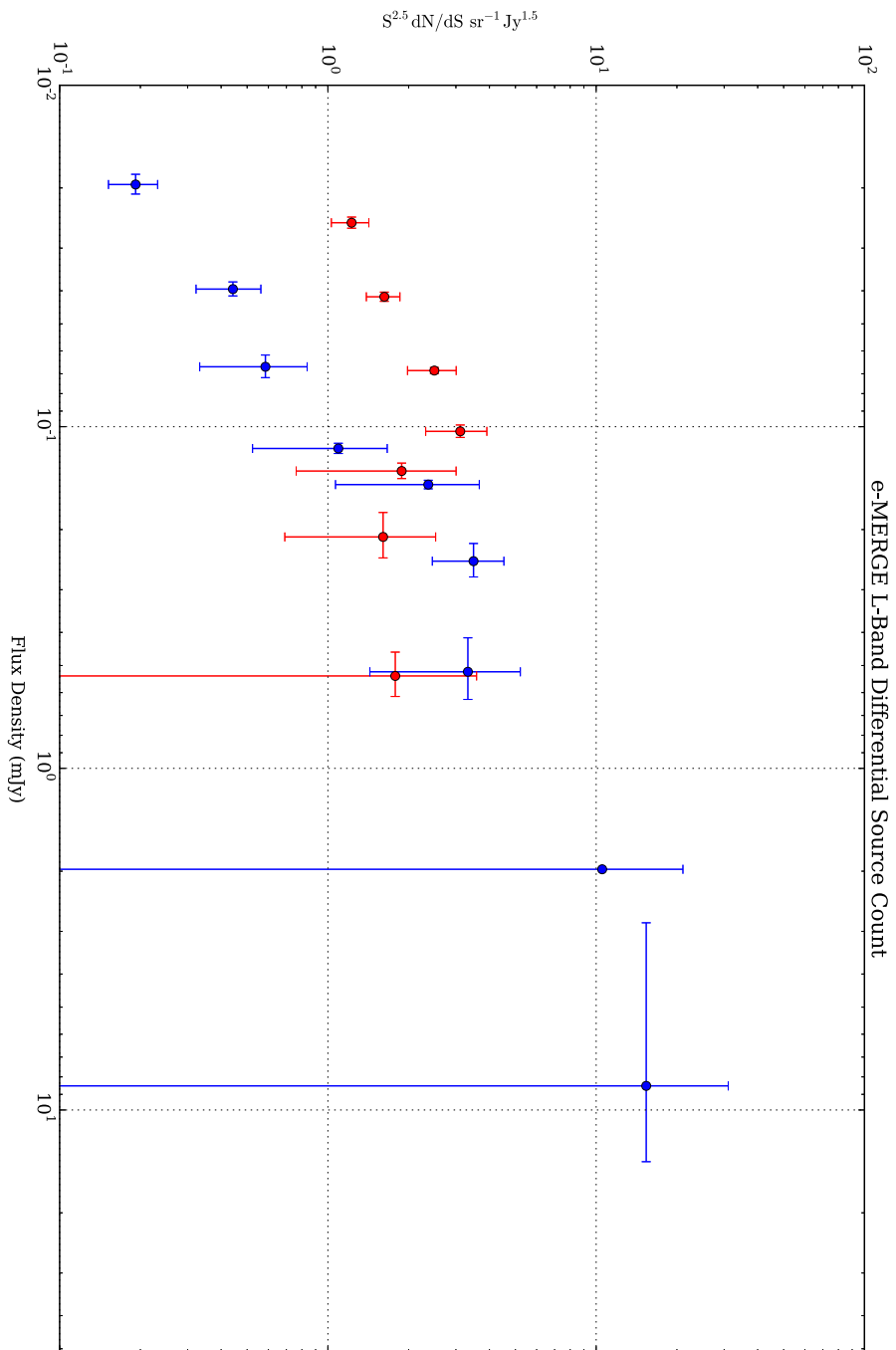


Figure 7.17: The uncorrected *e*-MERGE source counts divided into AGN and SFG categories along the SVM bisect.

uncertainties are derived from Poisson errors. There is also an additional error due to clustering, or cosmic variance, which can be determined from the fractional clustering variance:

$$\sigma_{\text{clustering}}^2 = \frac{1}{\langle n \rangle} + \sigma^2 \quad (7.3)$$

taken from [de Zotti et al. \(2010\)](#), where $\sigma^2 = 2.36 \times 10^{-3} \Omega^{-0.8}$ and Ω is the survey area in deg^2 . However, for the GOODS-N field, chosen because clustering is not evident, this contribution is negligible compared with the other errors. For well defined sources the uncertainties are a smaller fraction of the measured flux density and the source is unlikely to fall into an adjacent flux bin. However, for sources with large fractional errors it is possible that it could indeed fall into one of the bins at either a higher or lower flux.

To investigate the consequence of the uncertainties, each source was perturbed assuming a Gaussian distribution of width σ_{flux} based on the calculated error, and then differential source counts recalculated hundreds of times. This has the effect of sometimes pushing some sources into adjacent bins depending upon whether the flux or counts are perturbed up or down. The process was repeated to produce a variation in derived values which cascade throughout the calculations. The total error in source counts within each bin due to the spread includes the Poisson error to yield

$$\sigma^2 = \sigma_{\text{flux}}^2 + \sigma_N^2. \quad (7.4)$$

There are additional errors that remain unquantified: those errors arising from sources that have not been detected due to insufficient signal to noise ratios. This is understood by considering detection thresholds used in surveys designed to minimise false positives, for example an S/N ratio of at least 3. This is equivalent to a 98% probability of the detection actually lying below 5σ . However, it also works in the opposite direction, in that sources with true fluxes that should peak above the threshold may fall below the threshold due to a conspiracy of noise. For Gaussian noise statistics the probabilities can be calculated exactly, however, in the case of non-Gaussian noise (as exhibited by a radio interferometer) combined with a non-Gaussian distribution of the luminosity of sources, this cannot easily be quantified. Instead, previous studies have attempted to ‘boost’ the counts at low flux levels by attempting to estimate how many sources must have been omitted by injecting low level sources into the data set and trying

to detect them again blindly using a peak detection algorithm such as SAD. This is not attempted here because *e*-MERLIN has not yet been used to locate sources as the *e*-MERGE observations simply are not yet sufficiently deep. Instead, the differential source counts are compared with the results of an alternative methodology recently carried out by Vernstrom et al. (2014) known as the *probability of deflection* or $P(D)$ method.

7.2.2 Probability of Deflection $P(D)$

Vernstrom et al. (2014) derived the differential source counts using the Probability of Deflection or $P(D)$ (Scheuer, 1957) method directly from VLA images. The technique makes the assumption that each pixel within the dirty map contains the sum of sources that are detected throughout the entire synthesised beam. Thus if the point spread function is known exactly, as well as the noise characteristics of the image, then it is possible to derive the differential source counts directly without ever counting any individual sources (Condon, 1984). The result is a prediction of the total number density to a much deeper sensitivity than would be otherwise possible using traditional counting techniques. Their findings (shown in Figure 7.18) cannot as yet determine whether the sources are AGN or SFG and it therefore remains for astronomers to estimate the ratios of SFG to AGN sources using traditional counting techniques from high angular resolution imaging. It is noted by Vernstrom et al. that the derived differential source counts compare well with the model proposed by Condon in 1984 which is built on the premise that the source counts are equal to the sum of two classes of galaxies, AGN and SFGs. They also noted that clustering of sources (achieved by simulation) makes no significant difference to the predicted source counts. A comparison of the Vernstrom result with the *e*-MERGE differential source counts can hence be used to provide an estimate of the number of sources omitted within each flux density bin.

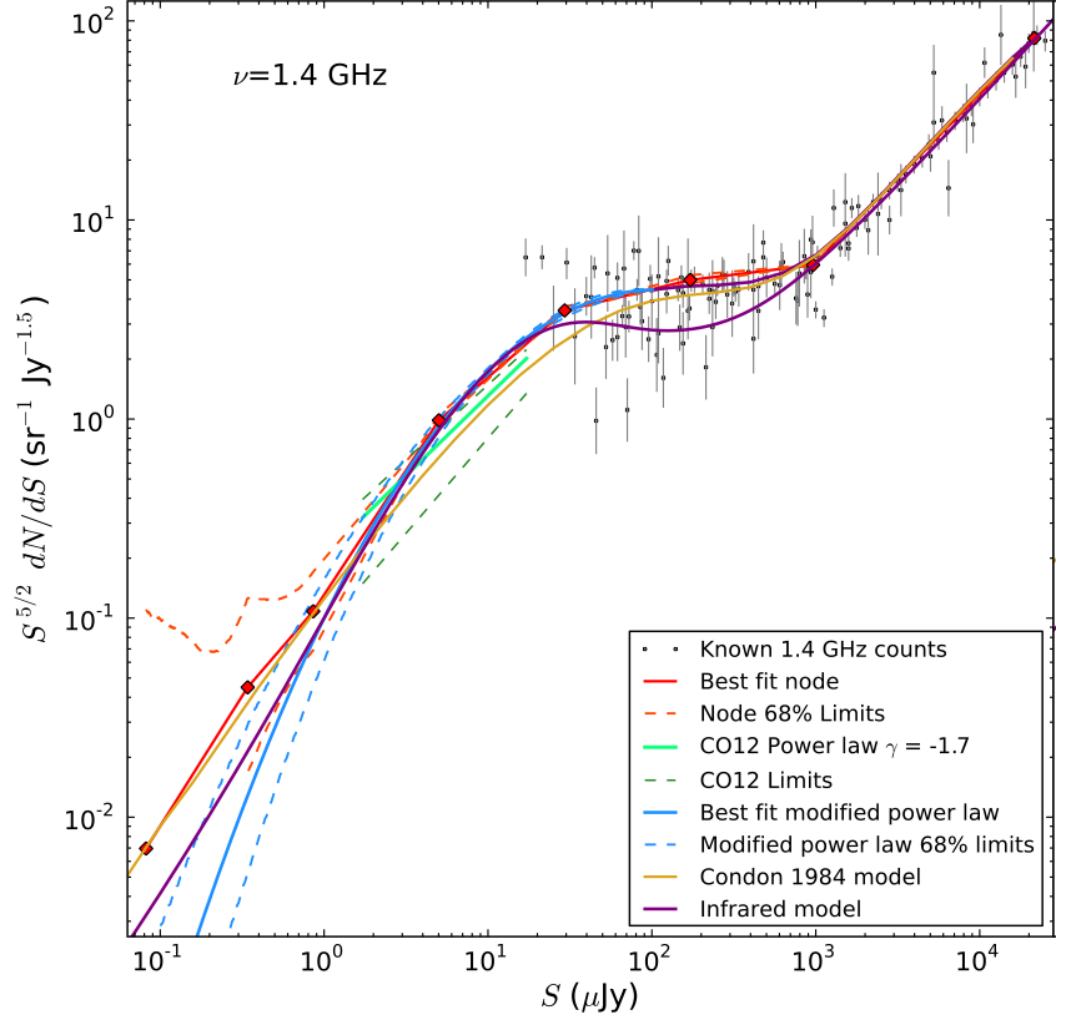


Figure 7.18: The total differential source counts calculated at 1.4GHz using $P(D)$ analysis of 3 GHz VLA data (transformed to L-band) taken from (Vernstrom et al., 2014). The widely scattered results of other studies are also plotted in black for reference as well as the predictions of other models. The 'best fit node' line represents the total expected differential source counts from all sources from the $P(D)$ measurement.

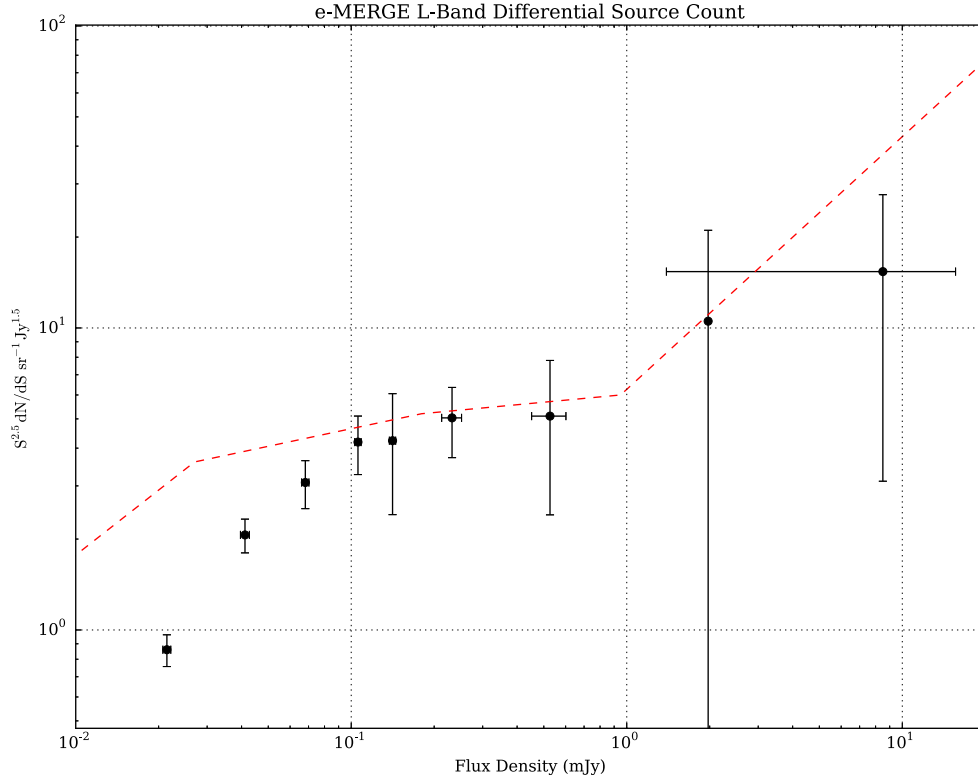


Figure 7.19: The *e*-MERGE L-band differential source counts compared with the Vernstrom $P(D)$ analysis (dashed line) reveals some scatter with a general count loss.

The comparison (Figure 7.19) indicates that a greater number of sources have been omitted at the lowest flux density ranges, as anticipated. This is attributed to a combination of incomplete uv sampling and insufficient depth to measure each source. There is also likely be a loss in sources at the upper flux density range due to the very small survey area. The Vernstrom $P(D)$ prediction lies well above the 1σ error bars for measured *e*-MERGE counts in the lowest flux density bins and therefore cannot be attributed to a simple error in flux measurement or normal scatter. The *e*-MERGE survey is therefore considered to be incomplete, an expectation that will persist until the bulk of the observations have been made. For the time being the Vernstrom analysis provides an estimate of the number of sources omitted from the *e*-MERGE data and hence the necessary correction factors. The three lowest flux density points lie outside the error bars and hence correction factors for them are derived by dividing values into the $P(D)$ result (see Table 7.1). It is obvious that this will cause those values to

Flux Density Bin (μJy)	Number Count Correction Factor from $P(D)$
20 - 30.0	2.8
30.0 - 56.8	1.9
56.8 - 85.9	1.4

Table 7.1: *e*-MERGE number count correction factors derived from a comparison to the results of [Vernstrom et al. \(2014\)](#).

automatically agree with the $P(D)$ prediction. However, an assumption is made here that these correction factors can be applied equally to the separated source counts: AGN and SFG SVM classifications. These corrected and separated populations (see Figure 7.20) can then be compared with luminosity evolution models.

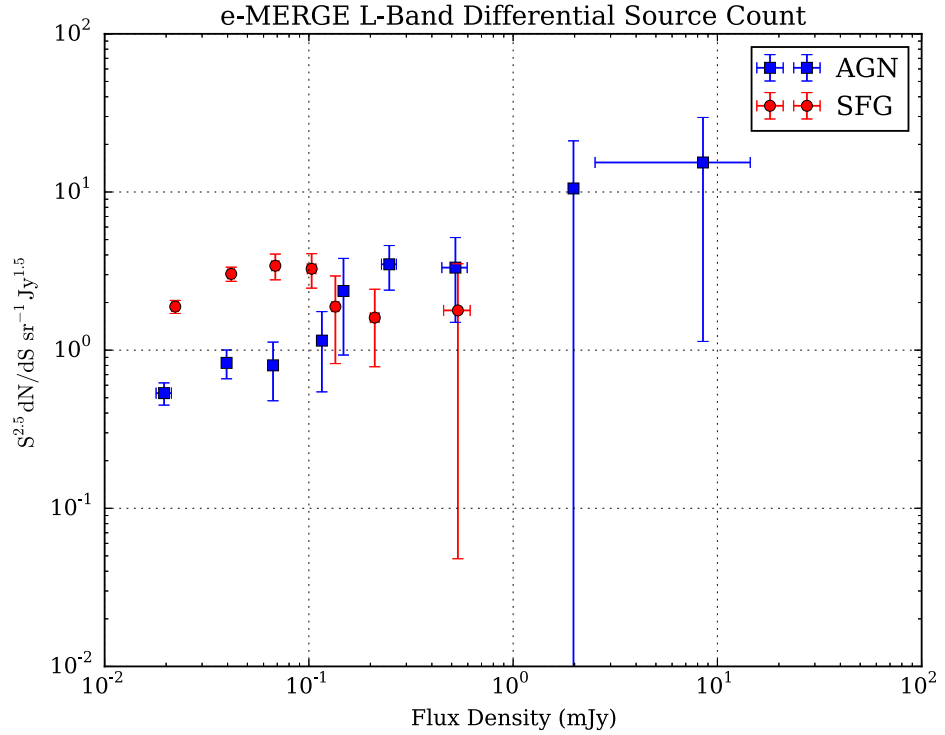


Figure 7.20: Corrected *e*-MERGE differential source counts from SVM separated along the SVM bisect. The counts at low flux densities have been corrected such that the sum of each bin is equal to the results of the Vernstrom $P(D)$ analysis.

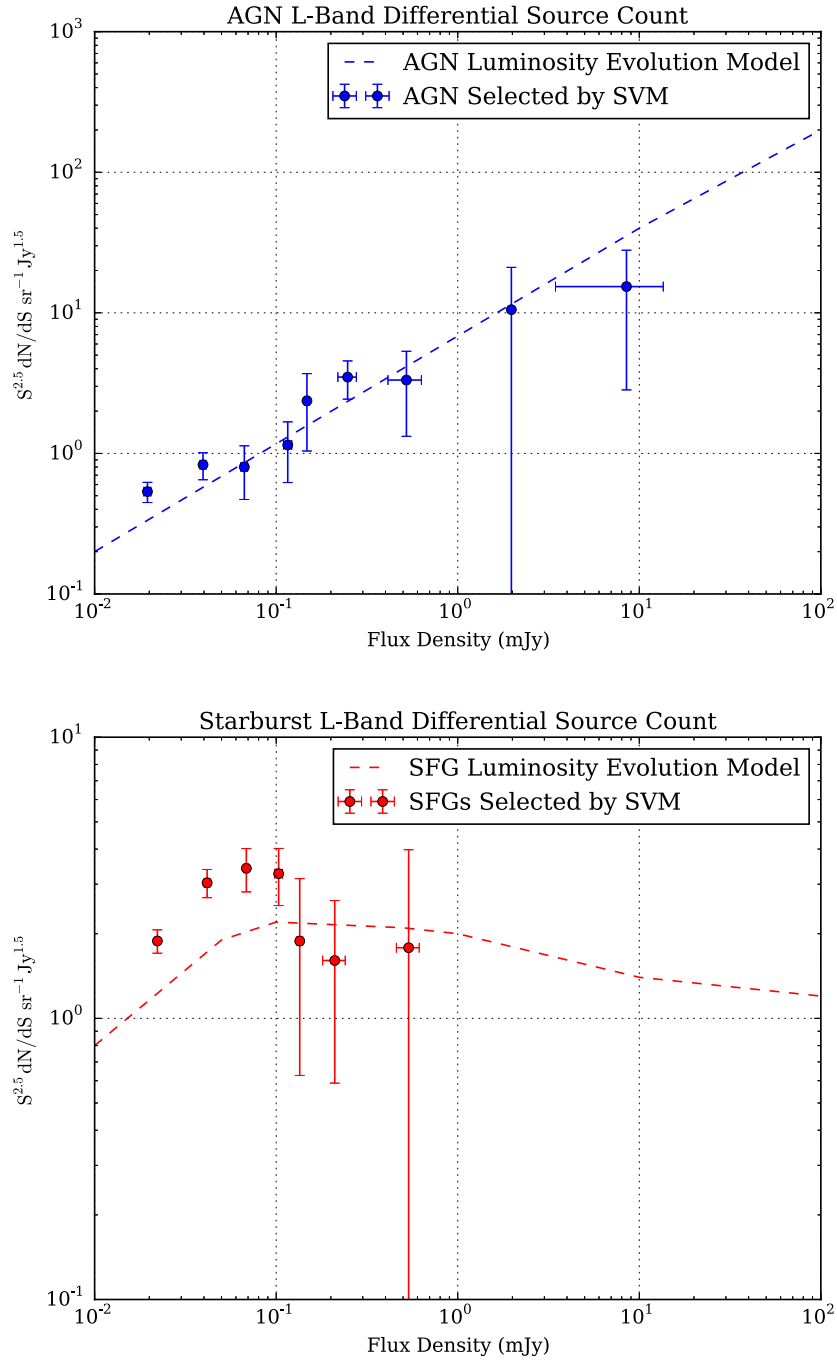


Figure 7.21: Corrected differential source counts for *e*-MERGE galaxies crudely separated into AGN or SFG dominated categories at the SVM bisect. These count corrected points are compared with example luminosity evolution modelling predictions made by [Seymour et al. \(2004\)](#) with a luminosity evolution of $Q = 3.3$.

7.2.3 Deriving Probabilities from SVM Data

Dividing the source counts into two groups using the crude method of 'either-or' neglects the probabilistic reality of classifying galaxies. It does not allow for the likelihood that a single galaxy may include a combination of both emission mechanism components, or that interlopers have strayed and have been erroneously identified. There is an increasing body of evidence that all galaxies contain embedded AGN that may be in active or quiescent states (de Zotti et al., 2010). To take these possibilities into account it is necessary to assign a probability based upon the certainty of each classification. The machine learning method enables this if the SVM score can be correctly calibrated. This is possible given the assumption that the original training set has a high number uncontaminated AGNs and SFGs. These can be plotted separately as a function of their SVM assigned scores and Gaussian distributions fitted representing a continuous probability distribution (see Figure 7.22).

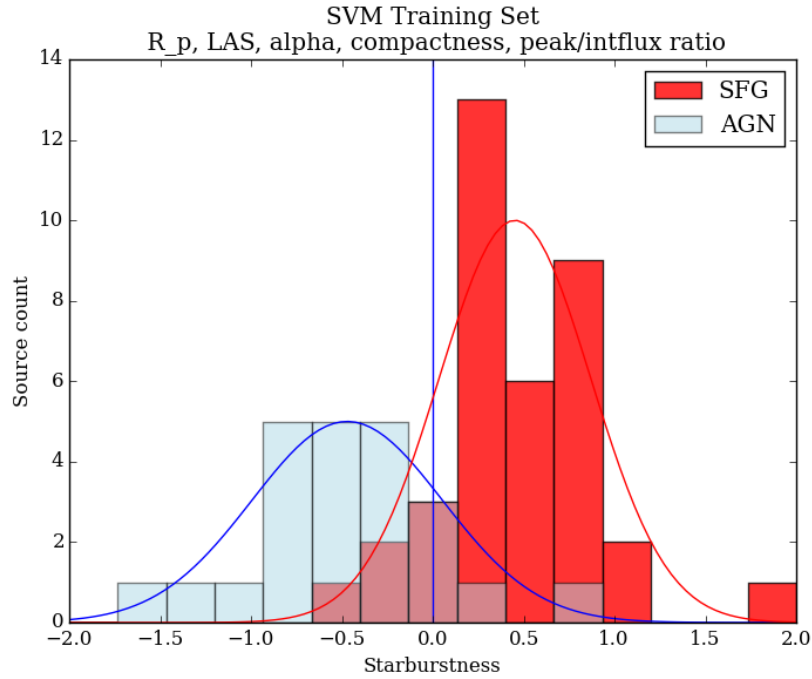


Figure 7.22: Fitting Gaussian Distributions to the Training Set to Determine Source Probabilities.

Once Gaussians are fitted to each of the two categories, then the probability of a source being either an AGN or a SFG can be determined directly from its score. The probability of a source being an AGN is related to the ratio of the Gaussians, G , at

each score point:

$$P_{\text{AGN}} = \frac{G_{\text{AGN}}}{G_{\text{AGN}} + G_{\text{SFG}}} \quad (7.5)$$

and of being SFG:

$$P_{\text{SFG}} = \frac{G_{\text{SFG}}}{G_{\text{AGN}} + G_{\text{SFG}}}$$

which generates the probability curves illustrated in Figure 7.23. A brief comparison of a key attribute (the LAS) with selected AGN probability does not produce an obvious size correlation as there is considerable overlap in angular size and galaxy type.

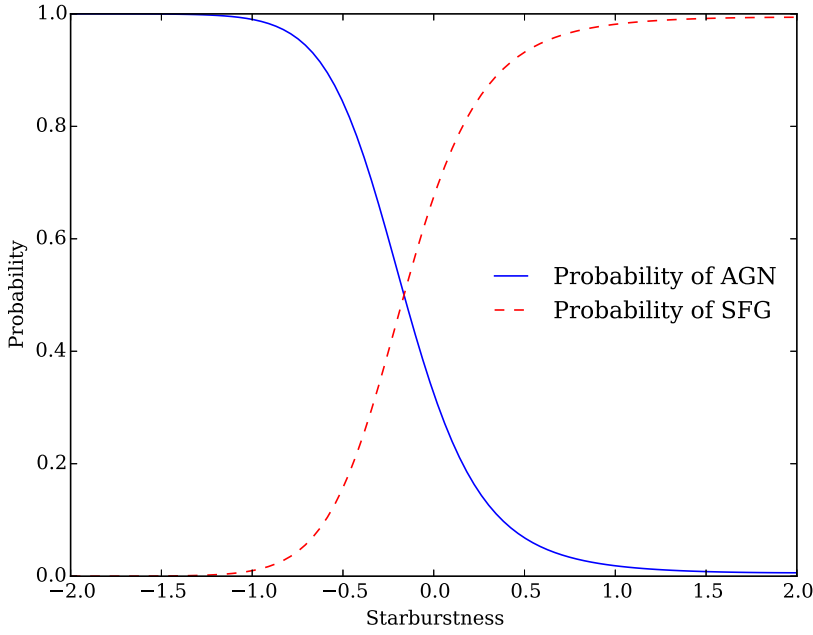


Figure 7.23: Probability of AGNs and SFGs from Calibrated *Starburstness Scores*.

The probabilities are used to modify the differential source counts by examining each source and assigning a weighting fraction to the count. In this way a source with a high positive 'starburstness score' retains its count, but one with a low score, close to the interloping bisect for example, becomes down-weighted near to 50%, and those with negative scores yield an even smaller contribution. This method removes the sharp binary problem of assigning classifications and instead each source retains elements of both such that when they are binned together the total source counts remain unchanged. It is now possible to present the components of the entire population of measurable galaxies and compare them with differential number count simulations.

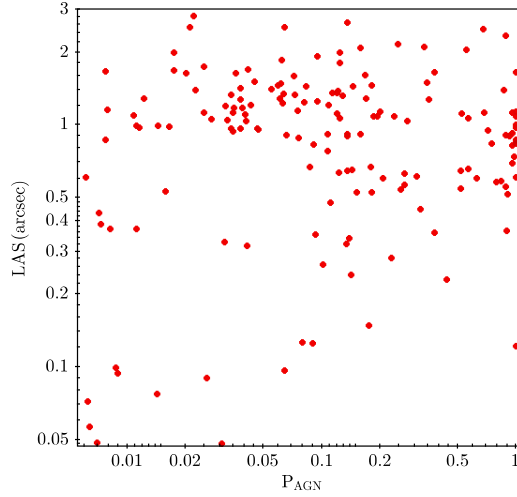


Figure 7.24: Probability of AGN vs LAS does not alone produce a direct correlation.

7.2.4 Comparison with simulations

The differential source counts can now be presented as *SFG components* and *AGN components* separately for comparison with simulations which sum to yield the results of the Vernstrom P(D) study. The simulations here are based upon parameterised luminosity functions of actual observations. It has been historically simpler to determine the luminosity functions of AGNs at higher redshifts due to their larger intrinsic luminosities, although some uncertainty still remains at the lowest flux densities. The shape at the brightest end of the differential source counts however is well characterised and has been parameterised as a function of redshift being split into both steep spectrum and flat spectrum components, i.e. the AGN jets/lobes and the AGN cores. The following describe the density of sources between luminosities L and $L + dL$:

$$\phi(\text{steep}) \left[\frac{L}{L_{\star}(z)} \right] = 10^{-6.91} \left\{ \left[\frac{L}{L_{\star}(z)} \right]^{0.69} + \left[\frac{L}{L_{\star}(z)} \right]^{2.17} \right\}^{-1}, \quad (7.6)$$

where $\text{Log} L_{\star}(z) = 26.22 + 1.26z - 0.286z$. For the flat spectrum core AGNs:

$$\phi(\text{flat}) \left[\frac{L}{L_{\star}(z)} \right] = 10^{-8.15} \left\{ \left[\frac{L}{L_{\star}(z)} \right]^{0.83} + \left[\frac{L}{L_{\star}(z)} \right]^{1.96} \right\}^{-1}, \quad (7.7)$$

where $\text{Log} L_{\star}(z) = 26.36 + 1.18z - 0.28z^2$ (Rowan-Robinson et al., 1993). A differential

source count simulation for the AGN was constructed based upon the above luminosity functions by generating a virtual survey, taking into account the current Λ CDM cosmology (see Figure 7.25). A 'concentric shell' technique for building the simulation can be summarised as follows:

- The Universe is divided into hundreds of small redshift interval shells Δz from $z = 0.0001$ to $z = 5$.
- The co-moving volume is computed for each Δz .
- The luminosity functions above are used to derive the density of galaxies between L and $L + \delta L$ by cycling through all luminosities within realistic ranges ($10^{20} - 10^{35} \text{W Hz}^{-1}$) with intervals δL .
- The densities ϕ are converted into the number of sources by multiplication of the co-moving volume determined by Δz .
- The sources are converted into flux densities using the luminosity distance relationship.
- The process is repeated for both types of AGN.
- The sources are binned according to their flux densities.

The binned sources are then converted to differential source counts and Euclidian normalised to a survey area of 1 steradian. The simulation allows freedom to change the luminosity evolution parameters as necessary. The simulation could be extended to include the SFGs using a Schechter function but this is deferred until after the AGN comparison. The simulated AGN steep and flat spectrum differential source counts are presented in Figure 7.26. Comparing the simulation of the AGN counts with the probability weighted *e*-MERGE counts (see Figure 7.27) reveals remarkably good agreement.

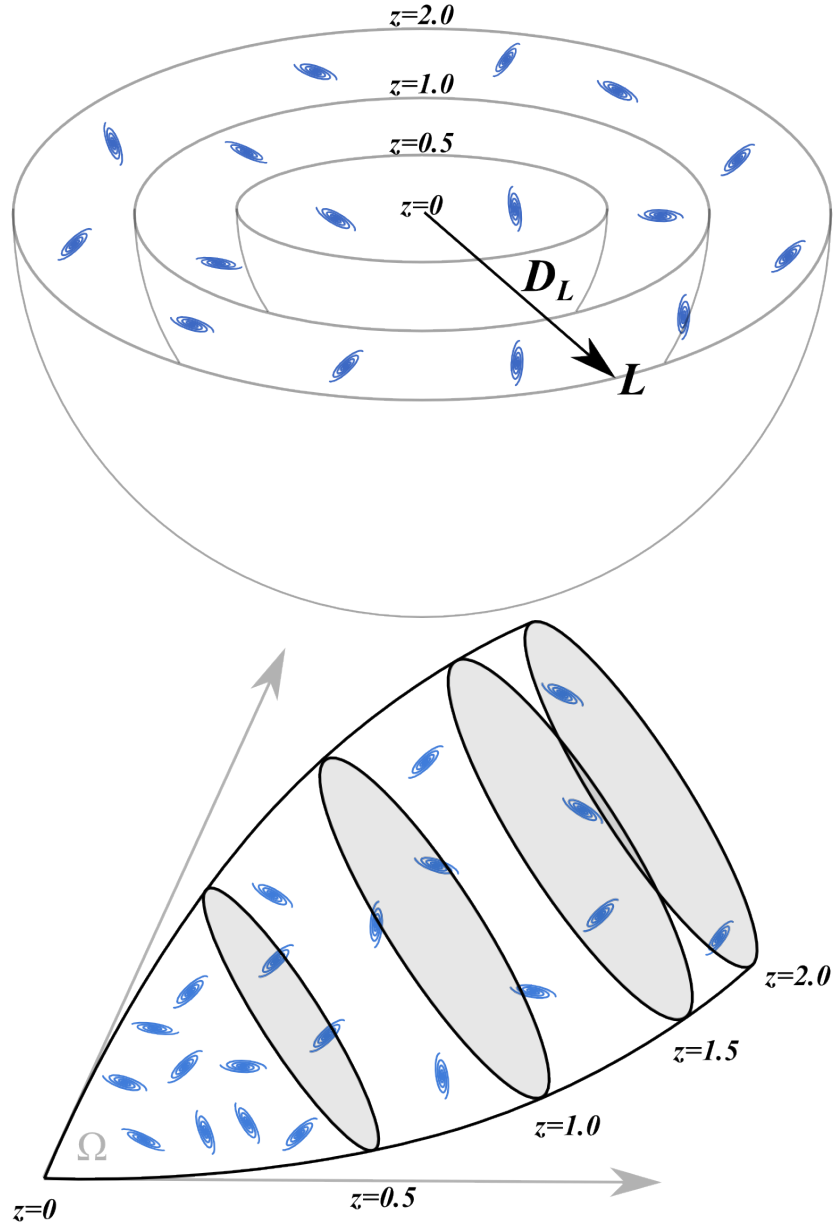


Figure 7.25: The simulation of number counts requires co-moving volumes to be calculated for each redshift interval, based upon cosmological parameters. The flux density S of the spread of luminosities is determined using the luminosity distance D_L . Co-moving volumes are calculated for each redshift interval to determine the spatial density of sources per Mpc^3 . A ΛCDM model is assumed and thus assumed to be embedded in the Hubble flow. The simulation is isotropic (top) but normalised to a survey cone of 1 steradian (bottom).

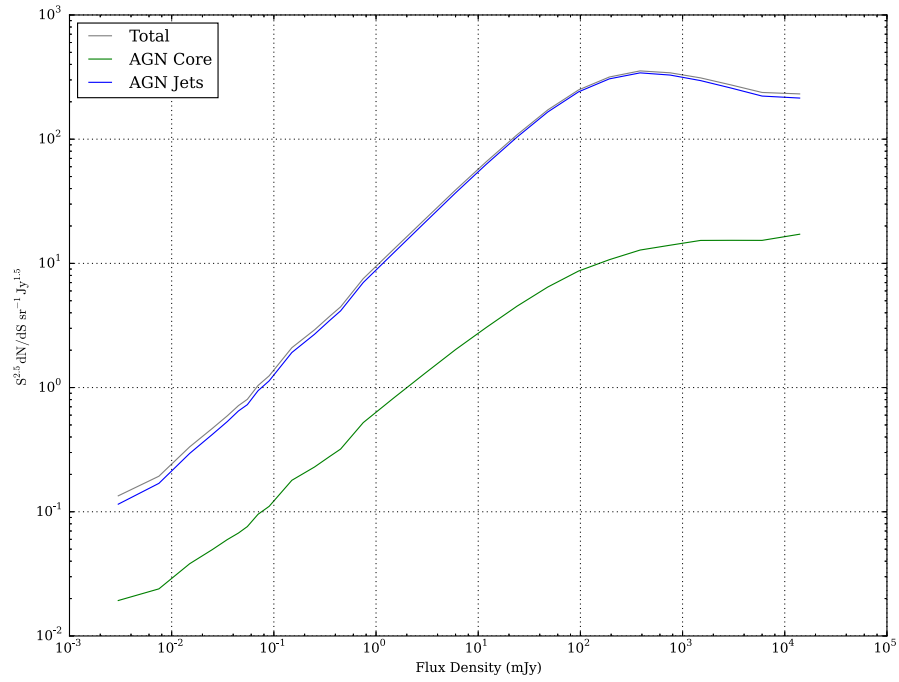


Figure 7.26: The results of the simulation of the AGN differential source counts using existing luminosity functions for both jets/lobes and cores. The jets/lobes dominate the number counts.

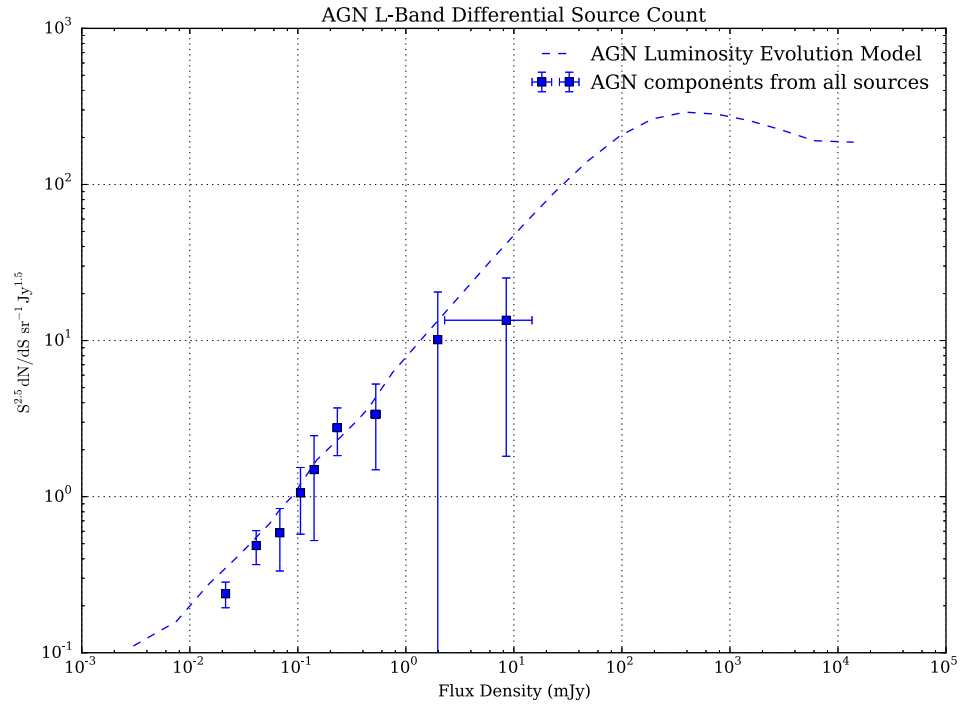
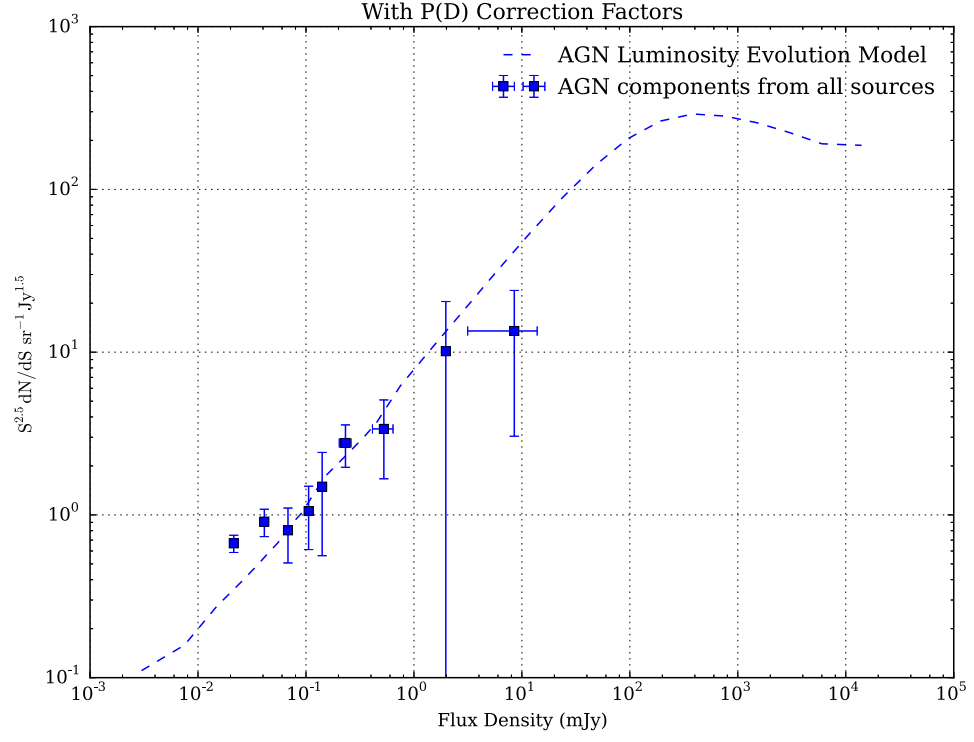


Figure 7.27: Comparison of the probability weighted *e*-MERGE AGN component counts with the AGN simulation. Top: With $P(D)$ correction factors. Bottom: Without $P(D)$ correction factors.

The two lowest flux bins between $20\mu Jy$ and $58\mu Jy$ appear to deviate from the simulation when the correction factors are applied. This could be interpreted as one, or a combination, of factors:

- Though based upon observed AGN luminosity functions, the simulation is incorrect as it fails to include an apparent sudden upturn in the AGN population at low flux densities ($< 60\mu Jy$).
- The simulation is essentially valid, and the correction boosting based upon the $P(D)$ result is not applicable to the AGN population, meaning that the AGNs are all well represented even at the lowest flux densities.

If the simulation is false at low flux densities then the upturn in the population of AGN would point to a new population of 'radio quiet' AGN, previously undetected. However, a combination of the two factors may be the most probable explanation, as it seems unreasonable to assume that *all* AGN components have been detected, but it is also not unreasonable that even more spatially extended SFGs have been omitted. If the AGN figure is replotted without any Vernstrom correction factors, then one finds that the counts are slightly lower than the simulation, which indicates that the latter is the more likely explanation. The SKA Simulated Skies (S3) semi-empirical model based upon [Wilman et al. \(2008\)](#) includes such a radio-faint population of AGN (see Figure 7.28).

The reason for the large scatter, observed in numerous studies (plotted in Figure 7.18), has often been attributed to calibration errors between surveys, omission of sources or simply errors in measurement that are either underestimated or overestimated. It is also likely to be a result of incorrect correction factors used to offset the count omissions. To compensate the corrective boosting, the SFG population would need to be boosted further, however there is no certain way of deciding from the present data just how the correction factors should be proportioned.

If the Vernstrom $P(D)$ predictions are assumed to be accurate, at least within these flux densities, then the SFG counts must be equal to the difference between the true AGN component counts and the $P(D)$ result, plotted in Figure 7.29. Retaining the equally proportioned correction factors shows that the results so far from the *e*-MERGE survey are in general agreement with the residual between the Vernstrom $P(D)$ result and the AGN differential source counts.

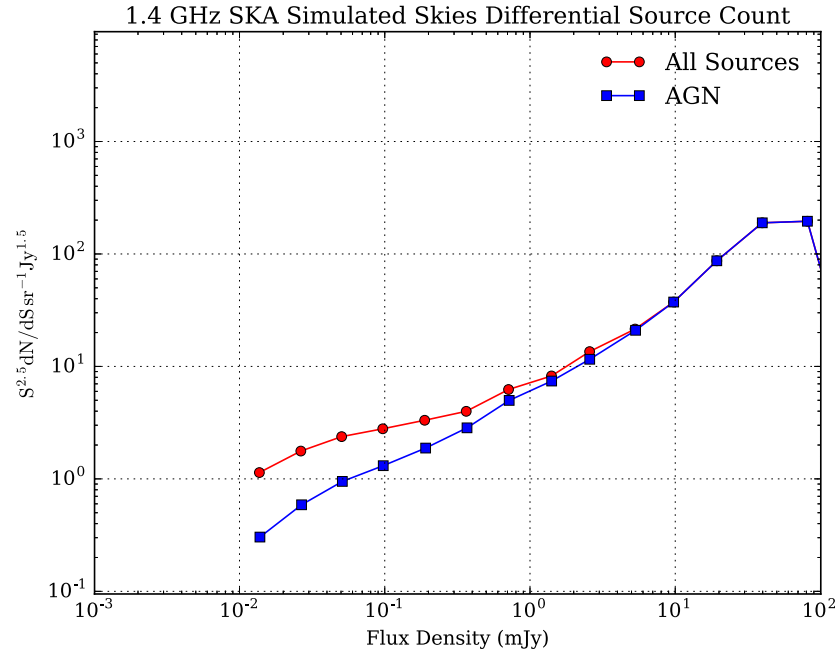


Figure 7.28: The S-Cubed Simulation includes a radio faint population of AGN.

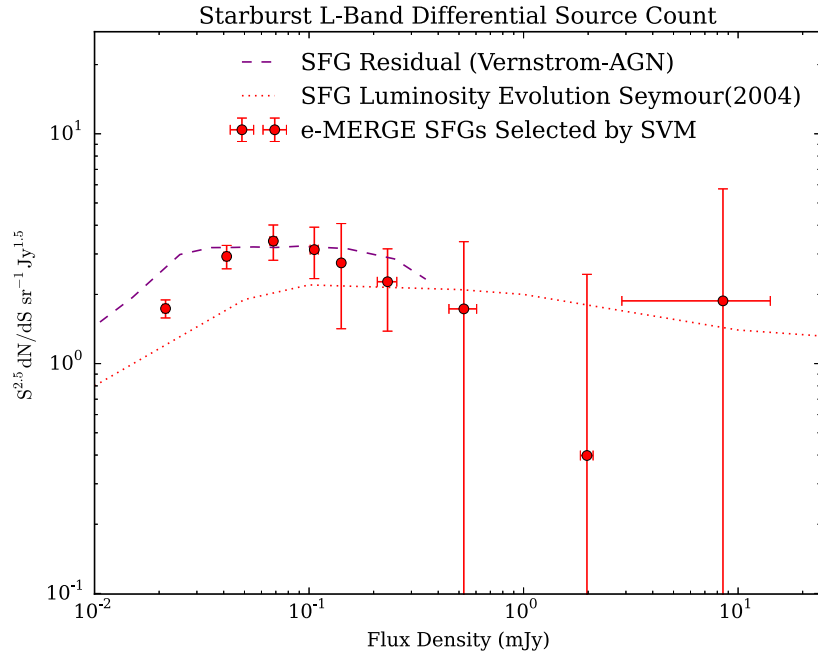


Figure 7.29: *e*-MERGE source counts based upon SFG components derived from SVM probabilities. The residual of the AGN counts from the Vernstrom $P(D)$ result is plotted for reference as well as evolution modelling from [Seymour et al. \(2004\)](#).

Comparing this with the SFG evolution models obtained previously, a general underestimate in the amount of luminosity evolution in the starburst population has been assumed. Models perturbing a Schechter function by a multiplication of $(1+z)^Q$ could perhaps be regarded as over-simplistic, as for the case of AGN it is probably more appropriate that a complicated redshift dependent function should be assumed, although the degeneracy between density and luminosity evolution make this difficult to fit with the present data. Pure luminosity evolution historically yields values of Q anywhere between 2 and 4.1 (Seymour et al., 2004). These first results from the *e*-MERGE survey would tend one to lean towards the higher luminosity evolution values in SFGs which more greatly affect lower flux densities and increase the relative proportion of SFGs over AGNs. This is because SFGs are generally more extended than AGN sources. Only with increasing numbers of characterisable sources, to be obtained when the *e*-MERGE survey matures, will this question be closer to a more robust resolution.

7.2.5 Comparison with other methods of classifying sources

Another method of classifying radio sources is based upon the radio-FIR correlation described in Chapter 1, which relies on the tight correlation in the observed fluxes in the radio and IR in star forming regions of galaxies. Those galaxies that differ significantly in accepting flux ratios are often attributed a non-star forming mechanism of emission. Source emission exhibiting an excess in radio flux compared with its IR counterpart is attributed to non-star forming processes. A useful quantifier of the amount of correlation between the radio and IR flux is the Q -factor introduced in Chapter 1. This can be plotted for all sources used in this study with classification probabilities labelled. One of the problems with the $q24$ classification method is, particularly, in cases of very low flux density (such as those examined in this study), for which the correlation appears to be less robust (Beswick et al., 2008), although there could be errors in flux density measurement. Those radio-faint AGN that are omitted from being identified as AGN by $q24$ hence require morphological classification. The plots in Figure 7.30 illustrate that whilst several bright AGN would appear to be obvious candidates, there are many more which would, due to their lack of radio excess flux densities, not be so obvious. It is therefore necessary to obtain high resolution radio imaging in all cases. Only a fully integrated multi-attribute sample of radio data can yield a classification, and even then only a statistical one.

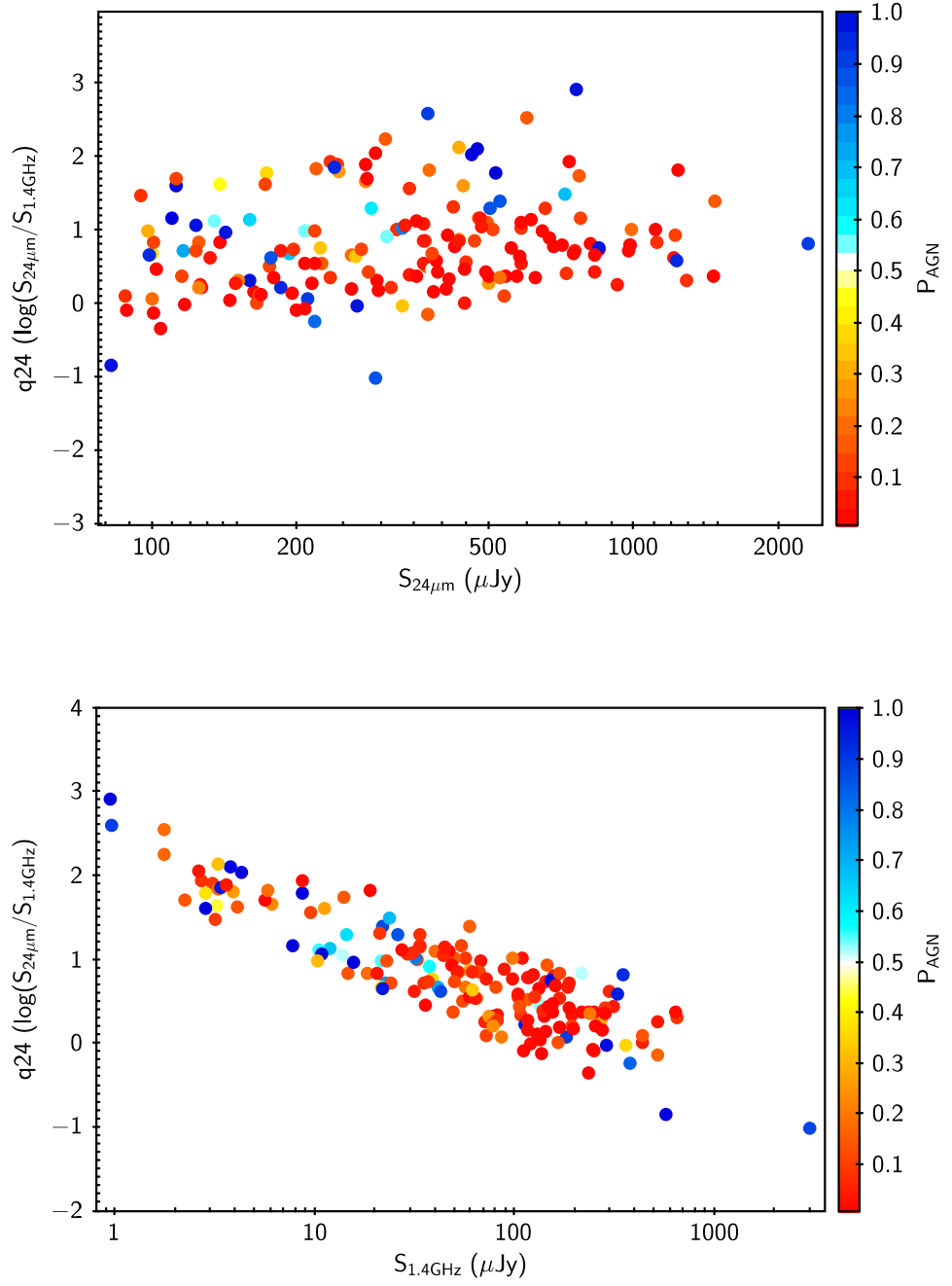


Figure 7.30: Q24 plots demonstrate that attributing classification based on FIR/Radio correlation alone can lead to a number of omissions and is considered a blunt discriminator tool for the radio-faint population. Incorporating morphological characteristics decreases the probability of miscategorising sources.

7.3 Luminosities and star formation rates

Luminosities can be derived from the integral flux density measurements obtained directly from the *e*-MERGE survey, provided that the distance (i.e. redshifts) for sources are known. Luminosities can be used to derive *Star Formation Rates* (SFR), capitalising on the radio-FIR correlation (Lisenfeld et al., 1996), using relationships developed by Rowan-Robinson et al. (1993); Hopkins et al. (1998) and others to transform the radio luminosities into *supernova creation rates* which can be extrapolated using an *Initial Mass Function* (Salpeter, 1955; Kroupa, 2001; Chabrier, 2003) into SFRs (Cram et al., 1998; Haarsma et al., 2000). This assumes that the Radio-FIR relationship is valid at high redshift for which there is some evidence (Garrett, 2002). The SFR per unit (co-moving) volume was first plotted for large samples of galaxies by Madau (1998), in which a non-varying source SED was assumed to derive a luminosity to convert to a SFR for each galaxy. This was followed up more recently by Hopkins (2007); Seymour et al. (2008) who adopt a Λ CDM cosmology,² correcting for the expansion of the Universe to obtain the SFR per co-moving volume measured in $M_{\odot}\text{yr}^{-1}\text{Mpc}^{-3}$.

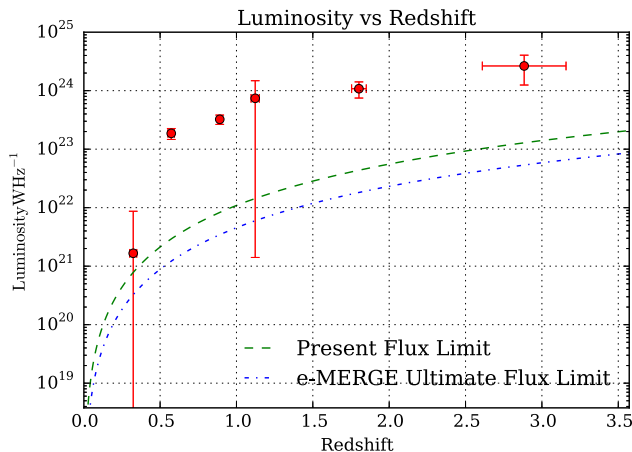


Figure 7.31: The mean L-band luminosity of SFGs plotted against redshift. The scatter in sources is represented by the error bars, revealing several outliers clearly under-sampled in flux density.

²The Lambda Cold Dark Matter (Λ CDM) model of the Universe includes a cosmological constant to produce an accelerating expansion but is geometrically 'flat' i.e. $\Omega_{\Lambda} + \Omega_M + \Omega_k = 1$ where $\Omega_k = 0$.

7.3.1 Star Formation Rates

The star formation rate can be estimated directly from the L-band luminosities using the assumptions described in Chapter 1 (Section 1.2.4) utilising Equation (1.19). Using this methodology SFRs were determined for sources binned by redshift and yield the star formation rates presented in Figure Figure 7.32 on page 219.

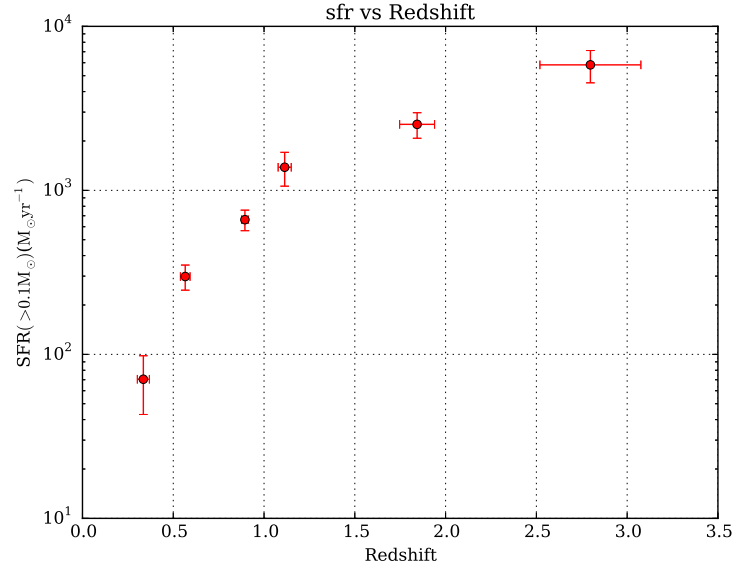


Figure 7.32: The Starburst SFR Plotted against Redshift.

The star formation rate is perhaps better presented as a global space density so that it can be compared as a function of cosmic time. Indeed, one of the primary goals of the *e*-MERGE survey is to determine the star formation history of the Universe, a non-trivial problem, but it is logical to assume that the star formation rate peaked at some cosmic epoch. However, the degeneracy between cosmological parameters and the evolution of galaxies is an obstacle that requires astronomers to either:

- Assume a cosmology of the Universe and derive the star formation rate or galaxy evolution parameters, or
- Assume the nature of galaxy evolution to help derive cosmological parameters such as expansion rates.

This calculation is perhaps premature but a SFR global density plot has been calculated by determining a co-moving volume in which to bin sources within redshift intervals.

The incompleteness of redshift information available at the present time for the field is however a significant obstacle. The Λ CDM model is adopted here using the following cosmological parameters: $h = 0.7$, $\Omega_M = 0.3$ and $\Omega_\Lambda = 0.7$, which determine the expansion rate and defines the comoving volume intervals.

The total star formation rate per unit volume of space is determined by summing *all* the SFRs and dividing by the comoving volume that they are embedded within (the 'Hubble flow'). This is calculated using the luminosity distance and angular size relationship (Hogg, 1999).

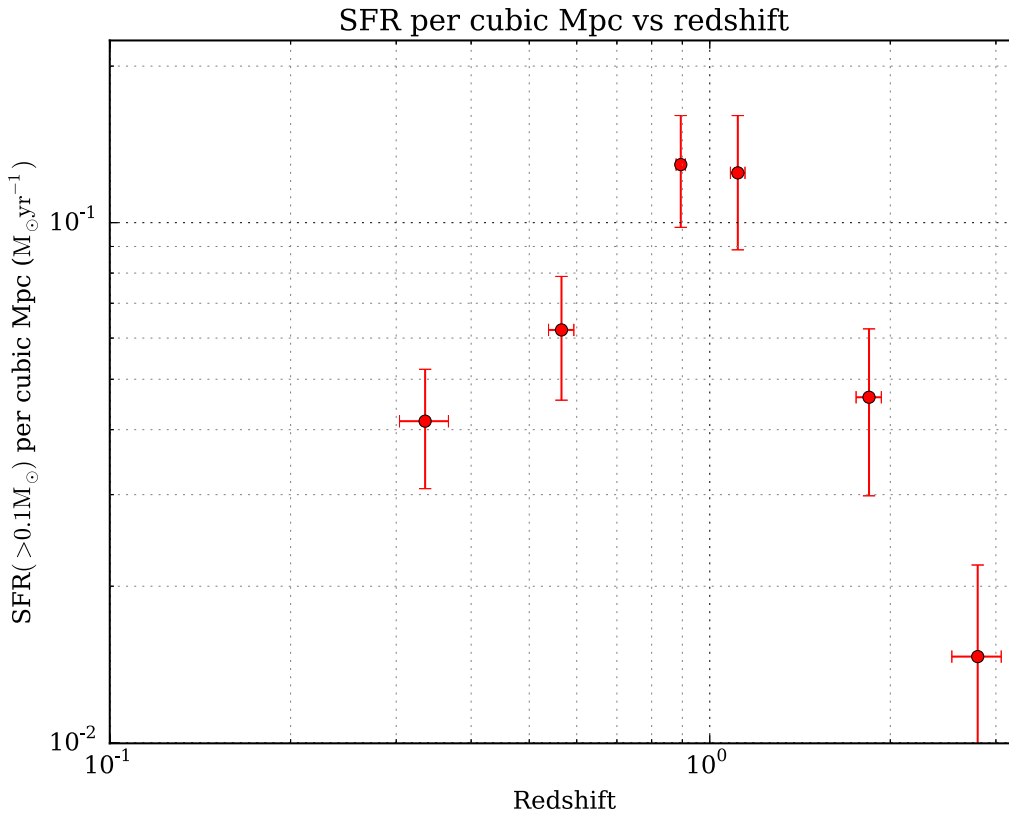


Figure 7.33: *e*-MERGE uncorrected star formation rates per comoving volume omitting numerous high-redshift sources. The final plot is must be deferred until the *e*-MERGE survey matures.

There will exist a number of correction factors that need to be applied in the future to the SFR per unit volume plot shown in Figure 7.33 to account for the number of sources lost at high redshifts. The generation of a global density SFR plot can in principle be derived by extrapolation of the integrated Schechter function over V_C from

L_{min} to L_{max} with an ever increasing L_{min} as a function of redshift. If it is assumed that there is no density evolution in the SFG population (and only luminosity evolution), then the number density ρ of sources will not change per co-moving volume, V_C , and the luminosities of galaxies can be calculated as a function of redshift. The calculation is therefore deferred until the SFR evolution is more robustly determined.

7.4 Summary

The high angular resolution of the *e*-MERLIN observations has led to the development of a classification methodology, using robust designations of sources from previous GOODS-North studies to train an SVM machine learning algorithm. The number of sources that could be classified robustly using this technique was 248 out of a total of 340 VLA detected sources $> 20\mu\text{Jy}$. 70% of classifiable sources ($T_f > 2.5\sigma$) are determined to be SFG dominated ($P_{SFG} > 0.5$), an increase over previous studies, and revealed by component separated differential source counts which statistically trace the component emission on a probabilistic basis.

An estimate of the number of sources omitted at low flux densities, derived from $P(D)$ comparisons, yields correction factors ranging between 1.4 and 2.8. Equally distributing the correction factors to both AGN and SFG dominated sources revealed agreement with AGN source count simulations with the exception of the very lowest flux densities. It is more likely, it is argued from the extended nature of SFGs, that the correction factor applies to an increase in the number of starburst galaxies at the lowest flux densities. SFRs for SFG sources with associated redshifts were derived and a preliminary SFR density plot generated, although a robust result will not be available until the *e*-MERGE survey matures.

Chapter 8

Conclusions and Future Work

In this thesis, various new and existing methodologies have been developed to process the first tranche of observations from the *e*-MERGE survey. Not only do these methods generate the deepest radio images ever produced of the GOODS-North region, they demonstrate that the *e*-MERLIN array, complemented by vital observations by the JVLA, is well placed to unravel the star formation contribution of the sub-mJy population of deep field galaxies, a key objective of the *e*-MERGE survey. The new techniques have enabled a rapid but comprehensive analysis of this first set of data. These methodologies act as a roadmap for the remaining observations of the *e*-MERGE survey and include both the image processing stages as well as deep field analysis using machine learning. This chapter summaries both the innovative technical developments and the results from the first analyses of the data products, including:

- Wide-Band Primary Beam Correction.
- High-Speed Wide-Band Wide-Field Imaging.
- Source Extraction using Largest Angular Size.
- Source Angular Size Distribution.
- Galaxy Classification using Support Vector Machine Learning.
- SFG Linear Size Measurement.
- Comparison to Galaxy Luminosity Evolution Modelling.

8.1 Technical Innovations

8.1.1 Wide-Band Primary Beam Correction

In Chapter 3 a method was developed to simulate the primary beam of an inhomogeneous array of telescopes based upon aperture illumination projections. The full bandwidth of the array is taken into consideration to generate an integrated or frequency dependent beam function. This technique was applied to the *e*-MERLIN array to generate a primary beam model for L-band, and can be extended to simulate the beam at any *e*-MERLIN band, or for that matter any other non-homogeneous array (including the European VLBI Network for example). The model is used to determine parameters for automatic beam correction within the latest version of the *e*-MERLIN pipeline.

The relative sensitivity weighting for each telescope can be adjusted which, due to the inhomogeneity of the array, alters the resulting primary beam, with the largest influence on the beam-shape being the sensitivity weighting of the Lovell telescope. Future extensions to the model will include dynamic weighting to provide optimisation of baseline sensitivities as a function of time. The utilisable primary beam width of the *e*-MERLIN array, with the Lovell telescope included, is nominally 15 arcmin at L-band using recommended relative telescope sensitivity weightings. The primary beam prediction is used within the high speed imaging technique, summarised below.

8.1.2 High-Speed Wide-Field Wide-Band Imaging

Chapter 3 also included the development of a high-speed wide-band wide-field imaging technique to produce rapid imaging from large wide-band datasets. This can mitigate the effects of *w*-projection limitations, and confusion due to bright outlying sources, as well as the induced spectral index due to the relative differences in primary beam across the field of view as a function of observing frequency. The resulting methodology is up to two orders of magnitude faster than conventional deconvolution techniques that consider these effects. The caveats include a small, quantifiable, increased level of smearing within the image. However, so long as the width of the image is chosen with care, smearing distortions can be kept acceptably small. The routine is incorporated into the latest version of the *e*-MERLIN pipeline, and has already been used to produce wide-field maps not only for this project but also for the SuperCLASS project for

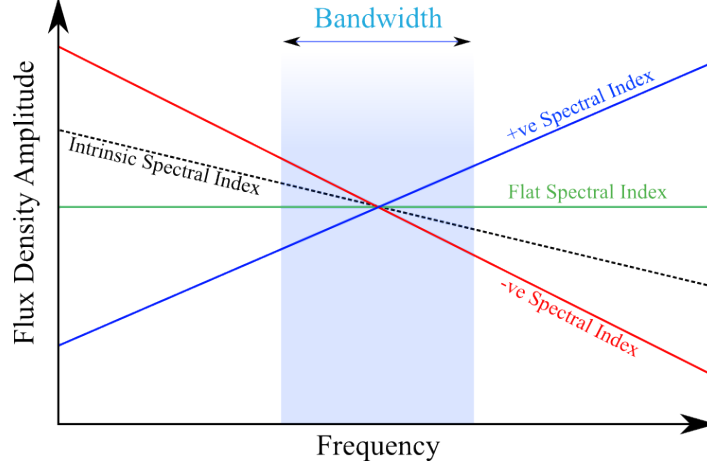


Figure 8.1: Spectral representation of the generation of 3 maps with 3 differing assumed spectral index optimisations. Fitting for the minimum measured amplitude error yields a way to derive the intrinsic spectral index for each source relatively quickly.

cataloguing purposes. Its application is expected to be used in all wide-field *e*-MERLIN projects as a method of generating extremely rapid results.

Planned future refinements will address sub-optimal cleaning due to the varying intrinsic spectral indices of sources, which was not considered a priority at this early stage in the project. The effect can be taken into account by repeating the deconvolution using three different assumed spectral indices and adjusting the synthesised beam for each spectral window accordingly, on top of the synthesised beams already modified to account for the primary beam spectral correction.

Deconvolution with an incorrect spectral index assumption leads to incomplete cleaning and hence an increase in flux density within the side-lobes, resulting in a proportional decrease in the peak amplitude of the source (i.e. an amplitude error). Measuring the amount of negative flux within the side-lobes therefore provides a measure of the amplitude error. At least three maps are required, each assuming a different intrinsic spectral index, to remove the possibility of degeneracy in solutions. The spectral index of the source can be derived by interpolation if the dependency can be understood. This is best investigated by simulation. The imaging time is increased, but will still remain significantly shorter than alternative methods. The proposed method is illustrated in Figure 8.1, in which the intrinsic spectral index of the example source could be derived from the amount of amplitude error. For example, the amplitude error in the maps derived from flat and negative spectral indices would appear comparable, whereas the amplitude error in the map derived assuming a positive spec-

tral index would appear significantly larger. This will not generate an optimised image, merely knowledge of how to re-clean each source optimally, or to adjust the derived flux density in each source.

8.1.3 Source Classification using Support Vector Machines

The application of a machine learning method to determine the likely classification of sources in the field was successfully tested. The motivation for machine assisted classification is summarised below:

- Minimise human bias from individual source classification which has hindered past surveys.
- Permit the future classification of thousands of sources rapidly.
- Remove binary type classification of galaxies and replace it with a probabilistic quantifiable result.

The number of galaxies in the sample was small enough to examine by visual inspection. Instead of representing each source with a binary style classification, i.e. AGN or SFG, a probability is now attached to each source based upon the score value derived from the SVM methodology and comparison to the training set. This has both statistical and physical justification because sources may have characteristics of both types of emission, or have morphologies that cause interloping.

Consequently, it became possible to include star formation component emission from almost every measurable galaxy in the field (galaxies with very low P_{SFG} values having negligible contributions) and statistically should produce a more robust picture of star formation history. Differential source count comparisons revealed excellent agreement with luminosity function models (when normalised to the latest $P(D)$ predictions), which increased confidence in the classifications produced. It is the intention that the methodology be applied to the *e*-MERGE survey when observations reach maturity.

8.2 First *e*-MERGE Data Products

The application of the methodologies described in Chapter 3 have enabled the generation of the first wide-field maps from the *e*-MERGE survey at L-band. These

data, in combination with the legacy MERLIN+VLA data, have generated a wide-field map some 15 arcmin in diameter with a sensitivity at the pointing centre equal to $2.4\mu\text{Jy/bm}$. These data, in combination with data taken from the JVLA in both L-band and C-band, have enabled measurements of the sub-mJy population of galaxies at high angular resolution, including angular sizes, classification by morphology and source count statistics.

8.2.1 Source Size Distribution

The source size distribution was analysed in two stages: the legacy data was at first examined to determine the size distribution of the brightest 178 sources in the field (Wrigley et al. in prep.) and, with subsequent addition of the first tranche of *e*-MERGE data, this was increased to a total of 248 sources that had good detections ($T_f > 2.5\sigma$).

Selecting sources on the basis of their probable classification reveals that the median source size increases with increasing certainty of SFG components, with sources with $P_{SFG} > 0.5$ accounting for almost 70% of all measurable sources. The median Largest Angular Size at L-band of all 248 measurable sources in the 15 arcmin *e*-MERGE field is:

- $\theta_{\text{median}}\{S_L > 20\mu\text{Jy}\} = 1.05 \text{ arcsec}$ with a peak near to 0.75 arcsec.

Using sub-sets based upon probability of SFG components alters the median LAS:

- $\theta_{\text{median}}\{P_{SFG} > 0.5\} = 1.115 \text{ arcsec}$, for 173 sources, and,
- $\theta_{\text{median}}\{P_{SFG} > 0.9\} = 1.178 \text{ arcsec}$, for 100 sources.

The angular size of sources influences the design of future surveys, and in particular the instruments that can probe with the required angular resolutions. Given that the peak angular sizes for the whole population lie between 0.5 and 0.75 arcsec, a radio interferometer with synthesised beam sizes between 0.1 and 0.25 arcsec would be desirable to extract morphological information. In comparison, Phase 1 of the SKA project will have nominal angular resolution around 0.6 arcsec at L-band, and will be unable to morphologically resolve these sources for classification purposes.

8.2.2 Linear Size of Sources

The largest angular sizes of sources were used in combination with redshift information where available, to determine the linear size of SFG dominated sources in the field. These were determined, using Λ CDM cosmology ($\Omega_M = 0.3, \Omega_\Lambda = 0.7, h = 0.7$), to be in the range of 4 -11 kpc, i.e. within the optical extent of galaxies.

8.2.3 Prevalence of increasing numbers of SFGs at Lower Flux Densities

Using a combination of probabilistic source selection from SVM, differential source counting and semi-empirical sky simulations, using the first data products from the *e*-MERGE survey, this study appears to confirm the increasing prevalence of Starburst galaxies at lower flux densities ($> 20\mu\text{Jy}$), indicated by an increase in luminosity evolution in the SFG population. Although the amount of evolution is not yet quantified it appears larger than previous predictions. A small increase in the AGN population is also observed in the $20 - 60\mu\text{Jy}$ range, but this only exists with the application of correction factors derived from $P(D)$ studies, and may be biasing the results. Until the remaining *e*-MERGE observations have been taken, this remains an outstanding question.

Appendix I

Source Attributes

The following tables describe key attributes collected from all sources examined. They include sources that could not be classified but are included for completeness. Redshifts, where available, have also been included, sourced from [Barger et al. \(2008\)](#) and others. An extended electronic version of the table, including peak flux densities, source peak positions and other metrics, is available.

Source	$Prob_{AGN}$	$T_f(\sigma)$	α	σ_α	$S(\mu Jy)$	$\sigma_S(\mu Jy)$	$R_p(arcsec)$	LAS(arcsec)	z
123547+621151		3.0	-1.96	0.37	37.2	5.3	0.28	1.13	
123547+621354	0.882	3.0	-1.31	1.57	49.8	3.1	2.35	1.0	
123548+621058	0.033	3.8	-0.39	0.09	67.6	4.8	1.05	1.13	
123549+621513	0.13	3.75	1.37	2.91	51.5	4.2	0.17	1.13	
123549+621537	0.158	3.8	0.7	0.31	68.4	5.2	0.71	1.13	
123550+621041	1.0	1.5	-0.94	15.04	2.7	2.3	0.03	0.13	
123551+621457	0.036	3.75	-1.13	0.09	63.0	3.8	1.64	1.25	
123553+620930		3.75	-0.31	2.4	28.2	4.2	0.67	1.13	
123553+621037	0.042	3.0	-1.29	0.37	27.1	3.3	1.7	1.25	
123553+621338	0.39	3.8	-1.05	0.46	35.5	4.2	1.02	1.0	
123554+621043	0.065	3.0	-1.99	0.34	230.7	13.2	2.54	1.5	
123554+621337	0.206	3.75	-1.56	0.12	28.4	4.0	0.6	0.88	0.881
123555+620902	0.868	3.8	-1.14	0.07	169.4	4.1	1.61	0.88	
123555+621506	0.0060	3.75	-3.36	4.77	18.0	4.8	0.07	2.5	
123556+621556	0.954	3.8	0.77	0.18	40.9	3.9	0.82	1.5	
123558+621354	0.013	3.75	-2.21	0.35	36.6	3.3	0.18	1.0	
123558+621537	0.043	3.8	-1.02	0.06	180.0	4.6	1.21	0.88	
123559+620952	0.0090	3.75	-3.39	3.89	26.1	5.2	0.08	1.13	
123560+621537		3.8	-1.35	7.5	546.8	30.4	6.07	0.13	
123560+621550	0.021	3.8	-1.64	0.06	637.8	35.6	2.54	1.5	
123600+621047	0.136	3.8	-0.51	0.06	112.5	3.8	0.92	1.0	2.002
123600+621053	0.01	3.75	-3.35	2.46	28.0	5.0	0.12	1.13	
123602+621126	0.044	3.8	-0.3	0.07	90.5	3.3	0.64	1.0	0.913
123603+620947	0.041	3.8	-0.63	0.13	37.6	4.3	1.11	1.13	
123603+621111	0.06	3.8	-1.05	0.06	124.5	3.5	1.47	1.0	0.638
123604+620812	0.716	3.8	0.35	0.12	60.2	5.1	0.95	1.0	
123604+621620	0.076	3.8	-0.98	0.11	82.0	3.9	0.88	1.25	
123605+621552	0.012	3.75	-1.66	0.64	29.4	3.3	0.98	1.38	
123606+621003	0.021	3.75	-1.01	0.24	24.7	3.6	1.17	1.25	
123606+621148	0.175	3.75	-3.65	2.62	16.6	4.4	0.02	0.63	
123607+620951	0.277	3.8	-0.94	0.06	165.1	6.0	1.04	0.88	0.6379
123607+621021	0.145	3.8	0.16	0.17	69.1	5.5	0.52	1.0	2.33
123607+621329	0.194	3.8	-0.75	0.09	69.2	4.0	1.09	1.0	0.4353
123607+621551		3.75	-2.68	1.76	14.7	3.6	0.68	1.38	
123608+621036	0.927	3.8	-0.6	0.06	190.4	5.2	0.9	0.38	0.681
123608+621543	0.0070	3.75	-4.04	4.26	24.4	4.7	0.05	0.88	
123608+621553	0.237	3.8	-1.21	0.14	44.0	3.8	1.09	0.75	0.4593
123609+621144	0.335	3.75	-1.17	0.1	74.2	3.7	2.1	1.13	
123609+621251		3.75	-3.31	0.85	22.0	3.6	0.08	1.13	
123609+621431	0.542	3.75	0.05	1.33	21.2	3.9	0.57	1.13	0.8495
123609+621435	0.04	3.0	-1.77	0.15	102.8	5.2	2.42	1.63	

Source	$Prob_{AGN}$	$T_f(\sigma)$	α	σ_α	$S(\mu\text{Jy})$	$\sigma_S(\mu\text{Jy})$	$R_p(\text{arcsec})$	LAS(arcsec)	z
123609+621436	0.019	3.0	-1.79	0.18	211.0	10.6	2.55	1.75	
123610+621350	0.018	3.75	-2.53	33.05	11.7	4.3	1.5	1.0	
123610+621422	0.0090	3.75	-2.07	0.13	26.6	3.4	0.09	1.13	
123611+620811	0.07	3.8	-0.69	0.2	50.8	4.0	0.54	1.25	
123611+621421	0.246	3.75	-1.41	0.13	83.9	4.1	2.15	1.13	
123611+621652	0.091	3.8	-1.19	0.06	89.3	3.8	1.87	1.25	
123612+620900	0.272	3.0	-1.23	0.15	97.2	5.2	2.69	1.5	
123612+621139	0.552	3.75	0.23	0.09	59.6	3.0	2.04	1.25	0.275
123612+621140	0.0060	3.8	0.34	0.21	39.6	3.9	0.61	2.5	0.275
123612+621439	0.035	3.0	-2.47	3.54	13.1	4.2	1.13	1.0	
123612+621619	0.0	3.75	-3.72	1.72	31.1	4.0	0.12	1.63	
123615+621135	0.024	3.0	-2.27	13.4	22.3	4.9	0.76	1.13	
123616+620643	0.083	3.8	-0.48	1.9	45.7	4.6	0.29	1.0	
123616+620946	0.143	3.8	-0.86	0.42	36.7	4.3	0.65	1.0	1.263
123616+621008	0.683	3.75	-0.36	0.68	20.9	3.6	0.53	1.13	0.337
123616+621108	0.139	3.8	-0.61	2.14	27.8	4.0	0.34	1.13	
123616+621514	0.108	3.75	0.52	0.91	39.2	3.8	0.49	1.0	3.61
123617+620703	0.064	3.8	-2.26	33.73	126.6	7.4	2.09	1.25	
123617+621011	0.108	3.8	-0.63	0.09	46.4	5.2	0.92	1.0	0.845
123617+621530	0.018	3.75	-1.95	0.08	23.3	2.9	0.02	0.88	
123617+621551	0.0090	3.75	-2.92	0.71	17.3	3.7	0.1	1.88	
123618+621541	0.785	3.8	-0.22	0.06	215.4	5.1	0.58	0.38	1.993
123618+621551	0.355	3.8	-1.08	0.05	143.6	4.1	1.27	0.5	1.87
123618+621635	0.032	3.75	-1.52	2.11	21.7	4.8	1.26	1.63	0.679
123619+621004	0.025	3.0	-2.07	0.18	27.0	4.0	1.74	1.25	
123619+621253	0.039	3.8	-1.21	0.05	74.7	3.5	1.18	0.88	0.473
123620+620639	0.038	3.75	-1.26	0.17	38.1	4.2	1.54	1.13	
123620+620844	0.49	3.8	-0.71	0.06	121.2	4.6	1.65	1.0	1.0178
123620+621238	0.047	3.75	-2.18	0.49	15.1	2.9	0.07	1.25	
123620+621730	0.955	3.0	-2.59	32.1	20.9	4.1	1.12	0.88	
123621+620711	0.01	3.75	-1.34	0.18	47.2	5.3	0.06	1.13	1.1497
123621+621109	0.021	3.8	-1.13	0.15	54.3	5.0	0.69	1.38	1.014
123621+621208	0.256	3.75	-1.17	3.85	13.4	5.0	0.54	1.63	
123621+621618	0.061	3.8	-2.65	1.07	25.5	4.8	0.44	1.13	0.6813
123621+621708	0.642	3.8	-0.39	0.07	152.7	4.9	0.52	0.63	1.993
123622+620654	0.998	3.8	-0.5	0.06	261.0	5.4	1.66	0.38	
123622+621545	0.687	3.75	-0.91	0.2	29.8	3.8	1.13	1.25	0.6471
123623+620946	0.226	3.8	-0.92	0.09	44.8	4.5	1.66	1.13	0.7479
123623+621346	0.042	3.75	0.79	2.39	26.6	4.4	0.32	1.5	
123623+621527	0.877	3.8	-0.07	0.14	36.2	3.5	0.91	1.13	2.583
123623+621630	0.034	3.8	-1.33	0.06	67.4	4.7	1.34	1.0	2.4
123623+621755	0.0080	3.75	0.67	1.34	40.5	3.8	0.37	2.25	
123624+620649	0.951	3.8	0.44	0.18	42.1	3.9	0.9	1.25	
123624+621017	0.132	3.8	-1.97	0.12	283.5	13.0	2.57	1.25	
123624+621643	0.979	3.8	-0.65	0.05	400.2	6.3	0.66	0.38	1.918
123624+621837	0.014	3.75	-3.53	5.72	20.1	4.2	0.08	1.25	
123625+621548	0.013	3.75	-2.74	0.32	20.3	3.7	1.34	0.88	
123625+621743	0.084	3.8	-0.32	0.18	64.6	4.1	0.6	1.0	
123625+621911	0.055	3.0	-1.16	0.29	27.6	4.2	0.99	1.0	
123626+620602	0.896	3.75	-1.01	0.11	21.3	3.0	0.07	0.88	
123627+620606	0.024	3.75	-1.36	0.15	35.1	3.8	0.03	0.88	
123627+620835	1.0	3.8	-0.09	0.29	35.4	3.9	1.09	1.0	1.4653
123629+620616		3.75	-2.39	2.74	38.3	4.6	0.98	1.25	
123629+621046	0.078	3.75	-1.33	0.05	282.7	12.2	3.58	1.88	1.013
123629+621614	0.0080	3.8	-3.6	8.49	16.5	3.9	1.66	1.38	
123630+620646	0.895	3.75	-0.8	39.72	22.3	5.1	0.37	0.75	0.798
123630+620851	0.011	3.75	-2.43	0.13	38.0	4.1	0.99	0.88	0.84
123630+620924	0.346	3.8	-0.96	0.14	34.6	4.0	1.49	0.88	0.953
123631+620958	0.038	3.8	-1.23	0.05	139.5	3.6	0.97	1.0	
123631+621114	0.062	3.8	-1.31	0.17	21.4	3.9	1.49	1.38	1.0124
123632+620644	0.107	3.75	0.96	0.45	39.9	3.5	0.78	1.38	
123632+621105	0.994	3.8	0.89	1.11	26.2	4.1	0.49	0.63	
123632+621604	0.983	3.75	-2.45	3.96	13.4	0.8	2.74	1.88	
123632+621659	0.022	3.75	-2.19	7.56	33.8	1.8	2.83	3.13	0.437
123632+621715	0.899	3.0	2.52	41.42	23.3	3.6	0.32	1.0	
123633+620621	0.045	3.75	-2.93	4.22	16.7	5.0	0.04	1.38	
123633+620760	0.02	3.8	-1.66	0.12	63.3	4.8	1.64	1.5	1.9939
123633+620835	0.151	3.75	-0.06	0.35	28.5	4.6	0.53	1.25	
123633+621409	1.0	3.0	-0.82	0.42	16.7	3.4	0.85	1.25	

Source	$Prob_{AGN}$	$T_f(\sigma)$	α	σ_α	S(μ Jy)	$\sigma_S(\mu$ Jy)	$R_p(\text{arcsec})$	LAS(arcsec)	z
123634+620628	0.013	3.75	-2.12	0.19	41.0	4.7	0.03	0.88	
123634+621006	0.012	3.8	-2.08	0.09	29.8	4.1	1.29	1.25	1.016
123634+621213	0.095	3.8	-1.54	0.04	128.3	4.5	1.93	0.88	0.456
123634+621241	0.055	3.8	-1.27	0.04	131.2	3.9	1.4	0.75	1.219
123634+621401	0.517	3.8	-0.78	0.3	19.6	3.5	0.55	1.0	
123634+621419	0.27	3.75	-3.36	5.22	12.2	3.3	0.01	0.25	
123634+621431	0.011	3.75	-3.47	2.37	18.5	4.0	0.11	1.13	
123634+621433	0.045	3.0	-3.01	4.1	103.0	4.1	2.39	1.25	
123635+621224	0.072	3.0	-1.48	0.22	21.0	4.3	1.6	1.13	
123635+621421	0.101	3.75	-0.31	1.91	22.5	3.0	0.27	1.0	
123635+621628	0.061	3.75	-0.75	0.09	38.1	4.0	1.29	1.25	
123635+621924	0.061	3.8	-0.87	0.1	78.9	3.6	1.05	1.0	
123635+621926	0.069	3.8	-1.07	0.16	64.3	4.5	0.98	1.13	
123636+620704	0.442	3.75	-1.4	24.6	21.1	4.8	0.5	0.88	
123636+620707	0.0070	3.75	-6.22	173.85	17.6	5.7	0.04	1.0	0.276
123636+620708	0.0070	3.75	-3.68	1.05	28.4	4.1	1.19	1.0	0.952
123636+621155	1.0	3.0	-0.45	0.65	2.7	1.8	3.09	1.75	
123636+621424	0.158	3.8	-0.7	0.06	45.7	3.6	0.92	0.75	2.011
123636+621436	0.0070	3.8	-3.86	1.05	29.9	3.5	0.44	1.13	1.018
123637+620852	0.075	3.8	-0.98	0.06	59.7	3.7	1.15	0.88	
123637+621135	0.938	3.75	-2.25	0.44	30.9	2.2	2.7	2.88	
123637+621320	0.028	3.8	-1.47	0.07	46.3	4.1	1.27	1.13	
123638+621117	0.032	3.75	-0.19	3.64	23.1	4.8	0.33	1.25	
123638+621747		3.0	-0.47	0.56	350.0	17.5	4.8	1.38	
123640+621029	0.941	3.0	-2.02	1.06	115.2	4.7	3.86	1.13	
123640+621250	0.0060	3.75	-2.52	0.09	37.8	3.4	0.06	1.13	
123641+621011	0.367	3.8	-0.2	0.08	38.2	4.1	1.59	1.38	1.958
123641+621129	0.013	3.75	-1.89	0.14	19.8	2.8	0.02	1.25	
123641+621833	0.882	3.8	-0.6	0.06	308.8	5.7	0.57	0.25	1.1456
123642+620948	0.266	3.8	-0.5	0.07	68.9	3.7	0.63	0.88	0.518
123642+621331	0.834	3.8	-0.76	0.04	409.8	5.8	0.59	0.25	4.424
123642+621546	1.0	3.8	-0.5	0.05	165.5	3.9	1.14	1.13	0.857
123642+621720		0.0	0.4	1.38	2.5	3.1	0.25	0.13	
123642+621722	0.12	3.0	-0.88	0.09	25.8	3.2	1.12	0.75	
123643+620934	0.124	3.8	-0.82	0.12	36.5	4.2	1.07	1.13	
123643+620959	0.851	3.75	-0.69	5.87	16.3	3.7	0.15	0.5	
123644+621133	0.998	3.8	-0.46	0.04	694.2	12.0	1.59	12.0	1.05
123644+621250	0.038	3.0	-1.23	0.06	25.3	3.8	1.42	1.13	
123644+621451	0.438	3.8	0.52	3.11	31.8	4.3	0.23	1.0	2.095
123644+621706	0.179	3.75	-0.81	3.71	20.9	4.7	0.67	1.25	
123645+621901	0.041	3.75	-1.87	0.76	39.7	4.1	1.04	1.0	
123646+620754	0.144	3.75	-0.65	0.08	44.2	3.9	1.45	1.13	1.433
123646+620825	1.0	0.0	0.44	0.31	3.0	2.7	0.75	0.38	
123646+621405	0.898	3.8	-0.01	0.05	257.6	6.5	0.52	0.38	0.961
123646+621449	0.129	3.8	-1.11	0.04	100.9	3.5	1.33	1.0	1.7
123646+621527	0.011	3.75	-2.01	0.06	33.9	4.1	0.37	1.13	0.8511
123646+621630	0.036	3.8	-1.01	0.05	90.7	4.1	1.68	1.25	0.502
123646+621940	0.07	3.75	-0.16	0.09	36.2	3.7	1.36	1.38	
123647+620833	0.035	3.8	-0.89	0.06	74.5	3.8	0.95	1.0	0.9712
123647+621049	0.023	3.8	-2.68	3.4	17.0	4.0	1.4	1.38	0.94
123647+621227	0.998	0.0	-3.41	2.18	12.5	3.8	0.0	0.0	
123647+621446	0.098	3.75	-1.68	0.05	174.9	6.6	2.17	1.38	
123648+620633		3.0	-0.51	1.22	19.2	3.6	0.91	1.13	
123648+621120	0.256	3.0	-2.22	113.2	14.1	4.5	0.33	0.63	
123648+621426	1.0	3.75	-2.21	9.26	14.7	3.5	0.98	1.25	
123649+620922	0.998	3.75	-0.14	0.05	11.2	3.7	0.12	0.88	
123649+620932	0.065	3.75	-3.96	5.78	12.1	3.6	0.1	1.38	0.517
123650+620738	0.516	3.8	-0.25	0.06	266.8	3.9	0.65	0.38	1.6095
123650+620802	0.436	3.8	1.51	3.58	28.2	3.8	0.2	1.63	0.559
123650+620845	0.087	3.8	-0.61	0.08	78.8	4.2	0.67	1.13	0.434
123650+621313	0.158	3.8	-1.48	0.05	137.5	4.3	2.08	1.0	0.475
123651+620529		3.75	1.14	1.91	46.0	4.5	0.25	1.0	
123651+621031	0.035	3.8	-1.12	0.05	79.9	4.1	1.18	1.0	0.41
123651+621052	0.731	3.75	-2.31	0.45	16.7	3.1	0.77	0.38	
123651+622017		3.75	-0.53	3.37	35.8	3.9	0.52	1.88	
123652+620644	0.0080	3.75	-1.61	0.09	48.1	3.5	0.0	1.13	
123652+621221	0.063	3.8	-0.83	0.05	56.1	3.7	1.23	1.38	2.7
123652+621226		3.75	-2.36	9.0	13.4	4.1	1.6	1.0	1.0857192464
123652+621504		3.0	-3.0	4.27	15.1	3.6	1.57	1.5	

Source	$Prob_{AGN}$	$T_f(\sigma)$	α	σ_α	$S(\mu\text{Jy})$	$\sigma_S(\mu\text{Jy})$	$R_p(\text{arcsec})$	LAS(arcsec)	z
123653+620647	0.013	3.75	-3.31	5.32	22.5	4.4	0.08	1.0	
123653+621140	0.111	3.8	0.01	0.13	60.5	4.0	0.48	1.0	1.275
123653+621355	0.382	3.0	-0.79	0.1	11.0	3.9	1.66	1.13	
123653+621444	0.855	3.8	0.12	0.04	174.6	4.3	0.67	0.38	0.321
123653+621808	0.048	3.8	-0.51	0.06	78.1	3.8	0.96	1.0	0.253
123654+620548		3.0	-2.03	3.95	34.1	4.2	1.67	1.13	
123654+620745	0.114	3.8	-0.31	0.07	49.4	3.9	1.36	1.25	0.2022
123655+620535	0.011	3.8	-1.28	0.14	59.2	5.5	1.1	1.38	
123655+620804	0.011	3.75	-3.57	0.77	19.9	3.8	0.04	1.13	
123655+620819	0.18	3.75	-0.73	0.26	26.7	3.9	0.53	0.88	
123656+620808	0.045	3.8	-1.24	0.06	97.6	5.2	1.51	1.0	0.792
123656+620917	0.025	3.8	-1.12	0.05	68.7	3.8	1.13	1.13	0.419
123656+621938		3.8	0.53	1.46	35.4	3.4	0.28	1.0	
123657+621208	0.548	3.8	-0.4	0.2	32.6	3.5	0.74	1.0	
123657+621408	0.016	3.75	-2.1	0.11	18.6	3.5	0.04	0.88	
123657+621513	0.043	3.8	-1.41	0.14	22.1	3.6	1.12	1.13	
123658+620958	1.0	3.75	-0.72	0.25	8.7	1.4	4.19	0.25	
123658+621455	0.066	3.0	-0.36	0.07	27.9	2.5	0.91	1.0	
123659+620932	0.011	3.8	-1.23	0.18	24.1	3.7	0.95	1.38	
123659+621833	0.883	3.8	-0.89	0.06	4400.5	63.6	0.56	0.25	
123700+620910	0.978	3.8	-0.69	0.05	281.0	6.1	0.74	0.38	
123700+620952	0.047	3.75	-1.11	0.17	28.8	4.6	0.97	1.0	
123700+621450	0.124	3.75	-1.27	0.07	37.7	3.9	2.0	1.25	0.761
123700+621617	0.859	3.75	-0.51	0.12	36.0	3.4	1.4	1.0	
123701+621030	0.167	3.75	-1.65	2.45	15.0	4.4	1.06	1.0	
123701+622008	0.212	3.75	-2.51	4.16	26.6	5.1	0.53	0.88	
123702+621025		3.75	-2.26	0.95	22.7	3.9	0.9	1.0	
123702+621146	0.016	3.8	-0.77	0.04	57.9	3.4	0.98	1.25	1.52
123702+621735		3.8	-1.0	1.93	41.2	4.8	0.47	1.88	
123703+620833	0.09	3.8	-2.08	0.2	23.2	3.0	0.13	1.13	
123703+621302	0.016	3.75	-1.8	0.07	27.0	3.0	0.35	1.13	
123703+621402	0.706	3.8	-0.95	0.05	26.5	3.3	1.92	0.88	1.2463
123703+621427	0.31	3.0	-1.7	0.85	115.3	4.5	2.75	1.38	3.214
123703+621544	1.0	3.75	-0.6	1.26	15.0	3.0	0.87	1.38	
123704+620755	0.182	3.8	-0.14	0.08	39.7	3.6	1.45	1.25	1.253
123704+621158	0.748	3.8	-0.54	0.13	36.6	3.1	0.84	1.38	
123704+621446	0.184	3.8	-2.99	34.57	14.5	3.6	1.09	1.0	2.214
123705+621429	0.379	3.8	0.54	2.33	22.2	3.4	0.36	1.0	
123705+621601	0.033	2.5	-2.25	0.24	25.6	3.7	1.73	1.0	
123705+621951	0.666	3.8	0.93	0.2	71.6	4.3	0.46	1.13	
123706+621154	0.081	3.75	-0.57	0.08	24.2	3.7	1.24	1.25	0.902
123706+621851	0.134	3.75	-4.4	22.58	19.5	4.2	0.33	0.75	
123707+620722	0.084	3.8	-1.79	0.16	65.1	4.2	1.45	0.88	
123707+620932	0.026	3.75	-3.17	1.94	13.4	4.5	0.09	1.63	
123707+621408	0.043	3.75	-2.19	0.12	24.4	4.2	0.73	1.0	2.48
123707+621729	0.0080	3.75	-2.65	1.49	15.8	5.7	0.01	1.5	
123708+621029	0.017	3.8	-2.17	0.13	26.7	4.0	1.68	1.25	
123708+621056	0.034	3.8	-0.82	0.07	53.9	4.3	0.97	1.0	0.422
123708+621122	0.12	3.8	-0.92	0.07	41.1	3.9	1.36	1.0	
123708+621410	0.08	3.8	1.04	3.05	33.6	3.6	0.13	1.0	
123708+621659	0.032	3.8	-1.07	0.07	46.6	3.7	1.2	1.0	0.4577
123709+620838	0.596	3.8	-0.23	0.05	187.9	4.1	1.11	0.75	0.907
123709+621051	0.093	3.75	0.56	2.7	29.0	4.2	0.35	1.13	0.4113
123710+620754	1.0	3.0	1.63	1.65	15.7	4.1	0.84	1.0	
123710+620841	0.109	3.8	-0.63	0.06	87.5	3.7	1.22	1.13	0.902
123710+620859	0.0060	3.75	-5.12	7.58	17.0	3.5	0.04	1.25	
123711+621331	0.136	3.8	-1.58	0.04	435.1	17.6	2.64	1.38	1.112
123711+621928	0.688	3.75	-2.12	0.68	16.7	4.7	0.05	1.5	
123712+621035	0.196	3.75	-0.77	0.39	17.6	4.3	0.86	1.13	
123712+621212	0.0070	3.75	-2.88	0.24	29.2	4.9	0.08	1.0	
123712+621326	0.17	3.8	-0.71	0.06	47.4	3.9	1.29	1.0	1.99
123713+620851	0.121	3.8	-1.39	0.17	40.8	4.6	1.39	1.0	
123713+621546	0.174	3.75	0.43	5.19	20.9	3.9	0.15	1.25	0.9363
123713+621953		3.75	-2.56	1.91	147.9	9.0	2.08	1.0	
123714+621604	0.0070	3.75	-2.44	0.1	36.1	3.2	0.39	1.38	0.9375
123714+621826	0.999	3.8	-0.71	0.06	582.4	8.9	0.9	0.25	
123715+620804	0.031	3.75	-2.51	0.99	22.7	4.5	0.05	1.0	
123715+620823	0.962	3.8	-0.3	0.06	1974.3	33.9	0.71	0.38	
123715+621617	1.0	3.75	-0.31	0.45	30.0	3.8	0.84	1.13	1.522

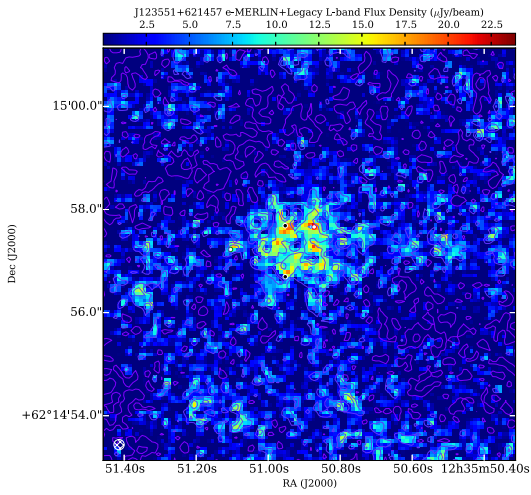
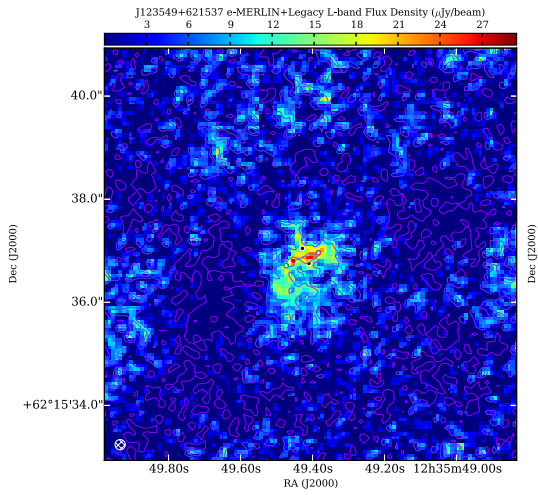
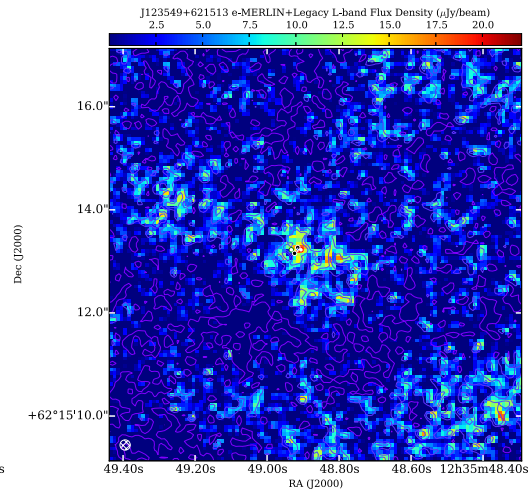
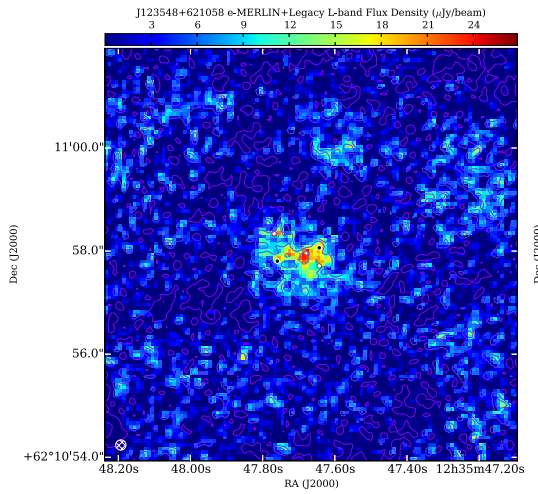
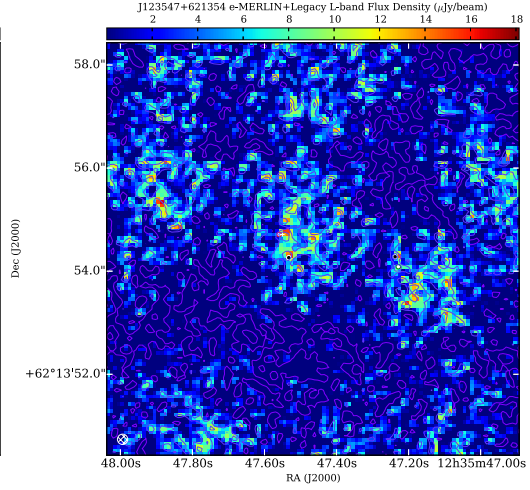
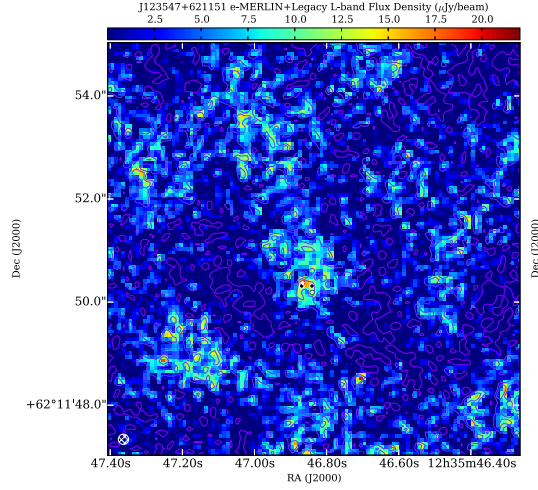
Source	$Prob_{AGN}$	$T_f(\sigma)$	α	σ_α	$S(\mu Jy)$	$\sigma_S(\mu Jy)$	$R_p(arcsec)$	LAS(arcsec)	z
123716+621213	0.673	3.0	-1.97	2.68	46.4	2.1	2.49	1.0	
123716+621512	1.0	3.8	0.17	0.05	149.7	3.8	0.72	0.38	0.23
123717+620804	0.038	3.8	-1.54	0.15	44.1	4.0	1.27	1.0	
123717+621007	0.064	3.8	-1.3	0.06	64.8	3.7	1.35	1.0	0.411
123717+621643	0.136	3.8	-0.46	0.1	56.6	5.1	0.91	0.88	0.557
123717+621733	0.949	3.8	-0.68	0.06	306.4	6.6	0.7	0.38	1.146
123717+621824	0.091	3.75	-0.48	0.26	31.5	3.8	0.83	1.63	0.839
123718+620828	0.029	3.8	-1.42	0.07	92.9	5.6	1.23	1.0	
123718+621133	0.141	3.75	0.29	3.66	23.4	3.5	0.24	1.13	
123719+620657	1.0	3.75	-0.71	2.31	23.7	3.8	0.96	1.0	
123720+620741	0.436	3.8	0.3	0.08	129.6	4.2	0.48	0.63	
123720+620903	0.339	3.8	0.93	0.17	62.7	3.5	0.54	1.13	
123721+620708	0.723	3.8	-0.22	0.07	264.5	5.9	0.64	0.5	
123721+621130	0.989	3.8	0.18	0.05	337.5	7.2	0.68	0.38	1.56
123721+621346	0.135	3.75	-0.76	0.2	30.9	4.4	0.65	0.88	1.019
123722+621035	0.998	3.8	-0.38	0.12	45.3	2.4	2.05	1.13	
123722+621216	0.015	3.0	-1.04	0.09	26.8	3.4	1.0	1.5	
123722+621927	1.0	3.0	-4.06	10.24	78.9	4.9	2.59	1.0	
123723+620910		3.75	-1.66	2.87	13.0	0.9	3.23	0.13	
123723+621357	0.07	3.75	-5.68	110.46	14.7	3.8	0.07	0.38	
123724+621304	1.0	3.0	-1.74	0.48	16.3	1.7	5.02	0.63	
123724+621714	0.992	3.75	-2.31	21.66	14.6	4.2	0.01	0.13	
123725+620856	0.016	3.8	-0.24	0.1	69.2	4.0	0.53	1.5	0.984
123725+621006	0.0070	3.75	-2.3	0.06	26.2	3.8	0.07	1.63	0.36
123725+621850	0.02	3.75	-1.87	0.32	30.4	4.0	0.02	1.0	
123726+620725	1.0	3.75	-0.93	20.1	9.3	4.2	0.97	0.13	
123726+621128	0.873	3.8	-2.12	0.05	12602.4	605.4	5.34	2.5	1.2653
123727+620823	0.229	3.8	0.82	1.41	45.5	4.3	0.28	0.88	
123727+621419	0.563	3.75	-2.0	6.38	16.9	4.1	1.06	1.75	
123727+621714	0.073	3.0	-1.09	0.43	24.0	3.9	1.33	1.13	
123728+620826	0.83	3.75	-1.34	0.39	14.1	2.5	0.06	1.13	
123728+621035		3.0	-2.23	0.94	13.0	3.6	0.01	0.13	
123728+621124		3.8	-0.21	4.19	28.3	4.2	0.21	1.0	
123728+621855		3.0	-1.38	1.56	28.0	4.3	1.03	1.0	
123731+620942	0.182	3.75	-4.4	1841.95	101.9	5.5	3.29	1.25	
123731+621153	0.787	3.8	0.04	0.12	42.7	3.8	0.58	0.88	
123731+621259	0.953	3.8	-0.76	0.07	105.2	6.0	0.92	0.38	
123731+621620	0.0060	3.75	-3.25	0.41	32.6	3.7	0.02	1.25	0.975
123733+620919	0.0080	3.75	-3.33	1.35	28.3	3.1	1.15	1.13	
123733+621013	0.095	3.8	-0.98	0.21	34.2	4.4	1.25	1.13	
123734+620931	0.027	3.8	-0.46	0.07	40.8	5.1	1.06	1.25	0.189
123734+621723	0.017	3.8	-3.0	0.89	46.6	4.7	1.99	1.38	0.6402
123735+620807	0.0060	3.75	-4.61	14.03	33.6	3.8	0.21	1.13	
123735+620941	0.626	3.75	0.52	0.28	29.2	3.7	0.6	0.88	
123736+621056	0.0080	3.75	-2.97	1.66	17.8	3.9	0.87	0.88	
123736+621058	0.011	3.75	-2.41	0.23	38.7	3.8	0.11	1.0	
123736+621805	0.062	3.0	-3.01	36.39	15.5	5.1	1.86	0.5	
123737+621205	0.998	3.75	1.46	5.53	16.5	3.3	0.61	1.5	
123737+621429	0.123	3.8	-0.42	0.23	58.3	4.1	0.63	0.88	
123738+620828	0.108	3.8	-1.73	0.2	100.2	4.6	1.48	0.88	
123738+620920	0.122	3.8	-0.88	0.59	48.4	5.0	0.76	1.25	
123738+621041	0.011	3.75	-2.73	0.79	25.4	3.8	0.03	1.0	
123738+621737		3.0	-0.85	2.36	18.8	3.8	1.44	1.13	
123739+621455	0.125	3.0	-0.92	0.13	18.9	4.0	1.81	1.13	
123739+621559	0.043	3.75	-1.48	0.19	20.6	3.5	0.01	1.13	
123741+620911	0.127	3.75	0.66	0.34	45.6	4.2	0.42	1.13	
123741+621200	0.909	3.75	-2.81	2.3	53.2	3.1	3.46	1.38	
123741+621221	1.0	3.75	0.63	0.54	20.8	3.5	0.86	1.25	
123741+621232	0.308	3.75	-1.55	0.06	23.6	2.7	0.02	0.5	
123741+621251	0.526	3.8	-0.69	0.07	144.9	3.9	1.12	0.88	
123741+621517		3.75	-0.71	36.28	6.6	1.3	3.06	0.25	
123742+621224	0.204	3.75	-1.87	0.61	19.4	3.6	0.04	0.88	
123742+621418	0.237	3.75	-2.14	3.69	90.9	5.0	2.19	1.0	
123742+621518	0.2	3.8	-0.14	0.07	107.9	3.3	1.14	1.13	0.07
123743+621557	0.567	3.8	-0.66	0.25	60.1	5.1	0.66	1.0	
123745+621219	0.266	3.75	0.66	0.56	44.2	4.3	0.57	1.0	
123746+621435	0.323	3.75	0.83	2.21	25.8	4.5	0.45	1.13	0.2995
123746+621457	0.307	3.8	0.74	0.55	57.9	3.5	0.62	1.13	0.9115
123748+621442	0.668	3.0	0.3	0.17	43.6	3.7	0.51	0.5	

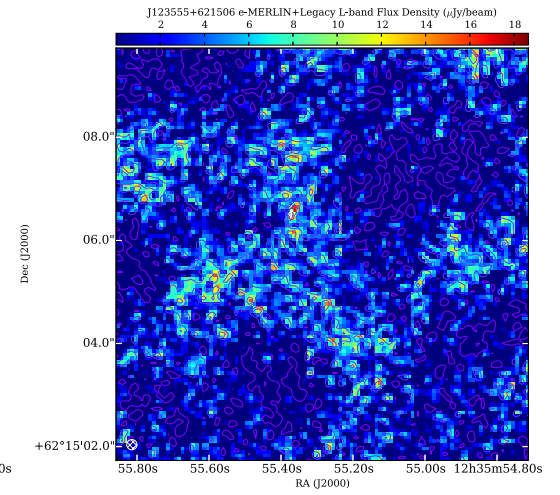
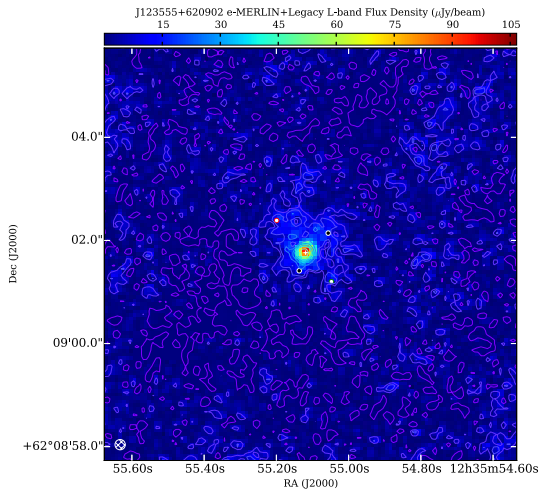
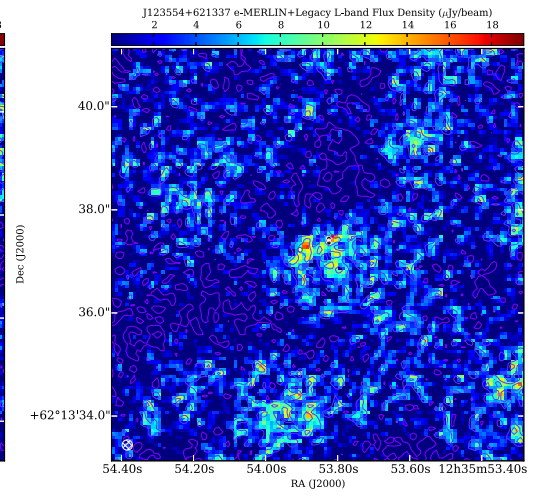
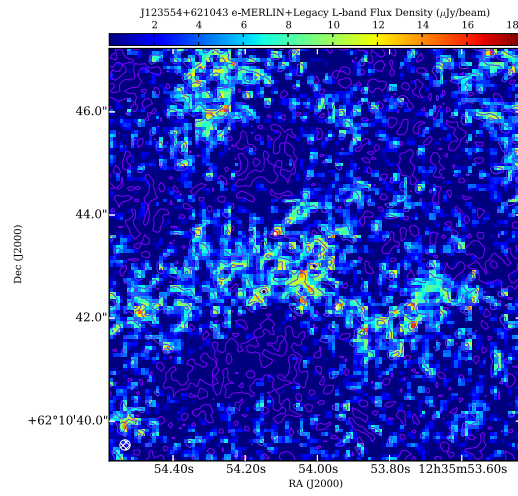
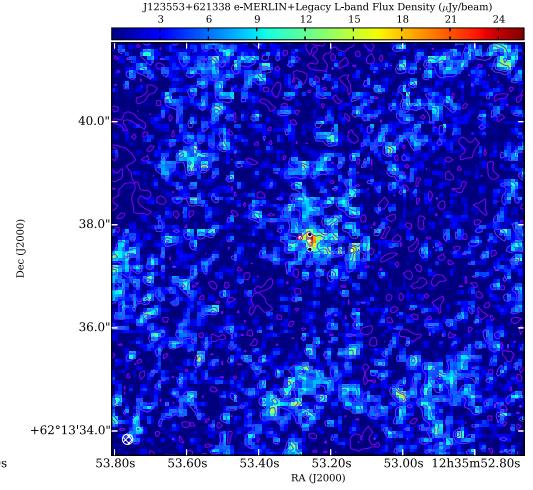
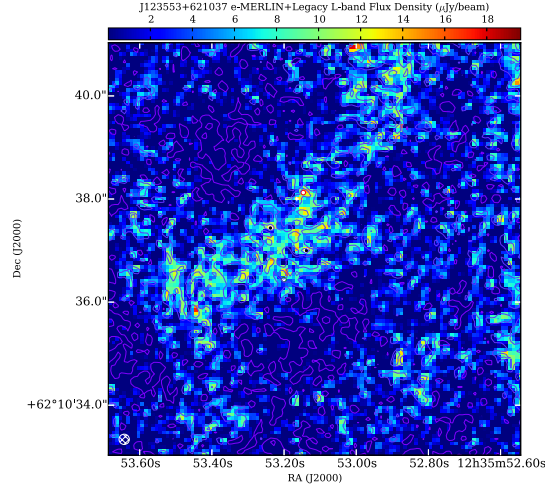
Source	$Prob_{AGN}$	$T_f(\sigma)$	α	σ_α	$S(\mu Jy)$	$\sigma_S(\mu Jy)$	$R_p(arcsec)$	LAS(arcsec)	z
123750+621143	0.015	3.75	-2.29	0.08	28.6	4.5	0.07	1.38	
123750+621206	0.014	3.0	-1.65	0.13	23.8	3.6	0.0	1.13	
123750+621359	0.062	3.8	-0.94	0.19	51.6	5.6	0.99	1.13	
123750+621401	0.043	2.5	-1.78	0.75	130.9	7.7	2.39	1.88	

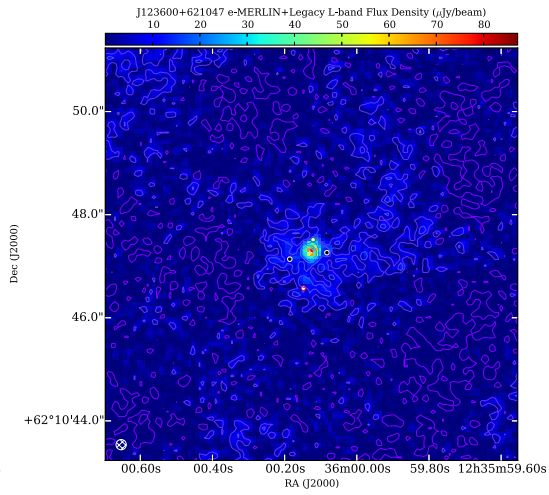
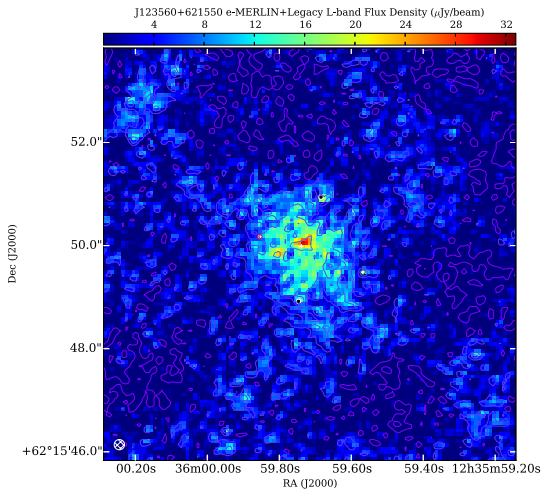
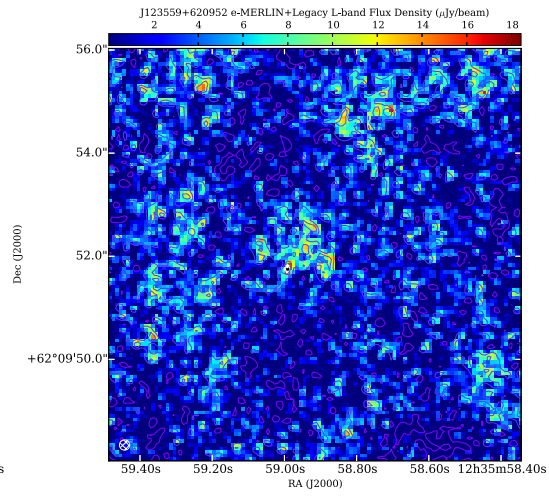
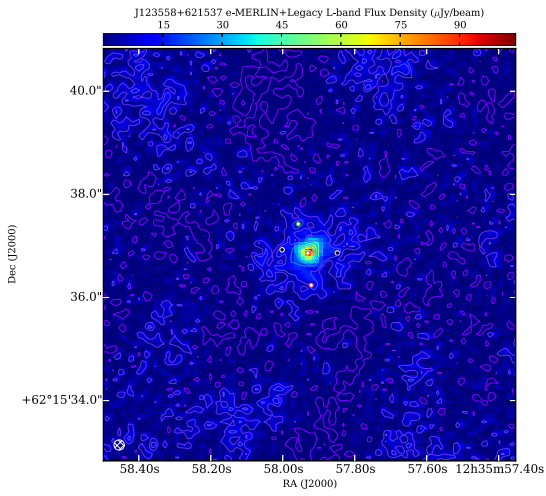
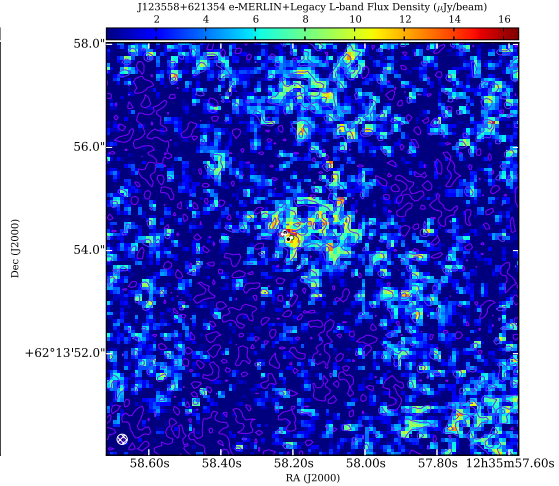
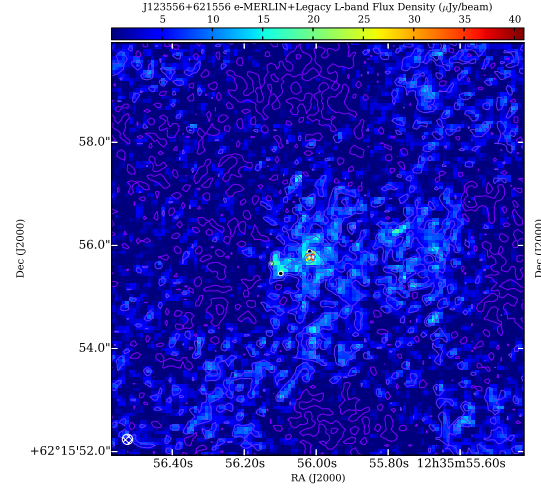
Appendix II

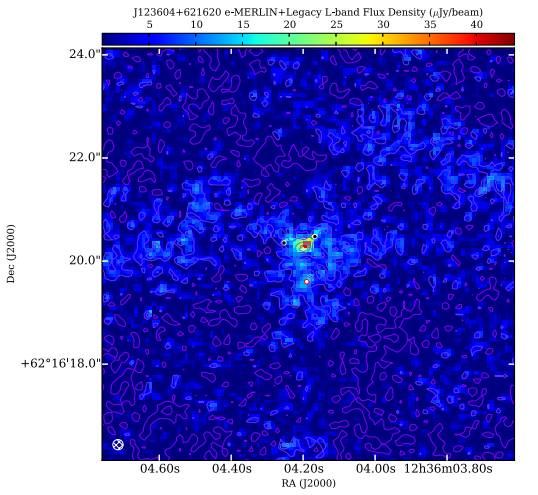
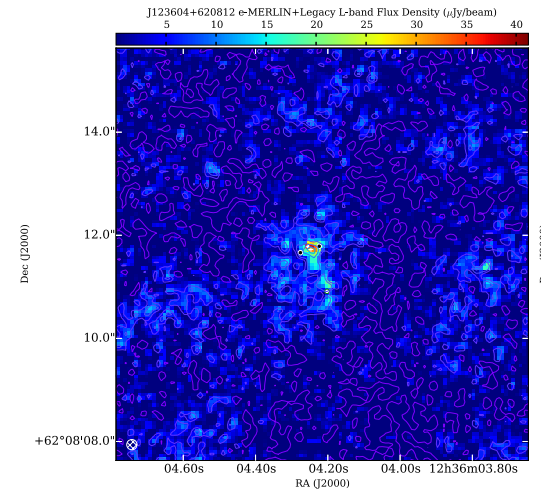
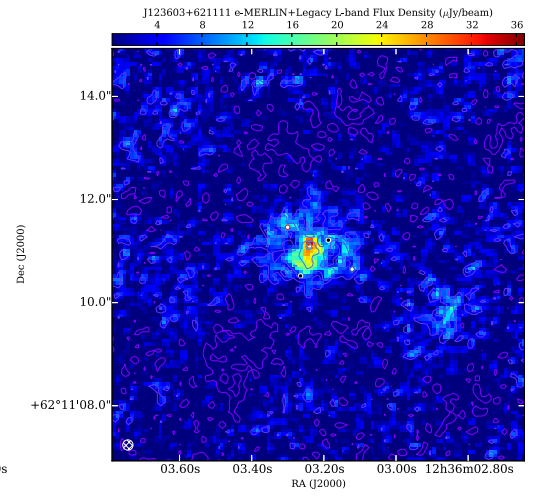
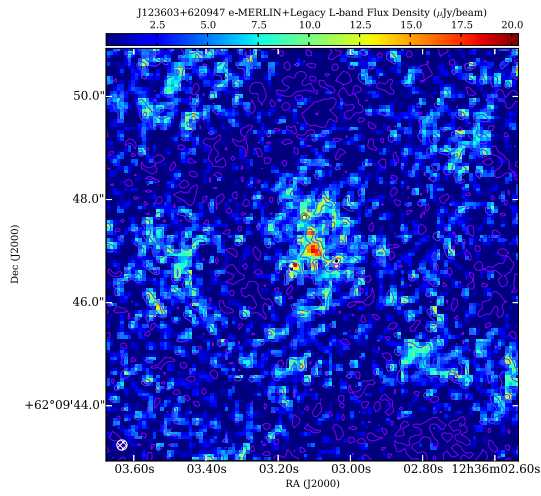
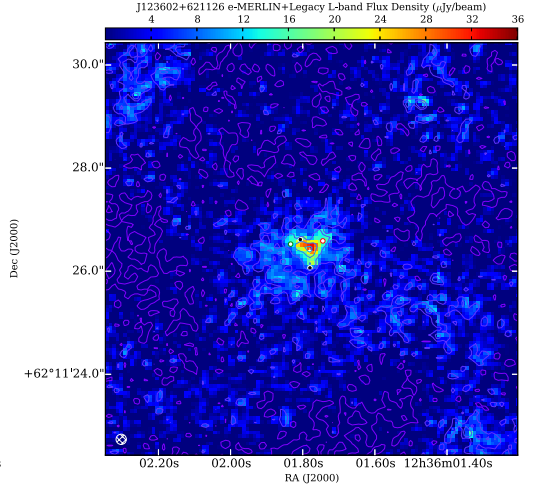
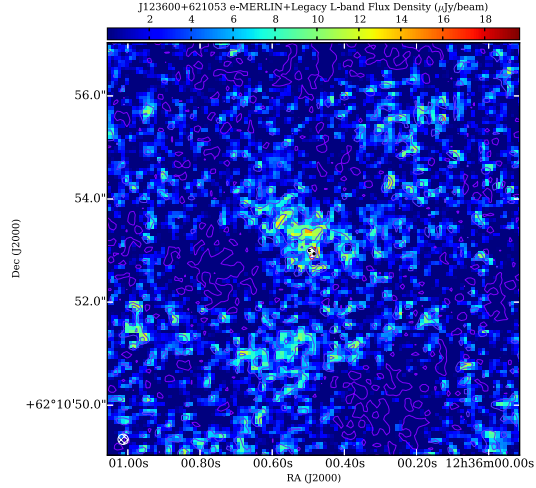
e-MERGE Source Plots

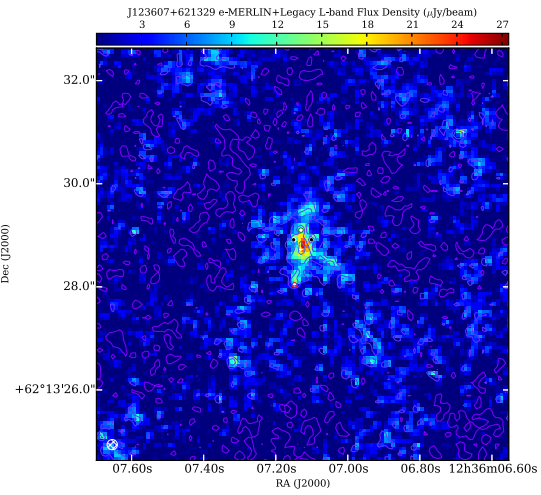
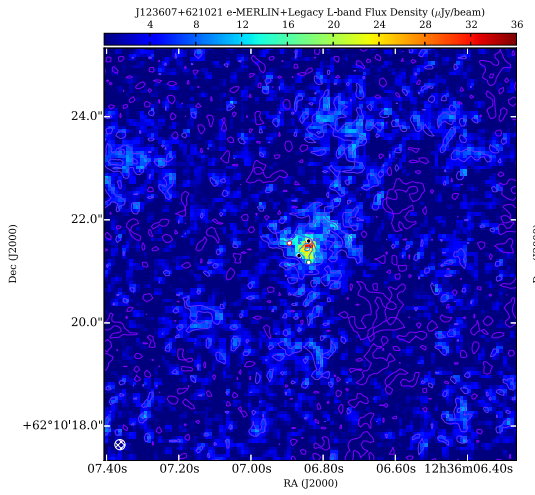
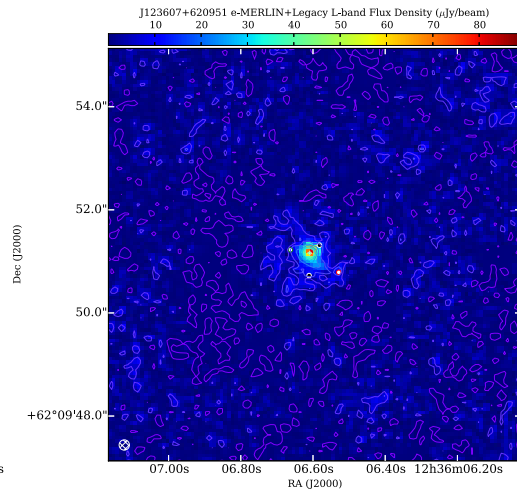
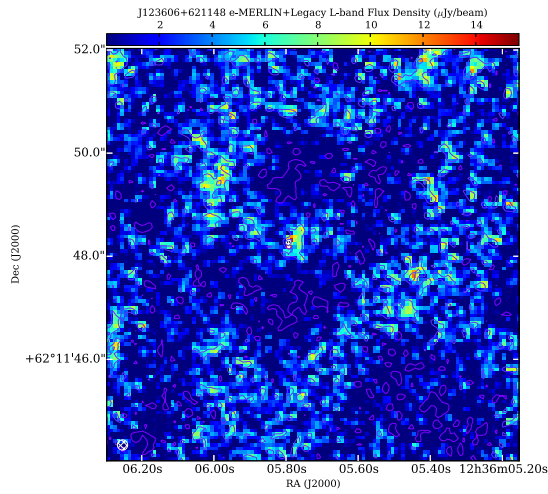
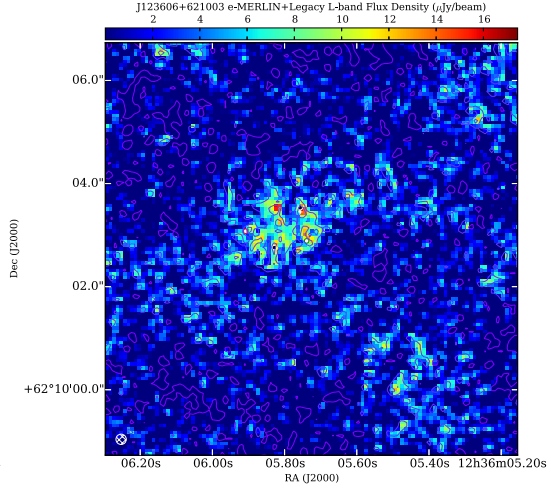
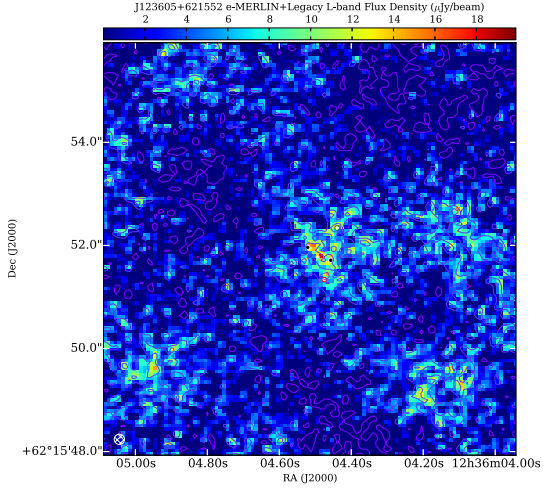
Sources identified in the GOODS-North field and observed in the *e*-MERGE survey are included for reference in this appendix. These are all the highest angular resolution images, with 0.2 arcsec beam, derived from *e*-MERLIN + Legacy data.

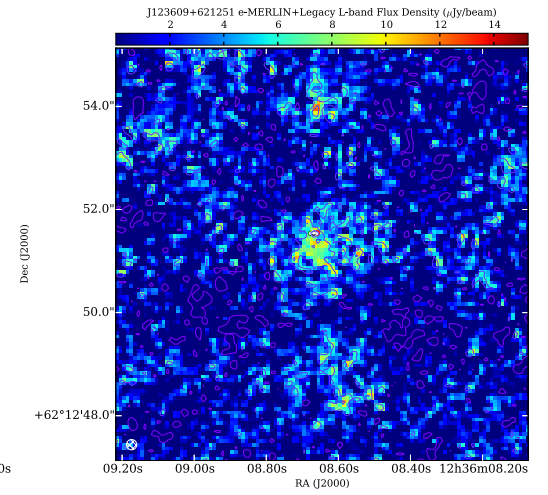
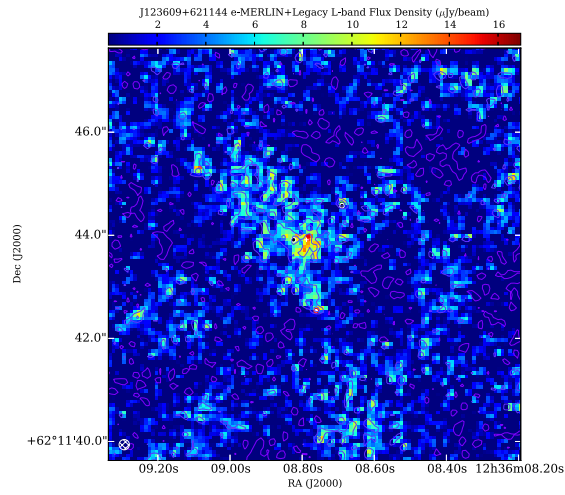
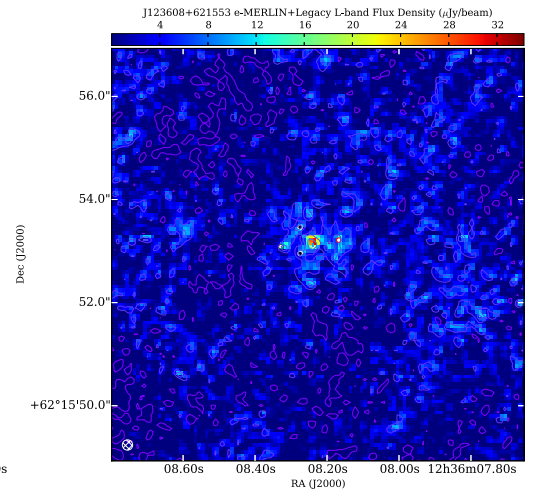
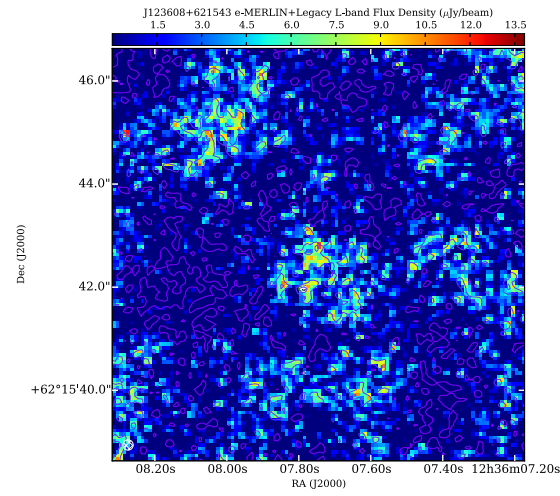
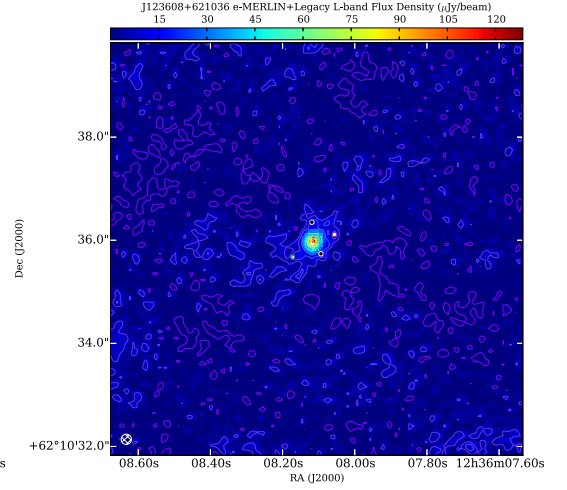
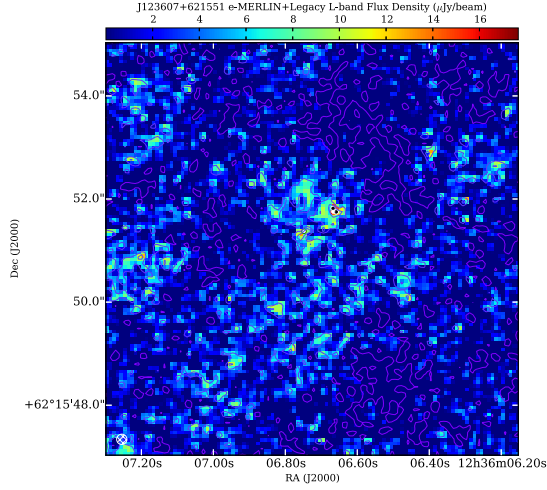


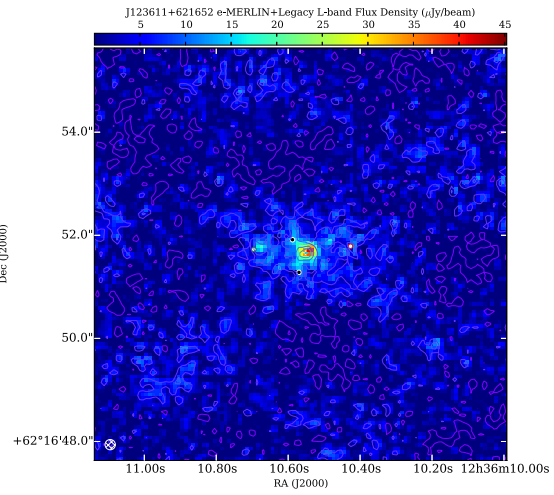
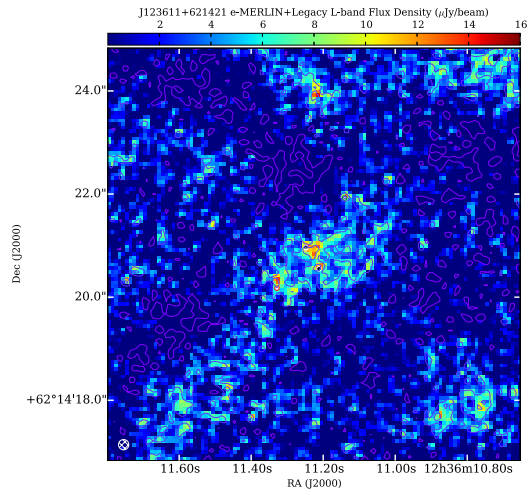
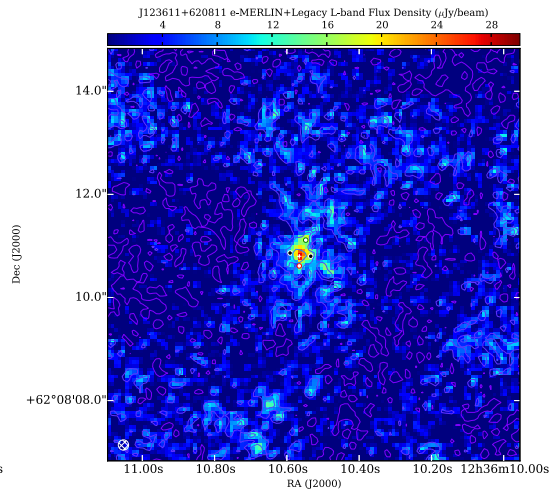
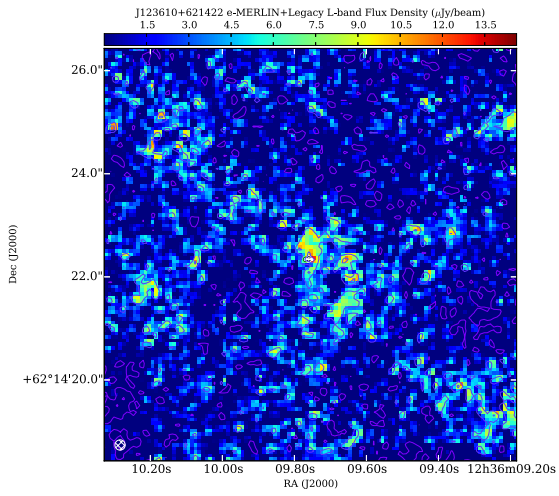
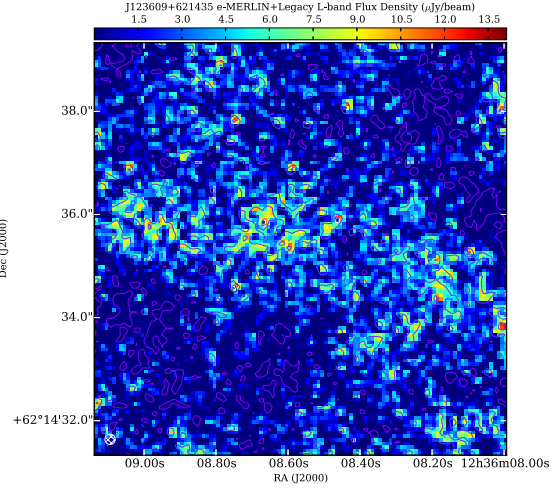
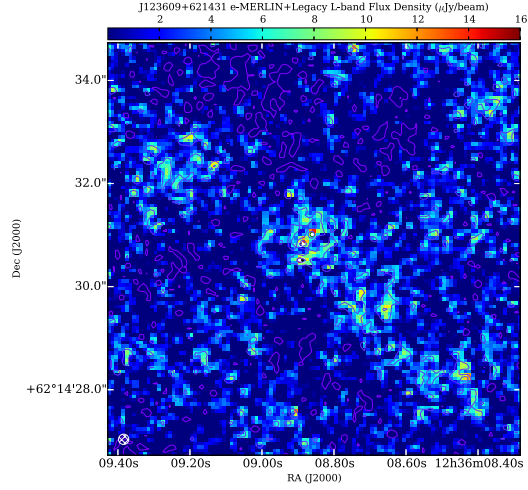


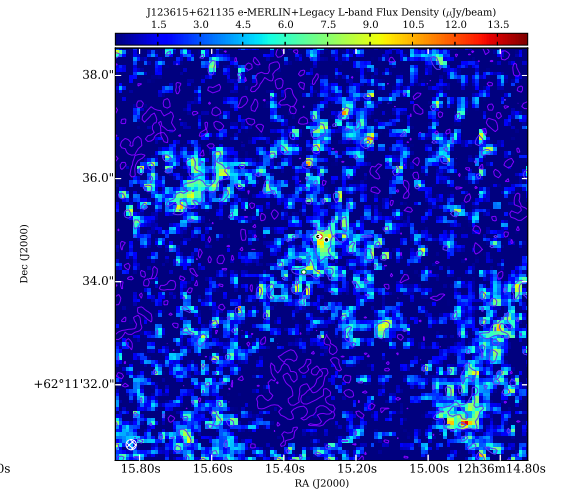
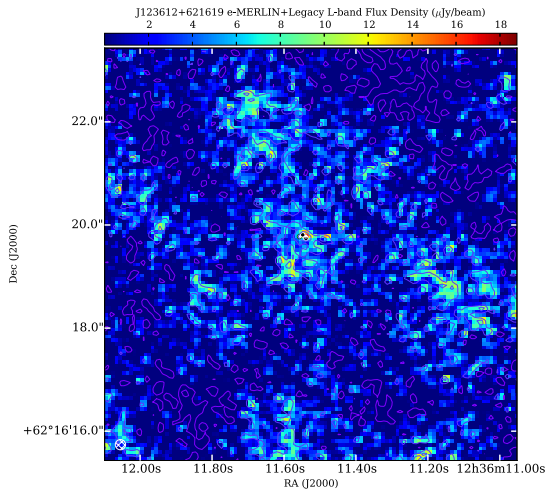
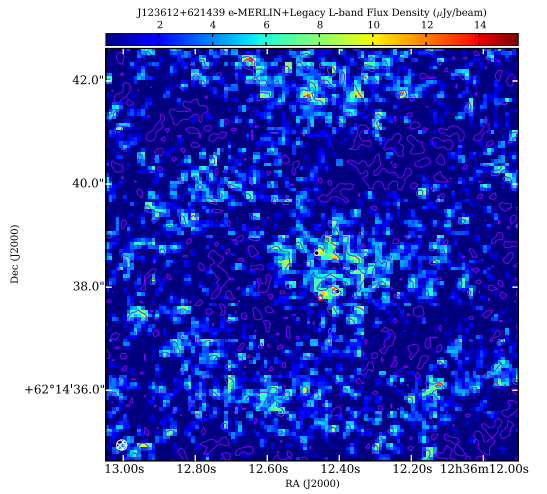
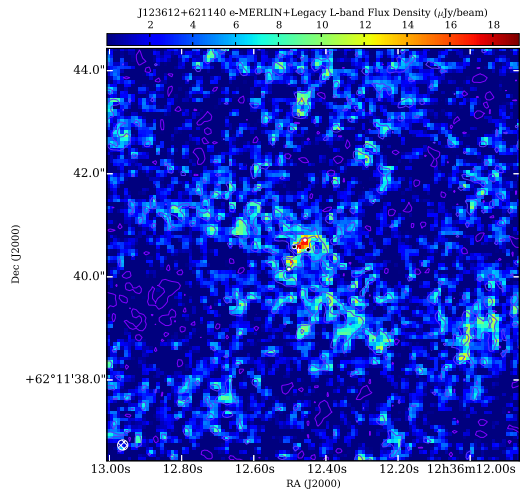
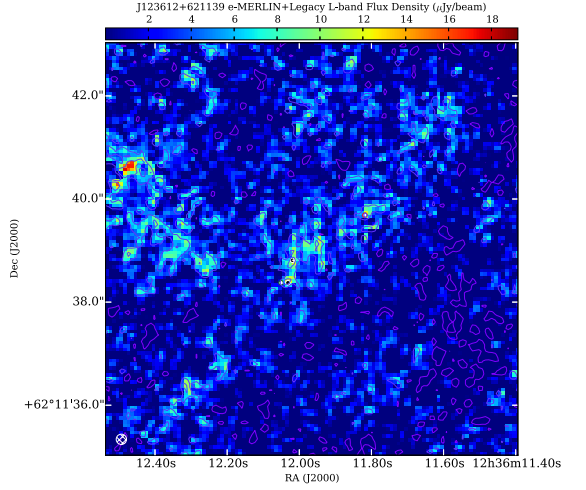
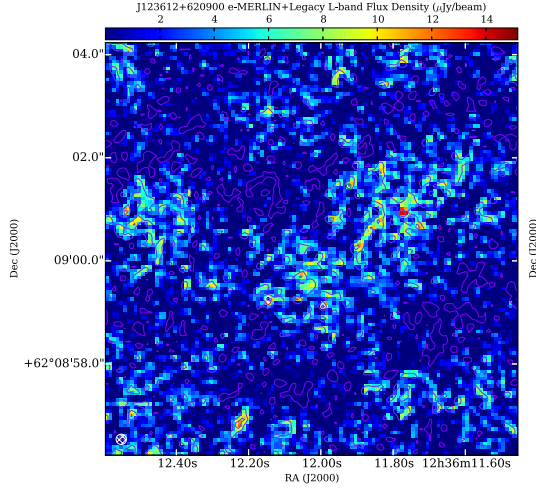


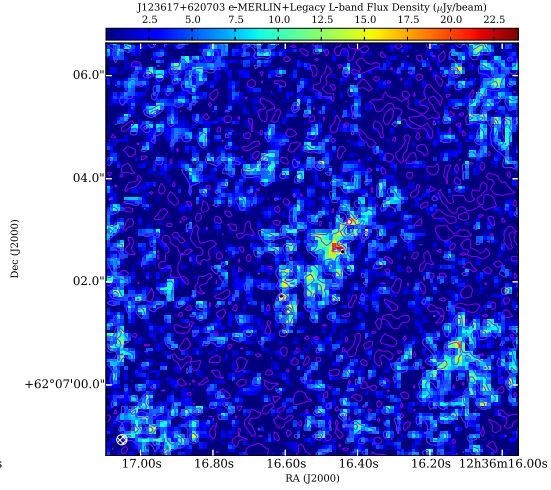
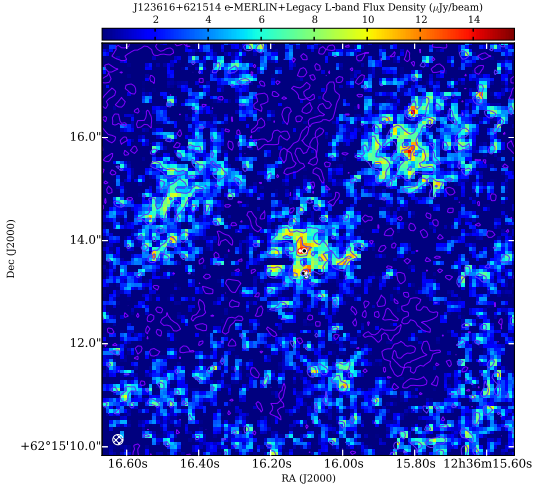
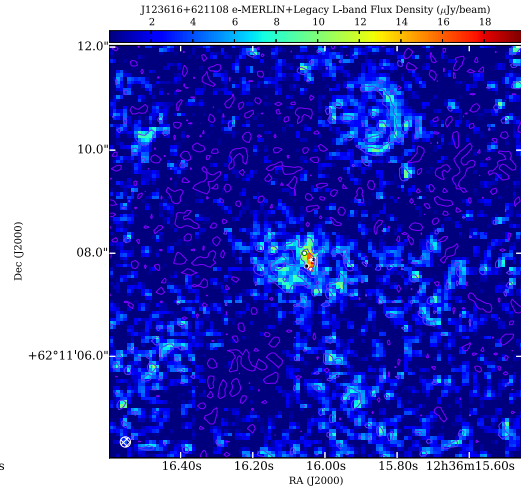
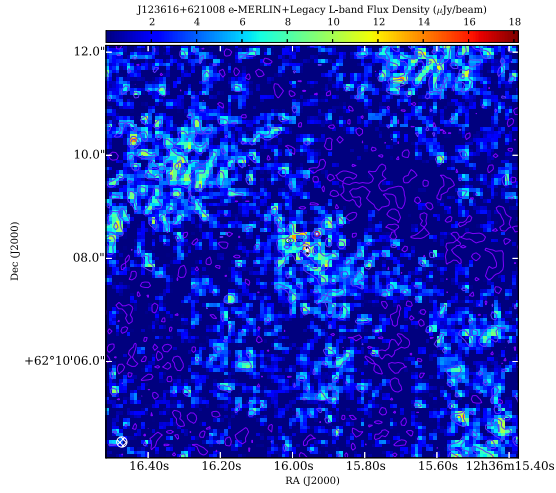
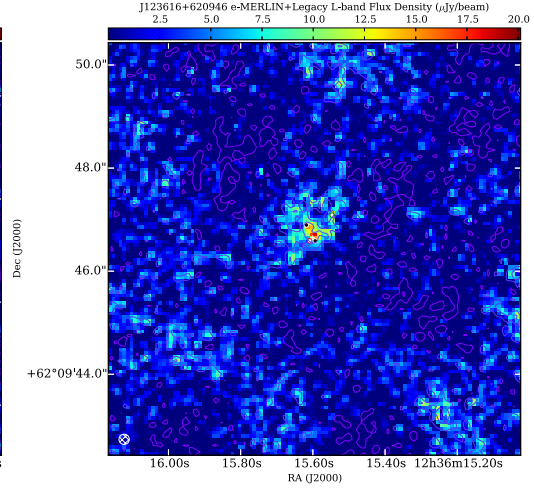
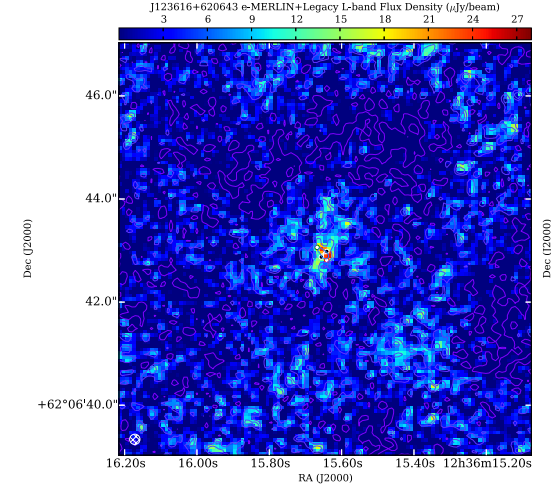


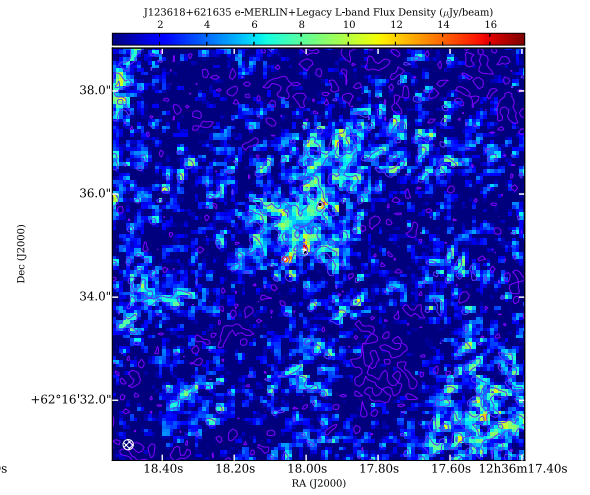
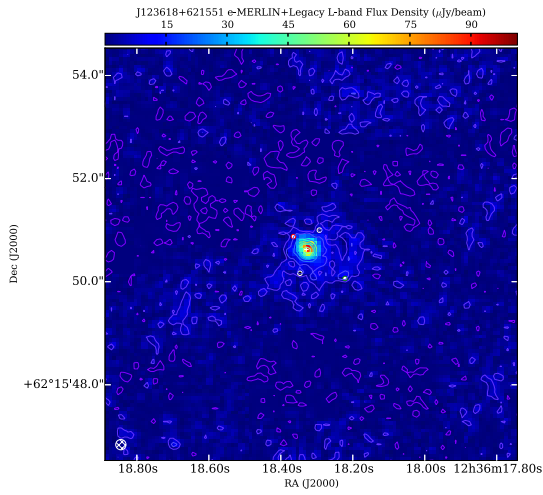
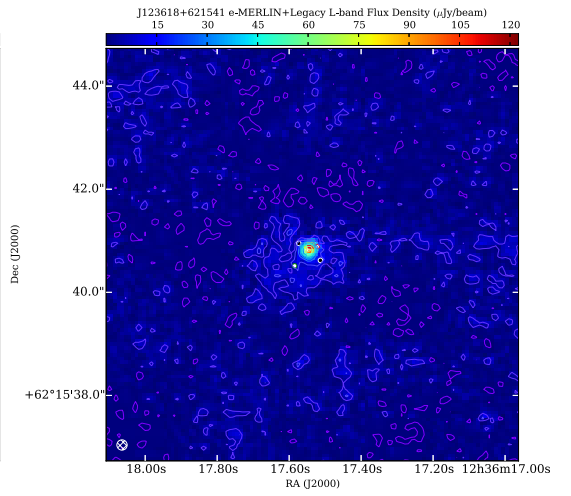
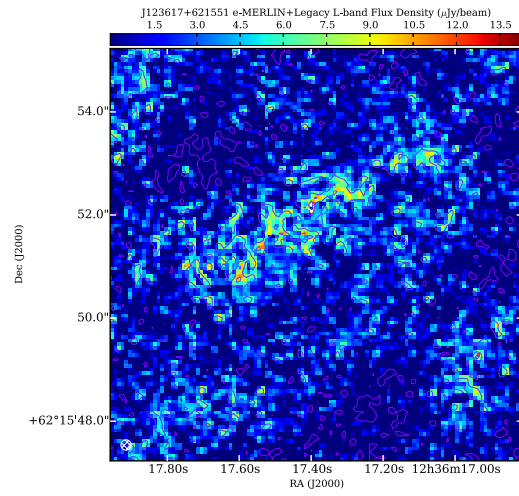
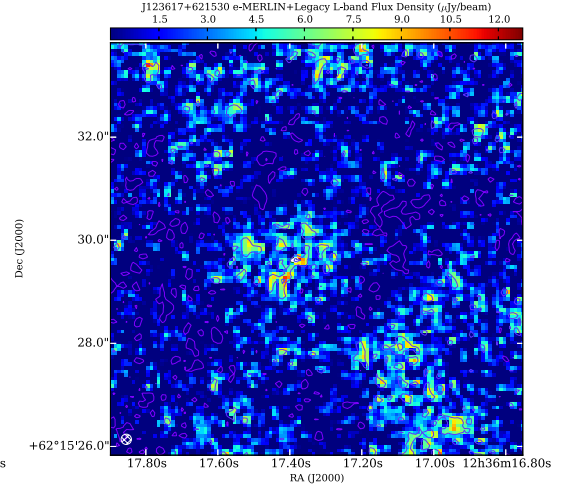
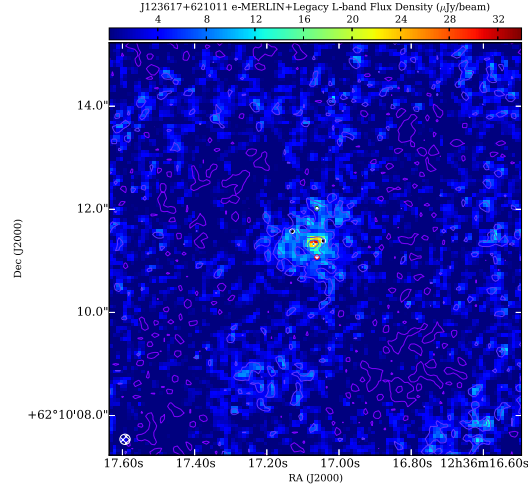


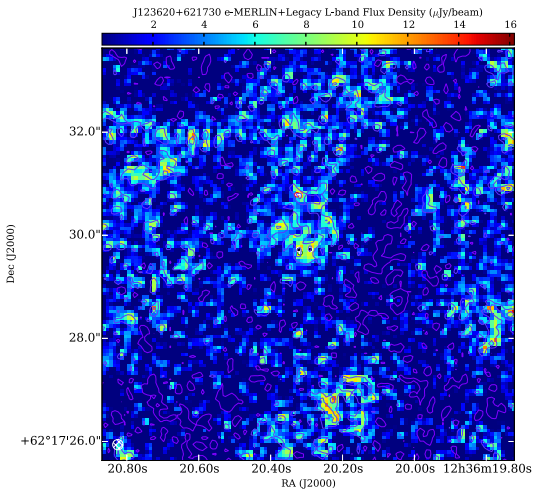
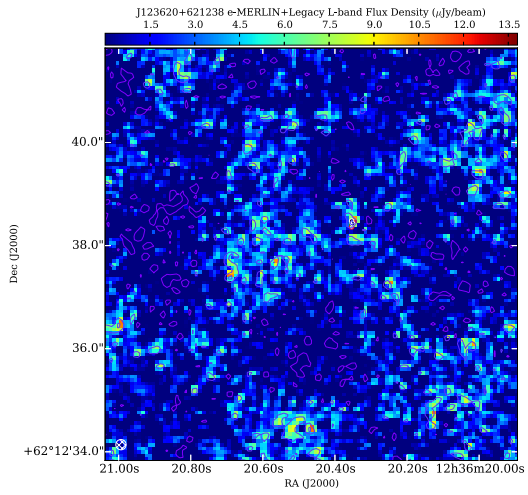
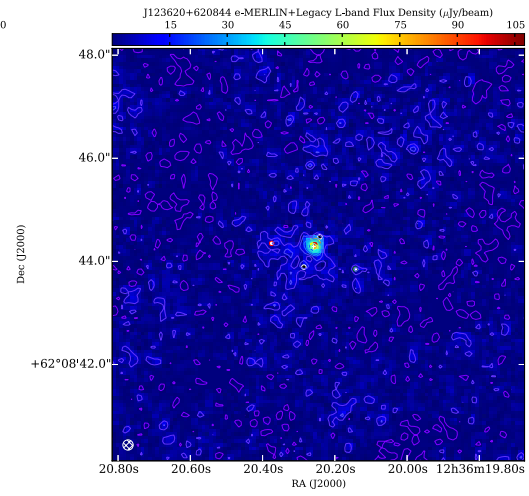
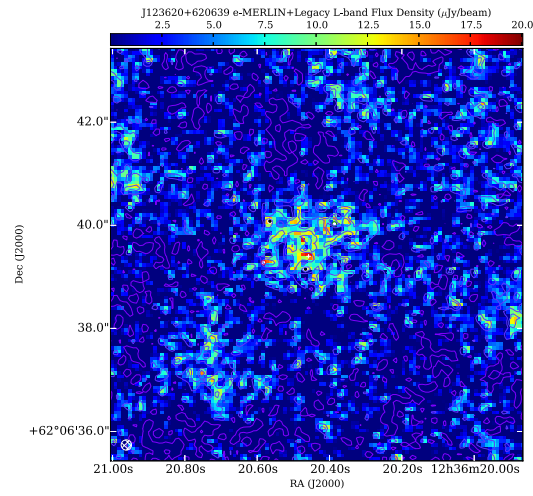
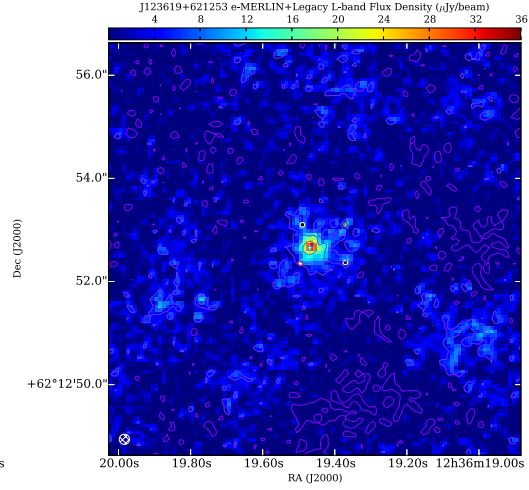
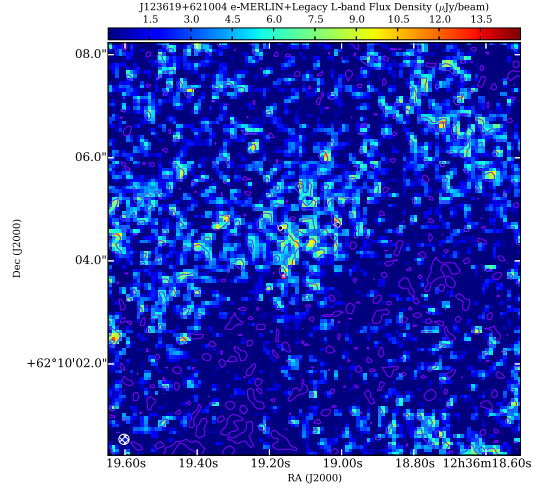


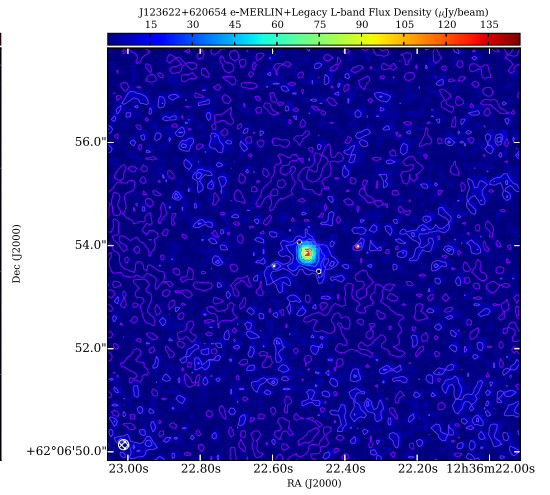
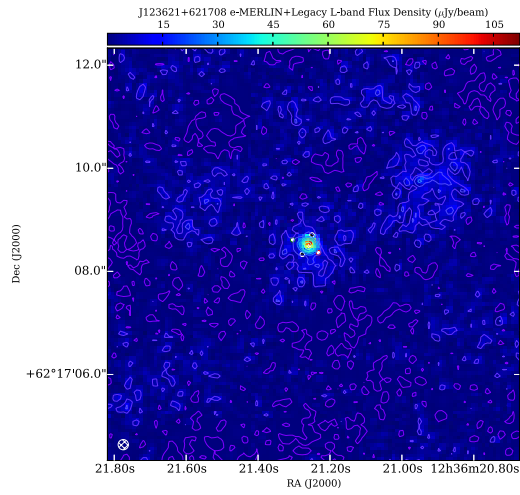
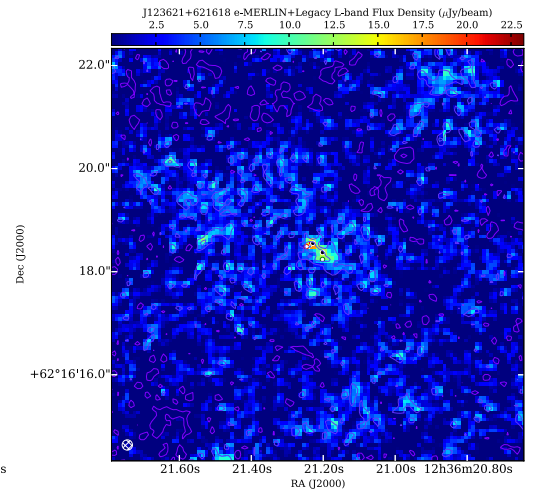
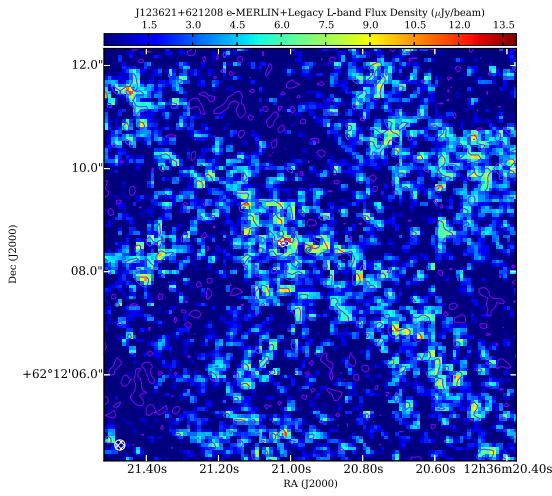
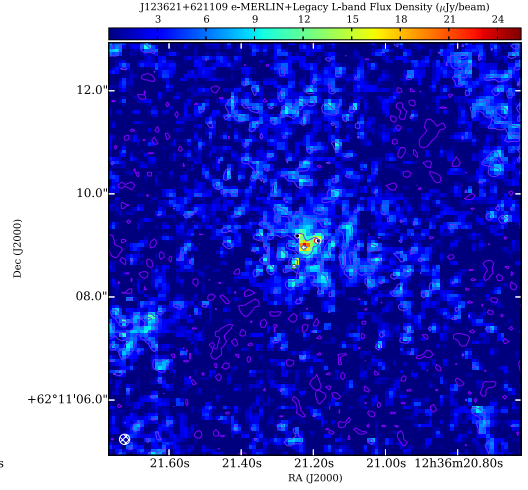
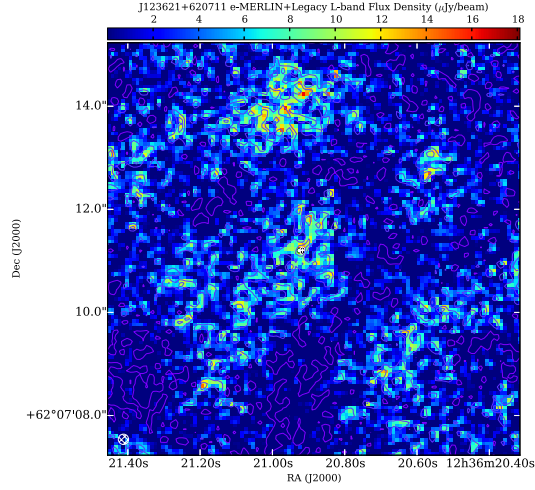


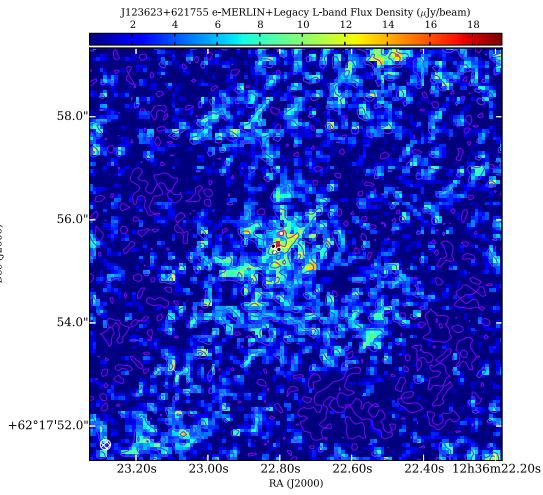
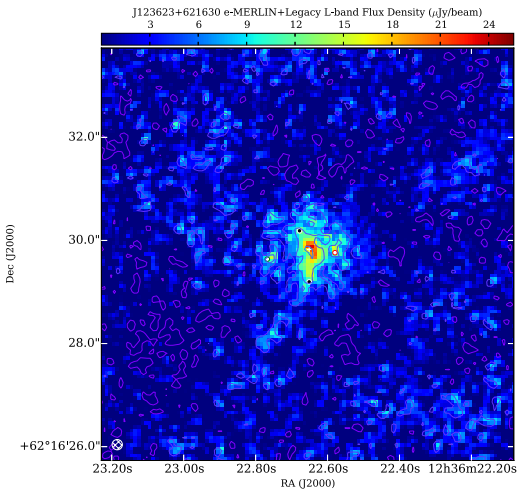
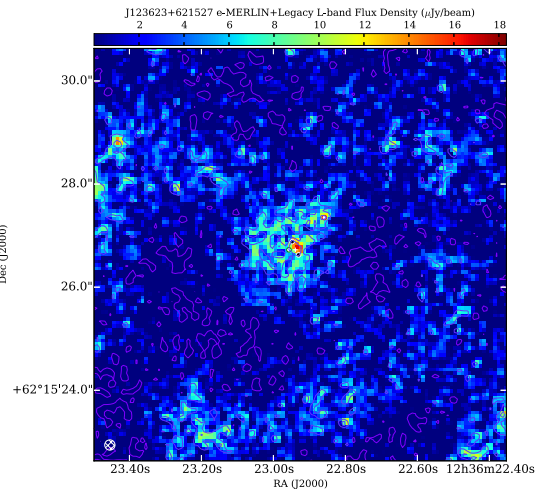
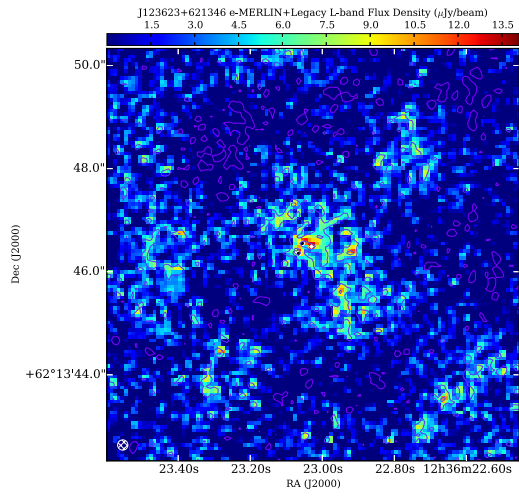
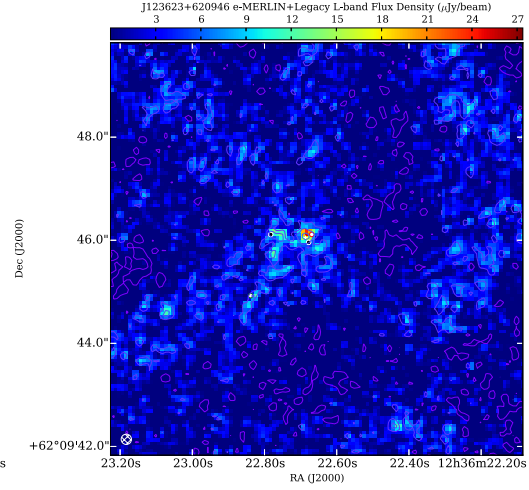
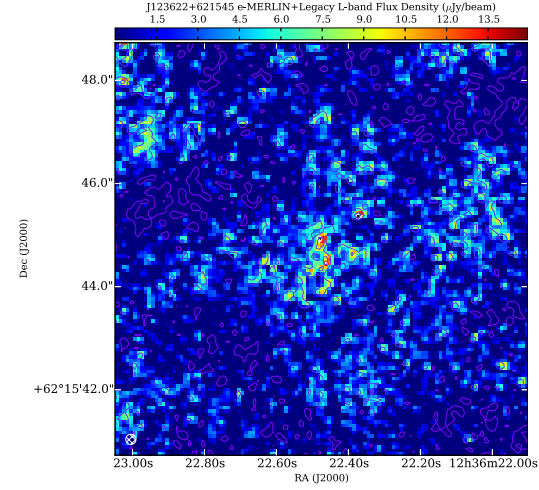


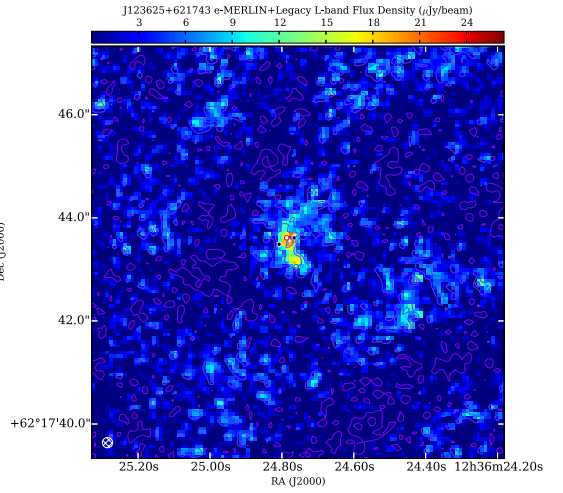
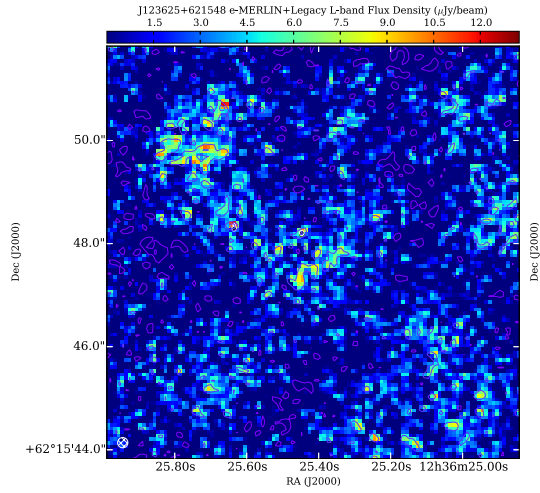
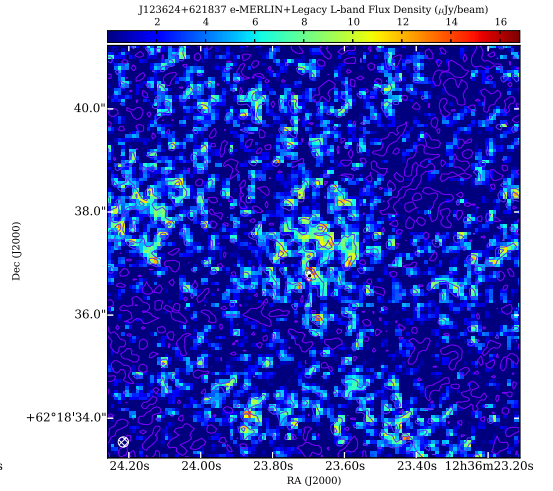
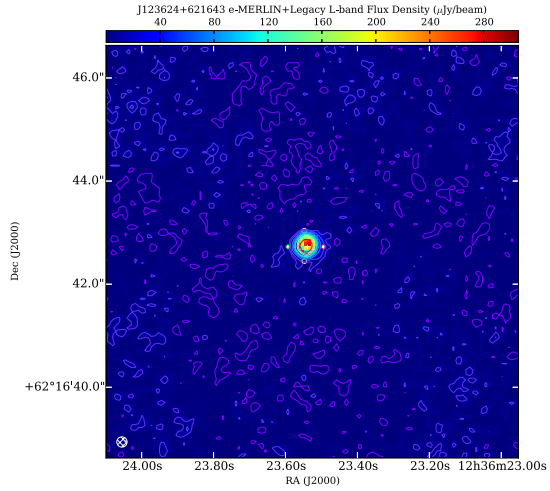
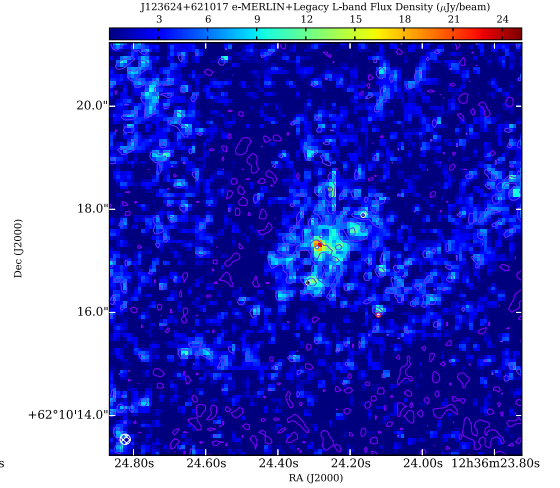
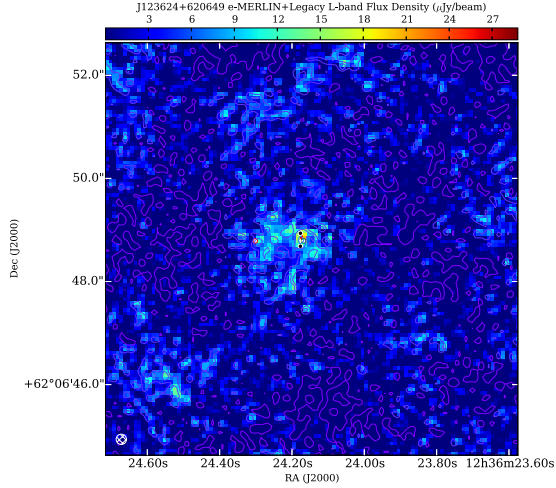


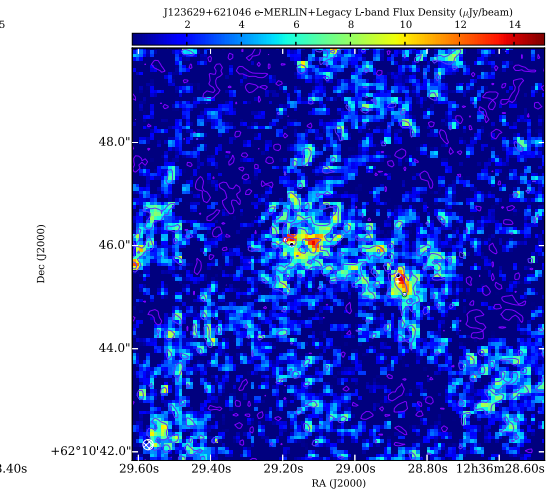
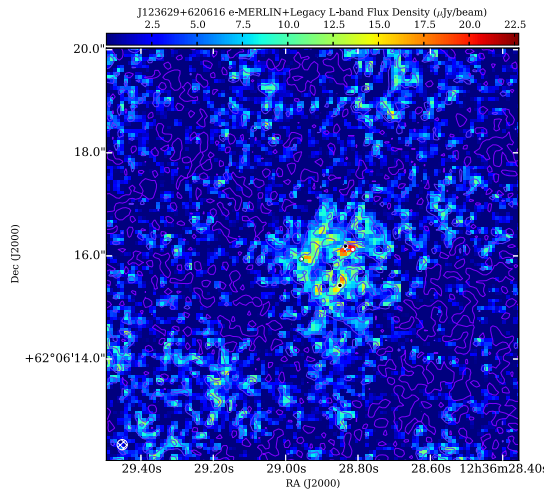
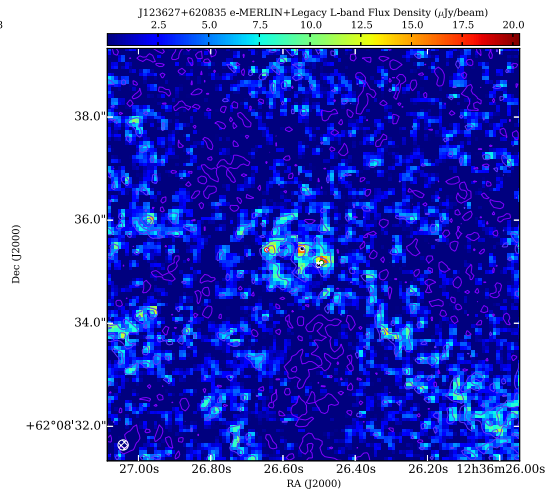
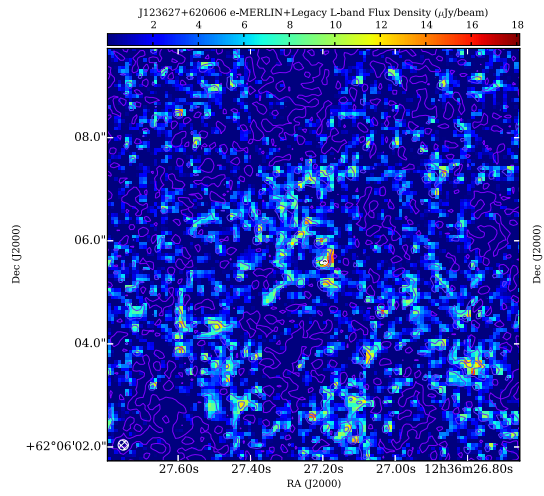
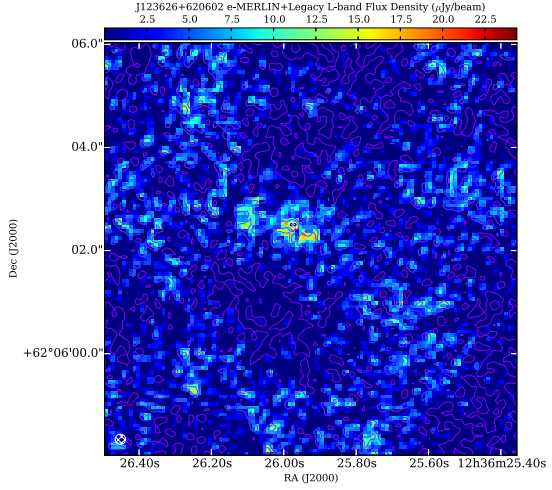
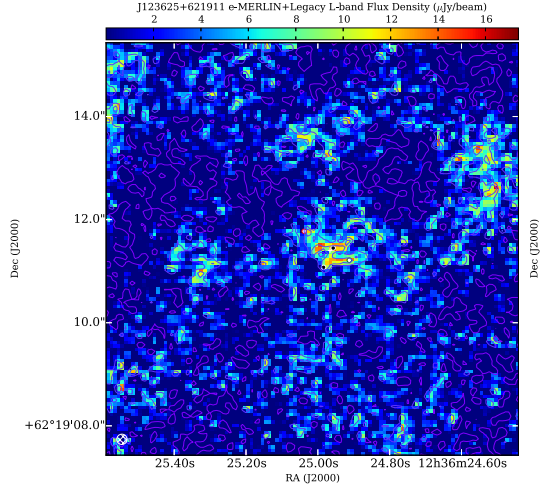


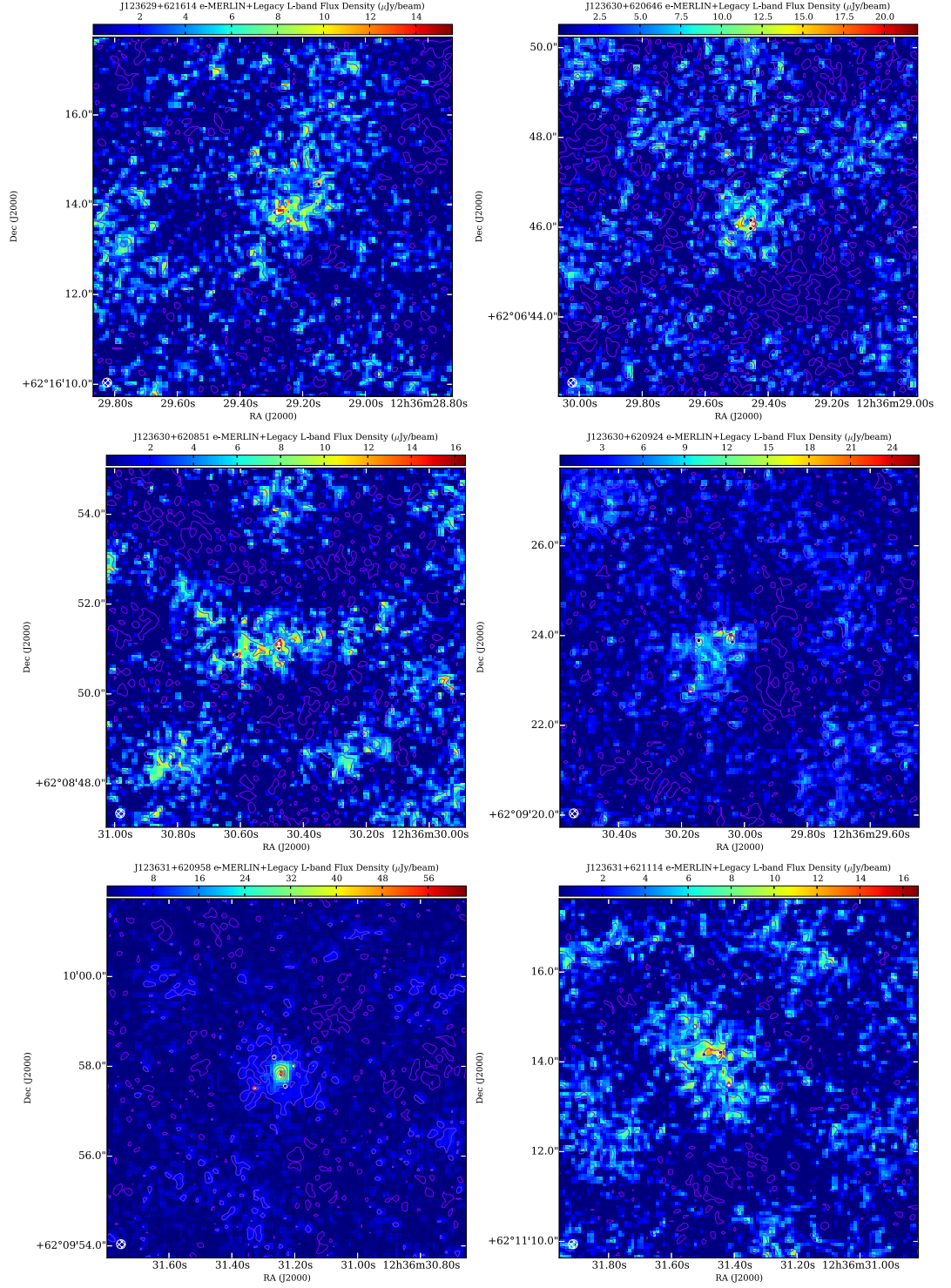


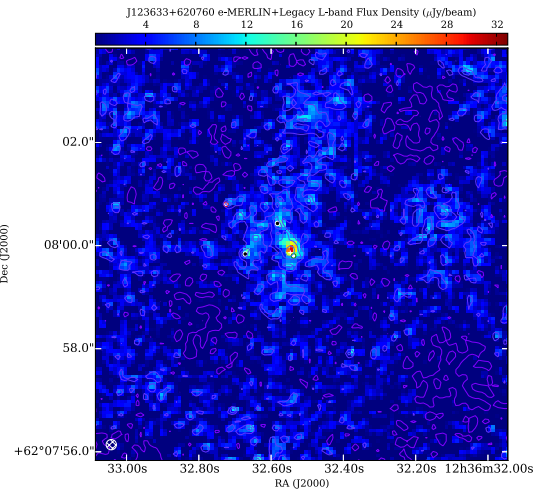
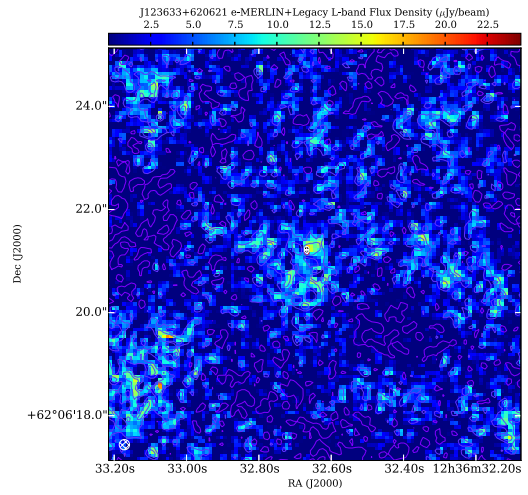
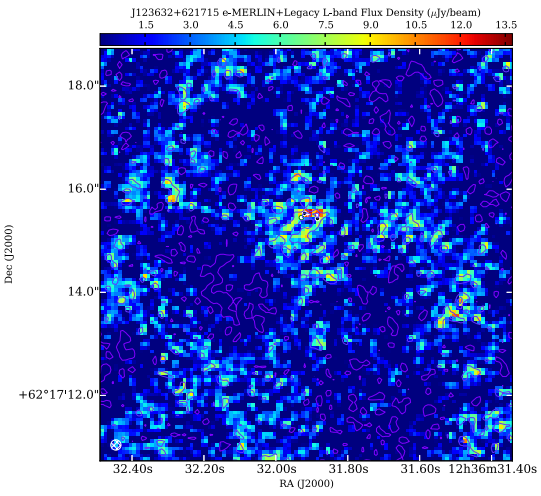
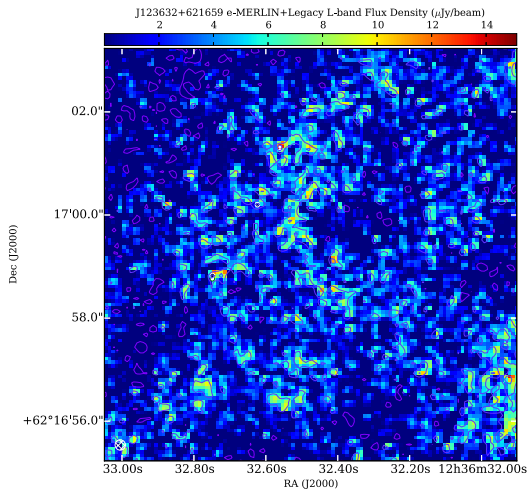
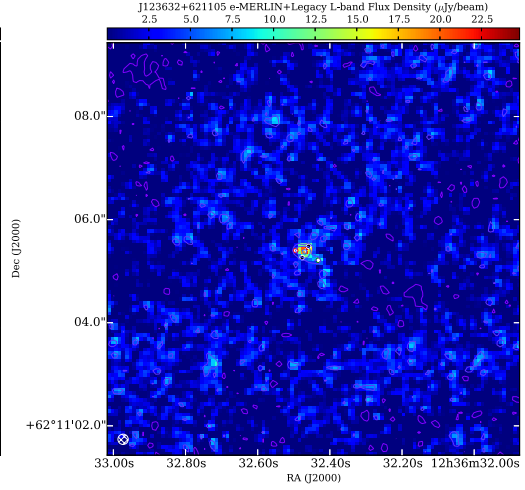
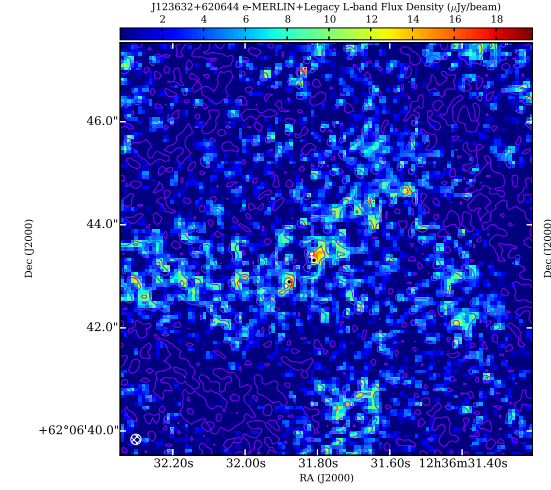


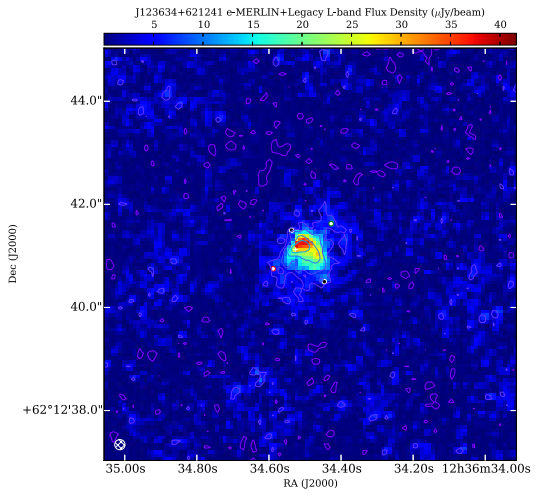
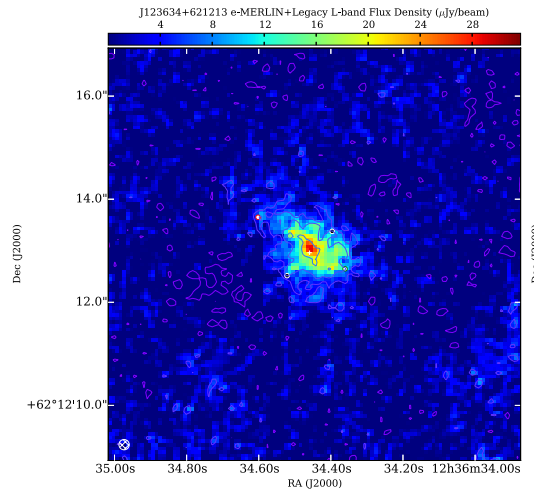
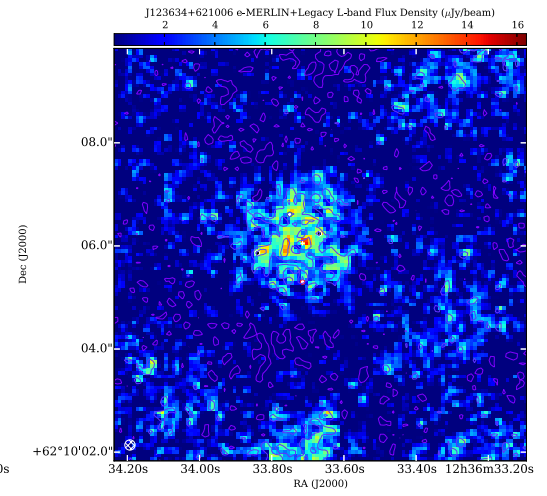
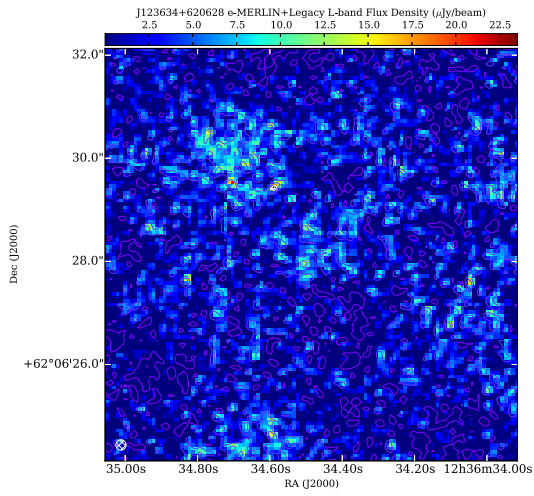
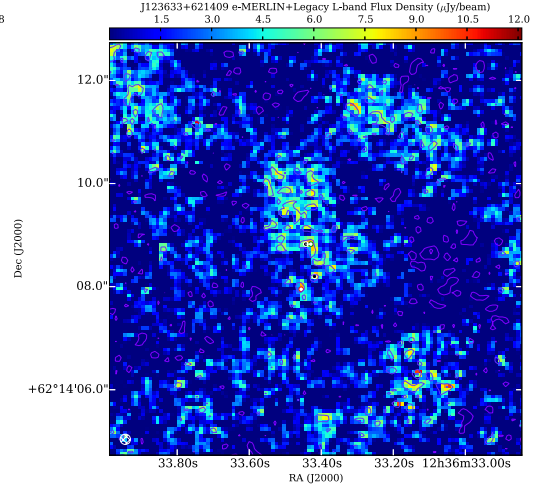
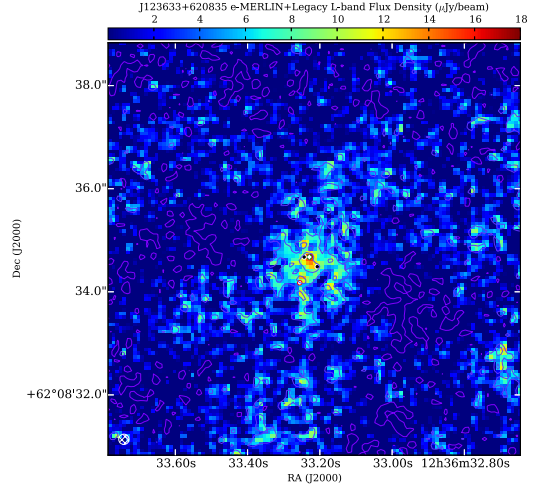


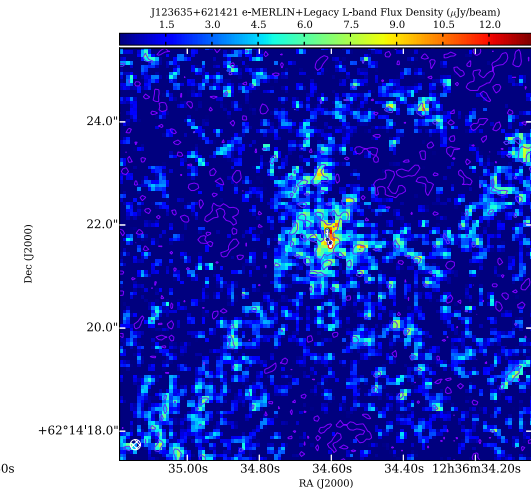
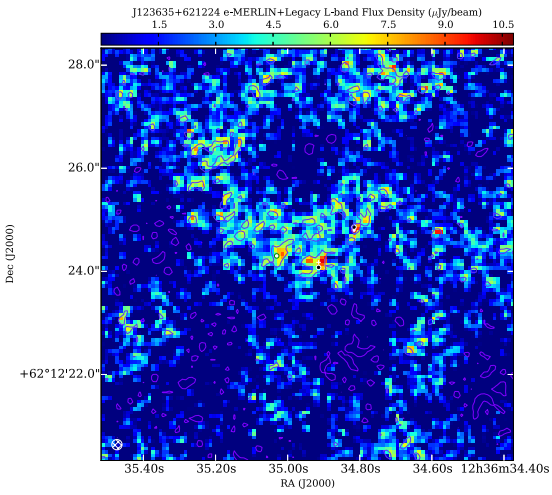
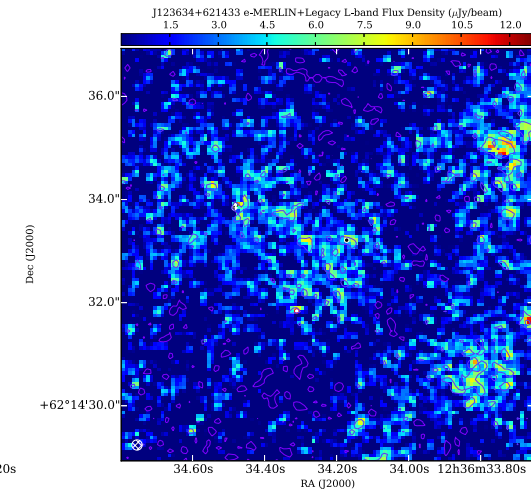
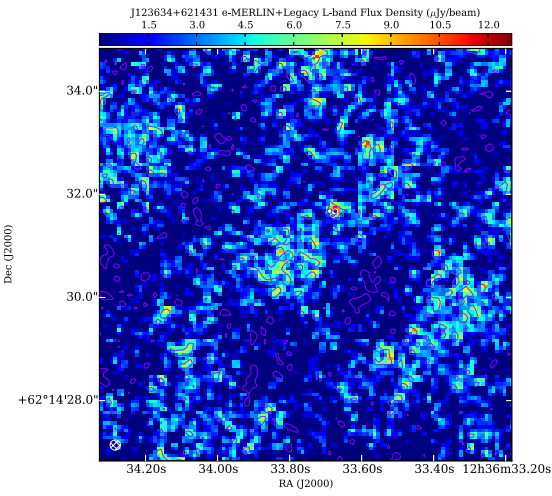
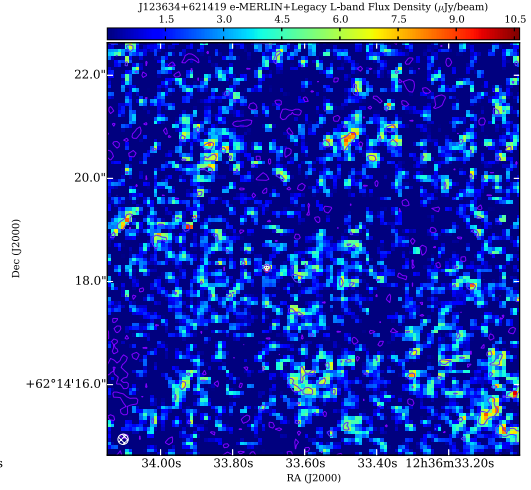
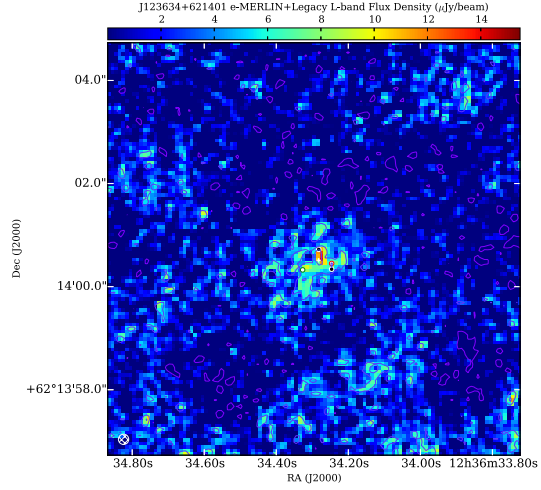


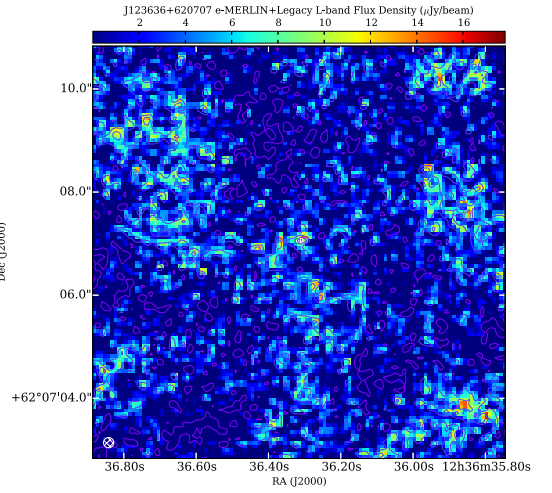
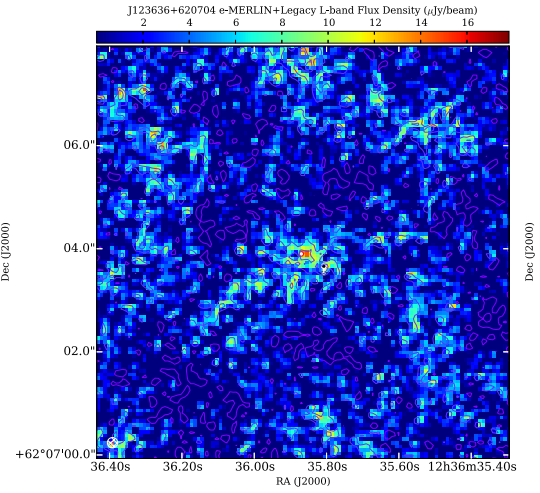
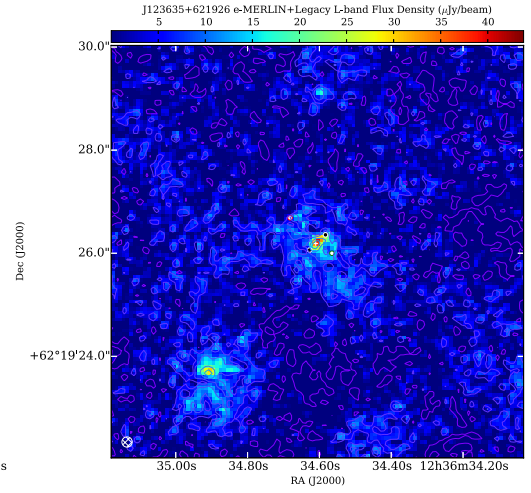
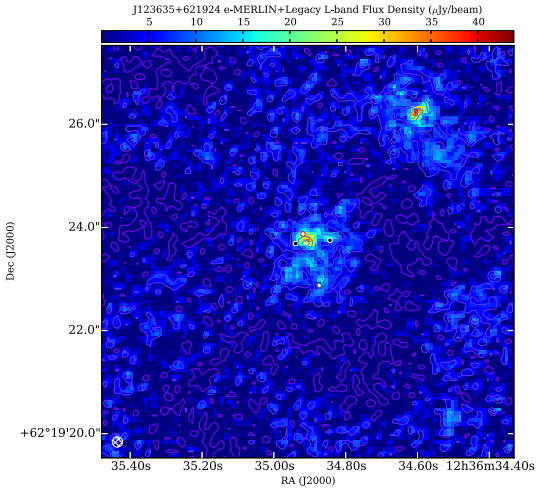
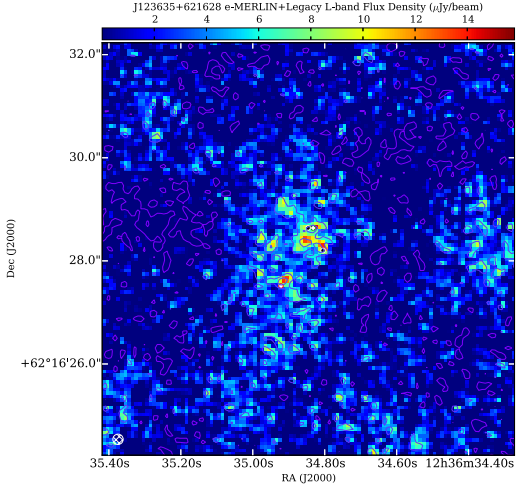
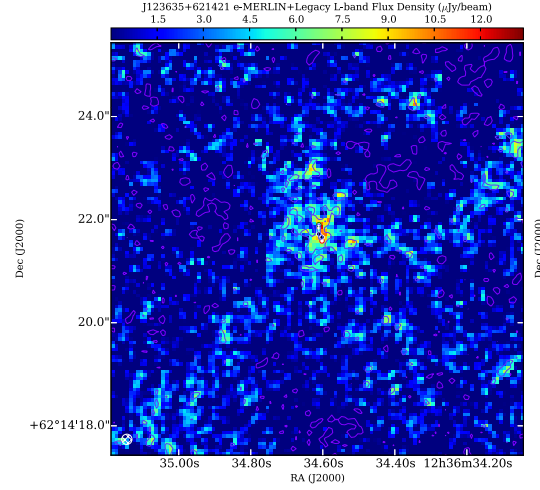


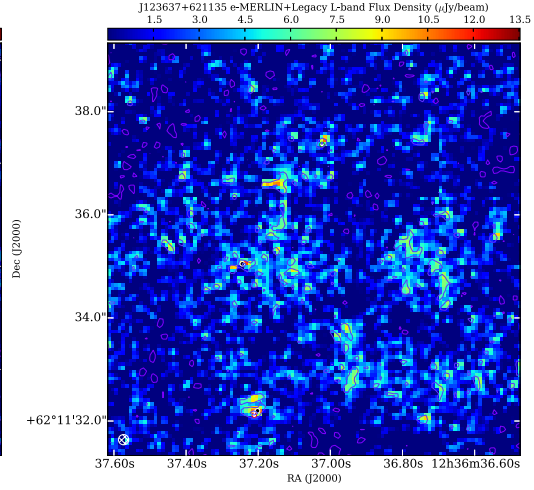
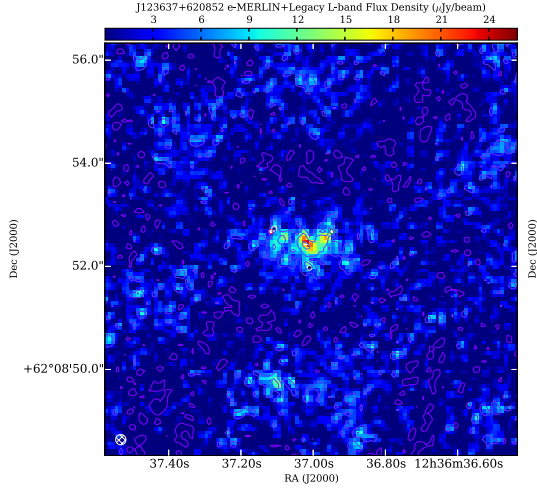
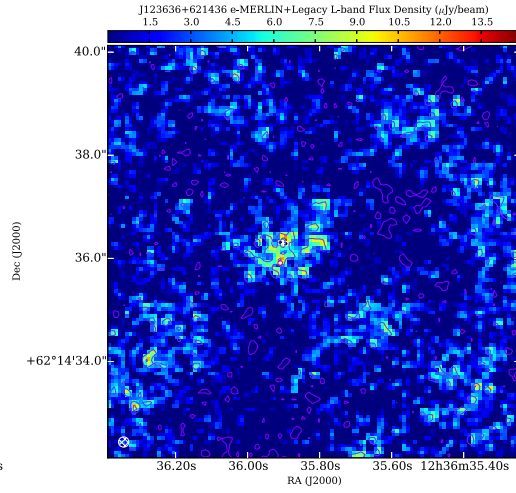
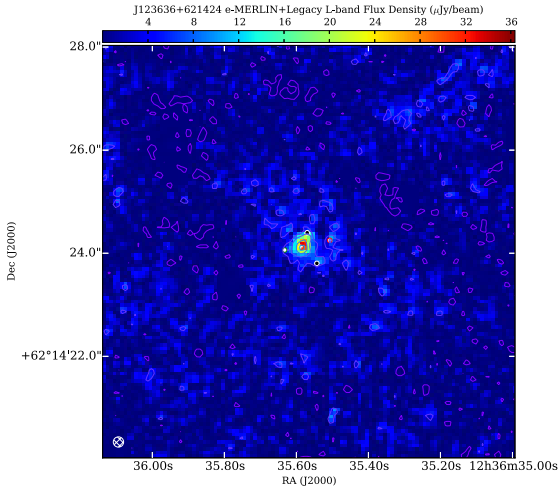
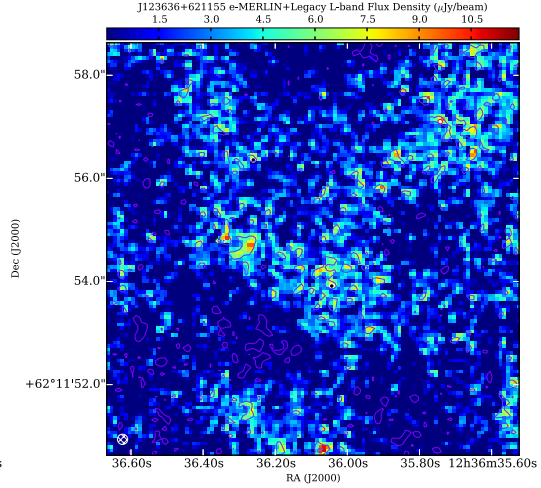
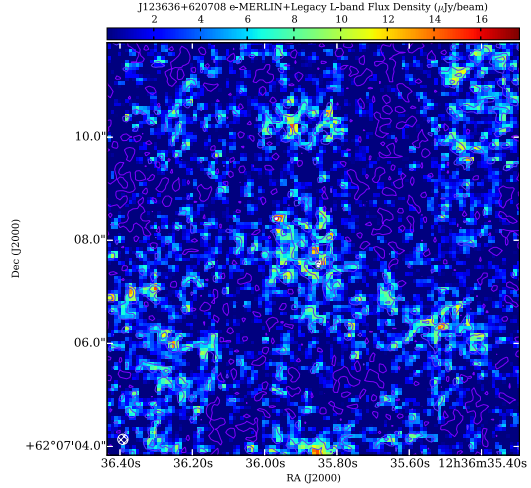


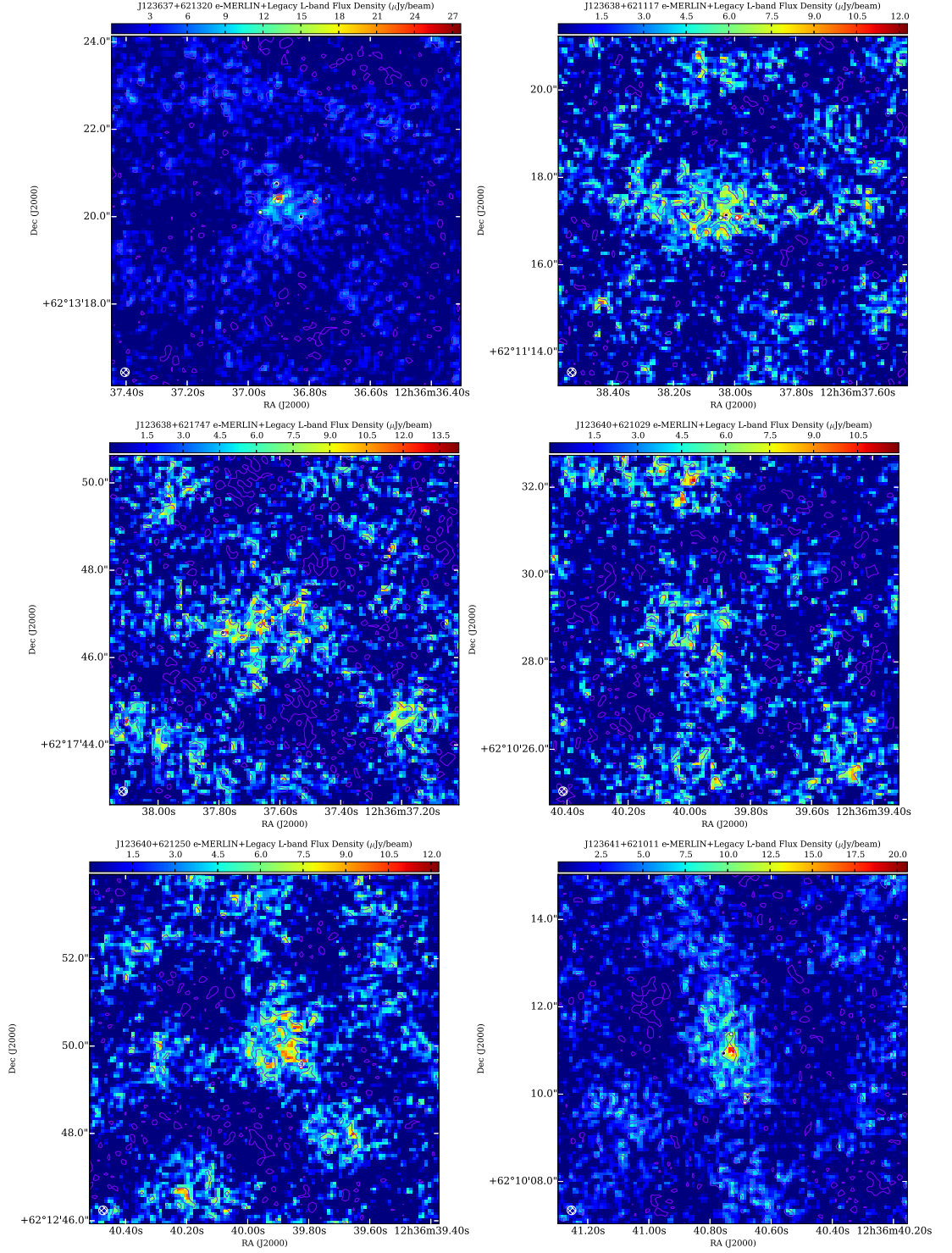


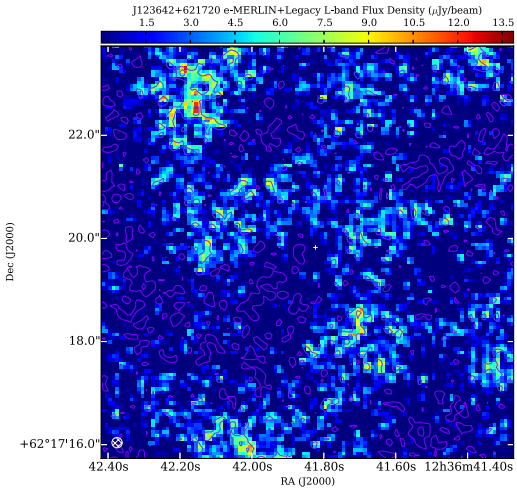
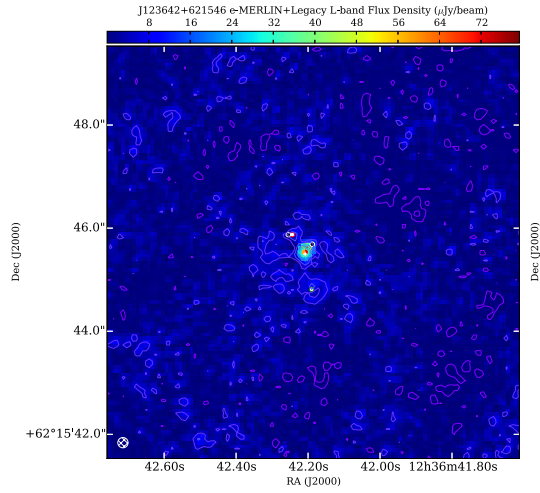
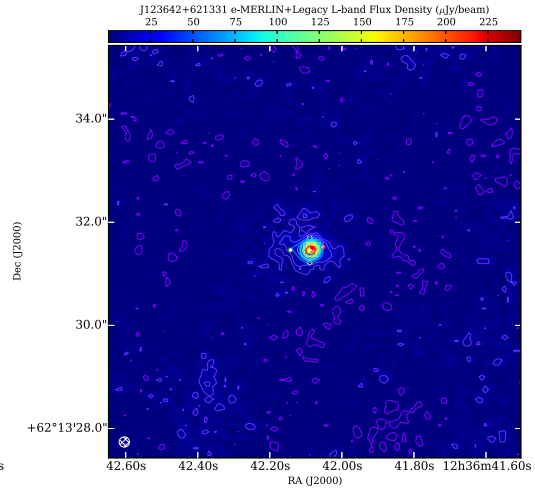
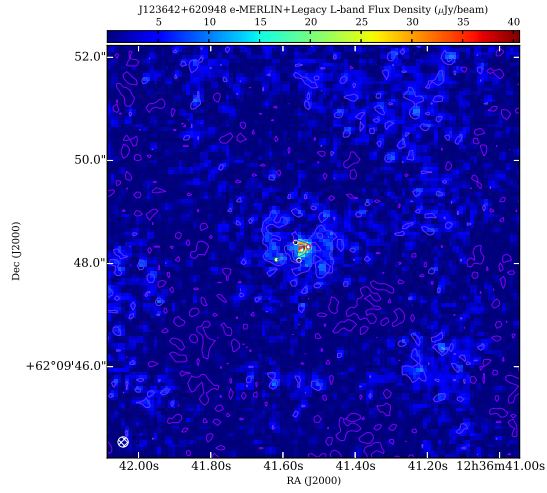
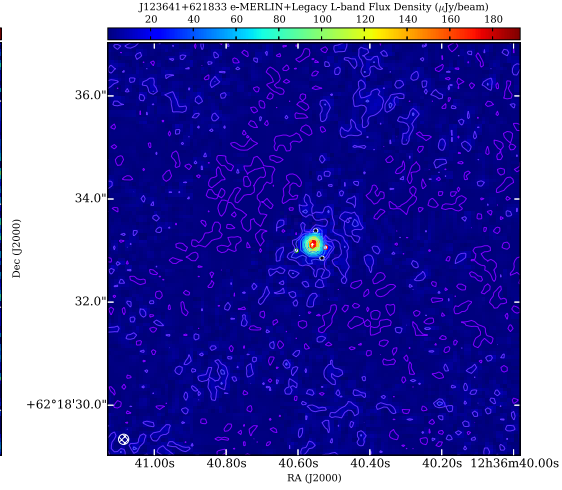
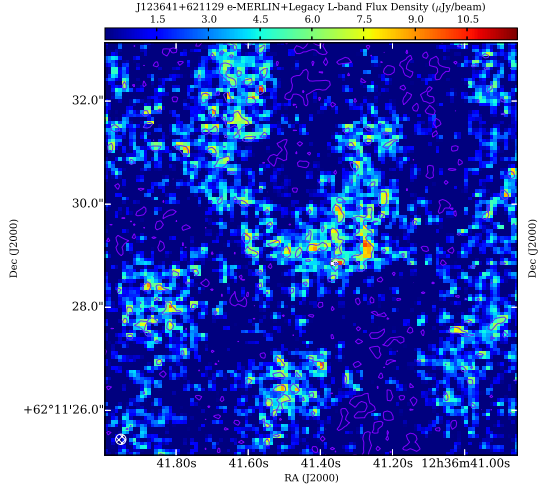


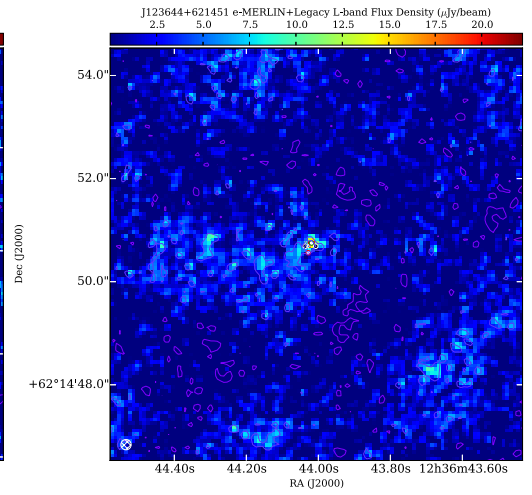
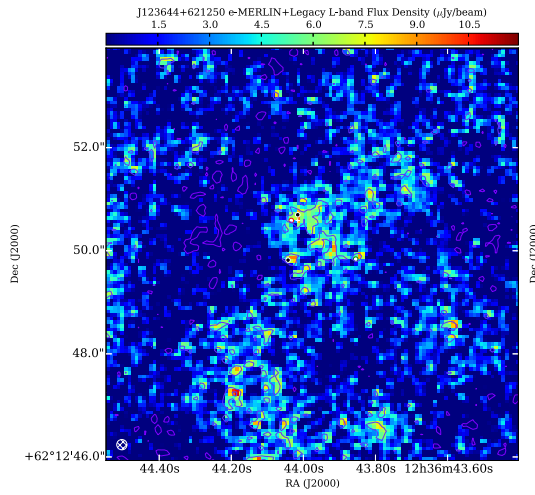
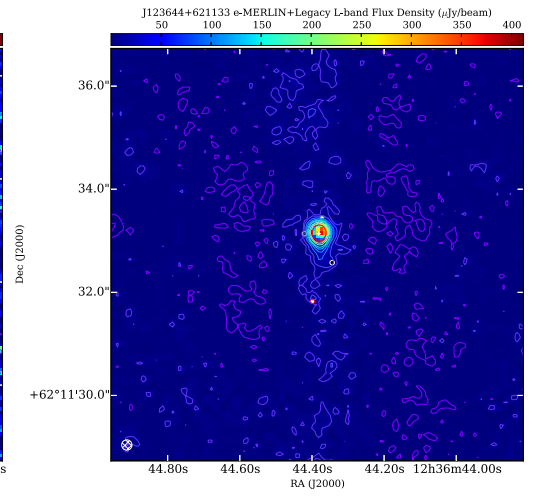
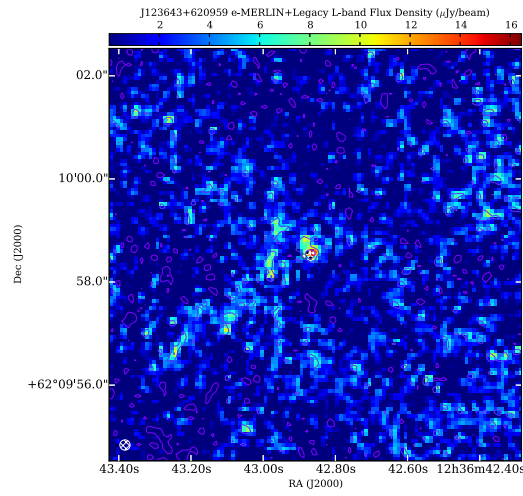
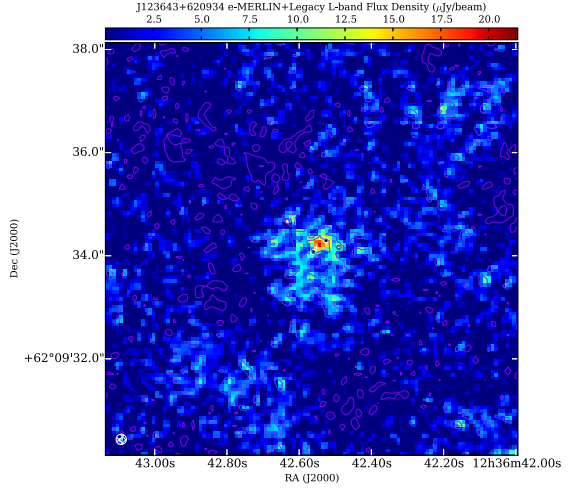
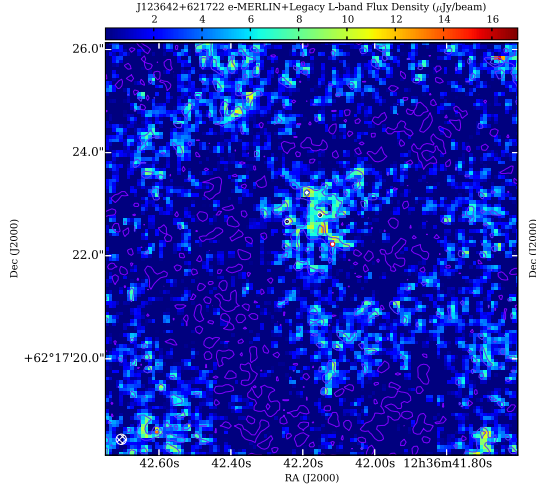


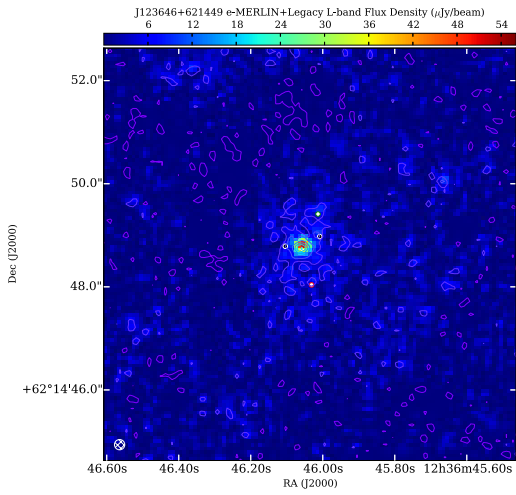
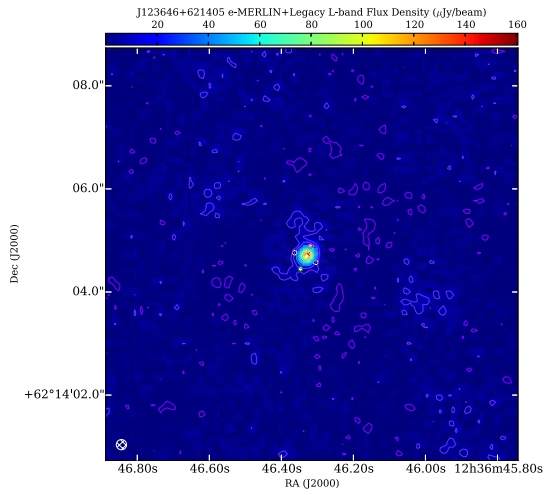
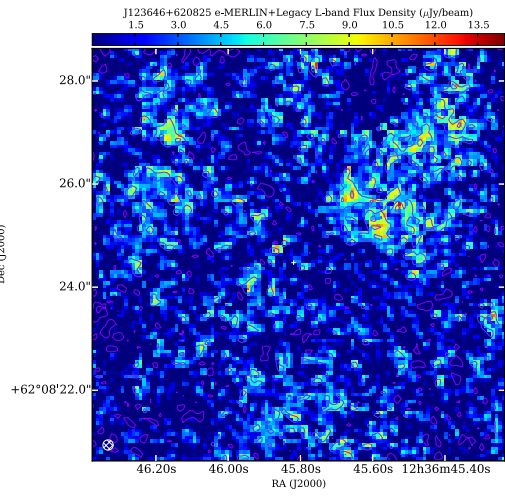
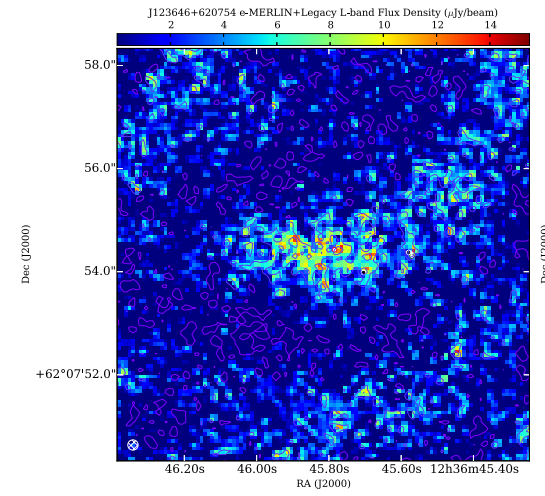
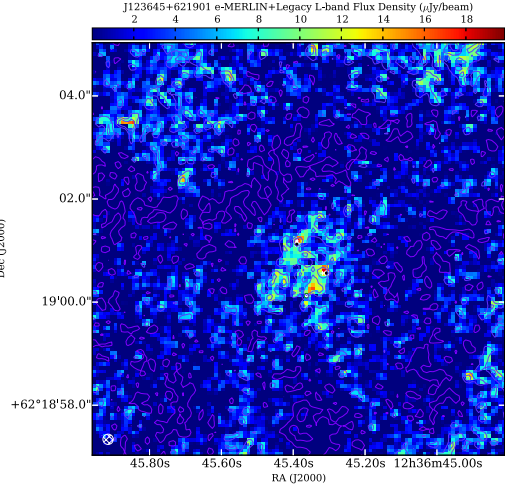
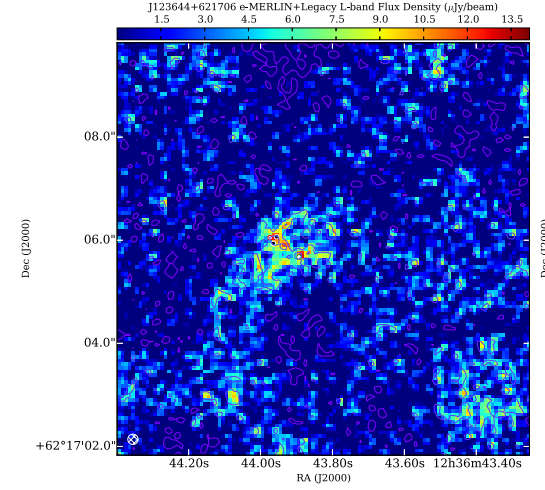


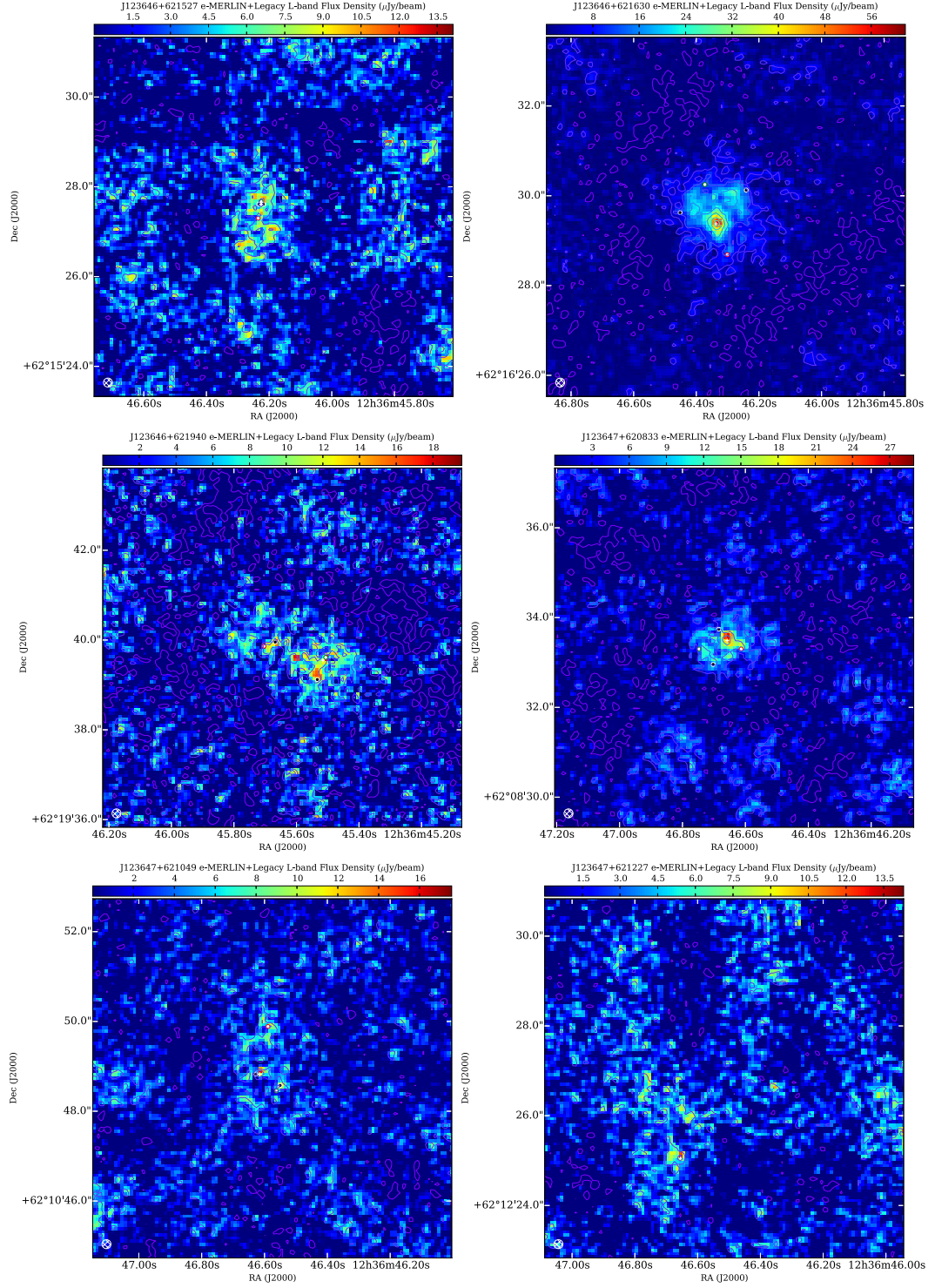


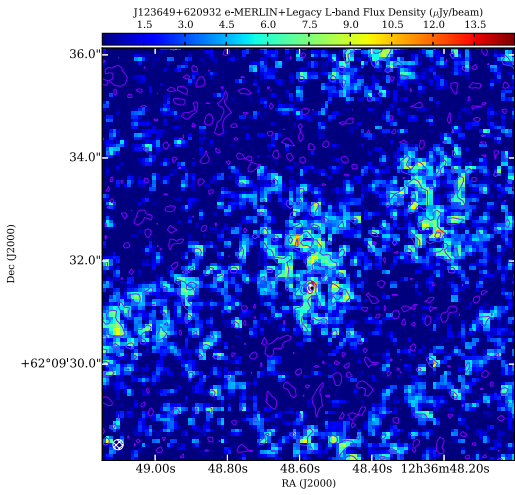
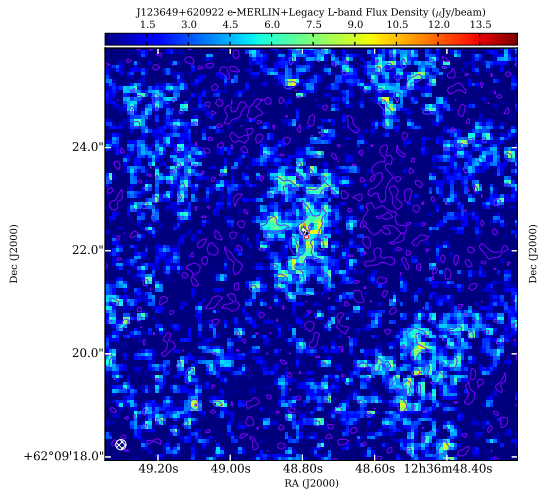
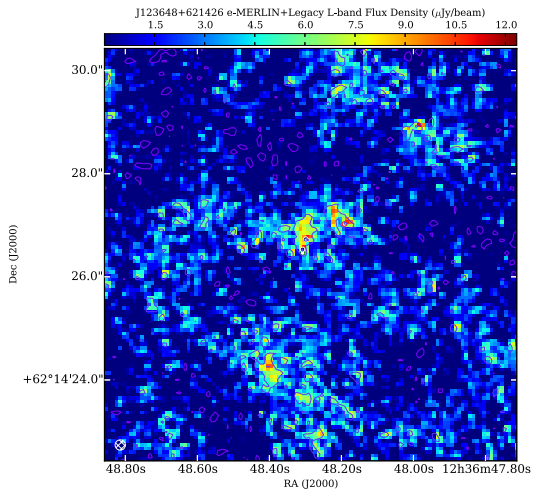
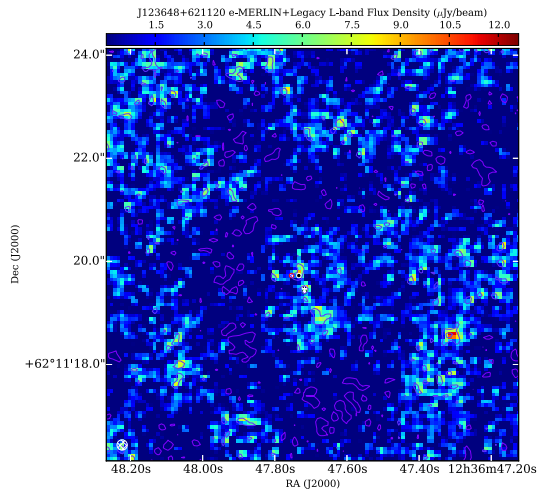
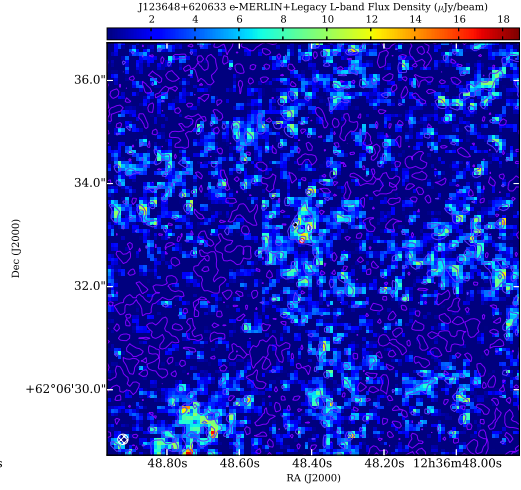
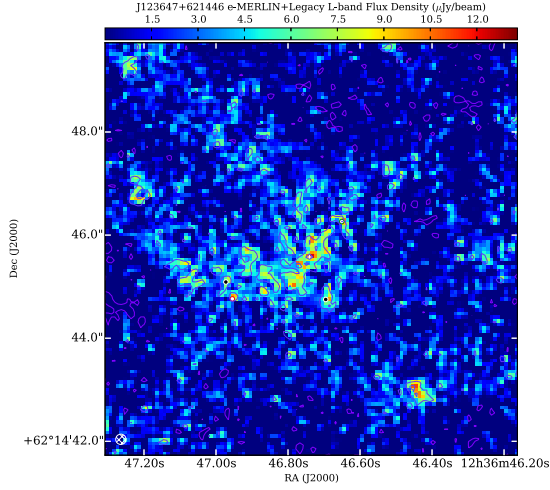


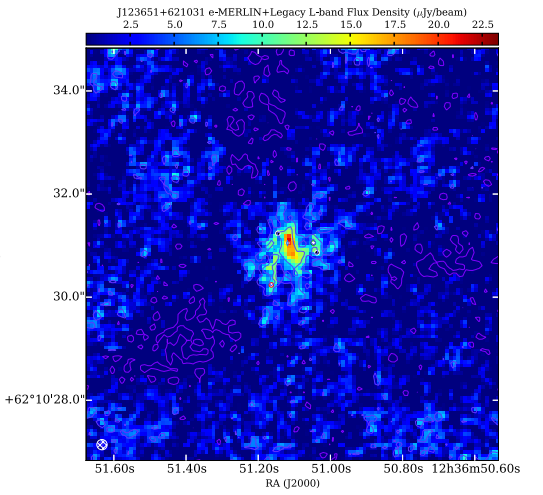
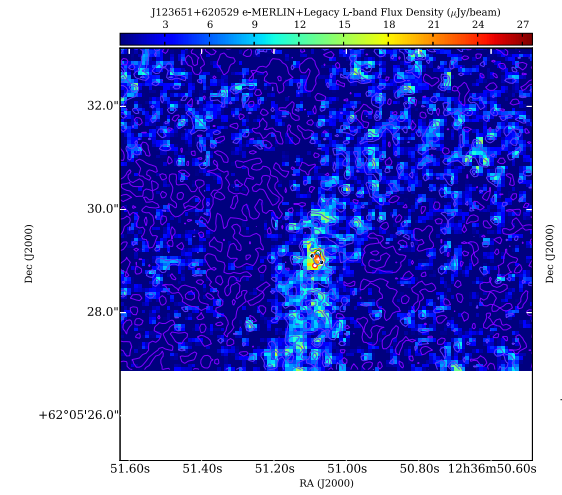
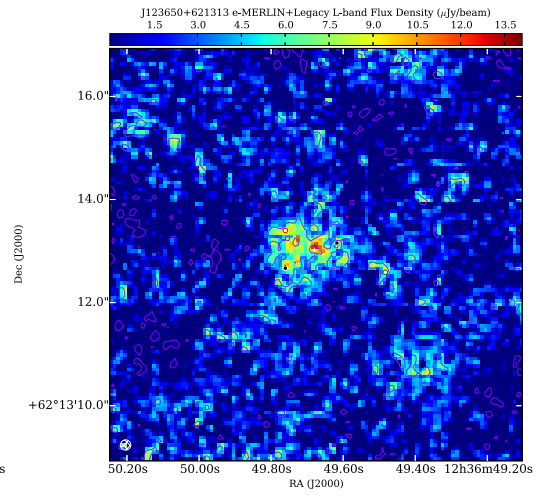
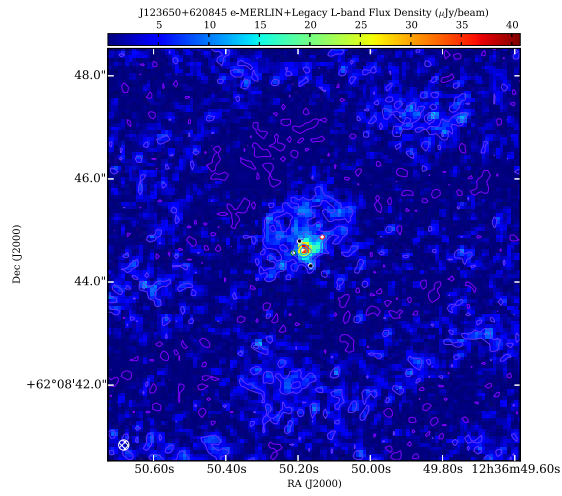
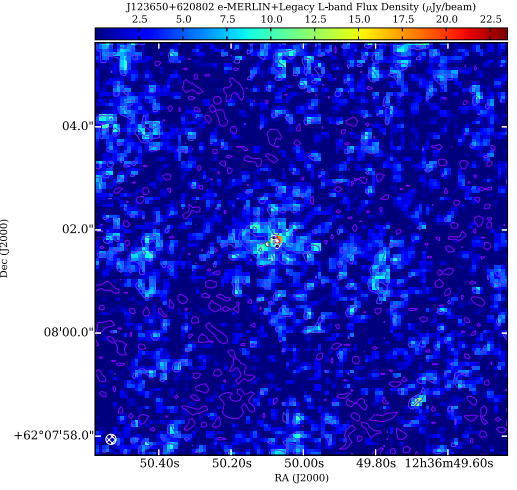
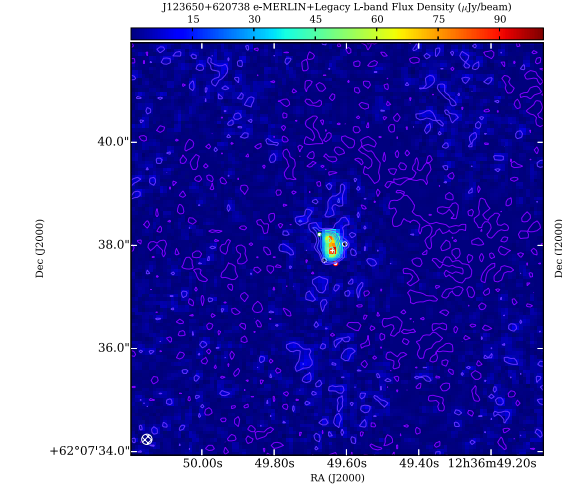


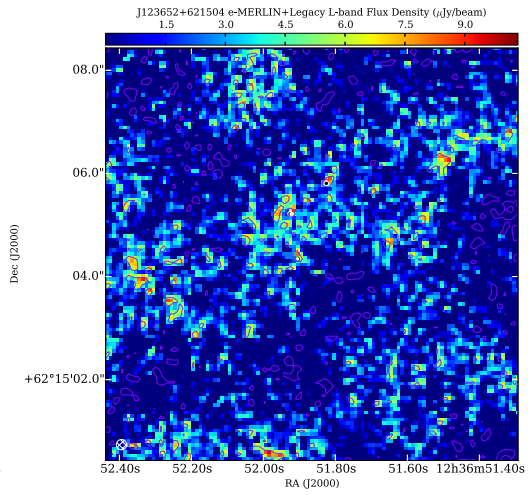
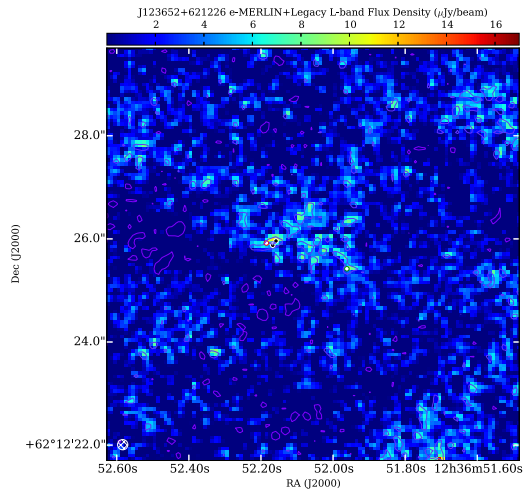
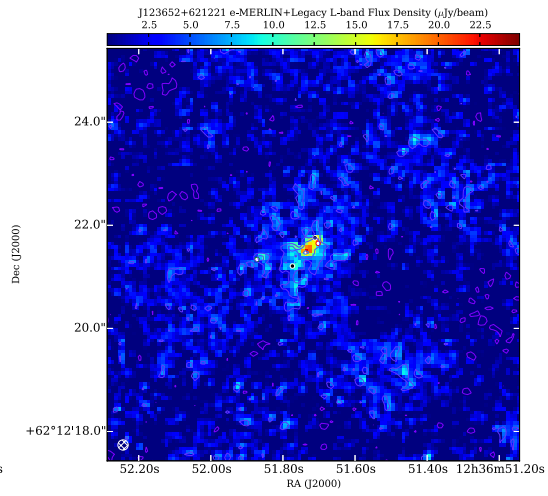
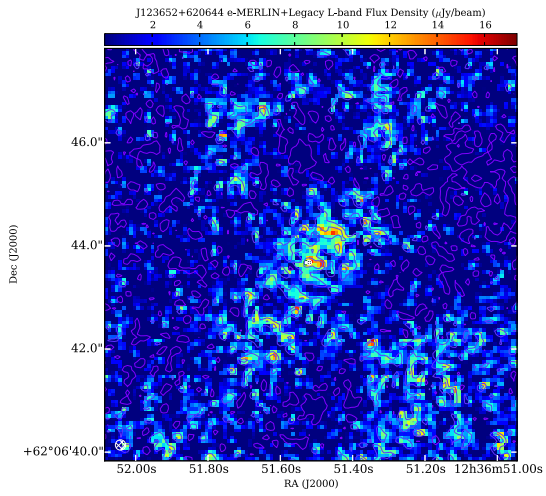
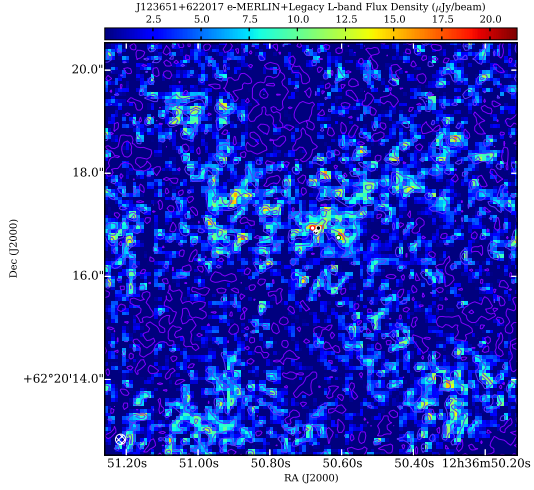
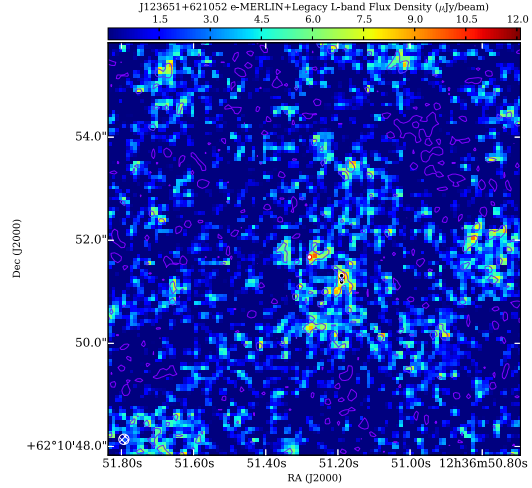


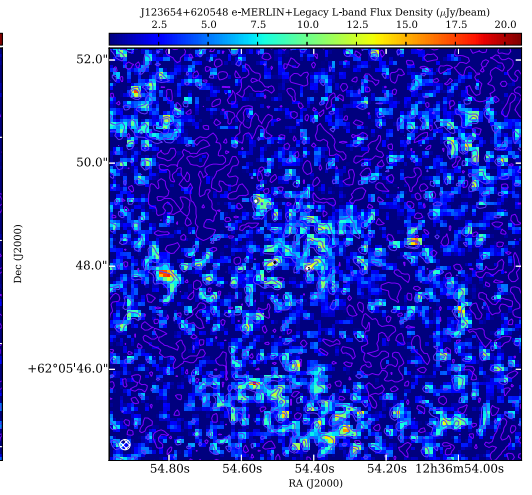
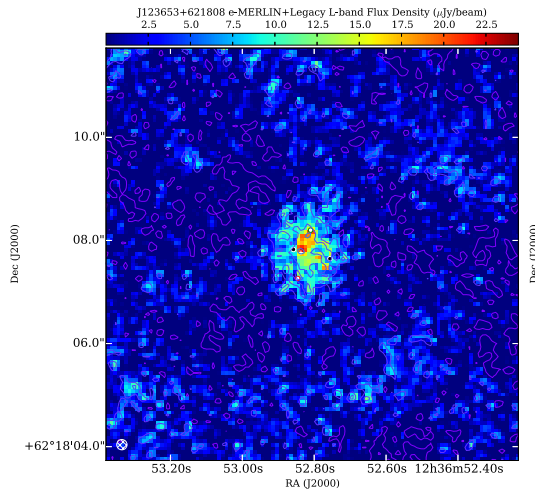
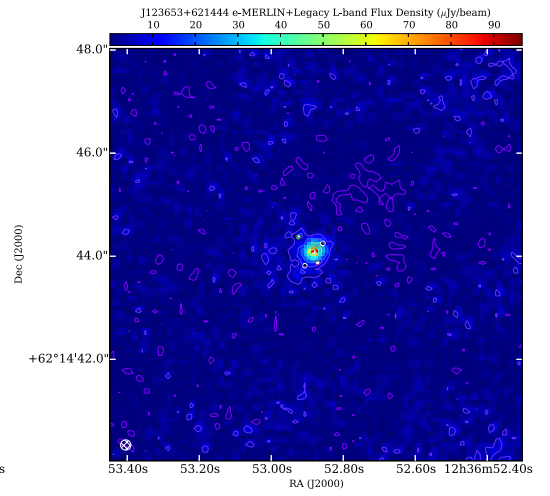
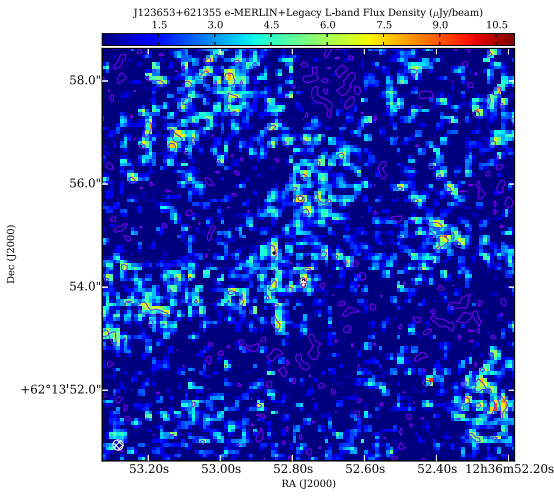
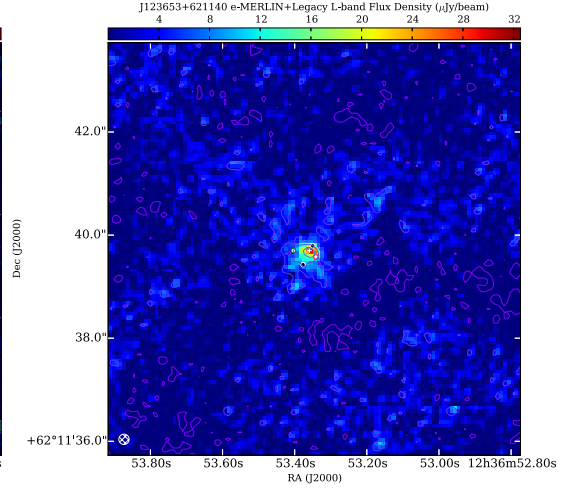
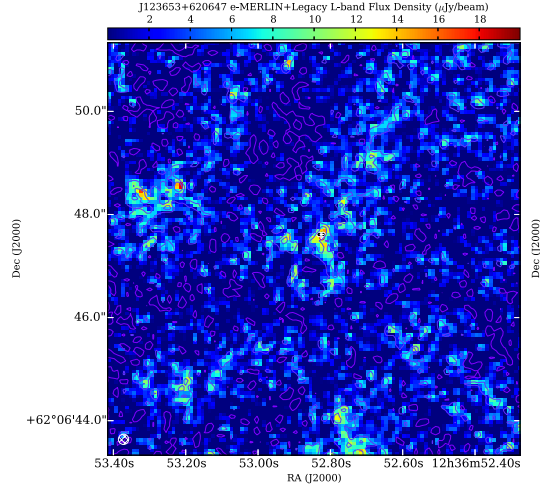


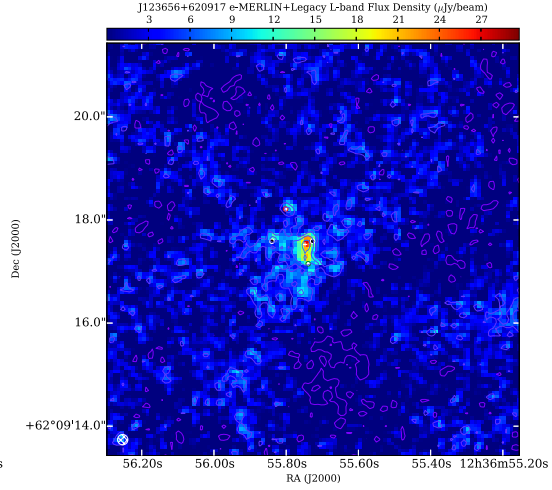
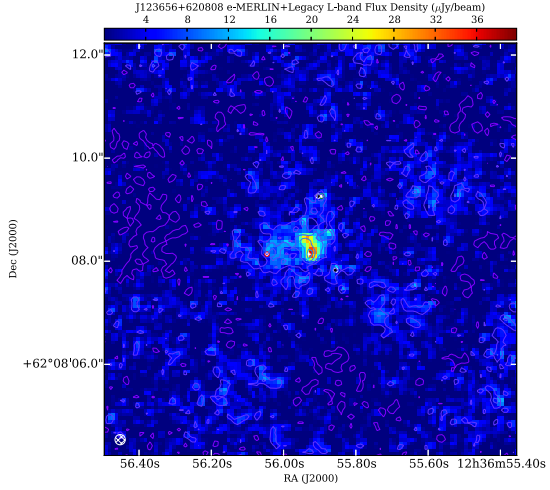
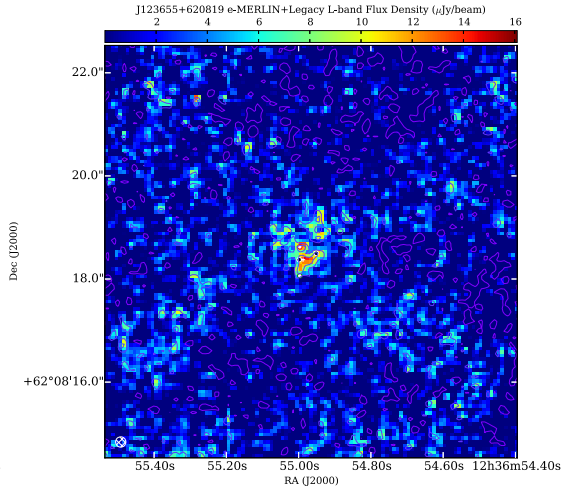
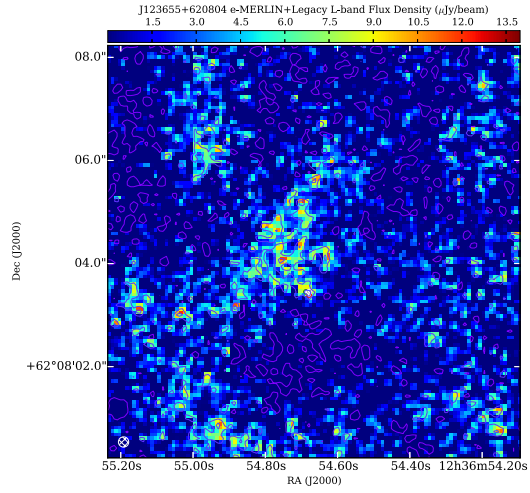
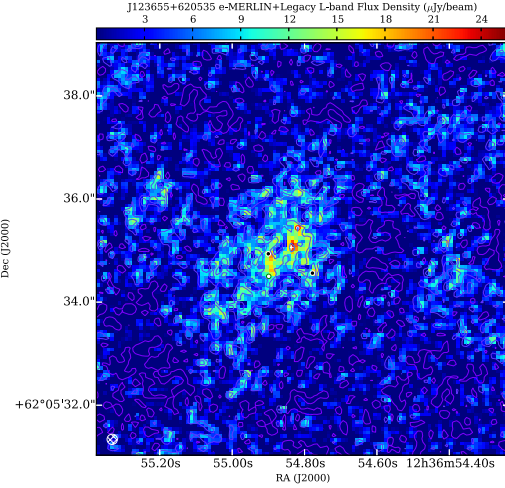
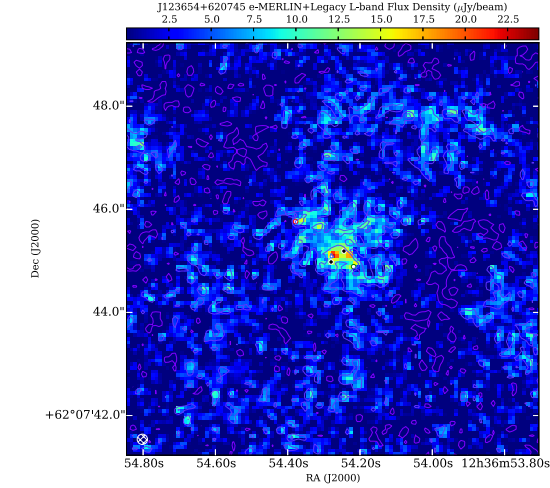


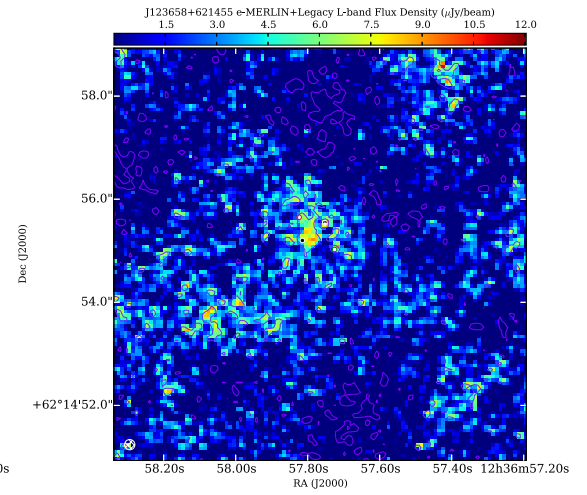
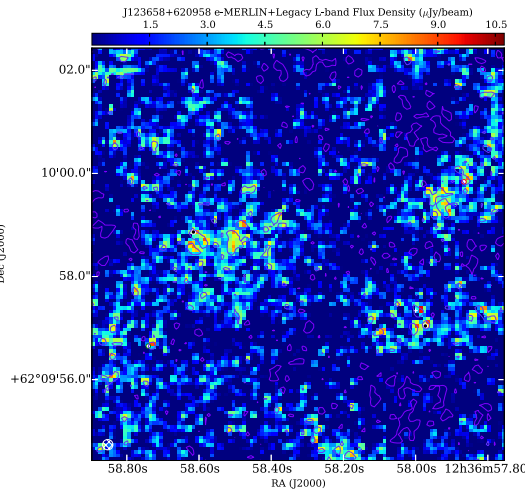
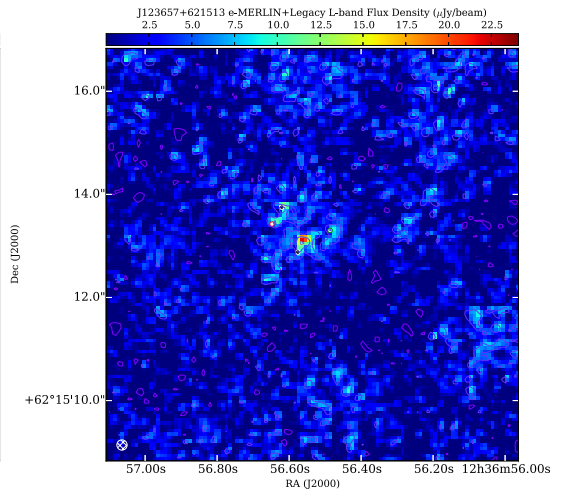
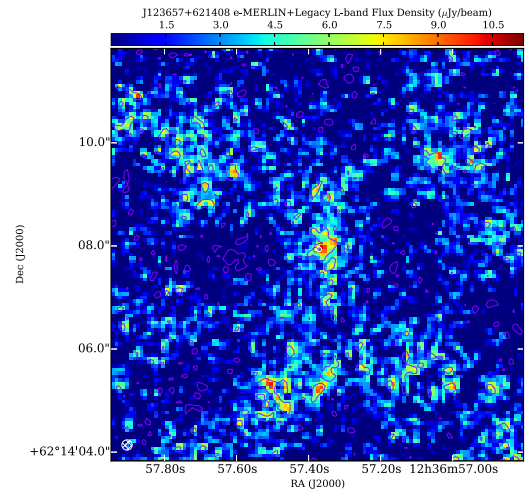
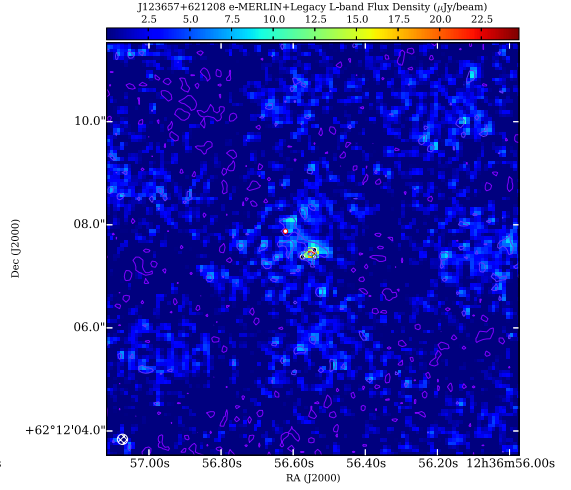
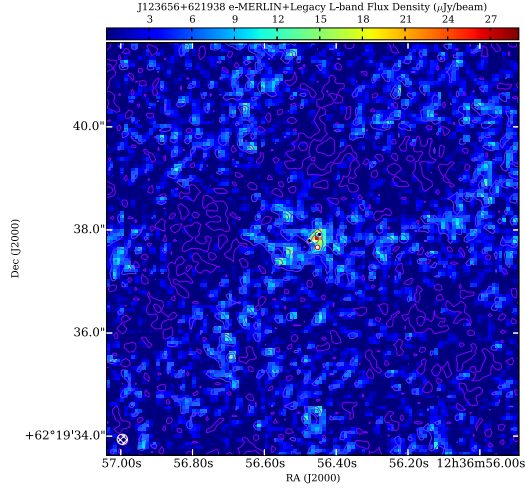


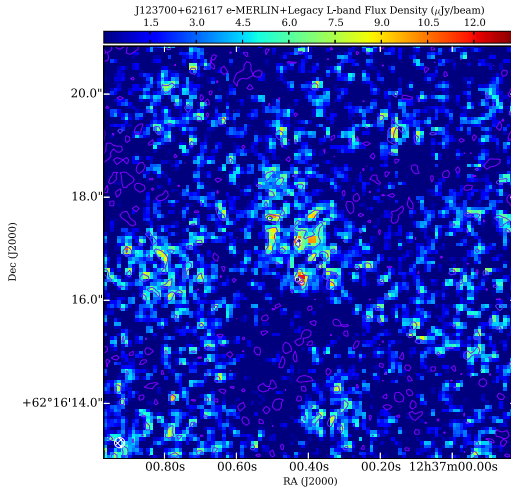
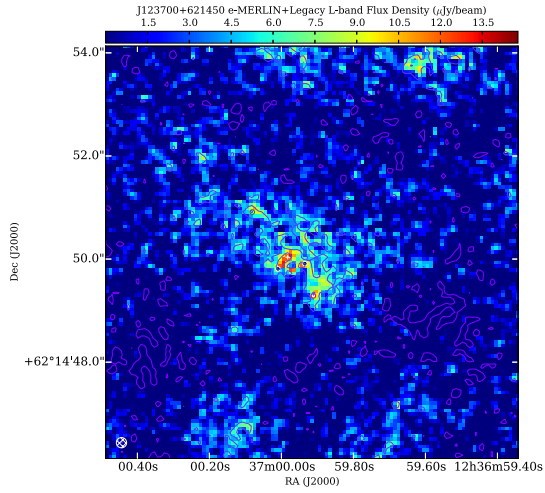
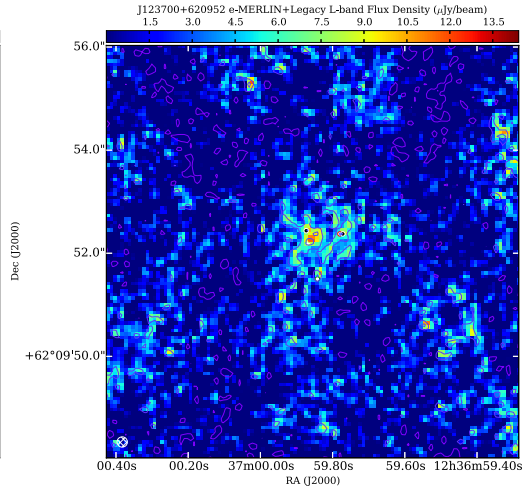
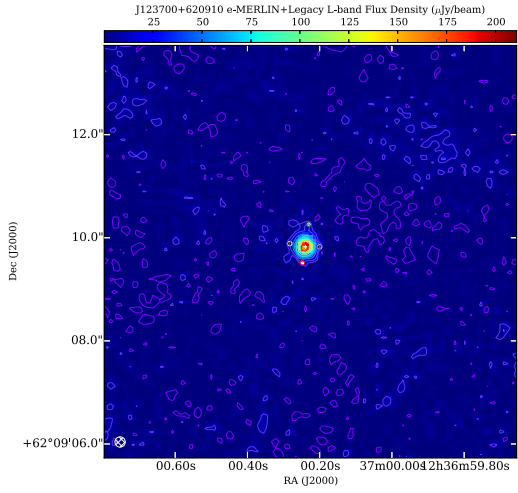
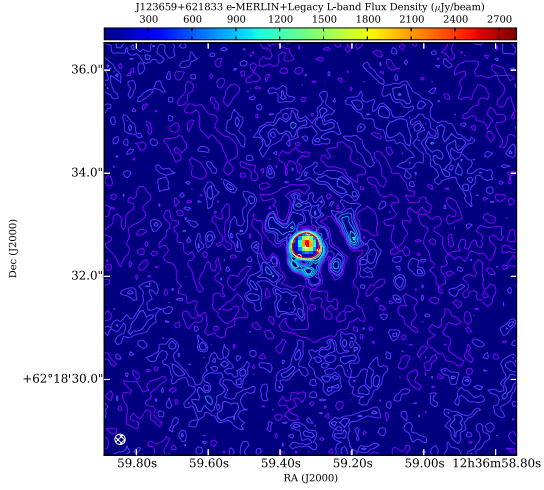
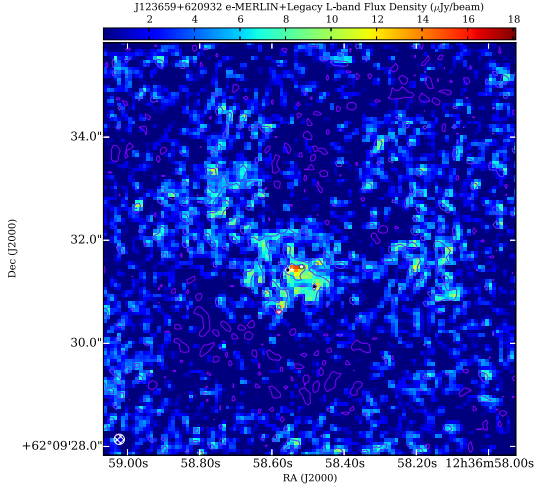


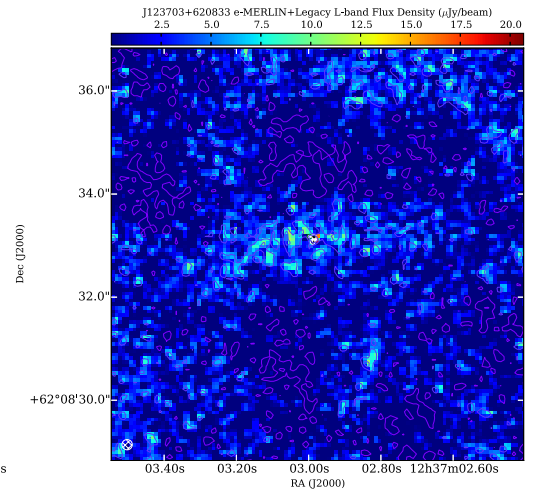
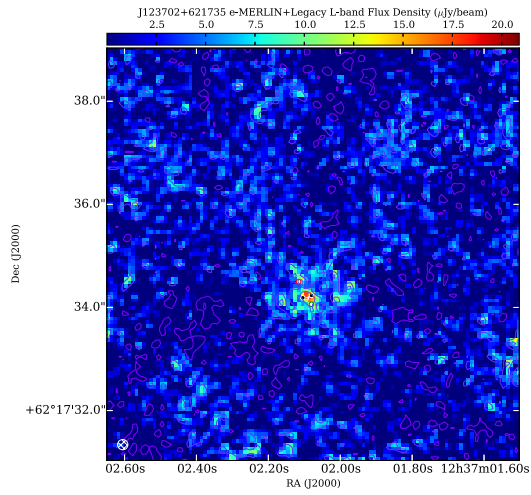
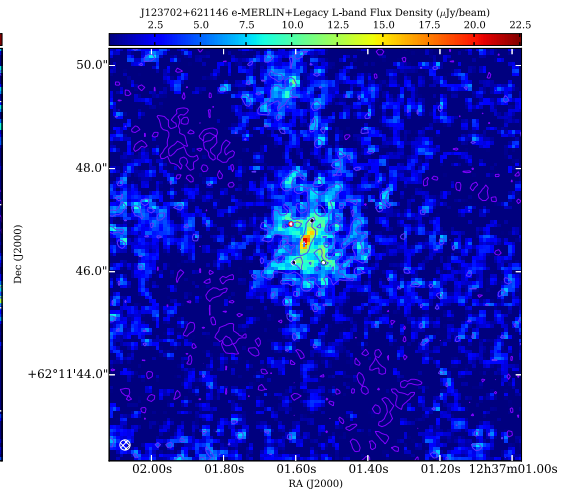
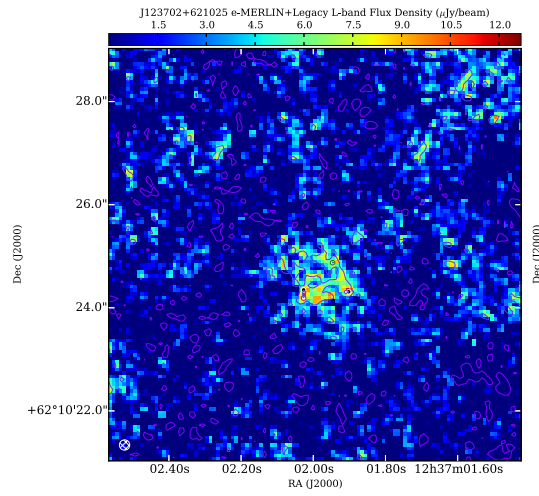
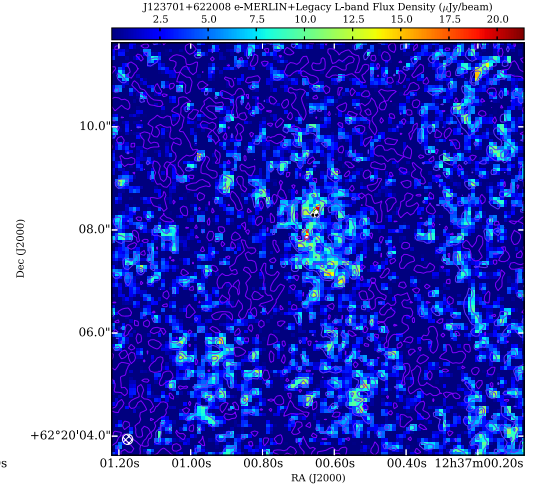
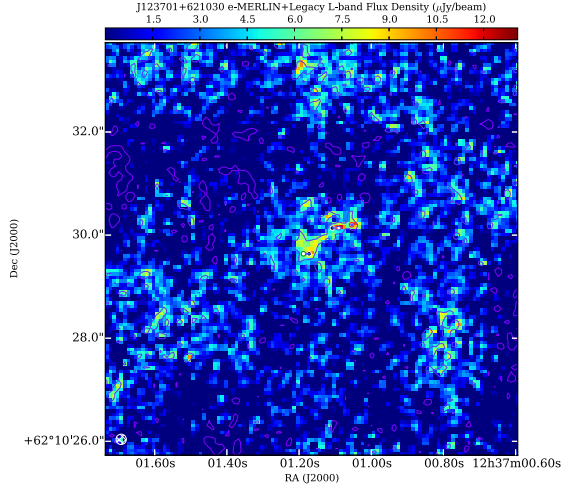


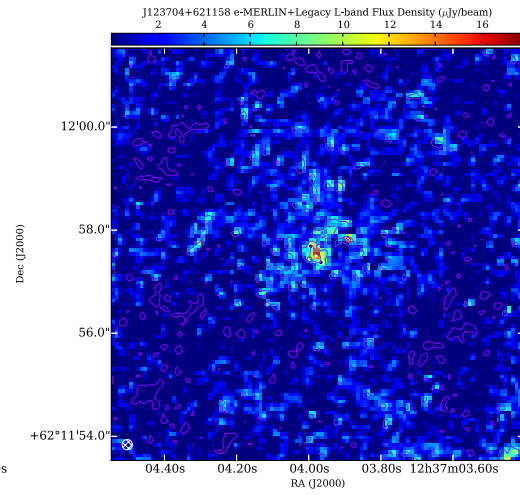
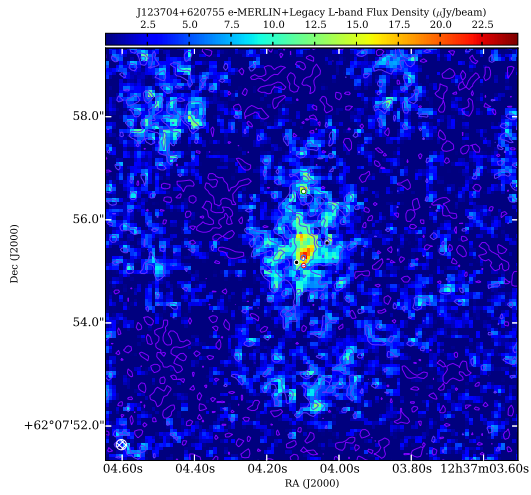
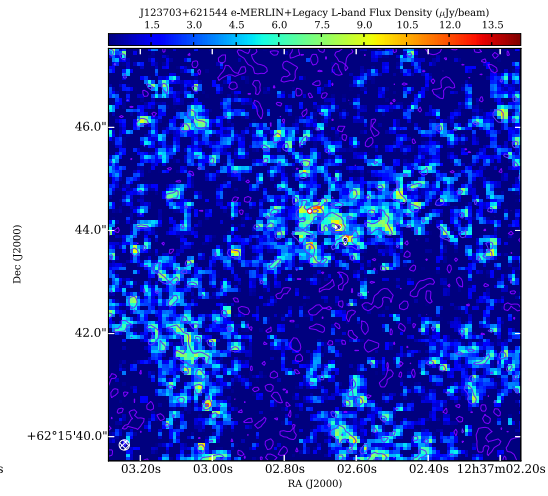
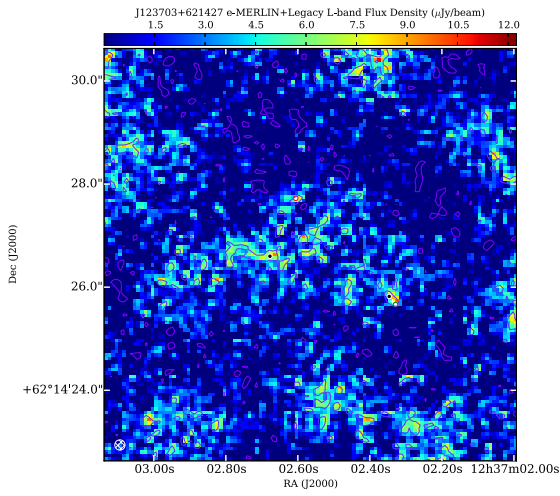
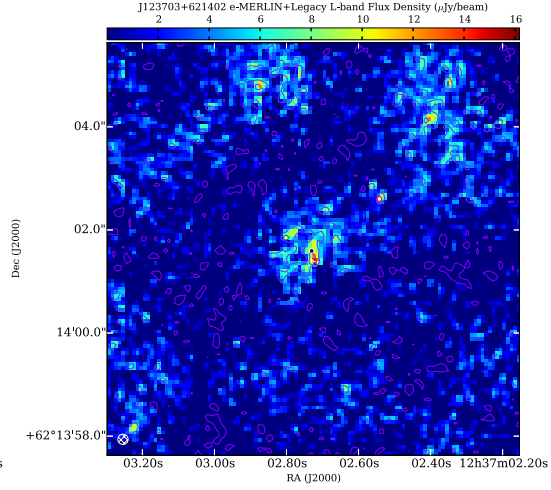
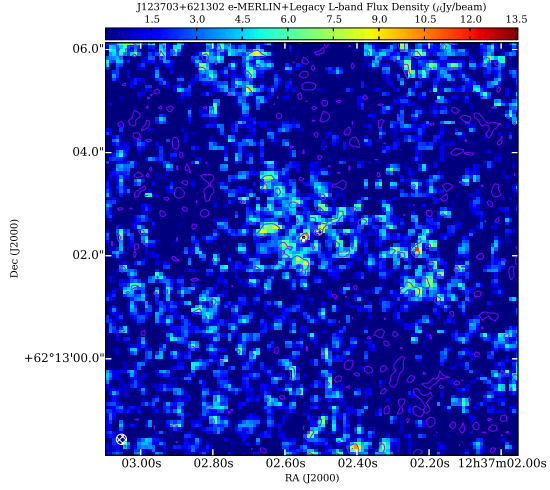


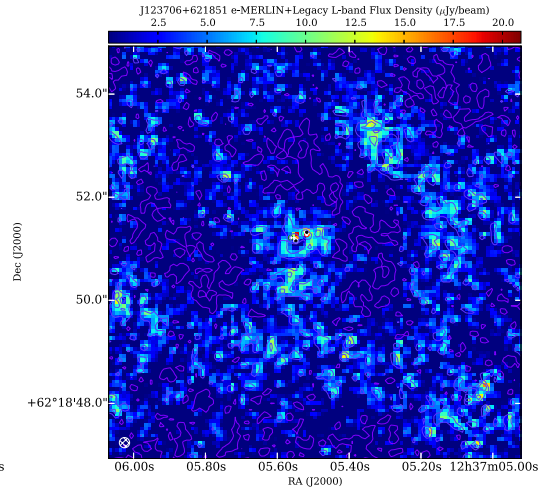
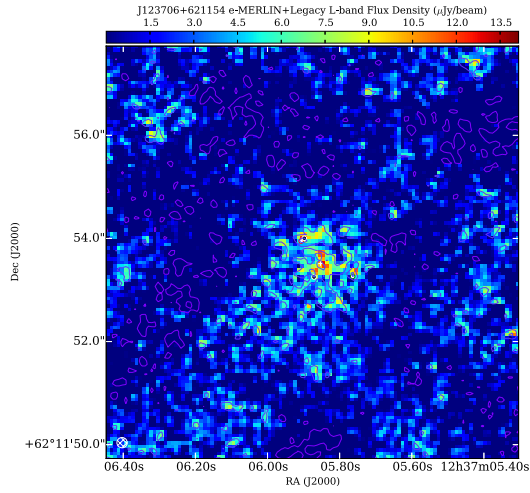
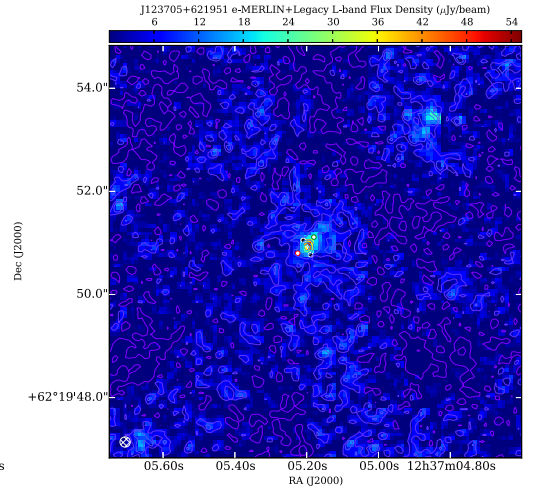
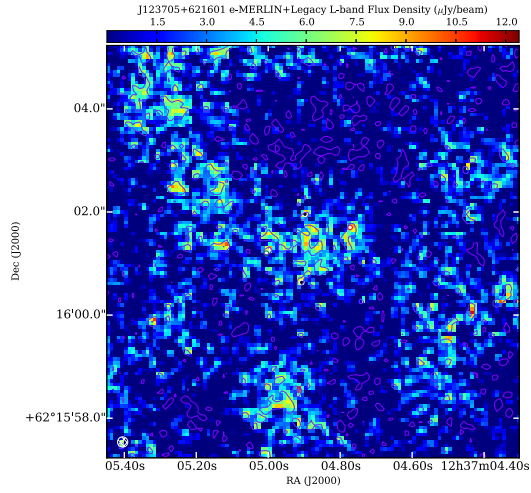
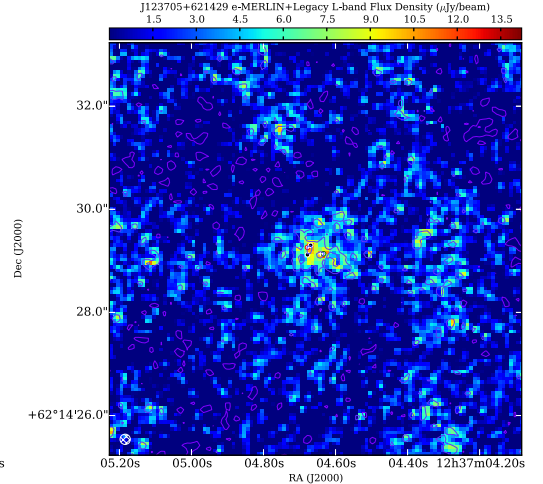
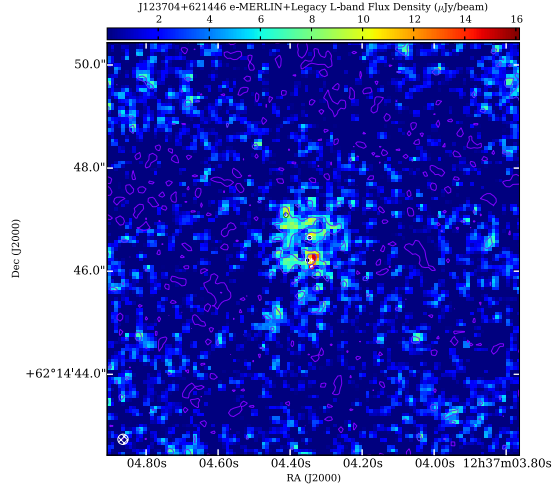


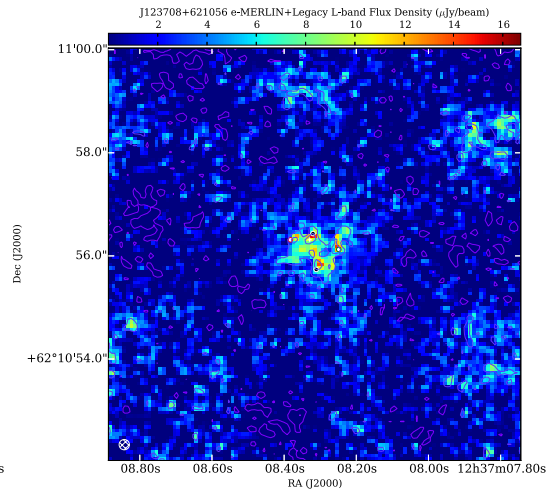
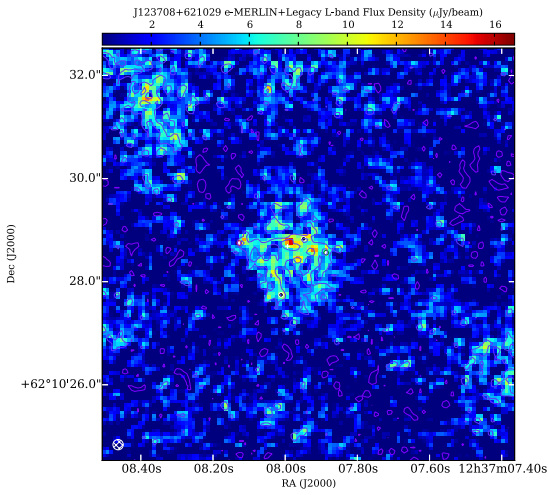
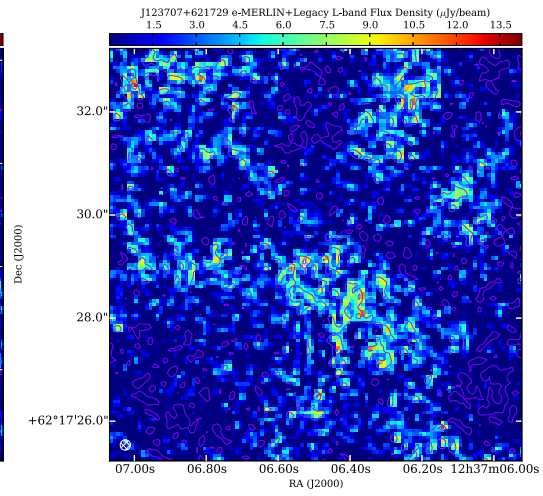
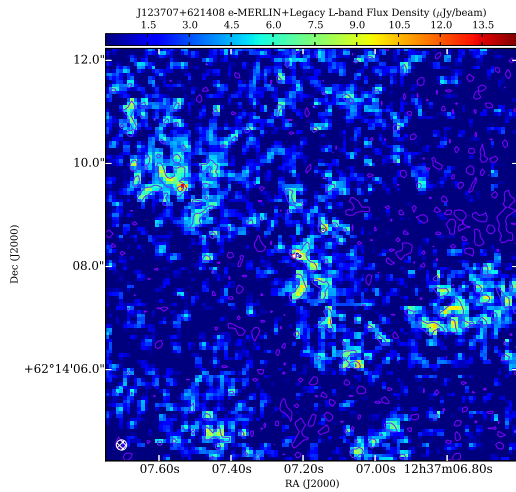
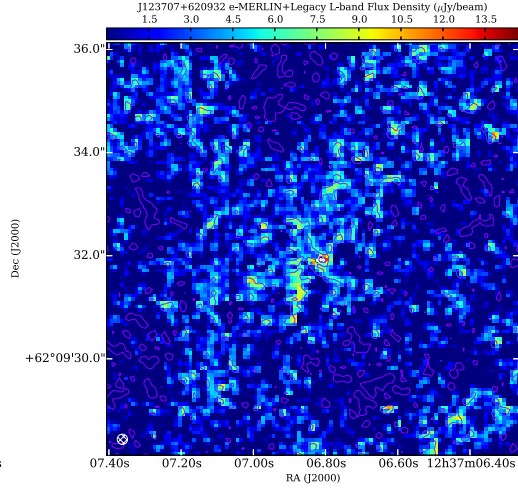
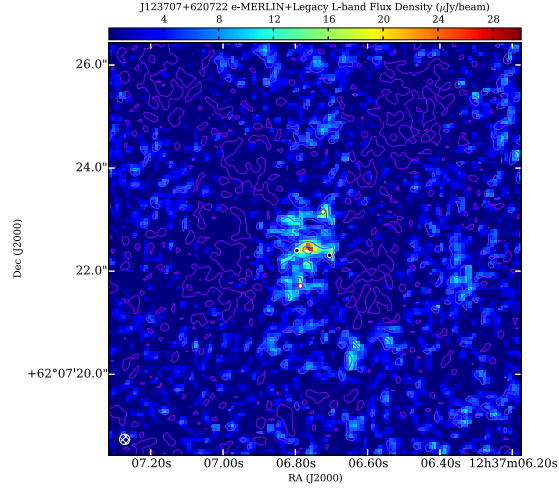


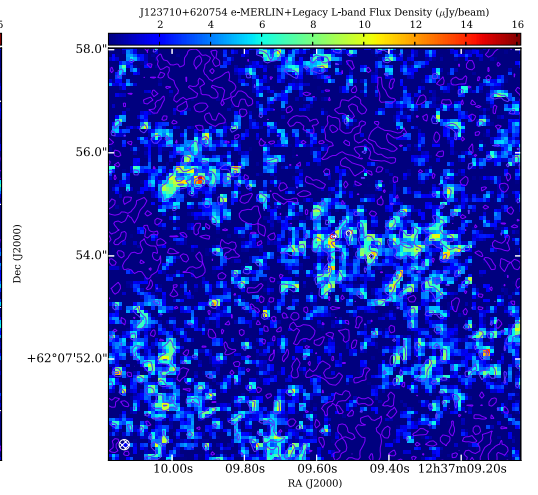
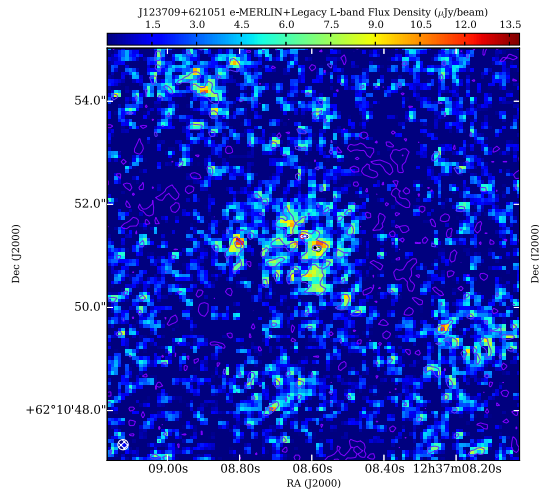
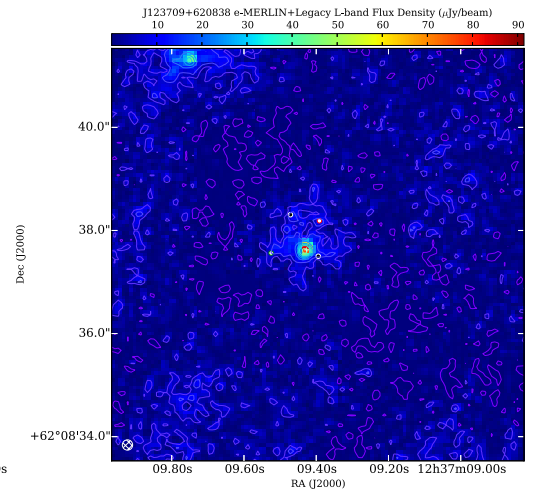
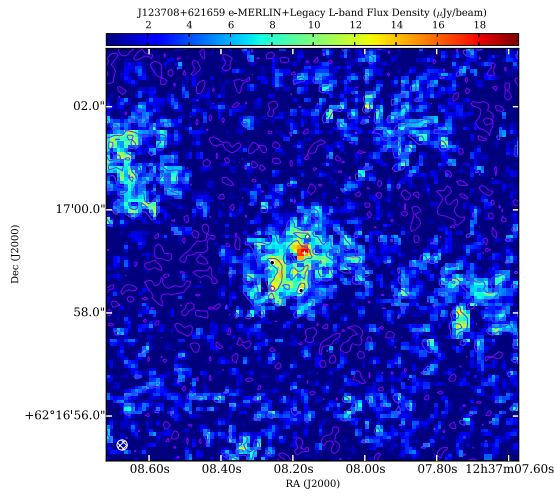
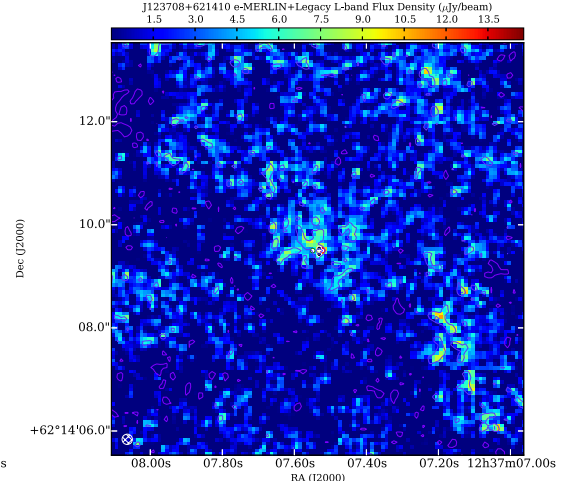
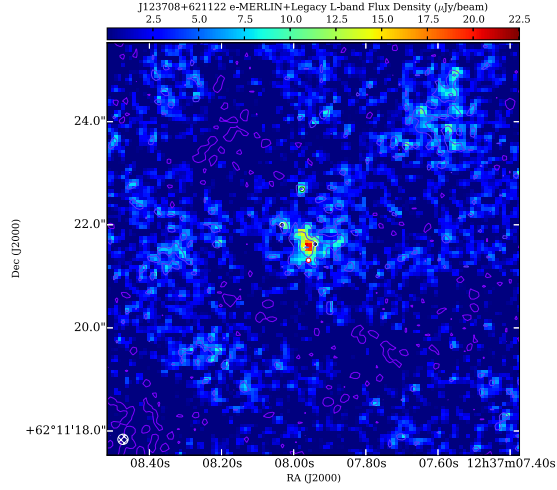


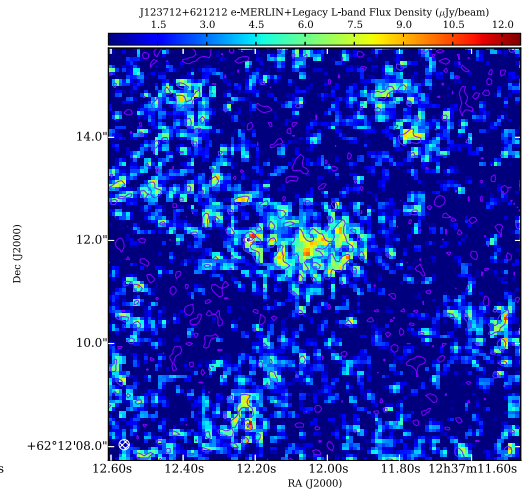
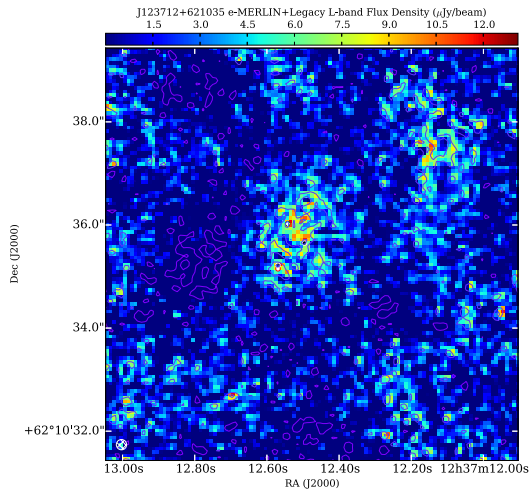
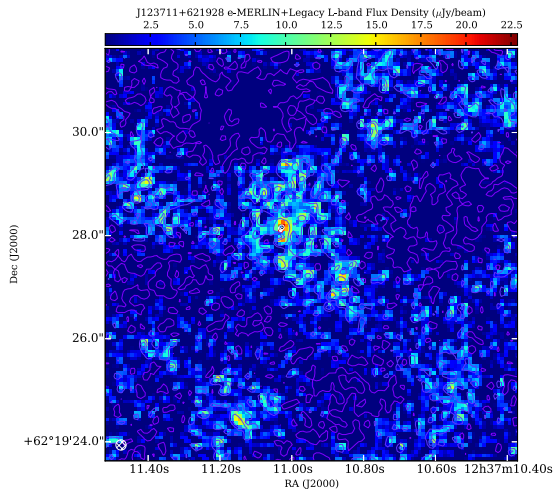
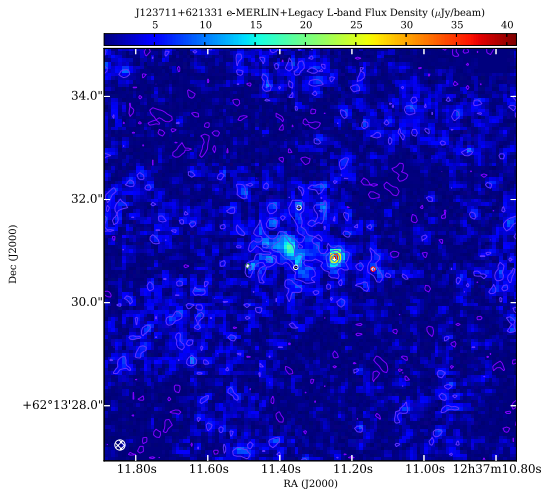
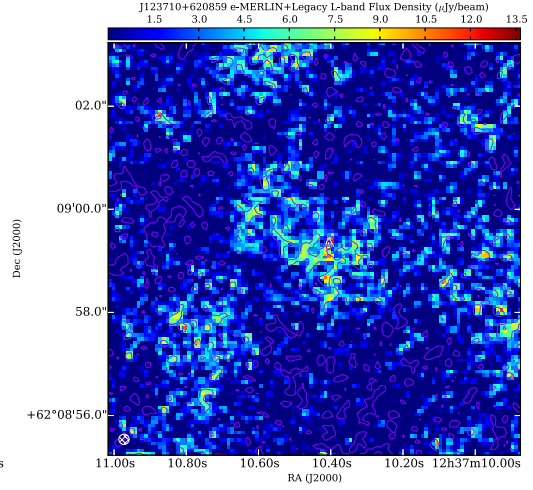
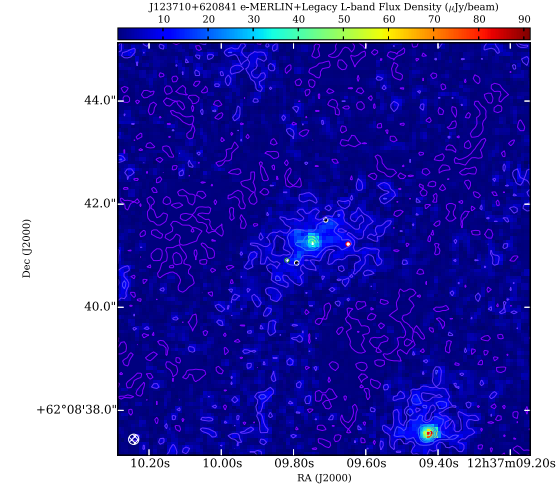


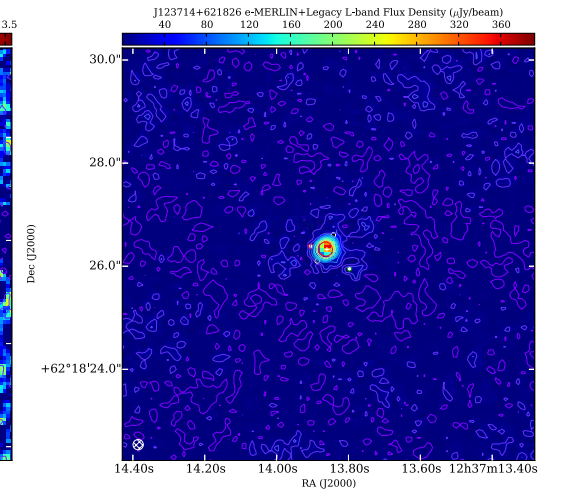
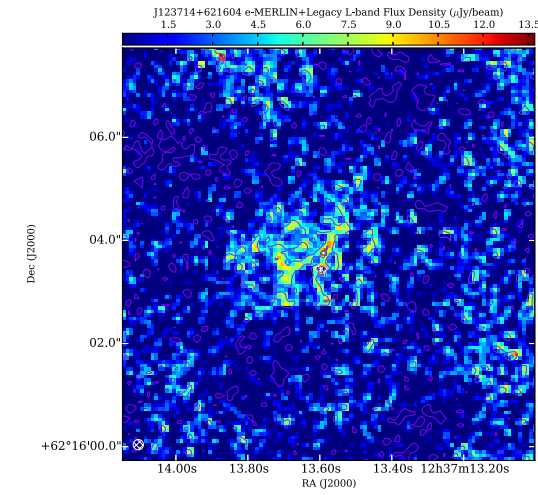
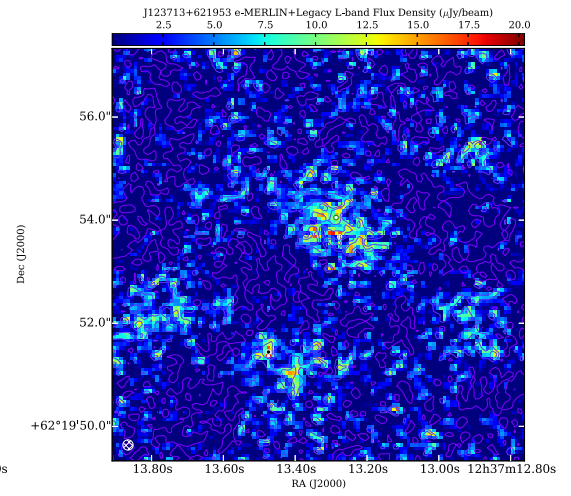
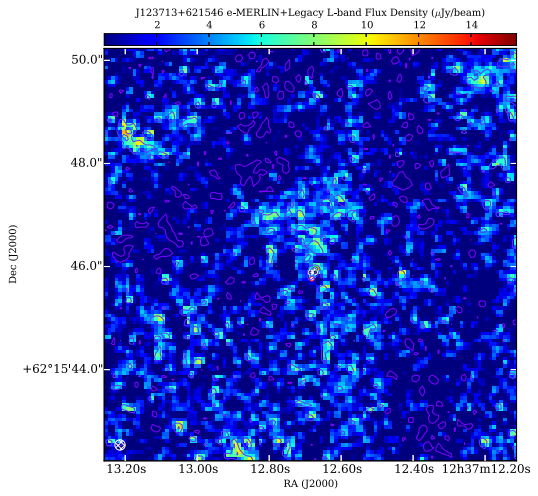
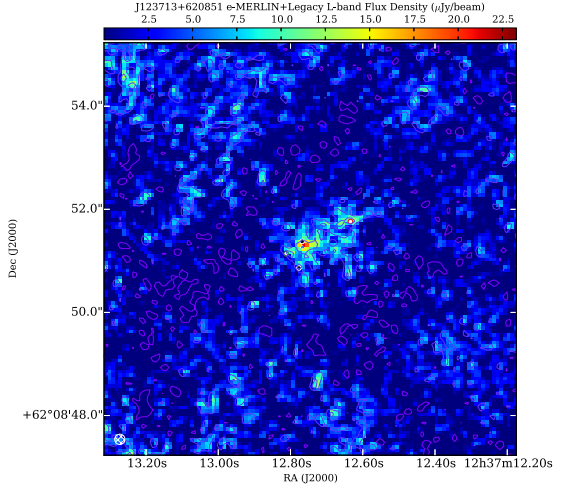
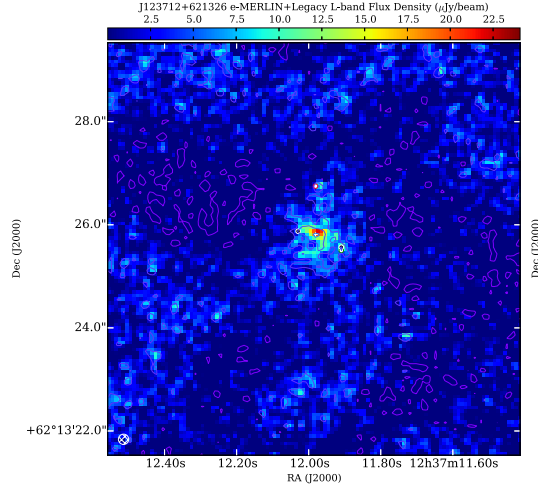


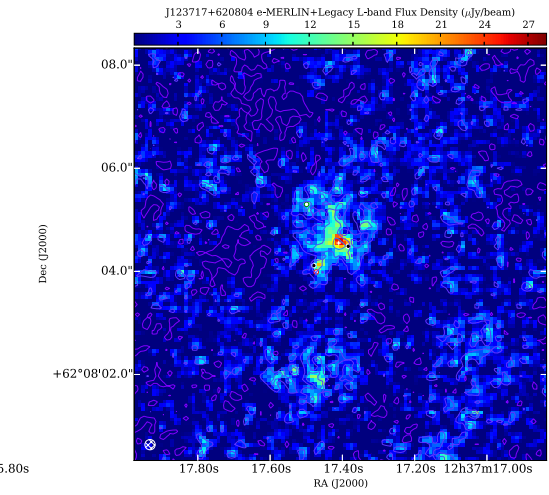
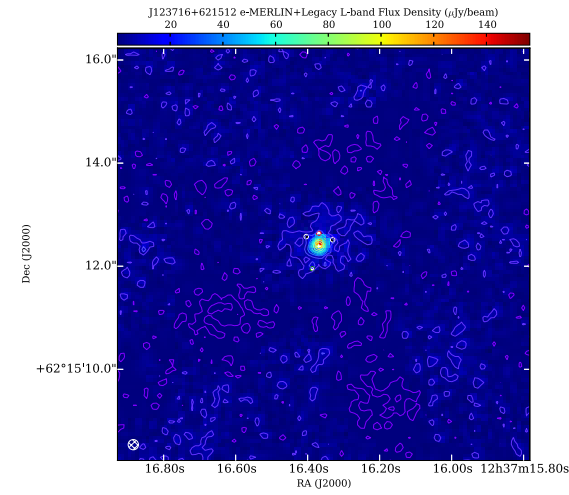
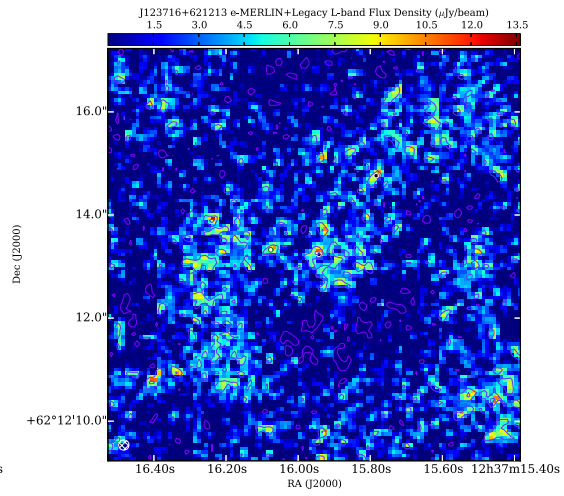
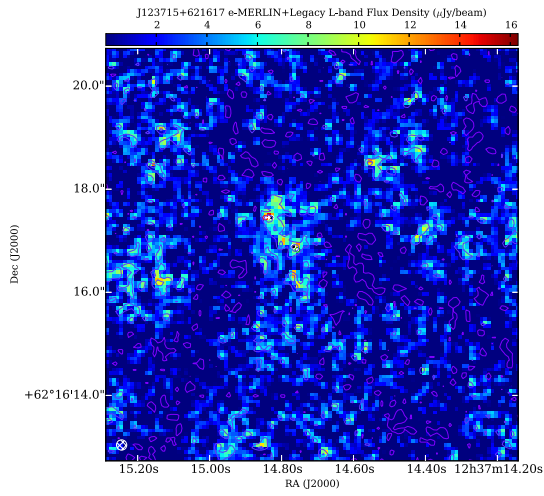
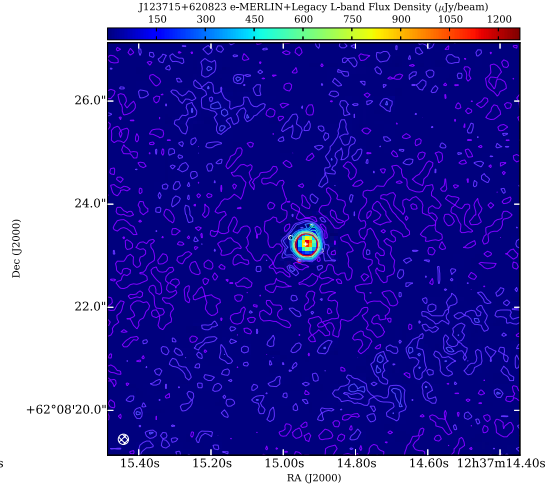
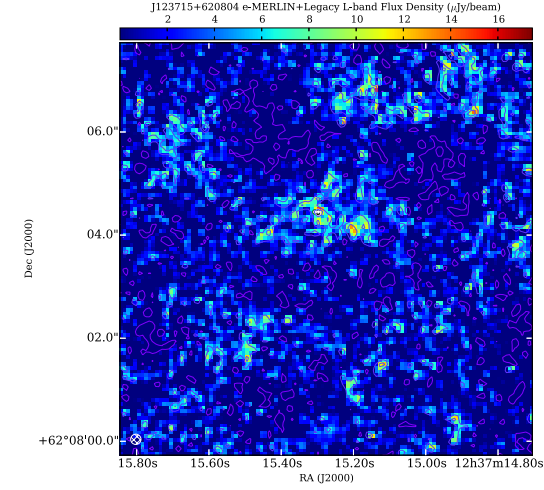


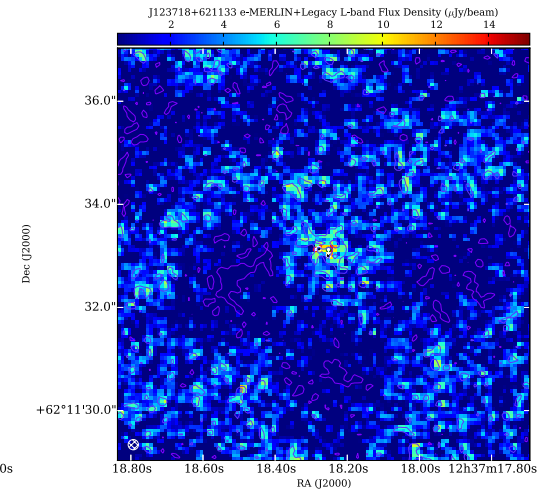
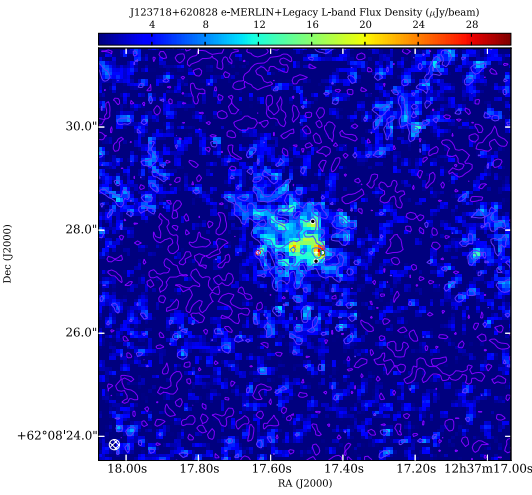
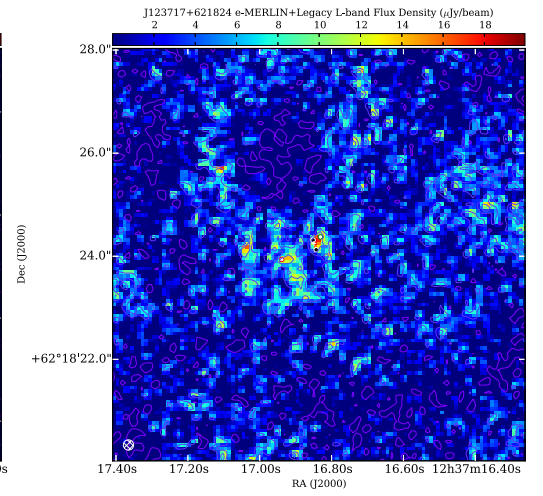
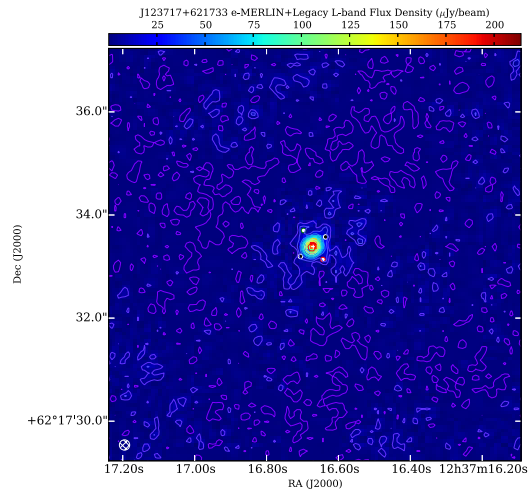
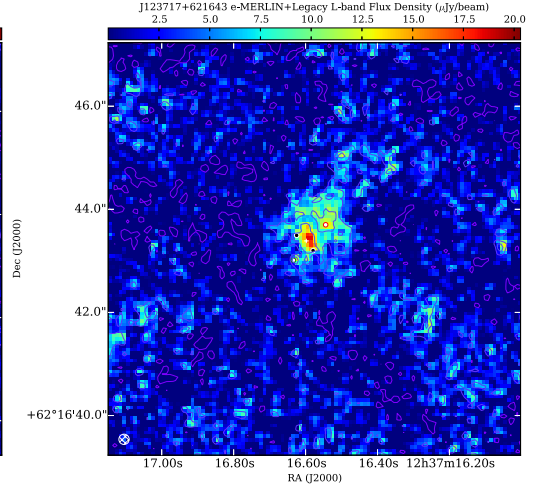
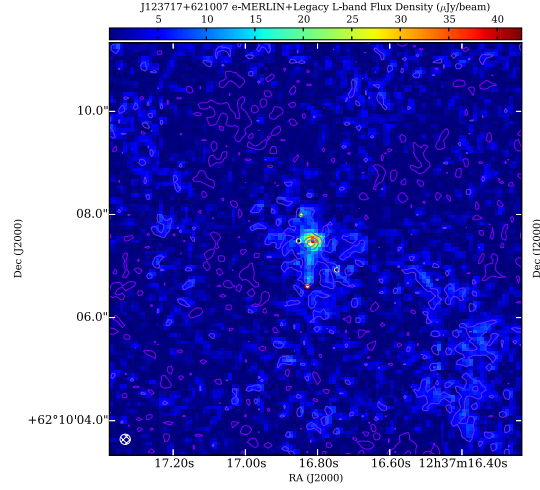


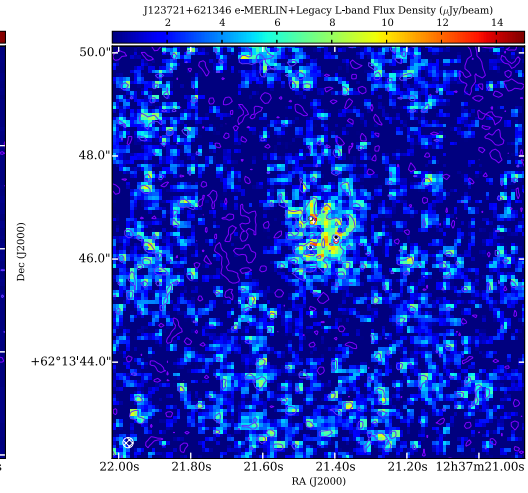
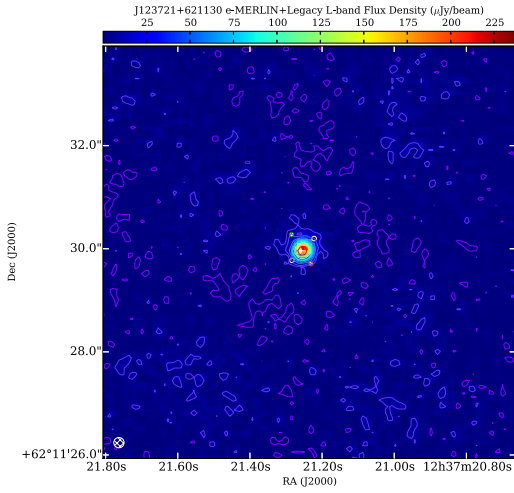
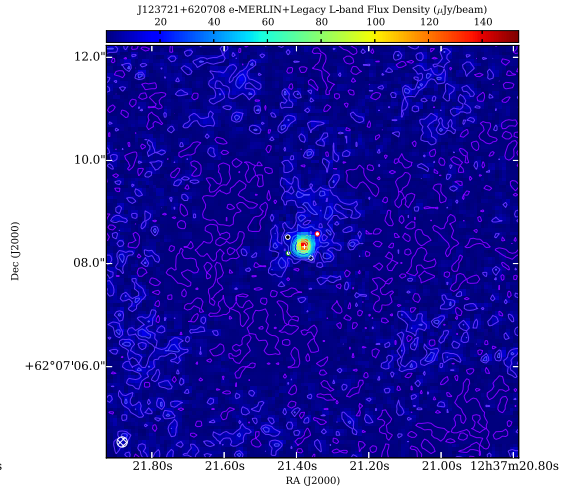
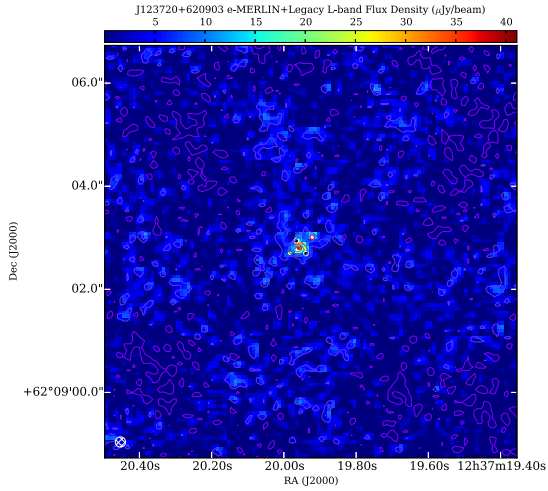
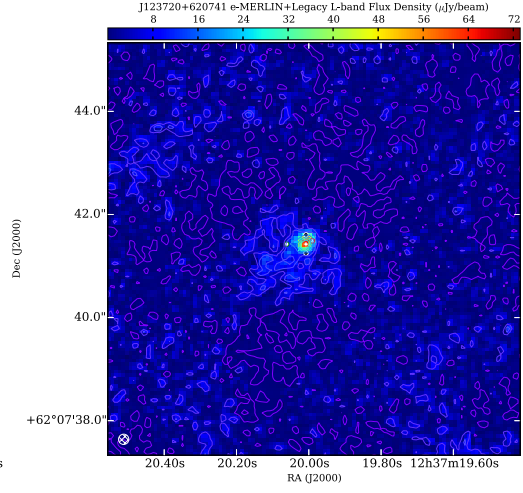
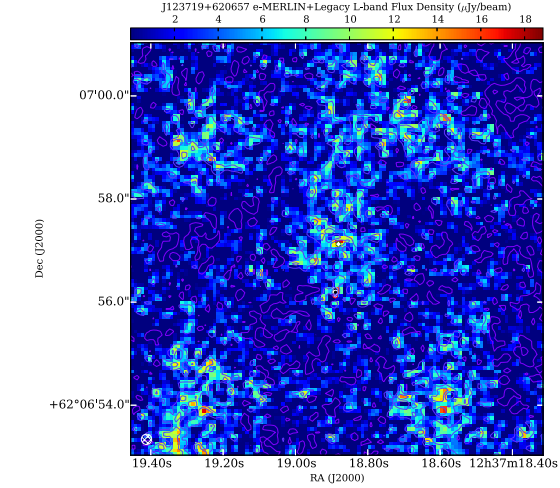


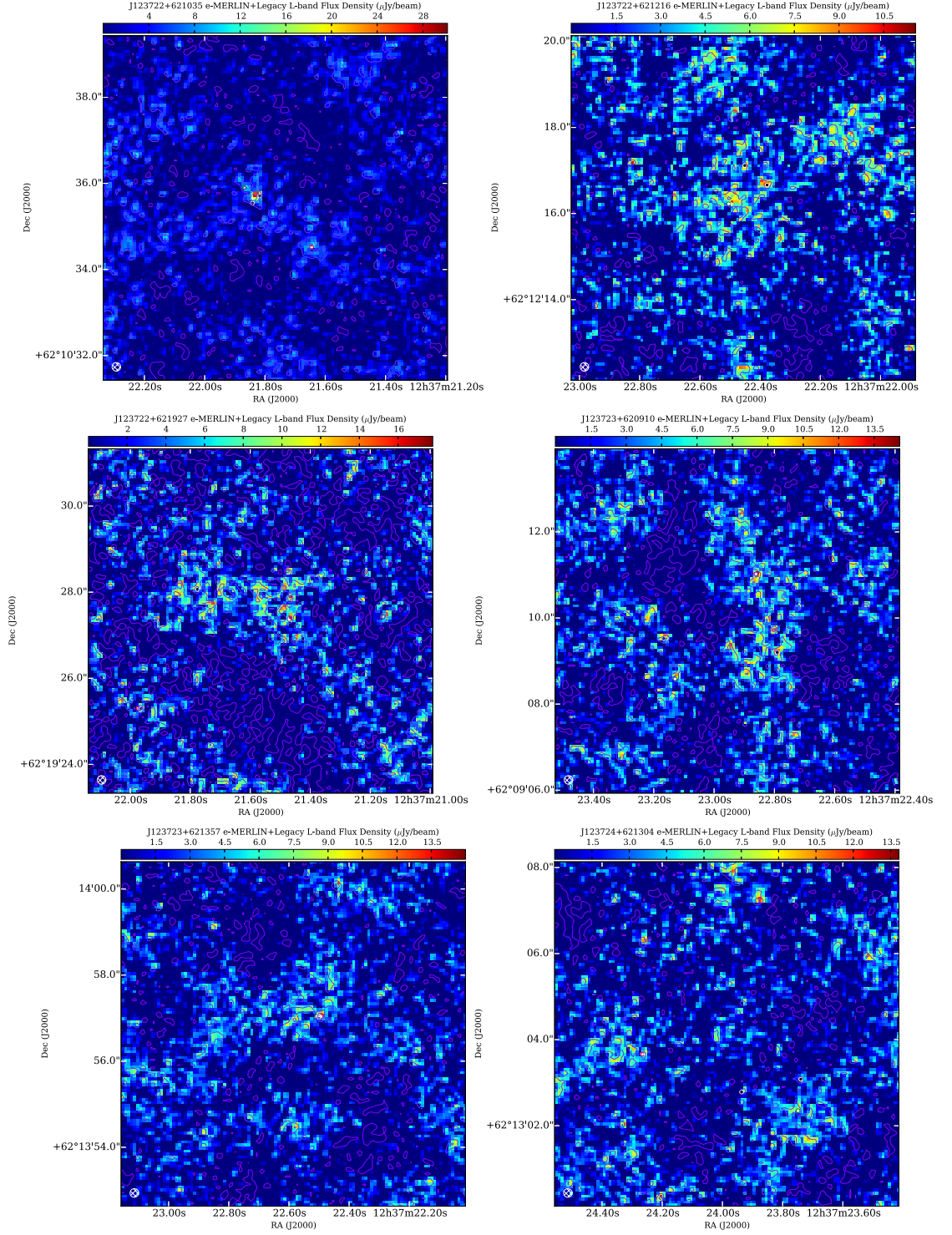


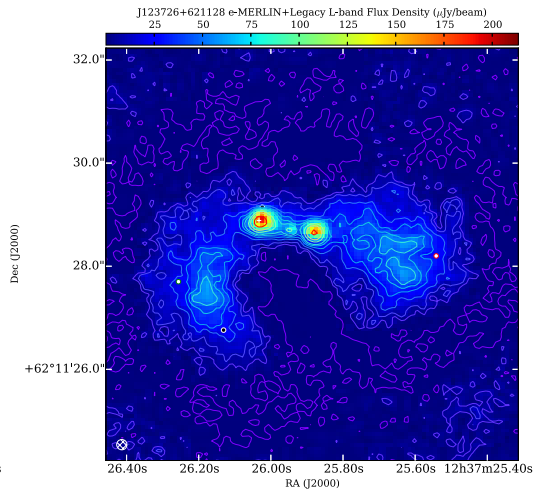
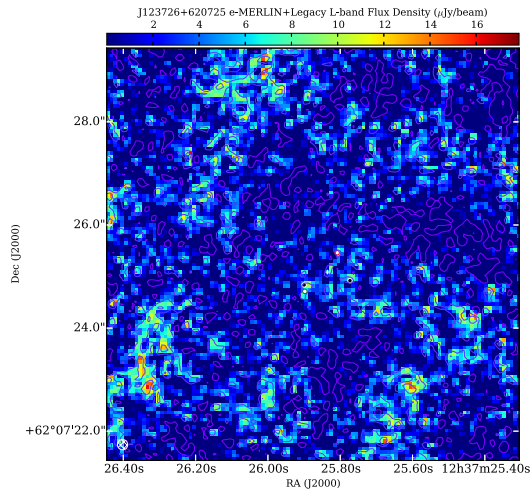
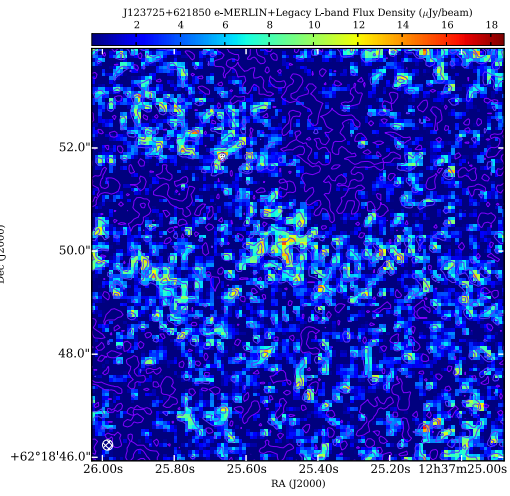
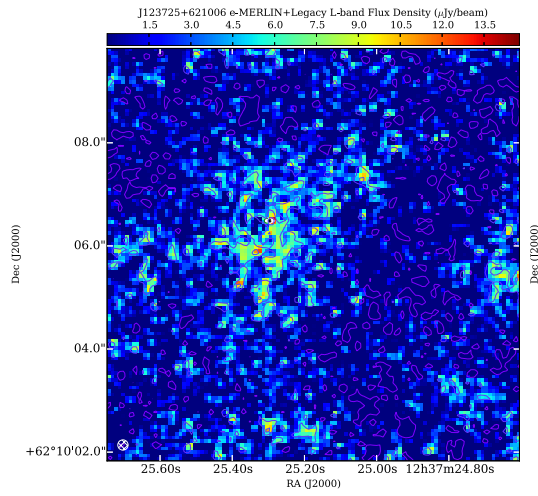
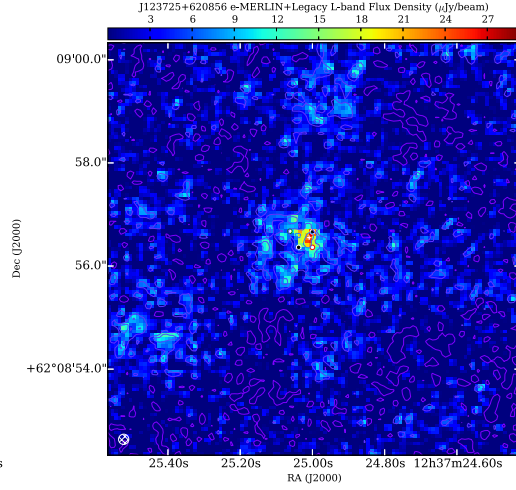
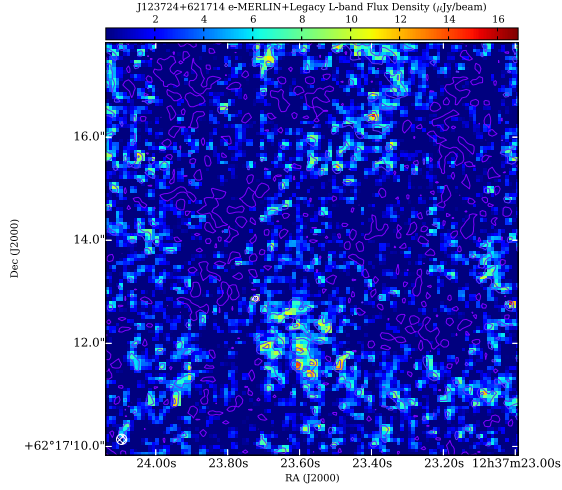


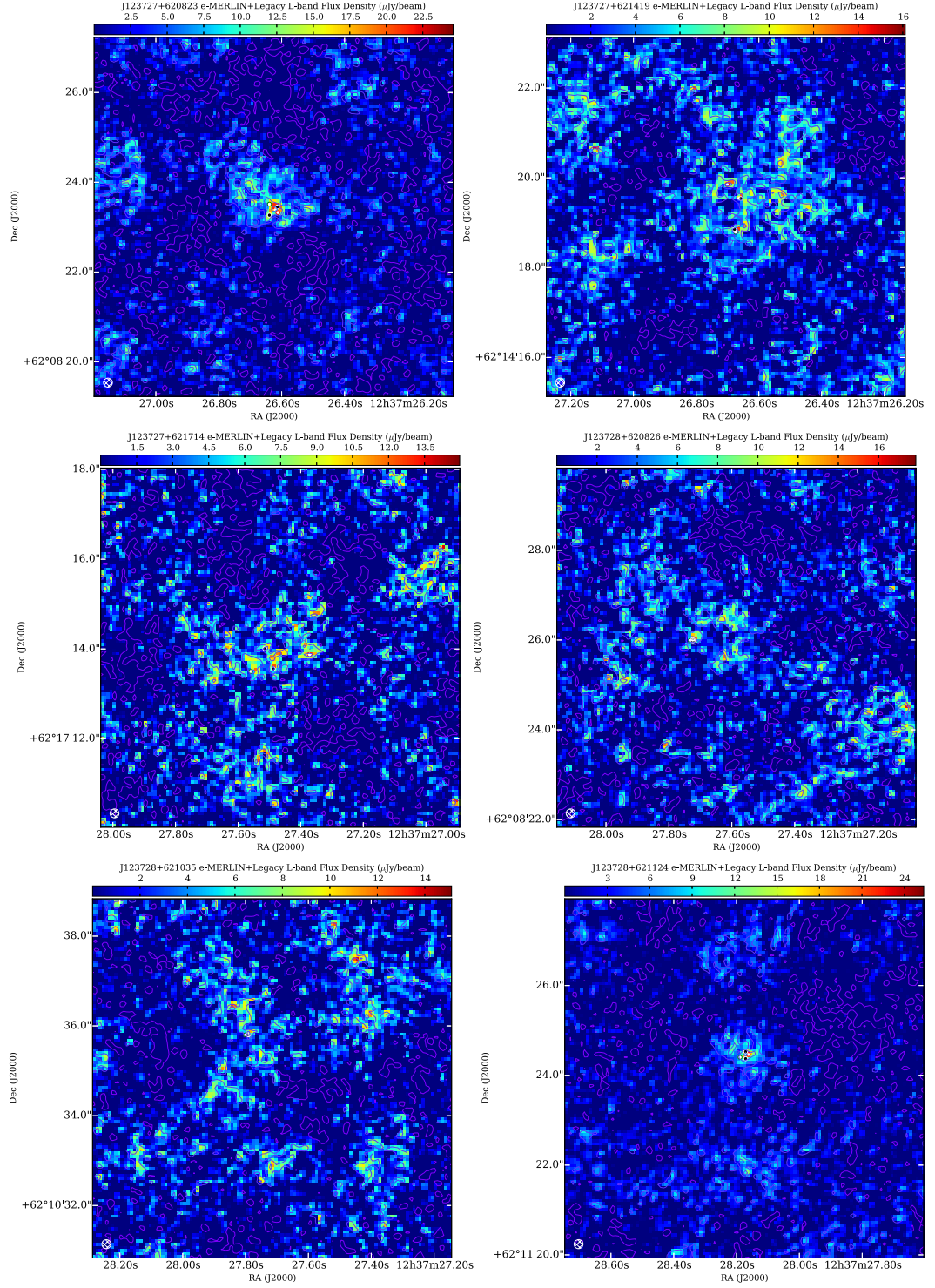


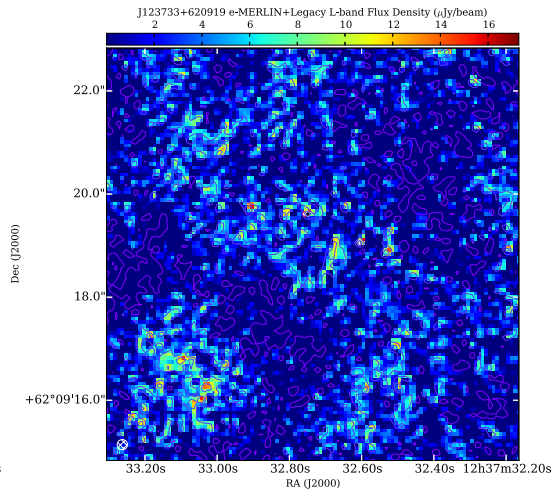
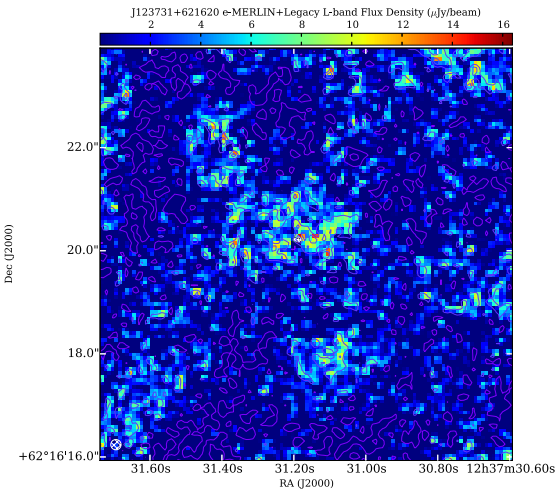
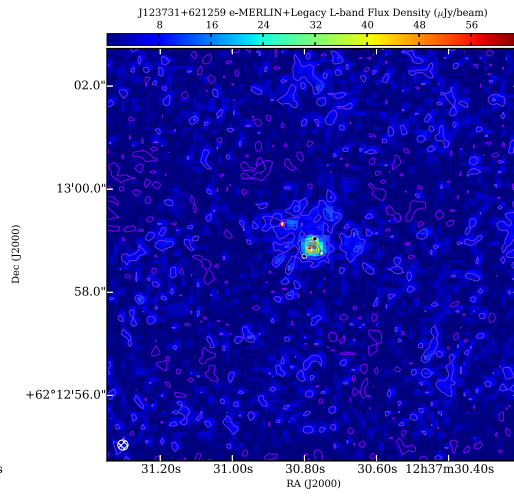
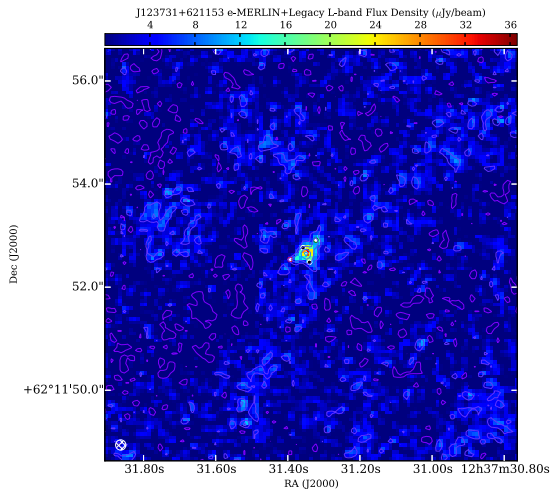
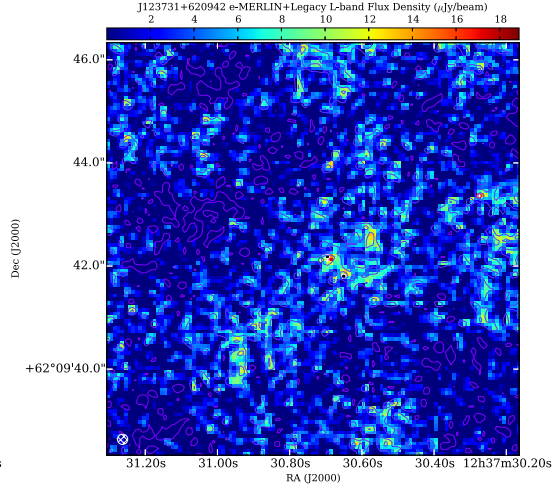
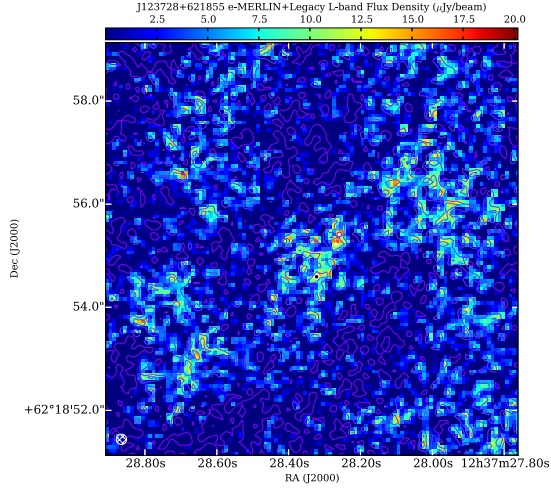


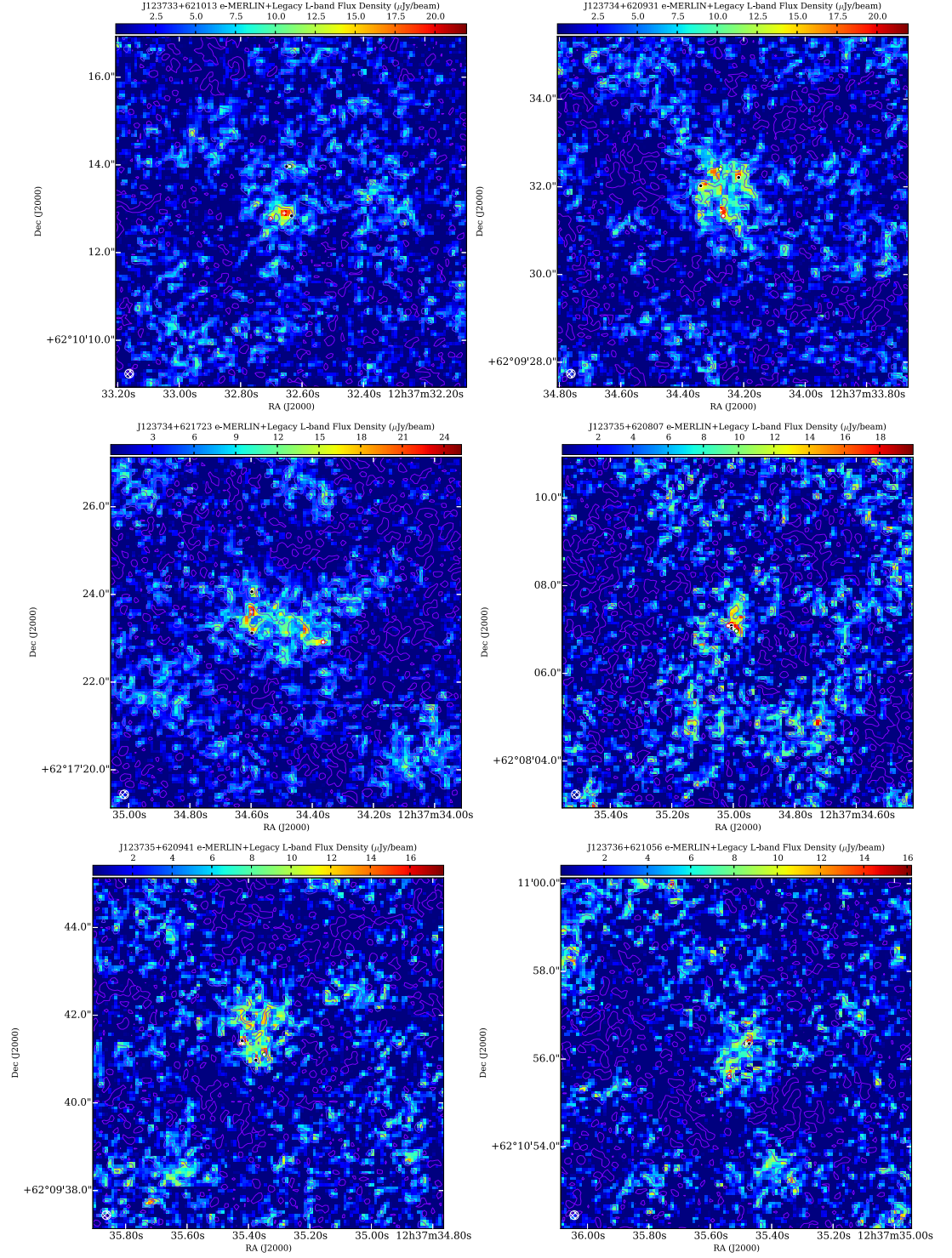


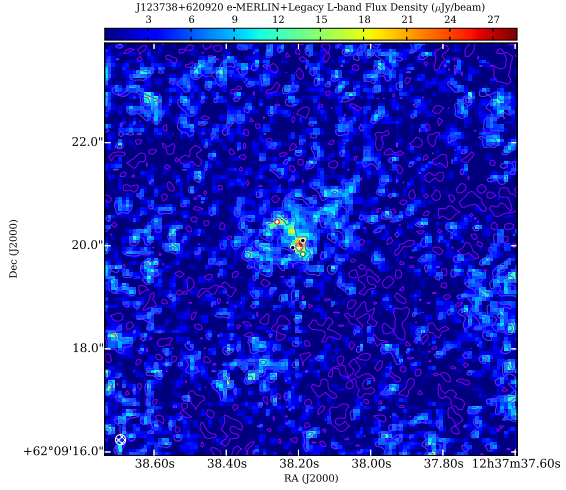
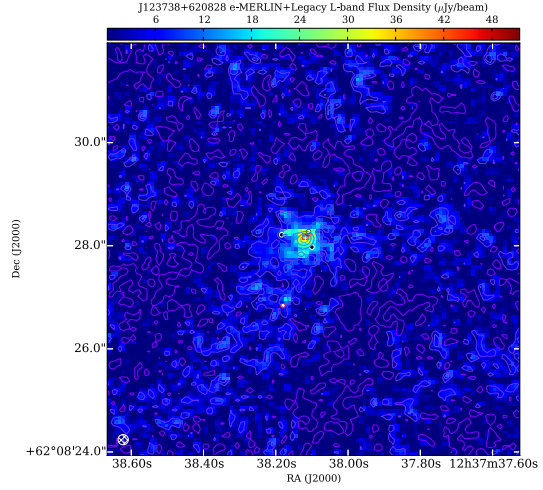
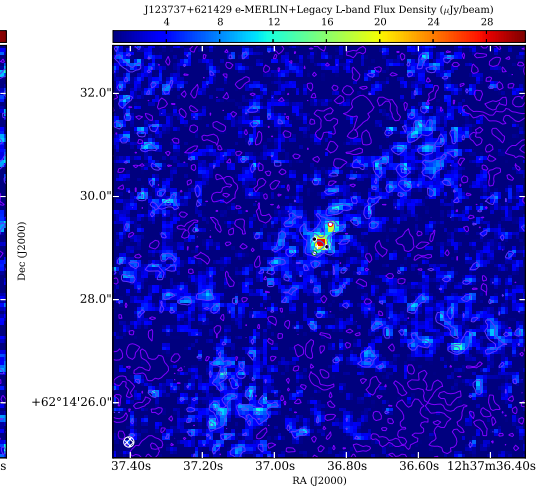
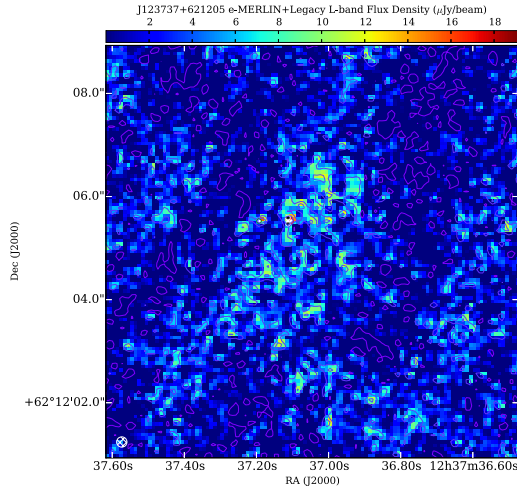
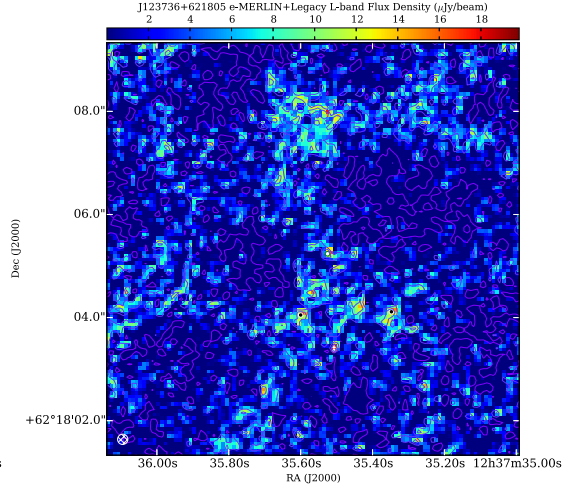
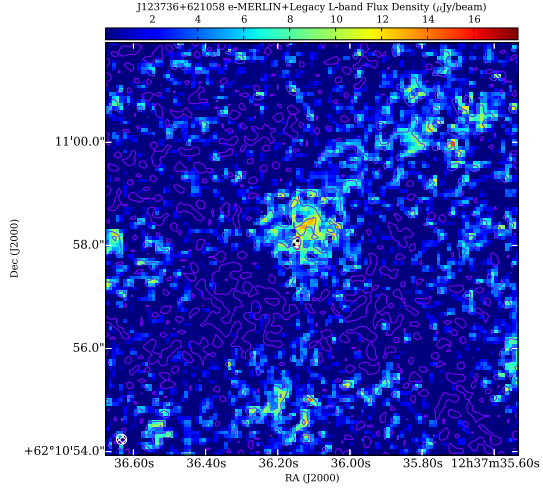


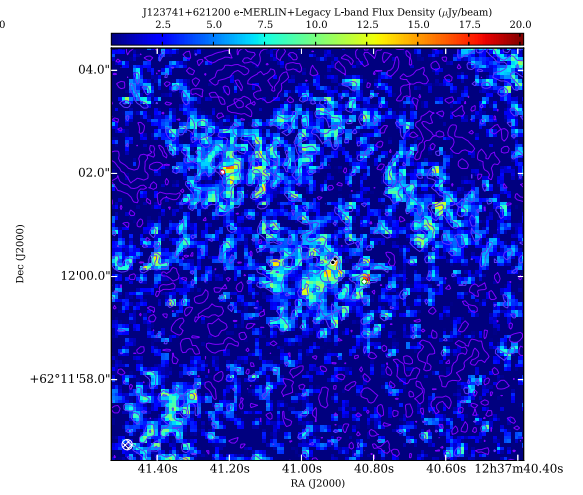
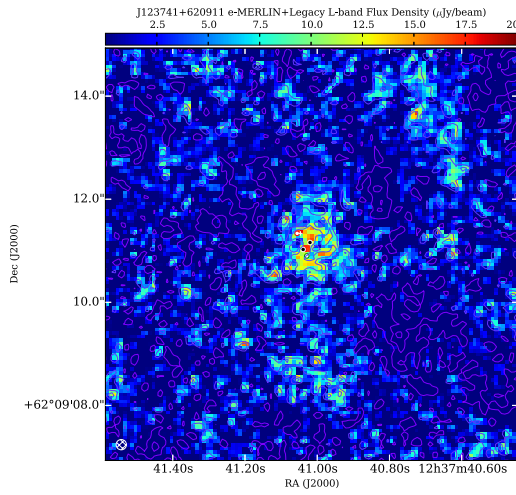
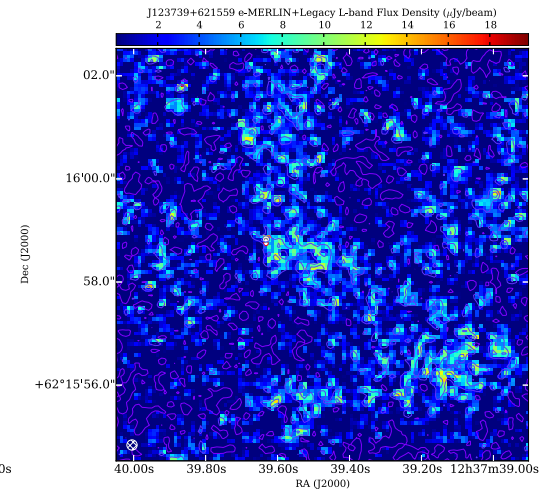
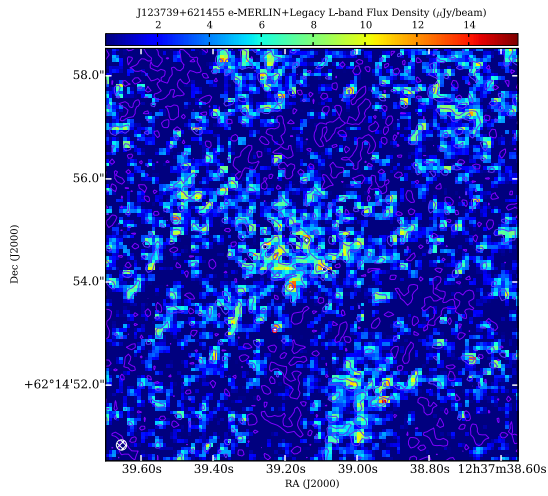
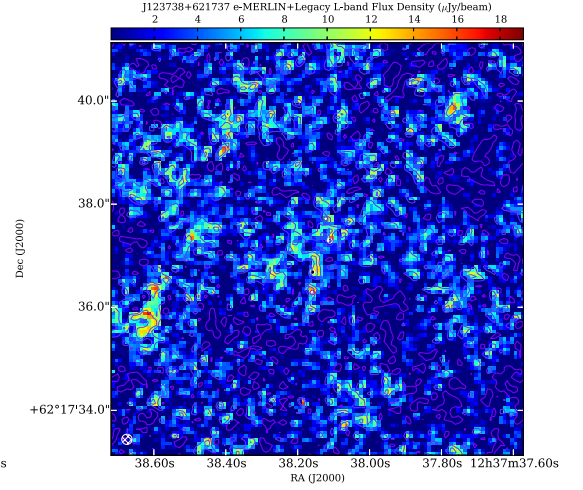
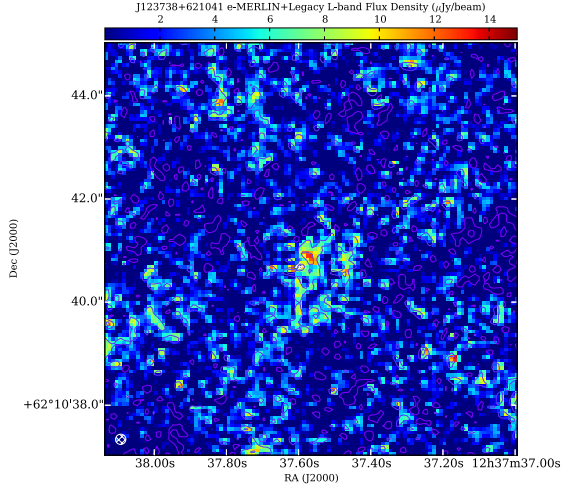


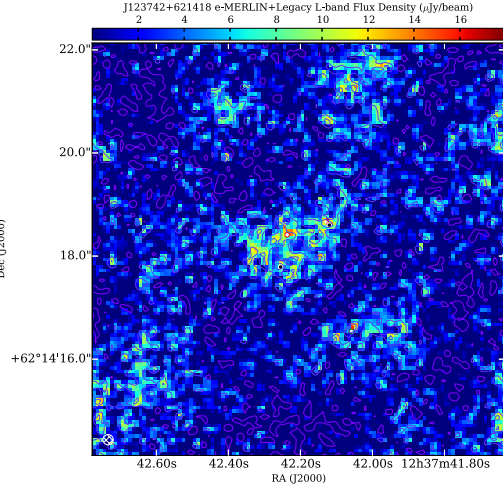
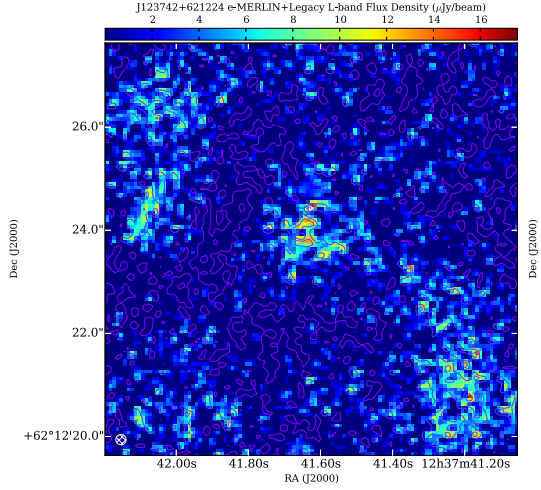
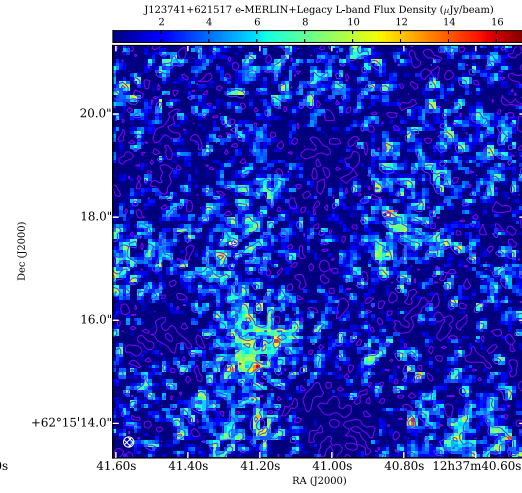
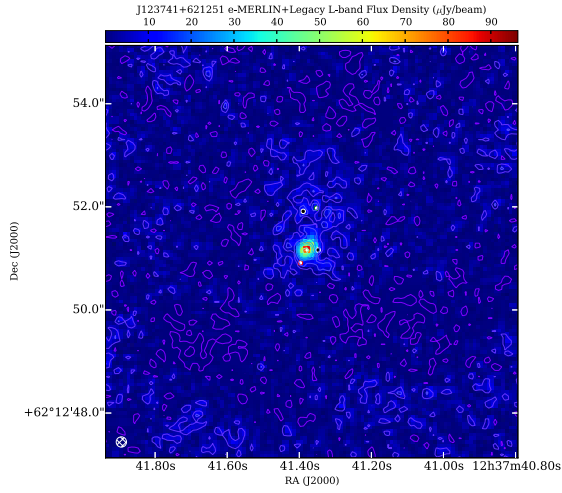
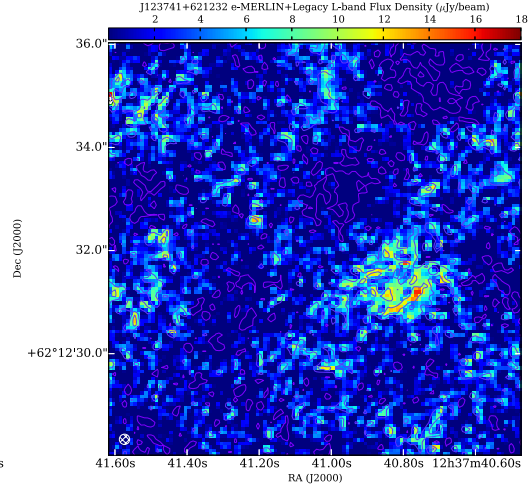
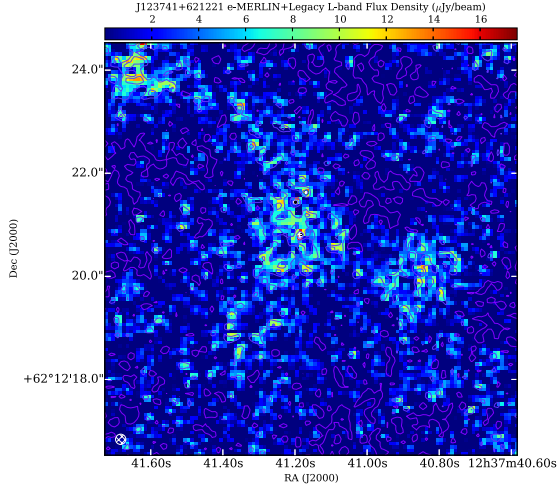


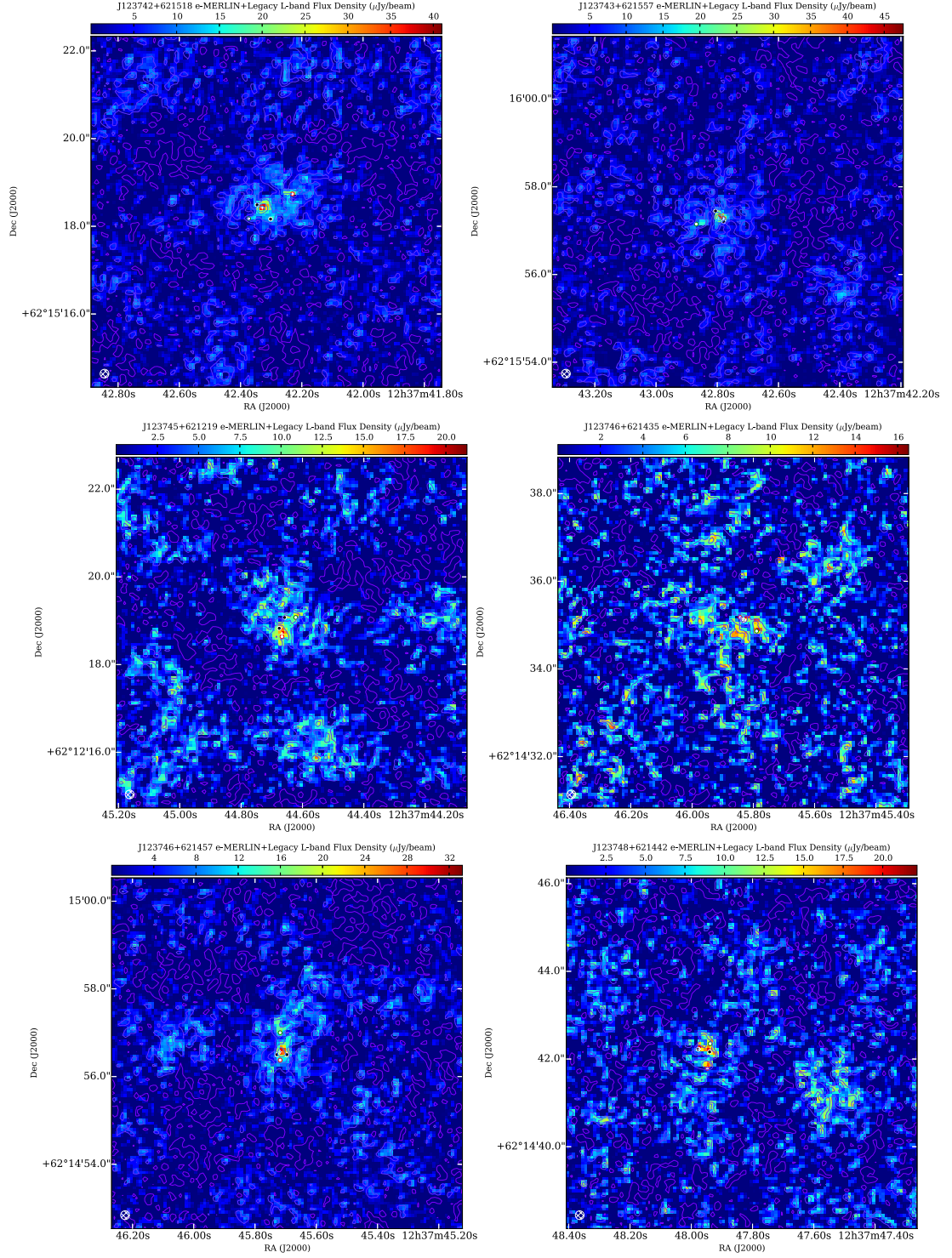


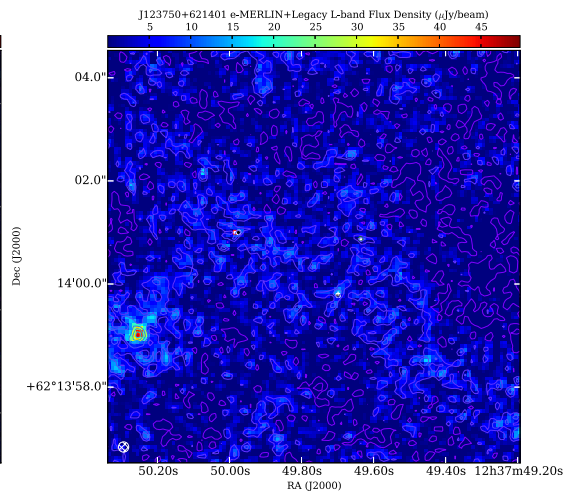
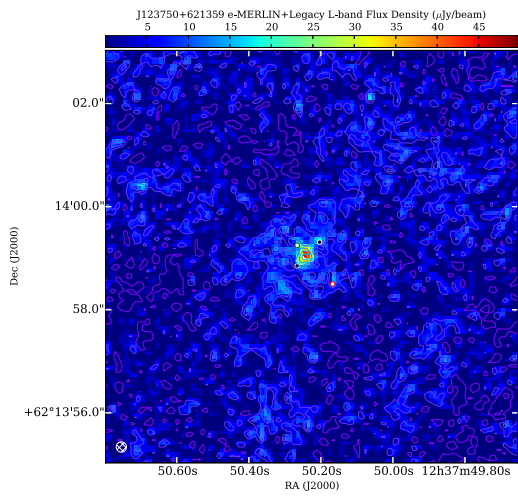
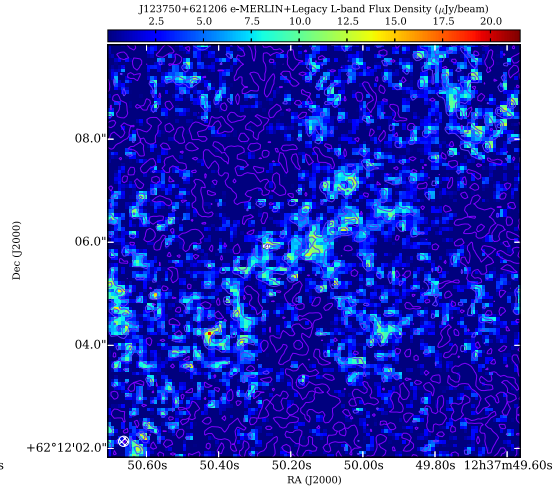
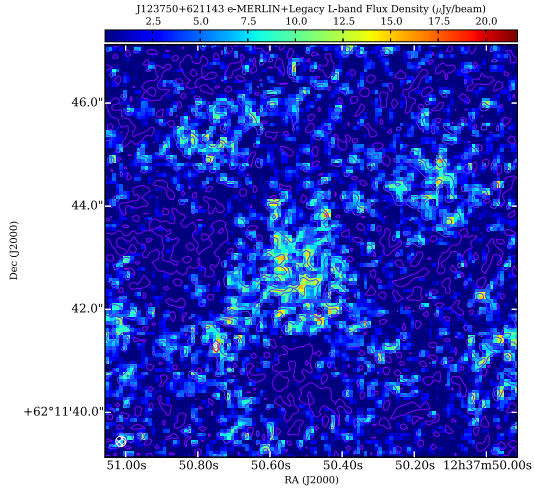












Index

G

Great Observatories Origins Deep Survey,
27

H

Hubble Deep Field North, 27

P

Particle exponent, 34

R

Rayleigh-Jeans Law, 36

S

Spectral Energy Distribution, 30

Supernova remnants, 30, 32

Synchrotron radiation, 33

Synchrotron self-absorption, 35

Bibliography

- Algaba, J. C., 2012. Probing Helical Magnetic Fields in AGN by Rotation Measure Gradients Studies. *International Journal of Modern Physics Conference Series* 8, 303.
- Antonucci, R., 1993. Unified models for active galactic nuclei and quasars. *Annu. Rev. Astron. Astrophys.* 31, 473–521.
- Argo, M. K., January 2015. The e-merlin data reduction pipeline. *Journal of Open Research Software* 3(1):e2, DOI:.
- Barger, A. J., Cowie, L. L., Wang, W.-H., Dec. 2008. A Highly Complete Spectroscopic Survey of the GOODS-N Field1,. *ApJ*689, 687–708.
- Bell, E. F., April 2003. Estimating star formation rates from infrared and radio luminosities: The origin of the radio-infrared correlation. *The Astrophysical Journal* 586, 794–813.
- Beswick, R. J., Muxlow, T. W. B., Thrall, H., Richards, A. M. S., 2006. Sub-arcsecond, microjy radio properties of spitzer identified mid-infrared sources in the hdf-n/goods-n field. In: *At the Edge of the Universe: Latest results from the deepest astronomical surveys*. Sintra, Portugal.
- Beswick, R. J., Muxlow, T. W. B., Thrall, H., Richards, A. M. S., Garrington, S. T., 2008. An evolution of the infrared-radio correlation at very low flux densities? *Mon. Not. R. Astron. Soc.* 385, 1143–1154.
- Bhatnagar, S., 2012. Wide-field imaging: I. In: *Thirteenth Synthesis Imaging Workshop 2012*, May29-June 5.
- Bothwell, M. S., Chapman, S. C., Tacconi, L., Smail, I., Ivison, R. J., Casey, C. M., Bertoldi, F., Beswick, R., Biggs, A., Blain, A. W., Cox, P., Genzel, R., Greve, T. R.,

- Kennicutt, R., Muxlow, T., Neri, R., Omont, A., Jun. 2010. High-resolution CO and radio imaging of ULIRGs: extended CO structures and implications for the universal star formation law. *MNRAS*405, 219–233.
- Bourne, N., Dunne, L., Ivison, R. J., Maddox, S. J., Dickinson, M., Frayer, D. T., Jan. 2011. Evolution of the far-infrared-radio correlation and infrared spectral energy distributions of massive galaxies over $z=0-2$. *MNRAS*410, 1155–1173.
- Bridle, A. H., Schwab, F. R., 1989. Wide field imaging i: Bandwidth and time-average smearing. In: *Synthesis Imaging in Radio Astronomy*. Vol. 6. p. 247.
- Briggs, D., 1998. High fidelity deconvolution of moderately resolved sources. Ph.D. thesis, New Mexico Institute of Mining and Technology.
- Brown, M. L., Battye, R. A., Jan. 2011. Polarization as an indicator of intrinsic alignment in radio weak lensing. *MNRAS*410, 2057–2074.
- Burke, Bernard F. Graham-Smith, F., 1998. *An Introduction to Radio Astronomy*, 2nd Edition. Cambridge University Press.
- Carilli, C., Yun, M. S., 1999. The radio-to-submm spectral index as a redshift indicator. URL <http://arxiv.org/abs/astro-ph/9812251v4>
- Carole Haswell, Ulrich Kolb, S. R., 2002. *Active Galaxies*. The Open University Press.
- Chabrier, G., Jul. 2003. Galactic Stellar and Substellar Initial Mass Function. *PASP*115, 763–795.
- Chang, T.-C., Refregier, A., Helfand, D. J., 2004. Weak lensing by large-scale structure with the first radio survey. URL <http://arxiv.org/abs/astro-ph/0408548>
- Charbonneau, P., Dec. 1995. Genetic Algorithms in Astronomy and Astrophysics. *ApJS*101, 309.
- Chi, S., Barthel, P., Garrett, M., 2013. Deep, wide-field, global vlbi observations of the hubble deep field north (hdf-n) and flanking fields (hff). *Astronomy & Astrophysics* 550, A68.

- Clark, B. G., 1999. Coherence in Radio Astronomy. In: G. B. Taylor, C. L. Carilli, & R. A. Perley (Ed.), *Synthesis Imaging in Radio Astronomy II*. Vol. 180 of *Astronomical Society of the Pacific Conference Series*. pp. 1–+.
- Condon, J. J., Sep. 1984. Cosmological evolution of radio sources found at 1.4 GHz. *ApJ*284, 44–53.
- Condon, J. J., 1992. Radio emission from normal galaxies. *ARA&A*30, 575–611.
- Condon, J. J., Ransom, S. M., 2010. *Essential radio astronomy*. Tech. rep., National Radio Astronomy Observatory.
- Cornwell, T. J., Golap, K., Bhatnagar, S., Nov. 2008. The Noncoplanar Baselines Effect in Radio Interferometry: The W-Projection Algorithm. *IEEE Journal of Selected Topics in Signal Processing* 2, 647–657.
- Cram, L., Hopkins, A., Mobasher, B., Rowan-Robinson, M., Nov. 1998. Star Formation Rates in Faint Radio Galaxies. *ApJ*507, 155–160.
- de Jong, T., Klein, U., Wielebinski, R., Wunderlich, E., Jun. 1985. Radio continuum and far-infrared emission from spiral galaxies - A close correlation. *A&A*147, L6–L9.
- de Zotti, G., Massardi, M., Negrello, M., Wall, J., Feb. 2010. Radio and millimeter continuum surveys and their astrophysical implications. *A&A Rev.*18, 1–65.
- Dole, H., Lagache, G., Puget, J., Dec. 2006. The Cosmic Infrared Background: Resolved, Unresolved and Spitzer Contributions. In: Armus, L., Reach, W. T. (Eds.), *Astronomical Society of the Pacific Conference Series*. Vol. 357 of *Astronomical Society of the Pacific Conference Series*. p. 290.
- Dopita, M. A., Fischera, J., Sutherland, R. S., Kewley, L. J., Tuffs, R. J., Popescu, C. C., van Breugel, W., Groves, B. A., Leitherer, C., Aug. 2006. Modeling the Pan-Spectral Energy Distribution of Starburst Galaxies. II. Control of the H II Region Parameters. *ApJ*647, 244–255.
- Dopita, M. A., Groves, B. A., Fischera, J., Sutherland, R. S., Tuffs, R. J., Popescu, C. C., Kewley, L. J., Reuland, M., Leitherer, C., Feb. 2005. Modeling the Pan-Spectral Energy Distribution of Starburst Galaxies. I. The Role of ISM Pressure and the Molecular Cloud Dissipation Timescale. *ApJ*619, 755–778.

- Etherington, I. M. H., 1933. On the Definition of Distance in General Relativity. *Philosophical Magazine* 15, 761.
- Fanaroff, B. L., Riley, J. M., May 1974. The morphology of extragalactic radio sources of high and low luminosity. *MNRAS* 167, 31P–36P.
- Fenech, D., Beswick, R., Muxlow, T. W. B., Pedlar, A., Argo, M. K., Oct. 2010. Wide-field Global VLBI and MERLIN combined monitoring of supernova remnants in M82. *MNRAS* 408, 607–621.
- Fenech, D. M., Muxlow, T. W. B., Beswick, R. J., Pedlar, A., Argo, M. K., Dec. 2008. Deep MERLIN 5GHz radio imaging of supernova remnants in the M82 starburst. *MNRAS* 391, 1384–1402.
- Ferguson, H. C., Dickinson, M., Giavalisco, M., Kretchmer, C., Ravindranath, S., Idzi, R., Taylor, E., Conselice, C. J., Fall, S. M., Gardner, J. P., Livio, M., Madau, P., Moustakas, L. A., Papovich, C. M., Somerville, R. S., Spinrad, H., Stern, D., Jan. 2004. The Size Evolution of High-Redshift Galaxies. *ApJL* 600, L107–L110.
- Fomalont, E. B., Perley, R. A., 1999. Calibration and Editing. In: G. B. Taylor, C. L. Carilli, & R. A. Perley (Ed.), *Synthesis Imaging in Radio Astronomy II*. Vol. 180 of *Astronomical Society of the Pacific Conference Series*. pp. 79–+.
- Garrett, M. A., Mar. 2002. The FIR/Radio correlation of high redshift galaxies in the region of the HDF-N. *A&A* 384, L19–L22.
- Gauci, A., Zarb Adami, K., Abela, J., May 2010. Machine Learning for Galaxy Morphology Classification. *ArXiv e-prints*.
- Gendre, M., Wall, J. V., Best, P. N., May 2011. Space Densities Of AGN And The FR Dichotomy. In: *American Astronomical Society Meeting Abstracts*. p. 317.02.
- Ginzburg, V. L., Syrovatskii, S. I., 1969. Developments in the Theory of Synchrotron Radiation and its Reabsorption. *ARA&A* 7, 375.
- Graham, A. W., Driver, S. P., Petrosian, V., Conselice, C. J., Bershad, M. A., Crawford, S. M., Goto, T., 2008. Total galaxy magnitudes and effective radii from petrosian magnitudes and radii. *ArXiv e-prints*.
URL <http://arxiv.org/abs/astro-ph/0504287>

- Gray, M. E., Wolf, C., Barden, M., Peng, C. Y., Häußler, B., Bell, E. F., McIntosh, D. H., Guo, Y., Caldwell, J. A. R., Bacon, D., Balogh, M., Barazza, F. D., Böhm, A., Heymans, C., Jahnke, K., Jogee, S., van Kampen, E., Lane, K., Meisenheimer, K., Sánchez, S. F., Taylor, A., Wisotzki, L., Zheng, X., Green, D. A., Beswick, R. J., Saikia, D. J., Gilmour, R., Johnson, B. D., Papovich, C., Mar. 2009. STAGES: the Space Telescope A901/2 Galaxy Evolution Survey. *MNRAS*393, 1275–1301.
- Groves, B., Dopita, M. A., Sutherland, R. S., Kewley, L. J., Fischera, J., Leitherer, C., Brandl, B., van Breugel, W., Jun. 2008. Modeling the Pan-Spectral Energy Distribution of Starburst Galaxies. IV. The Controlling Parameters of the Starburst SED. *ApJS*176, 438–456.
- Guidetti, D., Bondi, M., Prandoni, I., Beswick, R., Muxlow, T., Wrigley, N., Smail, I., McHardy, I., 2013. e-merlin observations at 5 ghz of the goods-n region: pinpointing agn cores in high-redshift galaxies. *Monthly Notices of the Royal Astronomical Society* 432 (4), 2798–2807.
- Guidetti, D., Bondi, M., Prandoni, I., Beswick, R. J., Muxlow, T. W. B., Wrigley, N., Smail, I., McHardy, I., Jul. 2013. e-MERLIN observations at 5 GHz of the GOODS-N region: pinpointing AGN cores in high-redshift galaxies. *MNRAS*432, 2798–2807.
- Haarsma, D. B., Partridge, R. B., Windhorst, R. A., Richards, E. A., Dec. 2000. Faint Radio Sources and Star Formation History. *ApJ*544, 641–658.
- Hales, C. A., Murphy, T., Curran, J. R., Middelberg, E., Gaensler, B. M., Norris, R. P., Sep. 2012. BLOBCAT: software to catalogue flood-filled blobs in radio images of total intensity and linear polarization. *MNRAS*425, 979–996.
- Hocking, A., Geach, J. E., Davey, N., Sun, Y., Jul. 2015. Teaching a machine to see: unsupervised image segmentation and categorisation using growing neural gas and hierarchical clustering. *ArXiv e-prints*.
- Hogg, D. W., May 1999. Distance measures in cosmology. *ArXiv Astrophysics e-prints*.
- Hopkins, A. M., Dec. 2007. The Star Formation History of the Universe. In: Afonso, J., Ferguson, H. C., Mobasher, B., Norris, R. (Eds.), *Deepest Astronomical Surveys*. Vol. 380 of *Astronomical Society of the Pacific Conference Series*. p. 423.

- Hopkins, A. M., Mobasher, B., Cram, L., Rowan-Robinson, M., Jun. 1998. The PHOENIX Deep Survey: 1.4-GHz source counts. *MNRAS*296, 839–846.
- Iribarrem, A. S., Lopes, A. R., Ribeiro, M. B., Stoeger, W. R., Mar. 2012. Relativistic cosmology number densities and the luminosity function. *A&A*539, A112.
- Jarvis, M. J., Smith, D. J. B., Bonfield, D. G., Hardcastle, M. J., Falder, J. T., Stevens, J. A., Ivison, R. J., Auld, R., Baes, M., Baldry, I. K., Bamford, S. P., Bourne, N., Buttiglione, S., Cava, A., Cooray, A., Dariush, A., de Zotti, G., Dunlop, J. S., Dunne, L., Dye, S., Eales, S., Fritz, J., Hill, D. T., Hopwood, R., Hughes, D. H., Ibar, E., Jones, D. H., Kelvin, L., Lawrence, A., Leeuw, L., Loveday, J., Maddox, S. J., Michałowski, M. J., Negrello, M., Norberg, P., Pohlen, M., Prescott, M., Rigby, E. E., Robotham, A., Rodighiero, G., Scott, D., Sharp, R., Temi, P., Thompson, M. A., van der Werf, P., van Kampen, E., Vlahakis, C., White, G., Nov. 2010. Herschel-ATLAS: the far-infrared-radio correlation at $z = 0.5$. *MNRAS*409, 92–101.
- Juhan Frank, Andrew King, D. R., 2002. *Accretion Power in Astrophysics*, 3rd Edition. Cambridge University Press.
- Kennicutt, Jr., R. C., May 1998. The Global Schmidt Law in Star-forming Galaxies. *ApJ*498, 541.
- Kettenis, M., van Langevelde, H. J., Reynolds, C., Cotton, B., 2006. Parseltongue: Aips talking python. In: *Astronomical data analysis software and systems XV*. Vol. 351. p. 497.
- Klamer, I. J., Ekers, R. D., Hunstead, R. W., Dec. 2007. Radio SEDs of High-redshift Radio Galaxies. In: Afonso, J., Ferguson, H. C., Mobasher, B., Norris, R. (Eds.), *Deepest Astronomical Surveys*. Vol. 380 of *Astronomical Society of the Pacific Conference Series*. p. 213.
- Kroupa, P., Apr. 2001. On the variation of the initial mass function. *MNRAS*322, 231–246.
- Krumholz, M. R., Dekel, A., McKee, C. F., Jan. 2012. A Universal, Local Star Formation Law in Galactic Clouds, nearby Galaxies, High-redshift Disks, and Starbursts. *ApJ*745, 69.

- Lilly, S. J., Le Fevre, O., Hammer, F., Crampton, D., Mar. 1996. The Canada-France Redshift Survey: The Luminosity Density and Star Formation History of the Universe to z approximately 1. *ApJL*460, L1.
- Lintott, C. J., Schawinski, K., Slosar, A., Land, K., Bamford, S., Thomas, D., Raddick, M. J., Nichol, R. C., Szalay, A., Andreescu, D., Murray, P., Vandenberg, J., Sep. 2008. Galaxy Zoo: morphologies derived from visual inspection of galaxies from the Sloan Digital Sky Survey. *MNRAS*389, 1179–1189.
- Lisenfeld, U., Voelk, H. J., Xu, C., Oct. 1996. The FIR/radio correlation in starburst galaxies: constraints on starburst models. *A&A*314, 745–753.
- Longair, M. S., 1994. High Energy Astrophysics: Volume 2 Stars, the Galaxy and the Interstellar Medium. Vol. 2. Cambridge University Press.
- Lonsdale, C. J., Diamond, P. J., Thrall, H., Smith, H. E., Lonsdale, C. J., Aug. 2006. VLBI Images of 49 Radio Supernovae in Arp 220. *ApJ*647, 185–193.
- Madau, P., 1998. Cosmic Star Formation History and the Early Evolution of Galaxies. In: P. Petitjean & S. Charlot (Ed.), *Structure et Evolution du Milieu Inter-Galactique Revele par Raies D’Absorption dans le Spectre des Quasars*, 13th Colloque d’Astrophysique de l’Institut d’Astrophysique de Paris. pp. 295–+.
- Madau, P., Dickinson, M., Aug. 2014. Cosmic Star-Formation History. *ARA&A*52, 415–486.
- Madau, P., Ferguson, H. C., Dickinson, M. E., Giavalisco, M., Steidel, C. C., Fruchter, A., Dec. 1996. High-redshift galaxies in the Hubble Deep Field: colour selection and star formation history to $z \sim 4$. *MNRAS*283, 1388–1404.
- Mao, M. Y., Huynh, M. T., Norris, R. P., Dickinson, M., Frayer, D., Helou, G., Monkiewicz, J. A., Apr. 2011. No Evidence for Evolution in the Far-infrared-Radio Correlation out to $z \sim 2$ in the Extended Chandra Deep Field South. *ApJ*731, 79.
- Mauch, T., Sadler, E. M., Mar. 2007. Radio sources in the 6dFGS: local luminosity functions at 1.4GHz for star-forming galaxies and radio-loud AGN. *MNRAS*375, 931–950.

- Miller, G. E., Scalo, J. M., Nov. 1979. The initial mass function and stellar birthrate in the solar neighborhood. *ApJS*41, 513–547.
- Morrison, G. E., Owen, F. N., Dickinson, M., Ivison, R. J., Ibar, E., May 2010. Very Large Array 1.4 GHz Observations of the GOODS-North Field: Data Reduction and Analysis. *ApJS*188, 178–186.
- Muñoz, J. A., Mediavilla, E., Kochanek, C. S., Falco, E. E., Mosquera, A. M., Dec. 2011. A Study of Gravitational Lens Chromaticity with the Hubble Space Telescope. *ApJ*742, 67.
- Muxlow, S., McHardy, 2011. The e-merge survey: e-merlin galaxy evolution survey. URL <http://www.e-merlin.ac.uk/legacy/projects/emerge.html>
- Muxlow, T. W. B., Richards, A. M. S., Garrington, S. T., Wilkinson, P. N., Anderson, B., Richards, E. A., Axon, D. J., Fomalont, E. B., Kellermann, K. I., Partridge, R. B., Windhorst, R. A., Apr. 2005. High-resolution studies of radio sources in the Hubble Deep and Flanking Fields. *MNRAS*358, 1159–1194.
- Niklas, S., Beck, R., Apr. 1997. A new approach to the radio-far infrared correlation for non-calorimeter galaxies. *A&A*320, 54–64.
- Patel, P., Bacon, D. J., Beswick, R. J., Muxlow, T. W. B., Hoyle, B., 07 2009. Radio weak gravitational lensing with vla and merlin. URL <http://arxiv.org/abs/0907.5156>
- Peck, L. W., Fenech, D. M., 2013. Serpent: Automated reduction and rfi-mitigation software for e-merlin. *Astronomy and Computing* 2, 54–66.
- Pedregosa, F., Varoquaux, G., Gramfort, A., Michel, V., Thirion, B., Grisel, O., Blondel, M., Prettenhofer, P., Weiss, R., Dubourg, V., et al., 2011. Scikit-learn: Machine learning in python. *The Journal of Machine Learning Research* 12, 2825–2830.
- Peel, M. W., Dickinson, C., Davies, R. D., Clements, D. L., Beswick, R. J., Sep. 2011. Radio to infrared spectra of late-type galaxies with Planck and Wilkinson Microwave Anisotropy Probe data. *MNRAS*416, L99–L103.
- Perley, R., 2000. Perley fit pbcor aips explain file.

- Perley, R. A., 1999a. Imaging with non-coplanar arrays. In: *Synthesis Imaging in Radio Astronomy II*. Vol. 180 of *Astronomical Society of the Pacific Conference Series*. p. 394.
- Perley, R. A., 1999b. Imaging with non-coplanar arrays. In: *Synthesis Imaging in Radio Astronomy II*. Vol. 180. p. 383.
- Perry, J. J., Ward, M. J., Jones, M., Oct. 1987. 3C 273 and the power-law myth. *MNRAS* 228, 623–634.
- Peterson, B. M., 1997. *An Introduction to Active Galactic Nuclei*. Cambridge University Press.
- Petrosian, V., 1976. Surface brightness and evolution of galaxies. *The Astrophysical Journal* 209, L1–L5.
- Planck Collaboration, Ade, P. A. R., Aghanim, N., Arnaud, M., Ashdown, M., Aumont, J., Baccigalupi, C., Balbi, A., Banday, A. J., Barreiro, R. B., et al., Dec. 2011. Planck early results. XX. New light on anomalous microwave emission from spinning dust grains. *A&A* 536, A20.
- Popping, A., Braun, R., Mar. 2008. The standing wave phenomenon in radio telescopes. Frequency modulation of the WSRT primary beam. *A&A* 479, 903–913.
- Prandoni, I., Aug. 2010. The AGN Component in Deep Radio Fields: Current Understanding. *ArXiv e-prints*.
- R. Thompson, J. Moran, G. S., 2001. *Interferometry and Synthesis in Radio Astronomy*, 2nd Edition. Wiley VCH.
- Rau, U., Bhatnagar, S., Voronkov, M. A., Cornwell, T. J., Aug. 2009. Advances in Calibration and Imaging Techniques in Radio Interferometry. *IEEE Proceedings* 97, 1472–1481.
- Ribeiro, M. B., Aug. 2002. Limited-frequency-range observations of cosmological point sources. *The Observatory* 122, 201–210.
- Ribeiro, M. B., Stoeger, W. R., Jul. 2003. Relativistic Cosmology Number Counts and the Luminosity Function. *ApJ* 592, 1–16.

- Richards, A. M. S., Muxlow, T. W. B., Beswick, R., Allen, M. G., Benson, K., Dickson, R. C., Garrett, M. A., Garrington, S. T., Gonzalez-Solarez, E., Harrison, P. A., Holloway, A. J., Kettenis, M. M., Laing, R. A., Richards, E. A., Thrall, H., van Langevelde, H. J., Walton, N. A., Wilkinson, P. N., Winstanley, N., Sep. 2007. Using VO tools to investigate distant radio starbursts hosting obscured AGN in the HDF(N) region. *A&A*472, 805–822.
- Rowan-Robinson, M., Benn, C. R., Lawrence, A., McMahon, R. G., Broadhurst, T. J., Jul. 1993. The evolution of faint radio sources. *MNRAS*263, 123–130.
- Salpeter, E. E., Jan. 1955. The Luminosity Function and Stellar Evolution. *ApJ*121, 161–+.
- Saunders, W., Rowan-Robinson, M., Lawrence, A., Efstathiou, G., Kaiser, N., Ellis, R. S., Frenk, C. S., Jan. 1990. The 60-micron and far-infrared luminosity functions of IRAS galaxies. *MNRAS*242, 318–337.
- Schechter, P., Jan. 1976. An analytic expression for the luminosity function for galaxies. *ApJ*203, 297–306.
- Scheuer, P. A. G., 1957. A statistical method for analysing observations of faint radio stars. *Proceedings of the Cambridge Philosophical Society* 53, 764–773.
- Schmidt, M., Mar. 1959. The Rate of Star Formation. *ApJ*129, 243.
- Scoville, N., Soifer, B. T., May 1991. *H₂ and Infrared in Global Starburst Galaxies*. the Cambridge University Press, p. 233.
- Sedgwick, C., Serjeant, S., Pearson, C., Matsuura, S., Shirahata, M., Oyabu, S., Goto, T., Matsuhara, H., Clements, D. L., Negrello, M., White, G. J., Sep. 2011. Far-infrared luminosity function of local star-forming galaxies in the AKARI Deep Field-South. *MNRAS*416, 1862–1870.
- Sersic, J. L., 1968. *Atlas de galaxias australes*. Cordoba, Argentina: Observatorio Astronomico, 1968 1.
- Seymour, N., Dwelly, T., Moss, D., McHardy, I., Zoghbi, A., Rieke, G., Page, M., Hopkins, A., Loaring, N., May 2008. The star formation history of the Universe as revealed by deep radio observations. *MNRAS*386, 1695–1708.

- Seymour, N., McHardy, I. M., Gunn, K. F., Jul. 2004. Radio observations of the 13th xmm-newton rosat deep x-ray survey area. *MNRAS*352, 131–141.
- Simpson, C., Rawlings, S., Ivison, R., Akiyama, M., Almaini, O., Bradshaw, E., Chapman, S., Chuter, R., Croom, S., Dunlop, J., Foucaud, S., Hartley, W., Apr. 2012. Radio imaging of the Subaru/XMM-Newton Deep Field- III. Evolution of the radio luminosity function beyond $z=1$. *MNRAS*421, 3060–3083.
- Singal, A. K., Singh, R. L., Aug. 2013. Incongruity of the unified scheme with a 3CRR-like equatorial strong-source sample. *MNRAS*435, L38–L42.
- Smith, H. E., Lonsdale, C. J., Lonsdale, C. J., Diamond, P. J., Jan. 1998. A Starburst Revealed—Luminous Radio Supernovae in the Nuclei of ARP 220. *ApJL*493, L17–L21.
- Smolčić, V., Schinnerer, E., Scodeggio, M., Franzetti, P., Aussel, H., Bondi, M., Brusa, M., Carilli, C. L., Capak, P., Charlot, S., Ciliegi, P., Ilbert, O., Ivezić, Ž., Jahnke, K., McCracken, H. J., Obrić, M., Salvato, M., Sanders, D. B., Scoville, N., Trump, J. R., Tremonti, C., Tasca, L., Walcher, C. J., Zamorani, G., Jul. 2008. A New Method to Separate Star-forming from AGN Galaxies at Intermediate Redshift: The Submillijansky Radio Population in the VLA-COSMOS Survey. *ApJS*177, 14–38.
- Sohn, B. W., Klein, U., Mack, K.-H., Jun. 2003. The spectral-curvature parameter: An alternative tool for the analysis of synchrotron spectra. *A&A*404, 133–144.
- Strong, A. W., Orlando, E., Jaffe, T. R., Oct. 2011. The interstellar cosmic-ray electron spectrum from synchrotron radiation and direct measurements. *A&A*534, A54.
- Taylor, G. B., Carilli, C. L., Perley, R. A. (Eds.), 1999. *Synthesis Imaging in Radio Astronomy II*. Vol. 180 of *Astronomical Society of the Pacific Conference Series*.
- Thompson, A. R., 1999. *Fundamentals of Radio Interferometry*. In: G. B. Taylor, C. L. Carilli, & R. A. Perley (Ed.), *Synthesis Imaging in Radio Astronomy II*. Vol. 180 of *Astronomical Society of the Pacific Conference Series*. pp. 11–+.
- Urry, C. M., Padovani, P., Sep. 1995. Unified Schemes for Radio-Loud Active Galactic Nuclei. *PASP*107, 803–+.

- Vernstrom, T., Scott, D., Wall, J. V., Condon, J. J., Cotton, W. D., Fomalont, E. B., Kellermann, K. I., Miller, N., Perley, R. A., May 2014. Deep 3 GHz number counts from a P(D) fluctuation analysis. *MNRAS*440, 2791–2809.
- Völk, H. J., Sep. 1989. The correlation between radio and far-infrared emission for disk galaxies. In: Böhm-Vitense, E. (Ed.), *Infrared Spectroscopy in Astronomy*. Vol. 290 of ESA Special Publication. pp. 531–534.
- Waddington, I., Windhorst, R. A., Cohen, S. H., Partridge, R. B., Spinrad, H., Stern, D., Dec. 1999. NICMOS Imaging of the Dusty Microjansky Radio Source VLA J123642+621331 at $z = 4.424$. *ApJL*526, L77–L80.
- Weiler, K. W., Panagia, N., Montes, M. J., Sramek, R. A., 2002. Radio Emission from Supernovae and Gamma-Ray Bursters. *ARA&A*40, 387–438.
- Wilman, R. J., Miller, L., Jarvis, M. J., Mauch, T., Levrier, F., Abdalla, F. B., Rawlings, S., Klöckner, H.-R., Obreschkow, D., Olteanu, D., Young, S., Aug. 2008. A semi-empirical simulation of the extragalactic radio continuum sky for next generation radio telescopes. *MNRAS*388, 1335–1348.
- Wold, M., Lacy, M., Armus, L., Aug. 2007. The influence of AGN nuclear parameters on the FRI/FRII dichotomy. *A&A*470, 531–538.
- Wrigley, N., 2011. High resolution wide-field radio imaging of the goods north field. Master’s thesis, Jodrell Bank Centre for Astrophysics, University of Manchester.
- Wucknitz, O., 2010. Efficient wide-field vlbi imaging. In: 10th European VLBI Network Symposium and EVN Users Meeting: VLBI and the New Generation of Radio Arrays. Vol. 1. p. 100.
- Yun, M. S., Reddy, N. A., Condon, J. J., Jun. 2001. Radio Properties of Infrared-selected Galaxies in the IRAS 2 Jy Sample. *ApJ*554, 803–822.